# THE UNIVERSITY OF HULL

## An Investigation of Liquid Crystalline and Semiconducting Blends for Applications in Photovoltaics

being a Thesis submitted for the Degree of

*Doctor of Philosophy (PhD)*

in the University of Hull

by

Steven A. Myers, BSc (Hons)

May 2012

# Acknowledgements

This thesis was only made possible thanks to the many individuals who provided invaluable help and guidance along the way.

First of all I would like to thank Prof. Mary O'Neill for her invaluable support and guidance throughout my research.

I would like to thank Prof. Steve Kelly for his insightful advice, particularly with respect to liquid crystals. I also extend my gratitude to Dr. Stuart P. Kitney for the synthesis of the liquid crystal semiconductors investigated in this thesis, and for guidance with the DSC.

Thanks also to my colleagues and staff at the University of Hull for providing a good working environment and a happy atmosphere. I am particularly grateful to Gordon Sowersby for the excellent technical support and advice he provided. I would also like to thank Dr. Matthew Wright for his invaluable help. As a recipient of an 80th Anniversary scholarship from the University of Hull, I would like to express my gratitude for financial support for my PhD studies.

I would also like to thank previous members of the organophotonics group. I extend my gratitude to Dr. Manea Alkhalifah and Dr C. H. Lei for teaching me many of the techniques used in this thesis. Thanks also to Dr Alicia Liedtke introducing me to the lab at the beginning of my research work.

Finally I would like to thank my wife, Sandra, my son, Alfie, and my father for their belief in me and their support throughout my studies.

# Abstract

We investigated a number of novel liquid crystalline semiconductors which have been synthesised in house at the University of Hull. The electrochemical and optical properties of these materials were studied, in order to assess their suitability as donor or acceptor materials for photovoltaic (PV) devices. We investigated the HOMO and LUMO energies of materials with similar chemical structures and hence identified the effect of adding or removing certain molecular groups. Compounds with a benzothiadiazole-thiophene structure were found to be potentially low band gap electron donor materials with perylene based compounds as electron acceptors. Fluorene-thiophene based compounds were also identified as potential electron donors. Charge mobility was studied for several electron donor compounds with similar chemical structures. Donor and acceptor (D/A) blends were investigated and compared to the pure compounds. The Time of Flight (TOF) technique was used to measure mobility. For the pure donor a reduction in mobility is seen when the molecule chain is extended with two additional thiophene groups. The electron mobility of the blends was higher by 2 orders of magnitude than that of the pure acceptor. This provides the blends with balanced charge transport for PV devices.

We fabricated and characterised bulk heterojunction PV devices mixing various donor materials with the same perylene acceptor. The highest device efficiency was produced by a fluorene-thiophene structured donor compound. The fill factor (FF) for all devices was poor and this may be attributed to the acceptor material. We investigated the phase transitions of several D/A blends. An improved device efficiency was produced when we annealed within the liquid crystal phase. We investigated the thin film morphology using an atomic force microscope (AFM) and correlated domain size to PV device performance.

## Table of Contents

# 1. Introduction

## 1.1 Motivation

There has been much interest recently in renewable energy, largely due to concerns over pollution caused by traditional methods of creating energy. Our need for energy is also increasing year on year, as illustrated in figure 1.1, and this trend is likely to continue. It can be seen that most of the projected energy demand increase is from countries which are not members of the Organisation for Economic Co-operation and Development (OECD). Energy is shown in British thermal units (Btu).
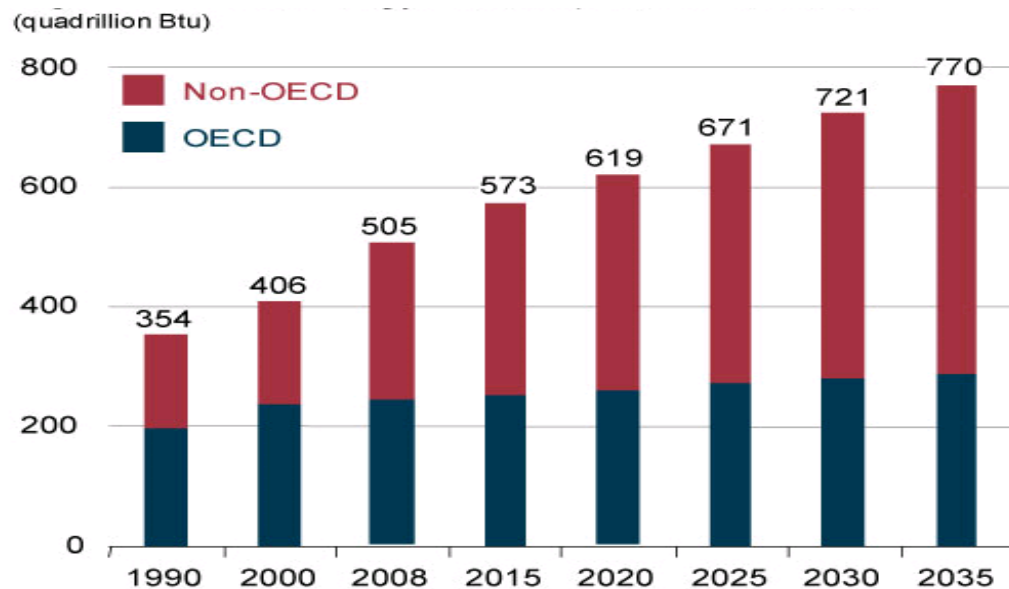


**Figure 1.1 – Rising global energy demand, historic up to 2008 and projected from 2015[1].**

As of 2008 it is claimed that 80% of the global energy demand was being met with fossil fuels[2]. In addition to concerns over environmental pollution caused by fossil fuels a further concern is our ever depleting stock of these resources. The effects of this are already being seen, recent figures stating that 3.5 million households in the UK were classed as being in fuel poverty in 2006, an increase of 1 million households from the previous year[3]. This has been directly linked to the number of excess winter deaths in the UK, which was 23,900 people during 2006/2007[3].

As supplies of our natural resources reduce and the demand for them increases there will come a point when there is simply not enough to meet all of our needs globally. Figure 1.1 shows that global energy demand is projected to increase by around 50% over the next 25 years, which clearly highlights the need for clean and renewable sources of energy. It has recently been claimed that by 2050 renewable energy could account for 80% of the world's energy needs[4]. However, this can only be achieved with more research now, and solar energy is considered to be a key renewable energy to be developed. It is said that in one hour more energy is incident on the earth's surface from the sun than the total amount of energy needed globally each year[5].

Here we focus on the development of organic photovoltaic devices to help meet this demand for energy in the long term, harnessing the power of the sun and converting it into useful electricity. Organic materials have a number of advantages over inorganic materials, such as lower fabrication costs and the potential for lightweight, flexible and semi-translucent solar panels. Whilst inorganic materials still provide higher power conversion efficiencies, there have been many recent advances with organic photovoltaic devices. A review conducted by Dennler et al[6] showed efficiencies of 5% for several poly(3-)hexylthiophene (P3HT): [6,6]-phenyl $C_{61}$-butric acid methylester (PCBM) devices. Sun et al[7] reported an efficiency of 6.7% for a small molecule based organic device. Recently Heliatek reported an efficiency of 9.8% for a tandem organic solar cell[8], claimed to be the current record. Model calculations based on P3HT:PCBM devices indicate that theoretically power conversion efficiencies approaching 11% are possible, when the device is fully optimised[9].

However, there is still a long way to go before matching efficiencies produced using inorganic semiconductors. Recently efficiencies of up to 25% have been reported for silicon (Si) crystalline devices, whilst a gallium arsenide (GaAs) thin film device achieved an efficiency of 28% under standard AM1.5 conditions[10].

We now consider the photovoltaic process in general followed by an overview of organic semiconductors. The main working principles of an organic photovoltaic device will then be discussed, along with fabrication techniques and the various architectures utilised. We will also investigate liquid crystalline materials and their potential advantages when incorporated into an organic solar cell.

## 1.2 The Photoelectric Effect

The photoelectric effect was first observed in 1839 by Becquerel, when an electrical current was produced by sunlight within an electrolyte solution[11]. It was later seen that the incident light could provide enough energy for an electron to completely escape the surface of a metal. This discovery eventually led to the theory of particle/wave duality and the quantum theory of light in Einstein's groundbreaking paper of 1905. Here it was first theorised that the amount of energy ($E$) contained in a single photon of light was determined only by the frequency ($v$) of the associated electromagnetic wave. This gave the now well known relation[12].

$$E = hv \qquad \textbf{(1.1)}$$

where $h$ is Planck's constant. It was also seen that certain insulators, now referred to as semiconductors, acted as conductors when exposed to light. The energy absorbed from the incident light was sufficient to excite a bound electron to a higher energy level where it could move freely. In semiconductors these levels are continuous bands separated by 'forbidden zones', referred to as the energy gap, which represent energy intervals containing no energy states.

For inorganic semiconductors the highest filled energy level is referred to as the valence band whilst the empty level above is known as the conduction band. The photon of energy $\geq h\upsilon$ is absorbed and excites an electron from the valence band into the higher energy level conduction band. This creates an unoccupied state in the valence band, referred to as a hole. The electron/hole then acts as a negative/positive charge which can be delivered to an external circuit using an applied potential. The in-built field of a pn junction can separate and drive the electrons and holes in opposite directions through an external load creating a photo voltage and a photocurrent. Figure 1.2 illustrates the photoelectric and photovoltaic effect, the latter needing a spatial asymmetry to drive the electrons and holes through the external circuit.
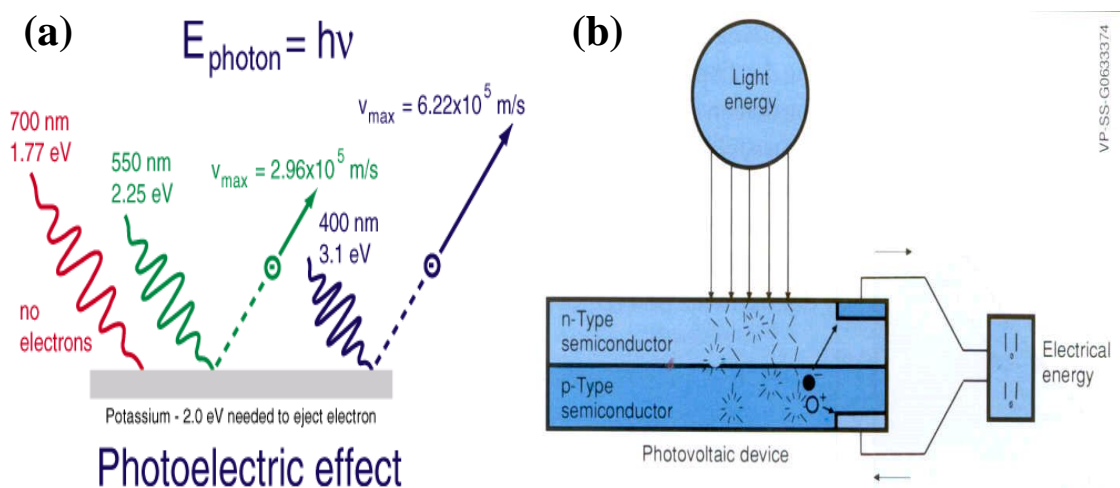


**Figure 1.2 – (a) The photoelectric effect[13] and (b) the photovoltaic effect[14].**

One of the first examples of a photovoltaic device was made by Frits in the late 1800's when he pressed a layer of selenium between a metal substrate and a gold top contact [11,12]. However it wasn't until the 1950's when these devices became widespread, starting in 1954 when researchers at Bell Labs produced a Silicon p-n junction solar cell with an efficiency of 6% [11].

Silicon is still the most commonly used material for photovoltaic devices today. Despite the high efficiencies reported for silicon based solar cells, this material is still far from ideal. The manufacturing process is energy intensive, needing high temperatures, which makes these devices very expensive in terms of both money and energy. An important factor to consider when looking at solar cell efficiency is the so called energy payback time. This is how long it would take for a solar cell to produce as much energy as it required for its manufacture. For crystalline silicon this time is high, estimated to range from 3 to 5 years [11].

Thin-film solar cells have been developed based on amorphous, microcrystalline and polycrystalline silicon in an effort to reduce the costs. The production of thin-film devices can be achieved without using high temperatures or expensive semiconductor substrates. Polycrystalline silicon thin film devices have so far produced efficiencies up to 10.4%[15] whilst CdS/CdTe thin film devices have achieved efficiencies as high as 16.5%[16]. However, efficiencies of small-area laboratory devices do not easily scale up to large modules during manufacturing. Overall in 2009 the market share for thin-film solar cells was around 15%[15].

As an alternative, organic materials have been investigated as these materials use a much less energy intensive process during manufacture, i.e. they can be processed at much lower temperatures[17]. In addition these materials can potentially be processed roll to roll making organics ideal for mass production commercially. Whilst they have good light absorption properties, organics also have relatively low charge carrying mobility which offsets this benefit[18]. The band gap of organic materials is also higher than silicon, generally more than 2eV[18], which means that lower energy photons from the visible spectrum cannot be utilised.

# 1.3 Organic Semiconductors

Conjugated organic materials consist of alternating single and double carbon-carbon bonds. The ground state configuration for carbon atoms is shown on the top line in figure 1.3. Carbon is known to form four bonds with neighbouring atoms which is achieved via a process known as hybridisation. Here, one of the $2s$ electrons is promoted to the $2p_z$ orbital, as shown on the second line in figure 1.3, to produce four unpaired electrons in separate orbits. As illustrated in the third line of figure 1.3, the $s$ orbital and two of the $p$ orbitals of carbon can form three $sp^2$-hybrid orbitals, known as $sp^2$ hybridisation, leaving the $p_z$ orbital unpaired[18,19,20].
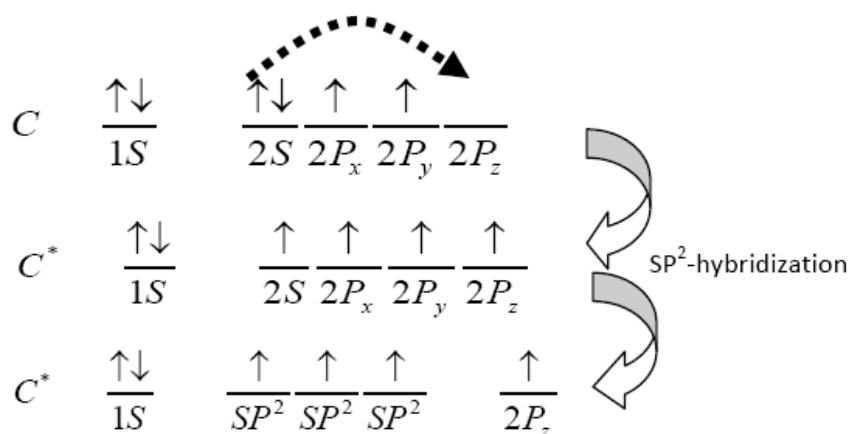


**Figure 1.3 - Formation of the SP² hybridization in the carbon atom[21]**

In conjugated materials the three $sp^2$ hybrid orbitals are used to form σ-bonds, normally two with the adjacent carbon atoms and one with a hydrogen atom or other substituent. The remaining $p_z$ orbital forms a π-bond with the $p_z$ orbital of the adjacent carbon atom, leading to alternating single and double bonds along the chain[19,20]. An illustration of these bonds is shown in figure 1.4 for polyacetylene.
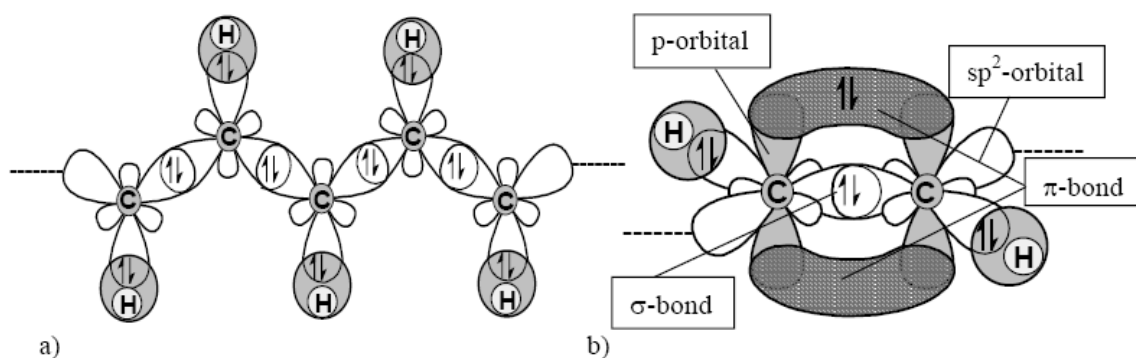
**Figure 1.4 - Formation of σ-bonds (a) and π-bonds (b) in polyacetylene[22]**

The π bonds are relatively weak due to their distance from the positively charged nucleus of the atom. This enables electrons to effectively 'hop' between carbon atoms, from one orbit to another. Hence the π bonds are considered as the basic source of charge transport in conjugated systems[23]. The π orbitals are split into filled π (bonding) and empty $\pi^{*}$ (anti-bonding) orbitals created between neighbouring carbon $p_z$ orbitals. This split occurs due the Pauli Principle for atomic orbitals, which is also valid for molecular orbitals. This means that no more than two electrons with paired spins can occupy one molecular orbit. Further, the number of molecular orbital created is always equal to the number of atomic orbitals that combine. Figure 1.5 illustrates this principle for two identical atoms which combine to form two new orbitals, shown as energy levels. ψ represents the wavefunctions of the electrons. The anti-bonding orbital and bonding orbital are also referred to as the lowest unoccupied molecular orbit (LUMO) and highest occupied molecular orbital (HOMO) respectively.
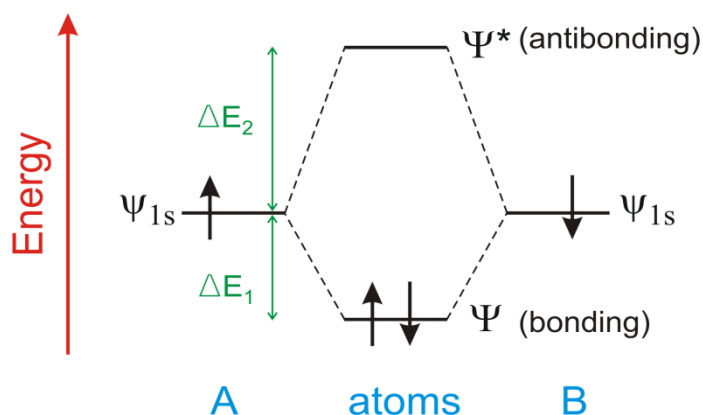
**Figure 1.5 - Energy level splitting when two identical atoms, A and B, are close together and form a bond. Ψ is the bonding and Ψ\* is the anti-bonding molecular orbital[24].**

The anti-bonding and bonding orbitals are analogous to the inorganic material's conduction and valence bands respectively. The difference in energy between the HOMO and LUMO is analogous to the energy gap, i.e. the energy needed to excite an electron from the HOMO to the LUMO. It is possible to measure the energy levels for the HOMO and LUMO of an organic material using a technique known as Cyclic Voltammetry, as discussed in section 2.2.

When an electron is excited to a higher energy level a bound electron/hole pair is created, referred to as an exciton. The coulombic energy, referred to as the exciton binding energy ($E_B$), binds this pair together. The small $E_B$ for most inorganic materials can easily be overcome thermally at room temperature creating free electrons and holes. Conjugated organic materials, or organic semiconductors, have a very high $E_B$ relative to inorganic semiconductors due a smaller dielectric constant, which in turn increases the screening length and hence the coulombic attraction force between the electron and hole[25]. Further, the weak non-covalent electronic interaction between organic molecules produces localised states with negligible band width[25]. Therefore easily obtainable electric fields are not sufficient to dissociate excitons so an alternative device configuration is required. The exciton binding energy is estimated to be between 0.2 – 0.4eV[26,27] for organic semiconductors, which is significantly higher that the thermal energy available at room temperature of around 0.02eV.

In addition to the exciton there are other excited states referred to as polarons and bipolarons, as shown in figure 1.6. Here the addition or removal of charge induces a deformation in the lattice, creating a local distortion of the molecular structure. A polaron can be viewed as a self-trapped charge carrier due to its associated lattice distortion. The addition of an electron to a molecule creates a negative polaron whilst the removal of an electron creates a positive polaron. The addition or removal of two electrons creates a negative or positive bipolaron respectively[28].
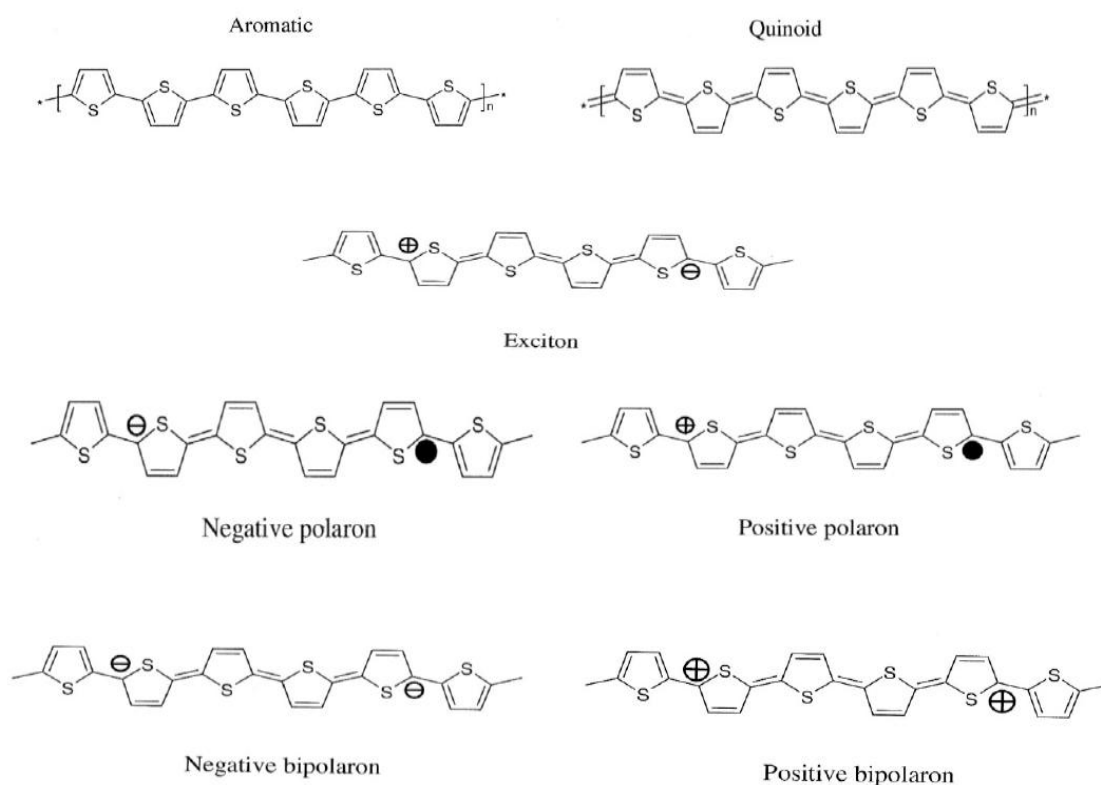


**Figure 1.6 – The ground and excited states of polythiophene[28].**

Although first observed by Becquerel in 1839, organic semiconductors have seen most of their progress during the last few decades. The first organic solar cell devices constructed were based on a single layer of organic, hole conducting material sandwiched between two metal electrodes with different work functions. Initially power conversion efficiencies were very low, although an efficiency of 0.7% was reported for a device using a merocyanine dye[18].

## 1.4 Main Working Principles of Organic Photovoltaic s

There are several steps involved in the conversion of light into useful electricity using an organic semiconductor: (i) Absorption of a photon to excite an electron to a higher energy level, in this case from the HOMO to the LUMO, creating an exciton. (ii) The exciton diffuses to the interface between the electron donor and acceptor (or active layer and electrode for single layer) the diffusion distance being limited to the materials diffusion length. (iii) Excitons which reach the interface prior to recombination are dissociated into free electrons and holes, in the electron acceptor and electron donor materials respectively. We investigate the criterion for dissociation for various device architectures in section 1.5. (iv) The separated charges are transported to and collected at the relevant electrode, the anode for holes and the cathode for electrons.

These four main factors, summarised in figure 1.7, can be quantified as follows: The fraction of incident photons absorbed ($\eta_A$), the efficiency of the exciton diffusion ($\eta_{ED}$), the fraction of electron-hole pairs dissociated into the donor and acceptor materials ($\eta_{CD}$) and the fraction of separated charges that make it to their respective electrodes ($\eta_{CC}$). These four factors give the total quantum efficiency ($EQE$) as[12,18,29],

$$EQE = \eta_A(\lambda)\eta_{ED}\eta_{CD}(V)\eta_{CC}(V) \qquad \textbf{(1.2)}$$
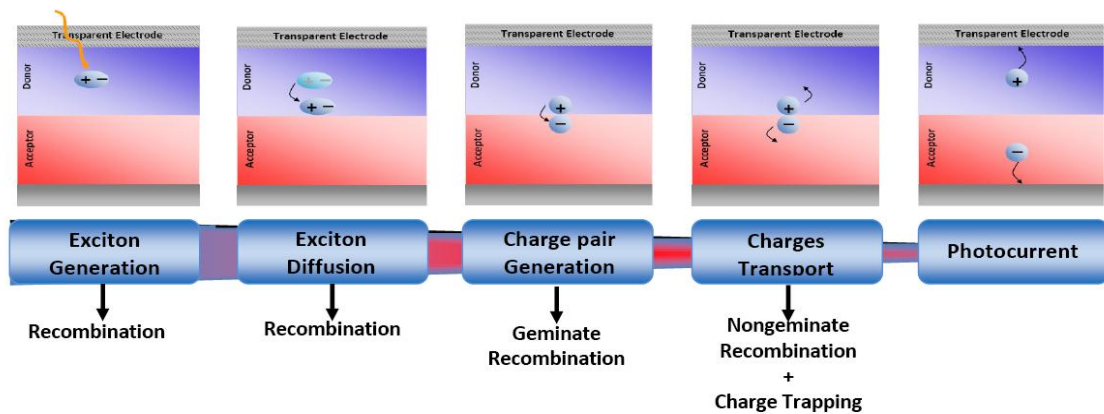


**Figure 1.7 – The stages of photo generated current for an organic semiconductor[30].**

## 1.4.1 Light Absorption

The amount of light transmitted ($T$) through a thin film of thickness $d$ can be expressed as[12],

$$T = \frac{I}{I_0} = \exp{(-\alpha d)} \qquad \textbf{(1.3)}$$

where $\alpha$ is the optical absorption co-efficient, $I_0$ is the input intensity and $I$ is the transmitted intensity. Most organic materials have a high absorption coefficient of $\alpha >$ $10^5 cm^{-1}$ [29]. This means that an active layer of around 100nm thickness is sufficient to absorb between $60 - 90\%$ of the incident light when a reflective back contact, such as Al, is used. However, the wide energy band gap ($E_g$) of most organic semiconductors, $>$ 2eV, means that incident light of wavelengths longer than around 600nm cannot be absorbed. In contrast, over 60% of the solar spectrum is at wavelengths longer than 600nm, as illustrated in figure 1.8, meaning that we are unable to exploit the majority of the incident sun light. For this reason low band gap organic semiconductors are of particular interest as they would allow us to exploit much more of the solar spectrum.
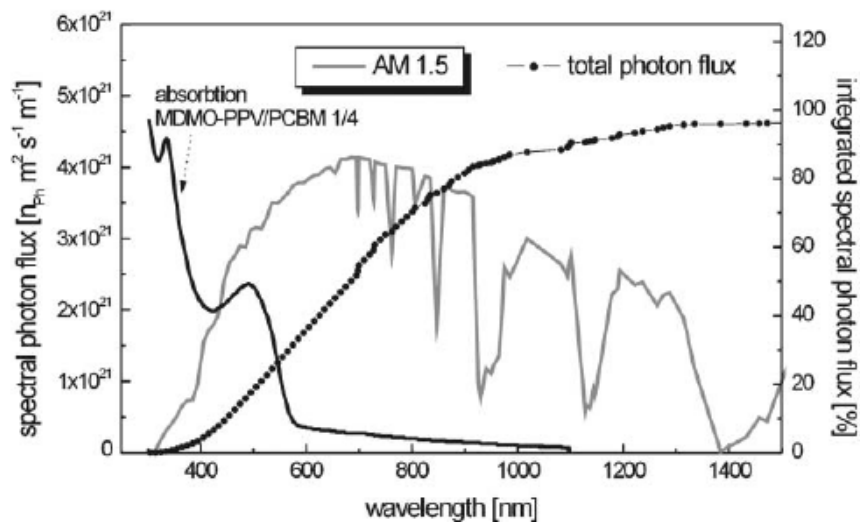


**Figure 1.8 – AM 1.5 solar spectrum compared to the absorption spectrum of MDMO-PPB:PCBM 1:4 wt film[31].**

## 1.4.2 Exciton Generation, Diffusion and Dissociation

When light has been absorbed by an organic semiconductor an electron is excited from the HOMO to the LUMO level, leaving a hole in the HOMO level. As discussed earlier, this creates an electron/hole pair bound together by coulombic forces and is referred to as an exciton.

Ideally we want all excitons created to separate into free negative and positive polarons (electrons and holes). This usually takes place at an interface between two materials with different energy levels such as work function, ionisation potential or electron affinity. As excitons are comprised of a hole and electron the overall electrical charge is neutral, hence they are not influenced by the electric field and diffuse via random hops[32]. The diffusion length for an exciton, before charge combination occurs, is generally around 10 – 20nm for an organic semiconductor[17]. However we need an active layer thickness of around 100nm for efficient light absorption[17,33]. We will investigate the various active layer architectures in section 1.5 used to optimise the interface area for more efficient exciton separation.

In order to dissociate charges at a donor/acceptor interface the energy gap between the HOMO and LUMO energy levels ($E_g$) minus the exciton binding energy ($E_B$) needs to be greater than the difference between the donor HOMO ($E_{D-HOMO}$) and Acceptor LUMO ($E_{A-LUMO}$). This is illustrated in figure 1.9, where in this case it can be seen that $E_g$ - $E_B$ > $E_{D-HOMO}$ - $E_{A-LUMO}$. If $E_g$ – $E_B$ < $E_{D-HOMO}$ - $E_{A-LUMO}$ then recombination of the charges would be favoured to charge separation.

We can also define the offset needed for charge separation in terms of the difference between the LUMO and HOMO energy levels, $\Delta E_{LUMO}$ and $\Delta E_{HOMO}$ respectively, of the donor and acceptor[6]. Here we need $\Delta E_{LUMO} > E_B$ and $\Delta E_{HOMO} > E_B$. It has been calculated that a minimum of 0.3eV is needed for $\Delta E_{HOMO}$ ($\Delta E_{LUMO}$), as this is generally sufficient to overcome the $E_B$. However, device performance is seen to reduce as $\Delta E_{HOMO}$ ($\Delta E_{LUMO}$) increases above 0.3eV, due to loss of charge carrier energy and a lower potential for the $V_{oc}$[6].
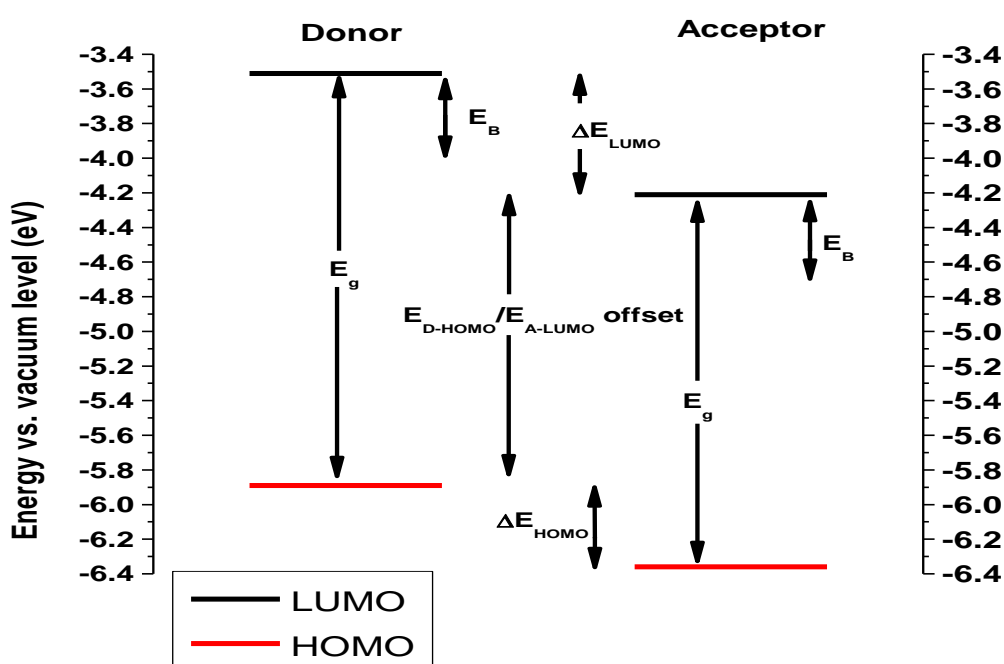


**Figure 1.9 – Energy diagram for charge separation at a D/A interface.**

## 1.4.3 Charge Transport and Collection

Following separation at a material interface, the separated charges travel towards their respective electrodes for collection, now under the influence of the electric field. Prior and during charge separation, the recombination mechanism is germinate, i.e. two charges generated as a pair recombining. During charge transport non-geminate charge recombination can take place between separated holes and electrons which meet whilst travelling to their respective electrodes. This is particularly the case for single layer devices, where both charge types travel through the same material.

Organic semiconductors are known to have low charge mobility ($\mu$), typically between $10^{-7}$ to $10^{-3}$ cm$^2$V$^{-1}$s$^{-1}$ [19]. Further, the electron mobility is generally lower than that for holes, leading to unbalanced charge transport. Impurities and defects in the material can also lead to charge trapping, which is investigated in more detail in chapter 2.6. Liquid crystalline order can also improve charge mobility[19].

Upon reaching the collecting electrodes, charges may have to overcome the potential barrier of a thin oxide layer. The electrode can also form a block contact at the interface with the organic active layer, which is a function of geometry, topology and interface formation[19]. Consequently, some of the charges which reach the electrode may not be extracted to the external circuit.

# 1.5 Photovoltaic Device Architectures

As discussed earlier, charge separation can take place at an interface between two materials with different energy levels. The differing energy levels at these interfaces create an internal electric field, which drives the electrons and holes towards their respective collecting electrode. Here we investigate the various device architectures used to accomplish charge separation along with their respective merits and drawbacks. The main categories are single layer, bi-layer, bulk heterojunction and tandem devices.

## 1.5.1 Single Layer Device

Single layer devices were the original structure for organic solar cells, which consist of a single organic layer sandwiched between two metal electrodes of differing work functions ($W_f$). Indium tin oxide (ITO) has a high work function and is often used with Aluminium (Al) which has a lower work function. Figure 1.10 shows the structure of these cells, the organic layer is generally between 40 – 200nm thick. Incident light passes through the glass substrate and transparent ITO electrode to be absorbed by the organic layer. Light which transmits through the film layer is reflected from the Al electrode and hence has a second chance to be absorbed on the return journey.
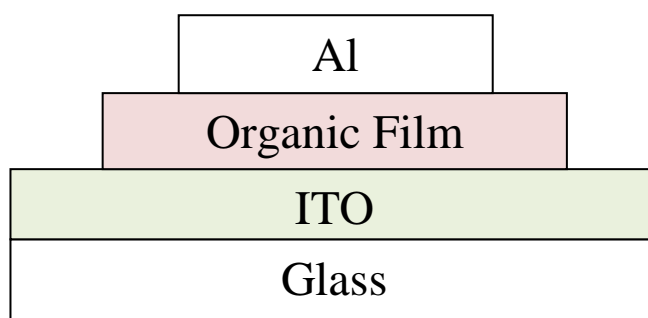


**Figure 1.10 – Schematic of a single layer solar cell[17].**

The absorbed light creates excitons, which then diffuse to the electrode contacts where charge separation takes place. The influence of the electric field provided by the asymmetrical work function of the two electrodes drives electrons towards the Al electrode and the holes towards the ITO contact. In the case of the Al electrode where the work function is lower than the semiconductor ionisation potential (IP) a Schottky, or rectifying, junction is formed[18,33] as shown in figure 1.11 (d). It is here that charge separation takes place, within the depletion region where the band bending is evident. The contact is ohmic for an electrode with a higher $W_f$ than the IP of the organic material, as shown in figure 1.11 (b).
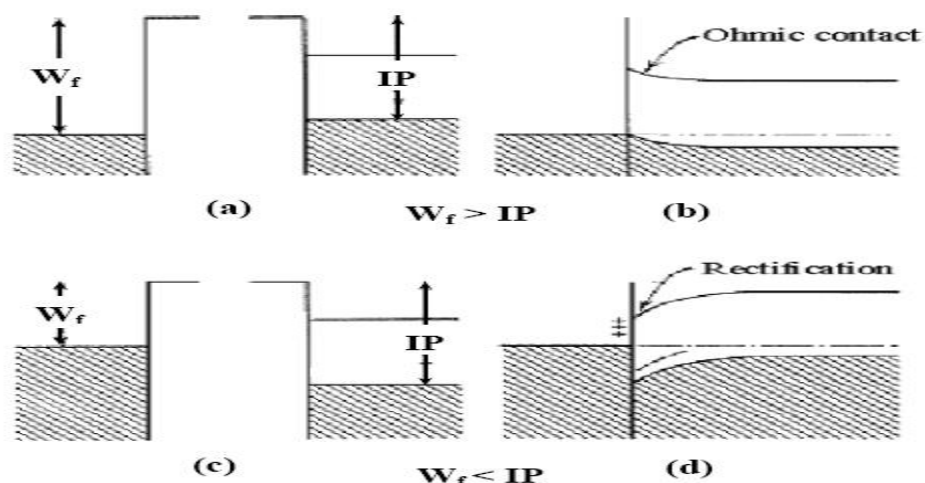


**Figure 1.11 – Energy levels for a metal/semiconductor junction before and after contact for $W_f >$ IP (a),(c) and $W_f <$ IP (b),(d)[19].**

The exciton diffusion length is very small in organic materials, around 10nm, which means that only excitons created within this distance of the contacts are dissociated. Furthermore, recombination is high as the electrons and holes travel through the same material. The absorption spectrum is also limited to that of a single material and a low fill factor is seen due to a high series resistance[18]. Consequently the performance of single layer devices tends to be poor.

## 1.5.2 Bilayer Device

Here we have two organic layers sandwiched between two metal electrodes in order to provide more efficient charge separation. Light enters the device to be absorbed as with the single layer device, but this time dissociation of the exciton takes place at the interface between the two organic layers. The materials are chosen to act as an electron donor and electron acceptor, based on differences in their respective HOMO and LUMO energy levels, in order to facilitate the charge separation.
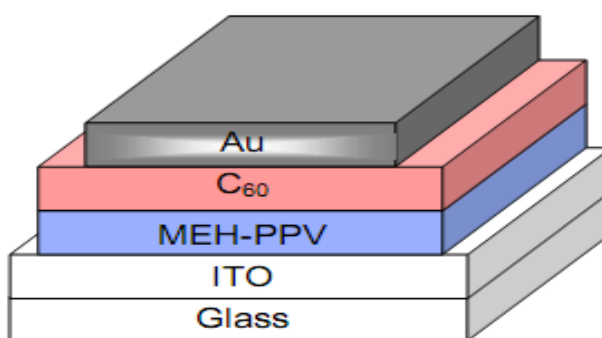


**Figure 1.12 – Schematic of a typical bilayer solar cell device[33]**

Figure 1.12 depicts a bilayer solar cell device using electron acceptor and donor materials. The electrodes are chosen to match the work function to the HOMO and LUMO energy levels of the organic material to facilitate extraction of the respective charge carriers[18].

Figure 1.13 illustrates the exciton dissociation taking place at the acceptor/donor interface. It can be seen that the electron transfers to the acceptor whilst the hole remains with the donor. The separated hole and electron can then travel to their respective electrode through the acceptor/donor material.
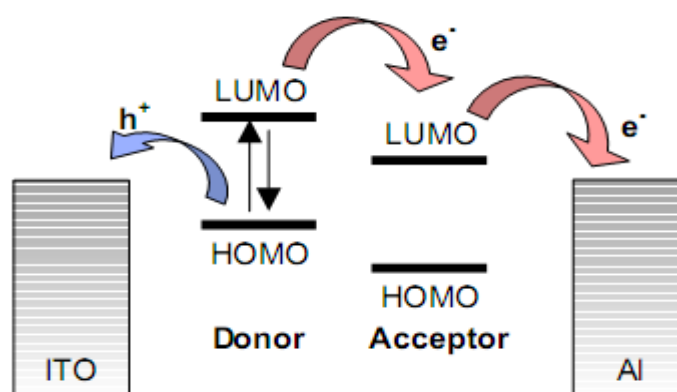
**Figure 1.13 – Dissociation of exciton at the donor/acceptor interface[33].**

Once again, only excitons created within around 10nm of the interface will diffuse far enough to be dissociated. The active area is twice as large as that of the single layer device due to excitons being created either side of the interface. As the holes and electrons are now travelling through separate materials following dissociation, recombination losses are also greatly reduced. Further, as we now have two materials with different absorption spectra a larger fraction of the solar spectrum can be absorbed. Thinner organic layers can also result in better fill factors[18,19]. This bilayer architecture for a PV device was first reported by Tang in 1986, who demonstrated a power conversion efficiency of around 1%. It was also shown that charge generation efficiency was largely independent of the bias voltage, resulting in fill factors as high as 0.65[34].

## 1.5.3 Bulk Heterojunction Device

Here we investigate an optically thick design which seeks to increase the interfacial area to allow more excitons to arrive prior to their recombination. Donor and acceptor materials are blended together and phase separated to form domains, as illustrated below in figure 1.14. This architecture was first reported in 1995 independently by Yu et al[35] and Halls et al[36], the former reporting a power conversion efficiency of 2.9% using MEH-PPV and $C_{60}$ as donor and acceptor.
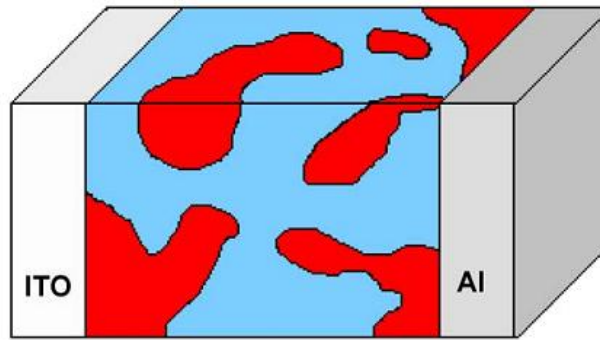
**Figure 1.14 – Donor and acceptor blend phase separated for efficient charge dissociation[33].**

Ideally the domains formed should be no larger than twice the diffusion length of the excitons, around 20nm, in order to maximise charge separation and avoid recombination losses. It is clear that most excitons will be able to reach a donor/acceptor interface within their diffusion length, even for layers over 100nm thick. Hence this architecture provides more efficient charge separation than the Bilayer devices. However these devices produce a lower $V_{oc}$ than single layer structures.

The nano morphology of the blend is crucial to the device efficiency with dead ends in the electron/hole pathways being a concern. Figure 1.14 illustrates how 'island domains' of material can form, which do not provide a charge pathway to the collecting electrode, resulting in higher charge recombination. Further, it can be seen that one of the materials can connect to both electrodes which can also lead to higher charge recombination, lowering the shunt resistance ($R_{sh}$). However, the more efficient charge separation produced by this architecture leads to an improved overall PV device efficiency relative to the bilayer structured devices. Power conversion efficiencies of 3 - 5% have been reported for bulk heterojunction devices (BHJ), and recent attempts have been made to improve this further using Titanium Oxide as an optical spacer/hole blocking layer[37,38].

Most attempts to improve the performance of BHJ solar cells have focussed on understanding and optimising the processing conditions of the active layer, particularly annealing conditions. Controlling the morphology of the bulk heterojunction, in order to ensure maximum exciton dissociation at the interface between the donor and acceptor, has been key to improvements in device efficiency. This has led to high device performance when combined with efficient charge carrier extraction[6,39]. Furthermore, the contact between the cathode and active layer of a BHJ device has been shown to have a significant effect on the fill factor (FF) of a device, and hence on the device overall efficiency[40].

## 1.5.4 Diffused Bilayer Device

This architecture is intended to combine the benefits of the bilayer and bulk heterojunction devices. Figure 1.15 shows that the diffuse bilayer device provides spatially uninterrupted pathways for the charge carriers to travel to their respective electrodes, as with the bilayer device discussed earlier. At the same time the interface is large, as with the blend device, providing a large area for dissociation of excitons.

.
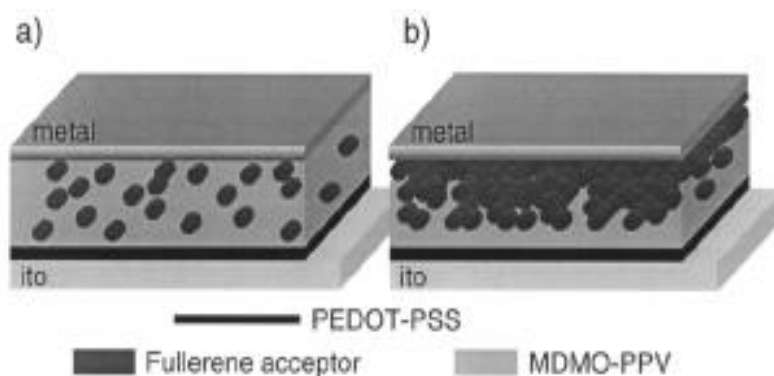


**Figure 1.15 – Comparison of blend (a) and diffused bilayer devices (b)[41].**

One method of achieving this interface is to ensure the first layer, the donor material, is uneven or grooved. When the acceptor layer is added it will then fill the grooves creating an interface similar to that shown in figure 1.15. The uneven layer can be created using a solvent to partially dissolve the top layer and leave the desired grooves. Another technique is to heat the bilayer close to the glass transition temperature before depositing the top electrode, which allows the two layers to diffuse into each other[18]. The morphology of the active layer can also be influenced using photo-polymerisation, or cross linking. Here two donor materials are used of similar molecular structure, the difference being that one has photo reactive polymerisable end groups. A laser or UV lamp can then be used to induce polymerisation of the donor layer, after which it is washed using the same organic solvent used to spin coat the donor layer. This results in an uneven donor layer, after much of the non-polymerisable component of the donor material has been washed away. Finally the acceptor material is spun coat onto the uneven donor surface to form the diffused bilayer. Monochromatic power conversion efficiencies of 0.6% and 0.8% have recently been reported using this architecture with a nematic liquid crystal gel[42,43].

## 1.5.5 Tandem Device

Tandem device seek to overcome the limitation of film thickness, due to the short exciton diffusion length, and hence increase light absorption. Here, relatively thin layer solar cells composed of materials with different absorption spectra are stacked. Each layer is thin enough to enable most excitons to diffuse to the dissociation region whilst the overall device thickness is sufficient to absorb a high proportion of the solar spectrum. The combination of narrow and wide band gap band gap semiconductors for each layer enables lower energy photons to be absorbed whilst still providing a good

potential $V_{oc}$. Each of the thin solar cells can be bilayer or trilayer, and are separated by a thin metallic nanocluster layer[44,45].
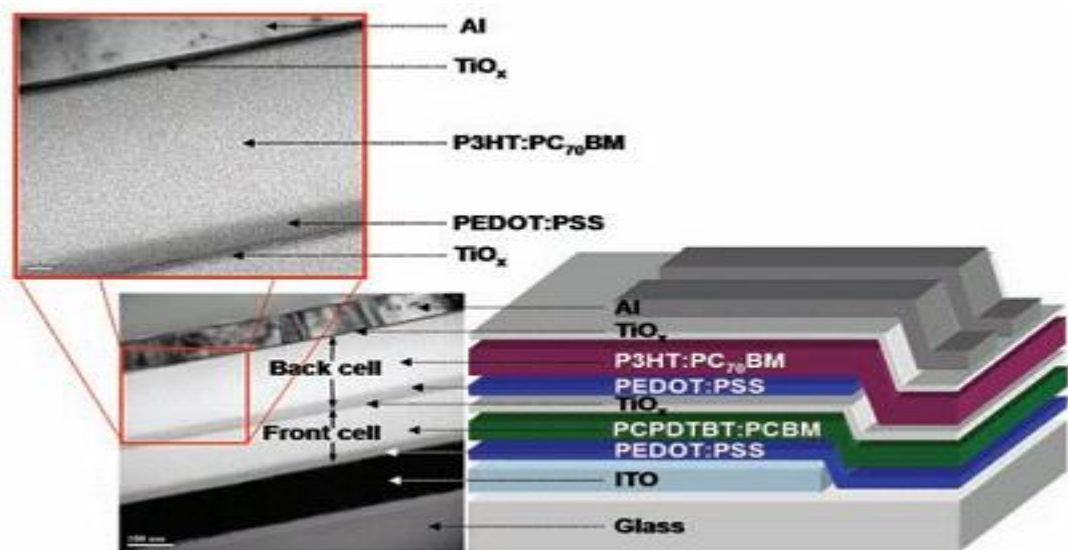


**Figure 1.16 – Schematic of tandem device structure (right) with TEM cross-sectional image (left), scale bar is 100nm (lower image) and 20nm (upper image)[46].**

Figure 1.16 shows a schematic of the tandem PV device structure, which is equivalent to two photovoltaic cells in series. Here a Titanium Oxide ($TiO_2$) layer is used to separate the stacked solar cell active layers. Generally the first cell uses a wide band-gap semiconductor whilst the second cell used a smaller band-gap material. The separated holes (electrons) in the lower (upper) cell are collected at the ITO (Al) electrode in the standard way. The hole (electron) in the upper (lower) cell diffuse to the central $TiO_2$ layer and recombine, which prevents a build of charge within the device[46]. This device architecture offers several advantages. As the two cells are in series, the open circuit voltage for the device is the sum of the that for the two individual cells. The absorption of the device is enhanced by using two semiconducting layers of different energy band-gaps, leading to broader absorption across the solar spectrum. Xue et al[45] reported a power conversion efficiency of 5.7% whilst Jin et al[46] reported 6.1%. More recently a new record was claimed by Heliatek, who reported an efficiency of 9.8% for a tandem organic solar cell[8].

# 1.6 Characterisation of Organic Photovoltaic Devices

When a voltage is applied in the dark an ideal solar cell acts as a diode, admitting current in the forward bias only. This rectifying behaviour is a result of the asymmetric junction which is required for efficient charge separation. The dark current density ($J_{dark}$) is given by equation 1.4 for an ideal diode[12].

$$J_{dark}(V) = J_o(e^{qV/k_B T} - 1) \qquad \textbf{(1.4)}$$

where $J_o$ is the saturation current density, $q$ is the electron charge, $k_B$ is Boltzmann's constant and $T$ is the temperature in Kelvin. It can be seen from equation 1.4 that the dark current increases exponentially with applied voltage. As shown in figure 1.17, the solar cell acts as a current generator in parallel with a diode. Upon illumination a potential difference is created across the two electrodes which drives the photo generated current in the opposite direction to the dark current through the external load.
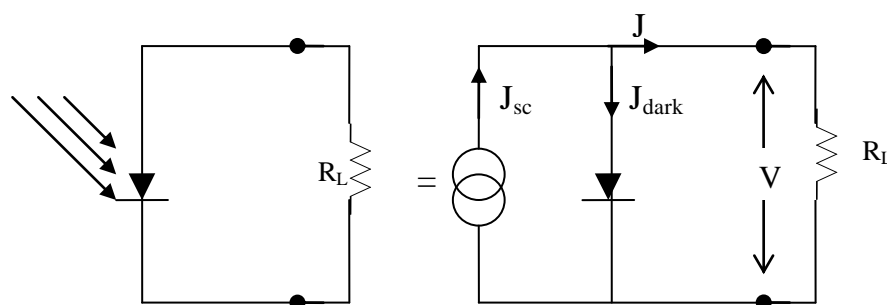


**Figure 1.17 – The equivalent circuit for an ideal solar cell[12]**

The current which flows through the external load is given by equation 1.5 and is illustrated in figure 1.17. This is referred to as superposition approximation[12].

$$J(V) = J_o(e^{qV/k_BT} - 1) - J_{sc} \qquad \textbf{(1.5)}$$

Here $J_{sc}$ is the short circuit current density, i.e. the current which flows upon illumination without an applied voltage. The open circuit voltage, $V_{oc}$, is the potential difference when the electrical contacts are isolated. This is the maximum value for the voltage, obtained when the net current produced is zero, i.e. when the photocurrent and dark current are equal and cancel each other out. The value for the $V_{oc}$ is given as [12],

$$V_{oc} = \frac{k_BT}{q} \ln\left(\frac{J_{sc}}{J_o} + 1\right) \qquad \textbf{(1.6)}$$
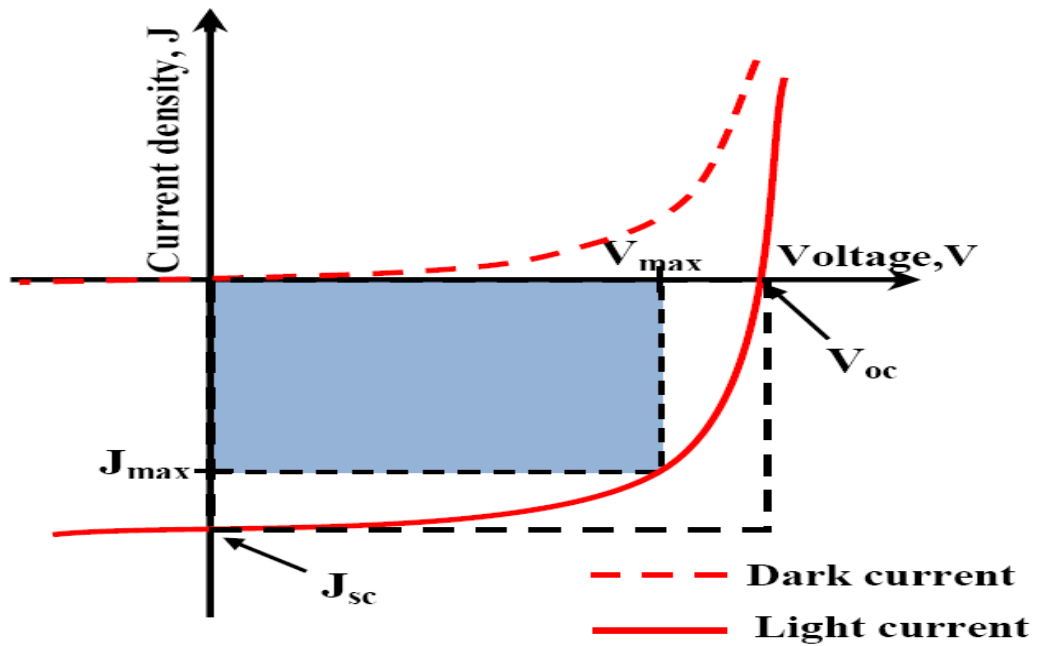


**Figure 1.18 – $JV$ characteristics of an organic solar cell in the dark and illuminated[33].**

Figure 1.18 shows the $JV$ curve under dark and illuminated conditions for an ideal solar cell. It can be seen that power is produced when the voltage is higher than zero but less than $V_{oc}$. In the event that $V > V_{oc}$ the cell consumes power and may emit light. For a voltage of less than zero the cell acts as a photo detector, again consuming power but this time to produce a current[12].

Figure 1.18 shows that there is a specific value for $J_{sc}$ and $V_{oc}$, shown as $J_{max}$ and $V_{max}$, at which the output power density is at a maximum, $P_{max}$. The output power density is given by[12],

$$P_{out} = JV \qquad (1.7)$$

Therefore the values of $J$ and $V$ which give the highest product also give the highest power achievable, equivalent to the largest area rectangle which can be fit within the $JV$ curve as illustrated in figure 1.18. The shaded rectangle in figure 1.18 is quantified by the fill factor ($FF$) which is defined as the ratio between the maximum power density produced and the potential power density available, given by[12],

$$FF = \frac{J_{max}V_{max}}{J_{sc}V_{oc}} \qquad (1.8)$$

It can be seen that a fill factor of 1 would mean that $J_{max}$ and $V_{max}$ would be equal to $J_{sc}$ and $V_{oc}$ which would give a $JV$ rectangle in figure 1.18 rather than a $JV$ curve. Clearly the higher the $FF$ is, the more efficient the solar cell. The overall efficiency of the cell, $\eta$, is defined as the ratio between the maximum power density output ($P_{max}$) and the incident light power density ($P_O$) given by[12],

$$\eta = \frac{P_{max}}{P_O} = \frac{J_{max}V_{max}}{P_O} = \frac{J_{sc}V_{oc}FF}{P_O} \qquad (1.9)$$

The external quantum efficiency ($EQE$) of a cell is defined as the number of electrons generated ($n_e$) per incident photon ($n_{ph}$) and is given by,

$$EQE = \frac{n_e}{n_{ph}} = \frac{J_{sc}}{P_o}\frac{hc}{\lambda e} = \frac{J_{sc}}{P_o}\frac{1240}{\lambda} \qquad \textbf{(1.10)}$$

where $c$ is the speed of light, $\lambda$ is the wavelength (nm) of incident light and $e$ is the electrical charge. The internal quantum efficiency is defined as the number of electrons generated per absorbed photon, and this can also used to characterise photovoltaic devices.

So far we have been looking at an ideal case for a solar cell, but unfortunately in the real world there are further considerations. Some power is lost through the resistance of the electrical contacts and through leakage currents. These two loss mechanisms are referred to as the series resistance ($R_s$) and shunt resistance ($R_{sh}$) respectively[12].
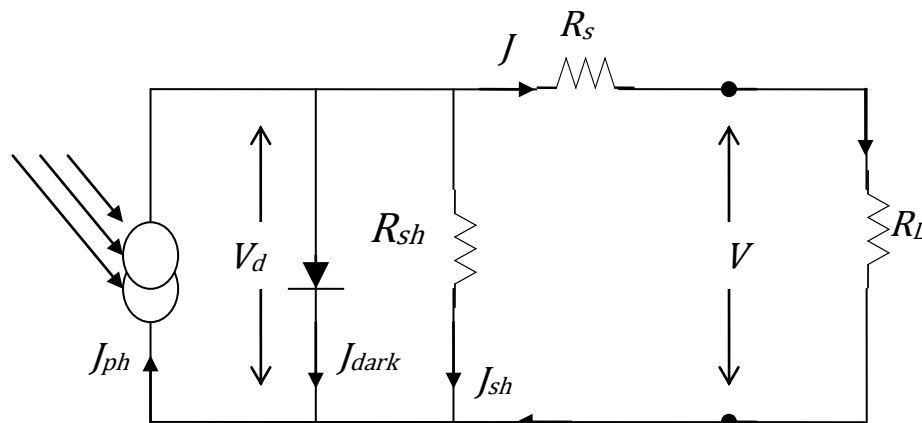


**Figure 1.19 – Equivalent circuit for a real solar cell[18].**

Figure 1.19 shows the equivalent circuit for a non ideal solar cell which incorporates the series and shunt resistance, which are both components of the internal diode resistance. Also shown is the load resistance, $R_L$, which is due to the external circuit. The $R_{sh}$ is a parallel resistance to the solar cell which restricts leakage current, which can be caused by recombination centres of impurities, pinholes in the film and shorts around the sides of the device. A high value for $R_{sh}$ is desirable as this will minimise leakage current and hence power loss from a PV device.

The $R_s$ is in series with the cell and is influenced by the resistivity of the material, electrodes and the interface between them. This resistance needs to be minimised in order to improve the power output of a PV device.



<center>(a)  (b)</center>
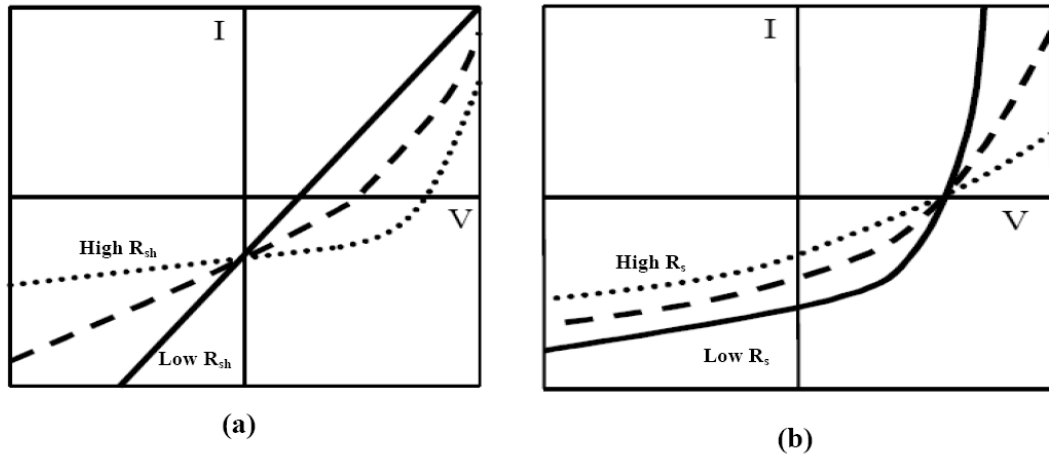
**Figure 1.20 – (a) The effect of $R_{sh}$ on the $JV$ curve and (b) the effect of $R_s$[47].**

Figure 1.20 (a) shows that the $JV$ curve changes significantly as the value for the shunt resistance varies. As the value for $R_{sh}$ falls both the $FF$ and $V_{oc}$ are seen to reduce, although the value for $J_{sc}$ remains unchanged. This is because $R_{sh}$ is significantly larger than $R_s$ meaning that the current through the shunt resistor can be neglected. It can also be seen that the gradient in the $3^{rd}$ quadrant, around $J = J_{sc}$ and $V = 0$, is inversely proportional to the $R_{sh}$ value. Figure 1.20 (b) shows that as the value for $R_s$ increases, the $J_{sc}$ decreases, as does the fill factor, although the $V_{oc}$ does not change significantly as the current flow through $R_s$ is zero at $V_{oc}$. The gradient in the first quadrant, around $V = V_{oc}$ and $J = 0$, is inversely proportional to the series resistance. Hence it can be seen how having a high $R_{sh}$ and a low $R_s$ will give a more rectangular shape $JV$ curve and hence a bigger fill factor.

An ideality factor ($n$) is introduced to take the internal diode resistance into account, which when added to equation 1.4 gives us the Shockley equation for the dark current[48],

$$J_{dark}(V) = J_o(e^{qV/nk_B T} - 1)$$ 

(1.11)

For an ideal diode $n$ is equal to 1, where $R_{sh} = \infty$ and $R_s = 0$. Using Kirchhoff's laws for current knots and voltage loops with the Shockley equation, the equivalent circuit can be given as[17],

$$J(V) = \frac{1}{1+R_s/R_{sh}} \left[ J_o \left( e^{\frac{e(V-JAR_s)}{nk_B T}} - 1 \right) - \left( J_{ph} - \frac{V}{AR_{sh}} \right) \right]$$ 

(1.12)

where $J_{ph}$ is the photo generated current and $A$ is the area of the solar cell. Using the open circuit and short circuit conditions equation 1.12 can be derived to give[17],

$$V_{oc} = \frac{nk_B T}{e} \ln \left[ 1 + \frac{J_{ph}}{J_o} \left( 1 - \frac{V_{oc}}{J_{ph}R_{sh}A} \right) \right] \approx \frac{nk_B T}{e} \ln \left[ 1 + \frac{J_{ph}}{J_o} \right]$$ 

(1.13)

$$J_{sc} = \frac{1}{1+R_s/R_{sh}} \left[ J_{ph} - J_o \left( e^{\frac{e(|J_{sc}|AR_s)}{nk_B T}} - 1 \right) \right] \approx -J_{ph}$$ 

(1.14)

Hence, for an efficient rectifying device the shunt resistance should be as large as possible whilst keeping the series resistance as small as possible.

# 1.7 Organic Materials for Photovoltaic Devices

Here we investigate the various different types of organic semiconductors available along with how they can be processed. Molecules with no repeat unit are called monomers (e.g. dyes and pigments), those with a few repeat units are oligomers whilst polymers have more than 10 repeat units[17].

Small molecules are organic conjugated materials with a low molecular weight, around a few 100u. Generally these materials are dry processed by sublimation within a high vacuum, although some can be processed via wet solution methods. Buckminsterfullerene ($C_{60}$) is an example of the former whilst PCBM (1-(3-methoxycarbonyl) propyl-1-phenyl[6,6]C61) can be processed using the latter method[18]. Figure 1.21 illustrates the chemical composition of some commonly used small molecular organic semiconductors.
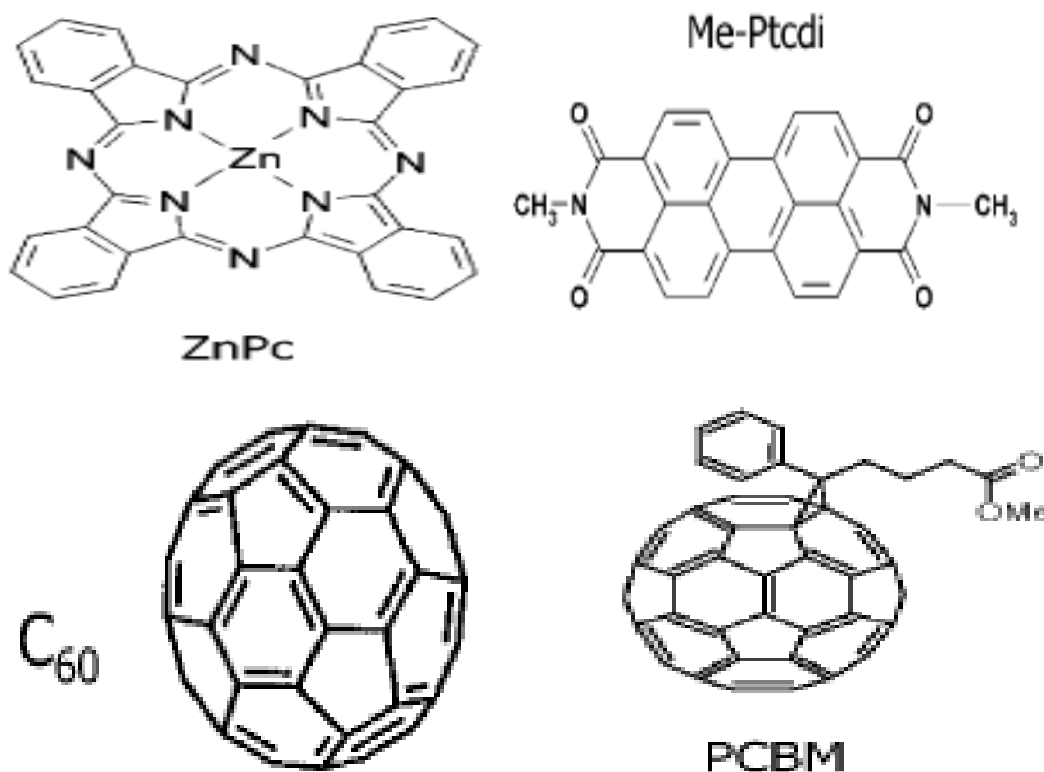
**Figure 1.21 - Chemical structure of some commonly used small molecule organic semiconductors: ZnPc (zinc-phthalocyanine), Me-Ptcdi (N,N'-dimethylperylene- 3,4,9,10-dicarboximide), and the buckminster fullerene C60, and a soluble derivative of C60, PCBM (1-(3-methoxycarbonyl) propyl-1-phenyl[6,6]C61)[18].**

Conjugated polymers consist of a large number of repeat aromatic units (monomers). Figure 1.22 shows the chemical structure for some commonly used conjugated polymers. Most polymers are processed via wet solution methods due to their solubility in various general solvents. It is not possible to use the dry method of sublimation for polymers due to the high molecular weight and low thermal stability of this material type[18].
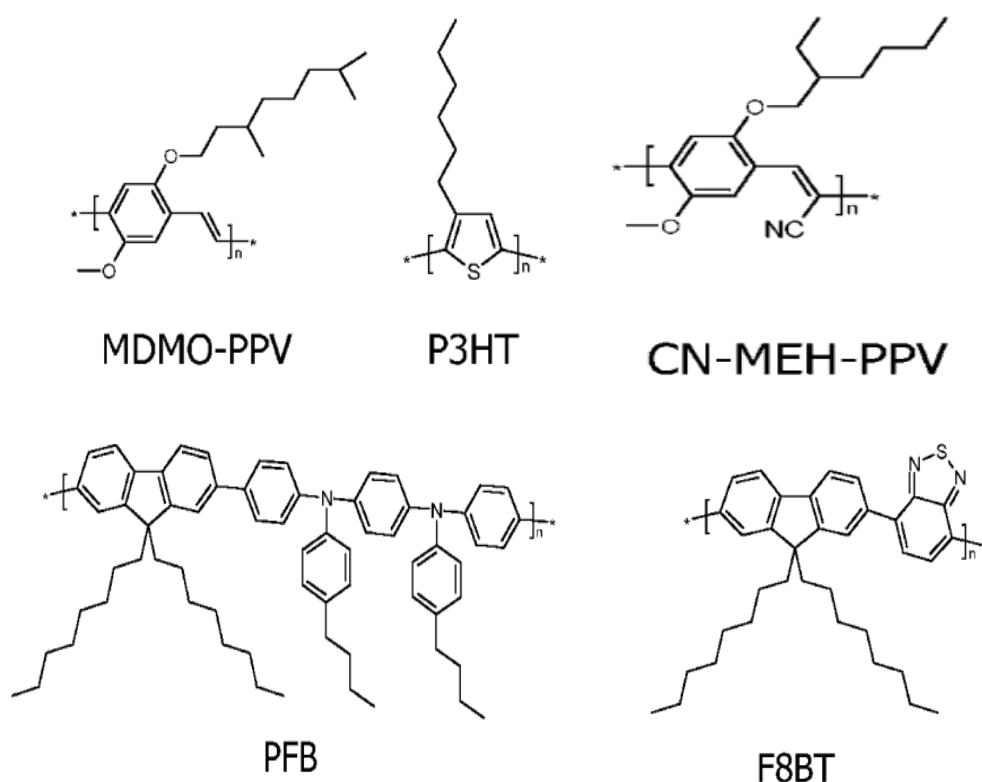


**Figure 1.22 – Chemical structure of some commonly used conjugated polymers. P-type hole-conducting polymers: MDMO-PPV (poly[2-methoxy-5-(3,7-dimethyloctyloxy)]-1,4-phenylenevinylene), P3HT (poly(3-hexylthiophene-2,5-diyl) and PFB(poly(9,9'-dioctylfluorene-co-bis-N,N'-(4-butylphenyl)-bis-N,N'-phenyl-1,4-phenylenediamine). The electron-conducting acceptor polymers: CN-MEH-PPV (poly-[2-methoxy-5-(2'-ethylhexyloxy)-1,4-(1-cyanovinylene)-phenylene) and F8TB (poly(9,9'-dioctylfluoreneco-benzothiadiazole)[18].**

# 1.8 Liquid Crystalline Organic Materials

## 1.8.1 Introduction

Liquid crystals are an intermediate phase of matter which lies between the solid crystal and isotropic liquid phases of a material. This phase of matter was originally discovered by Friedrich Reinitzer in 1888, whilst investigating the physical-chemical properties of cholesterol benzoate. Two melting points were observed; the first at 145.5°C produced a cloudy liquid which then became clear when heated above the second melting point of 178.5°C. Together with Otto Lehmann, it was determined that the cloudy liquid has some order, and hence the term 'liquid crystal' evolved to describe this phenomena. Lehmann also coined the term 'cholesteric liquid crystals' shortly after in 1904. However, liquid crystals remained little more than a curiosity for almost 80 years until 1969, when their optoelectronic properties were first investigated[49,50].

In 1970 M. Schadt, W. Helfrich and E. P. Raynes independently discovered the twisted nematic field effect, which is used in basic liquid crystal display devices. Following this, in 1973 the first stable, room temperature nematic liquid crystals were developed by George Gray at the University of Hull, and these were used for the first liquid crystal display devices[49,50]. In 1994 Haarer reported on the photoconductive properties of liquid crystalline materials[51].

Within a solid crystalline structure the molecules are fixed in a specific position within the lattice, exhibiting positional and orientational order. This generally leads to anisotropy of the optical, electrical, mechanical and magnetic physical properties of the material. Conversely, within an isotropic liquid phase the molecules are free to move and as such they exhibit no positional or orientational order.

The liquid crystal phase, also referred to as a mesophase, can exhibit some degree of orientational and/or positional order over long and short ranges like a crystal, whilst still allowing some freedom of movement for the molecules, like a liquid. Compounds which exhibit a mesophase under suitable conditions are generally referred to as mesogens[50,52], and they can exhibit high anisotropy of the physical properties when in this phase. There are two main categories for mesogens, commonly referred to as thermotropic and lyotropic. Both classes consist of amphiphilic organic compounds, which have both hydrophilic and lipophilic groups localised in the same molecule. Lyotropic LC's show solubility in water and organic solvents respectively, examples include soaps and fatty acids. This class of mesogens generally exhibit a liquid crystal phase when dissolved at an appropriate concentration into an suitable solvent[50,53,54].
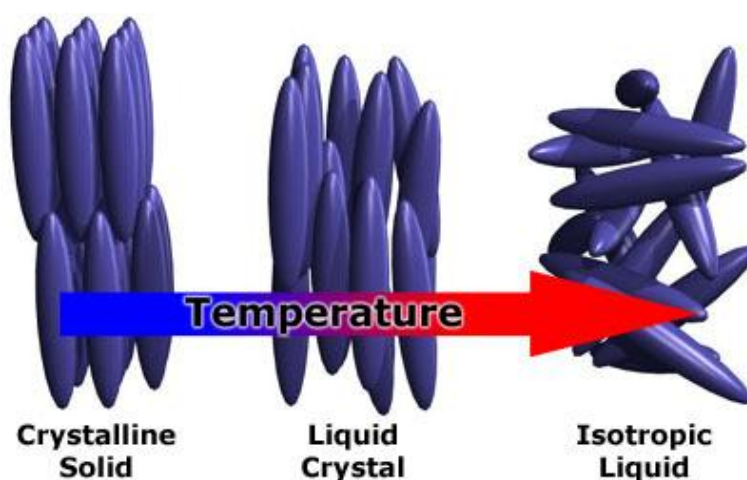


**Figure 1.23 – Illustration of the molecules as the phase changes from crystal to liquid[55].**

The phases of a thermotropic LC varies with temperature as illustrated in figure 1.23. One or more liquid crystal phases exist on heating between the crystal and liquid phases.

## 1.8.2 Liquid Crystal Phases and Transition Temperature

The two main categories of thermotropic liquid crystals are calamitic 'rod-like' and discotic[56]. The calamitic molecules have a long and short axis, with the orientational order based on the former. The discotic mesogens also have a long and short axis and are disk shaped[56]. The type of liquid crystal phase is in part determined by the shape of the molecules, as will now be shown.

Calamitic liquid crystals can form several different liquid crystal phases, the most common of which are nematic, smectic and cholesteric. Typical liquid crystal molecular arrangements are shown in figure 1.24 for the nematic and smectic phases.
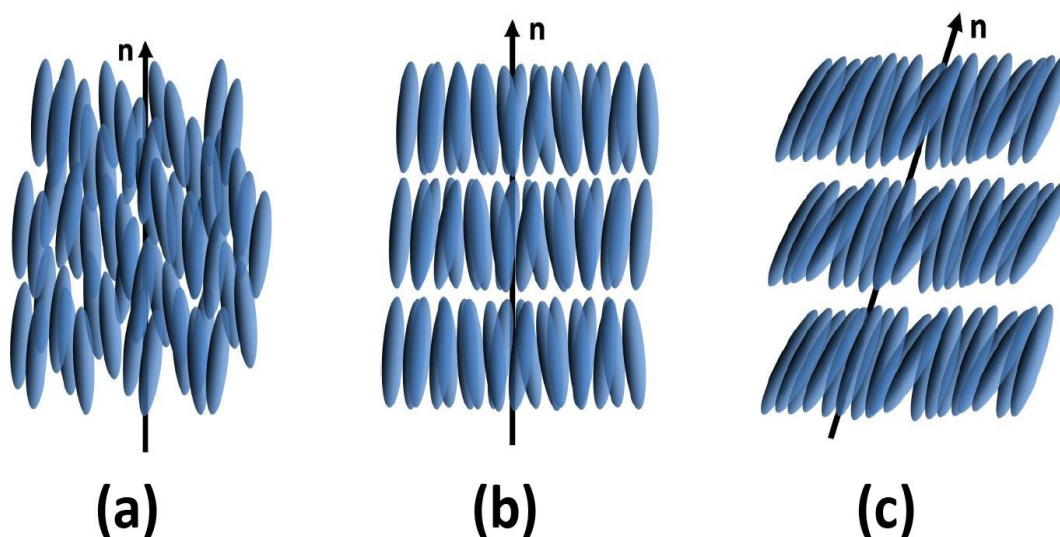


**Figure 1.24 – Illustration of liquid crystal molecular arrangement for (a) Nematic, (b) Smectic A and (c) Smectic C phases[57].**

The nematic phase can be considered as a one-dimensionally ordered elastic fluid where the molecules have orientational order but no long range positional order. This is the least ordered liquid crystal phase and is seen as an opaque liquid. The cloudy appearance is due to light scattering caused by the birefringent nature of the anisotropic ordering and optical properties of the molecules. This birefringent nature can be used to identify the phase type using a thermal polarising microscope, which we investigate further in section 2.3.

As shown in figure 1.24, the molecules align parallel to each other with their long axes oriented in approximately the same direction, the average direction is denoted by **n** and referred to as the director[53,56]. The director, and hence the optic axis, can be controlled using an electrical field which makes it useful for display applications. Normally, the molecules are uniformly oriented in domains, with a random change in **n** between domains. Uniform macroscopic alignment can be obtained by surface alignment or by using electric or magnetic fields, resulting in large mono-domains. The long-range orientational order can be characterised by the order parameter given by[53],

$$S = \frac{1}{2}\langle 3\cos^2\theta - 1 \rangle \tag{1.15}$$

where $\theta$ is the angle between the axis of an individual molecule and the director of the liquid crystal, with the average taken over the material. For a perfect crystal the value for $S = 1$ or -0.5, whilst for an isotropic liquid $S = 0$. In principle $S$ can take any value in the range $1 \geq S \geq -0.5$ ($S \neq 0$) for a nematic, but in practice $S$ is positive for all known nematic phases formed by rod-like molecules[53].

The smectic phases exhibit both positional and orientational order. The molecules are free to move and generally align along the same director arranged in layers. There are many different types of smectic phase, which are dependent on the local packing of the calamitic molecules. The main difference between smectic A and C shown in figure 1.19 is that the director is tilted for the smectic C phase. This tilt is temperature dependant, which means that the texture exhibited by the smectic C phase is also temperature dependent[53,56].

The choleristic phase is similar to the nematic phase, in that it has identical local molecular ordering. It is often referred to as the chiral nematic phase and denoted (N*). The molecules have chiral groups or a chiral dopant is added to the mesogens. Hence the director rotates perpendicular to the long axis of the molecule and pack in layers to form a helical macrostructure as shown in figure 1.25.
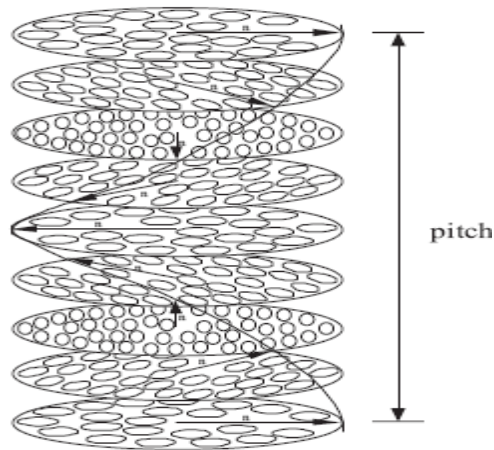


**Figure 1.25 – Liquid crystal molecular arrangement for the cholesteric phase[58].**

The pitch ($p$) of the helix is the distance over which the director has rotated 360° and can vary from around 0.1µm to almost infinity. As the LC is birefringent the helical structure provides a periodic modulation of refractive index, which produces a 1D photonic stop band. This prevents the propagation of circularly polarised light of the same handedness as the helix along the helical axis over the wavelength range $\Delta\lambda_R \approx \Delta n \lambda_R / n$. The stop band is centred at $\lambda_R = np$, where $n$ is the average refractive index = $\{(n_o^2 + n_e^2)/2\}^{1/2}$ and $\Delta n$ is the birefringence[58]. For light emitting materials where the photoluminescence (PL) spectrum matches the stop band, highly circularly polarised light has been produced. When the pitch is comparable to the wavelength of incident light, the material will reflect a relatively narrow wavelength band of light and appear iridescent[53,56,58,59].

Discotic liquid crystals form two liquid crystal phases, the columnar phase and the discotic nematic phase. The molecules in the former phase pack together in columns, but their arrangement within an individual column can be either random or ordered. The full columns can be grouped into hexagonal or cubic lattices[53,60]. The discotic nematic phase exhibits orientational but not positional order, the molecules appear to be randomly scattered whilst the planes of the discs are approximately parallel. This phase is optically uni-axial, but the birefringence is generally negative[56]. The molecular arrangement for two examples of discotic liquid crystal phases is shown in figure 1.26.



**Discotic Nematic**　　　**Discotic Columnar**
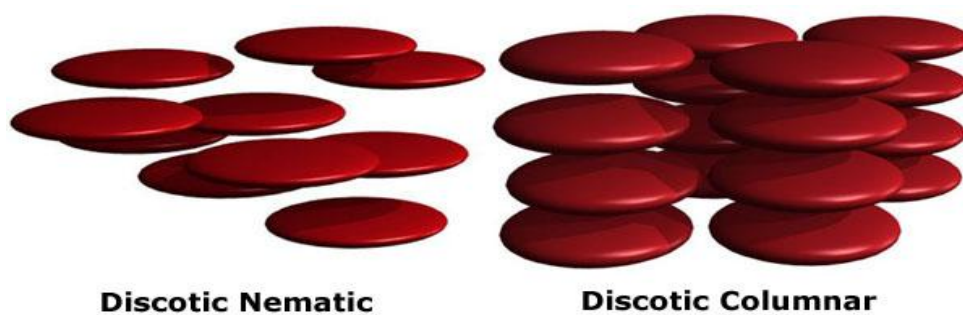
**Figure 1.26 – Molecular arrangement for discotic nematic (left) and columnar (right) liquid crystal phases[55].**

The phase transition temperature for a liquid crystal phase is dependent on the material and can be indentified using differential scanning calorimetry (DSC) and polarisation microscopy, which will be explored in more detail in section 2.3. As mentioned earlier, it is possible for a material to have more than one liquid crystal phase transition temperature and this is illustrated in figure 1.27. There are two intermolecular forces holding the asymmetric molecules together, referred to as lateral and terminal, which act across the long axes and the ends of the molecules respectively. Both of these forces can be overcome when the material is heated to a sufficient temperature.
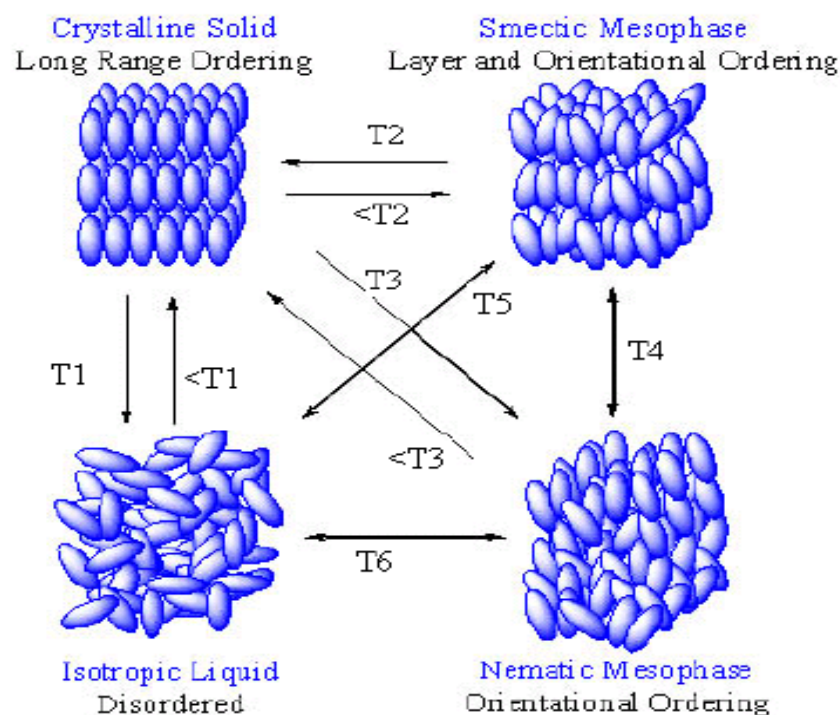
**Figure 1.27 – The various phase transition temperature sequences for a liquid crystal[61].**

Figure 1.27 shows that *T1* is the melting point for a crystalline solid to become an isotropic liquid. This is as a result of both the lateral and terminal intermolecular forces being overcome at temperature *T1*, which in turn results in a loss of both positional and orientational order. Whilst this scenario would generally apply to non liquid crystalline materials, there are some liquid crystals which melt in this way and only show a liquid crystal phase during cooling.

The crystalline solid to smectic phase (Cr-Sm) is denoted by the temperature *T2*, where the terminal force has been weakened but the lateral force remains strong. This gives the molecules some freedom of movement at the ends but holds them together in layers as shown in figure 1.27. *T3* is the transition temperature for a crystalline solid to nematic phase (Cr-N) where both intermolecular forces are weakened, allowing the molecules freedom of movement whilst retaining long range orientational order. *T4* is the transition temperature from smectic to nematic phase (Sm-N), where the lateral force is weakened and hence the molecules are no longer held together in layers but long range orientational order is retained.

43

Finally, *T5* and *T6* are the transition temperatures from smectic to isotropic liquid (Sm-I) and nematic to isotropic liquid (N-I) respectively. These transition temperatures are referred to as clearing points, where the lateral and terminal forces are completely overcome. This causes loss of orientational and positional order for (Sm-I) and loss of the remaining long range orientational order for (N-I). A high clearing point is a sign of good thermal stability for a material[53].

## 1.8.3 Liquid Crystal Materials

As discussed in the previous section, liquid crystalline materials consist of rod-like (calamitic) or disk-like (discotic) shaped molecules, referred to as mesogens. It is the shape and rigidity of these mesogens which give a material its liquid crystal properties. Further, the uniaxial nature of the mesogens produces interactions which favour alignment. Meanwhile, the chemical structure of the material's aromatic core (chromophore) influences the optical and electrical properties, and this can be determined during chemical synthesis[50,52,53,56]. Most Liquid crystals are transparent to visible light and re-orient in an electric field due to dielectric anisotropy. We particularly focus on a different class of liquid crystals with semiconducting properties. There are two main categories of liquid crystal materials based on their molecular structure, monomer liquid crystals (MLCs) and polymer liquid crystals (PLCs)[62]. The MLC has an aromatic core with one or more aliphatic terminal groups and has a low molar mass. Figure 1.28 shows the molecular structure for a semiconducting MLC (a) and PLC (b).
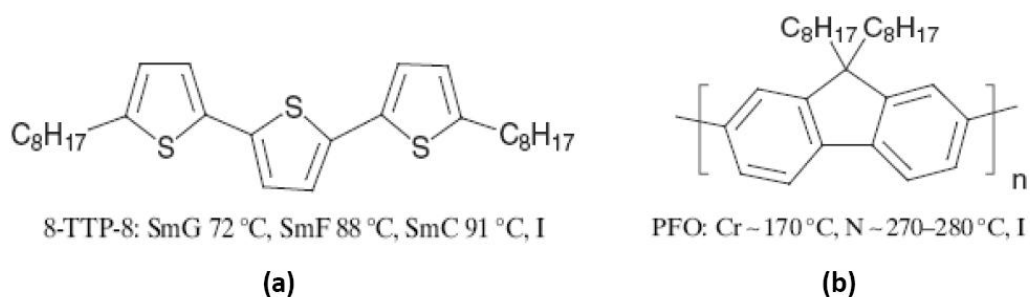
**Figure 1.28 - Molecular structure for (a) Terthiophene, 8-TTP-8, (MLC) and (b) 9,9-dioctyl polyfluorene PFO (PLC)[58].**

Modification of the aromatic core and terminal groups can be used to control the mesophase morphology and tune the physical properties, such as the phase transition temperature and solubility[53,63]. Hence it is possible to synthesise liquid crystals with properties tuned specifically for the intended application. Further, reactive end groups can be added to the terminal chains of the mesogens to enable polymerisation. Examples of reactive end groups include acrylate, methacrylate, diene and oxetane[64]. The reactive mesogen consists of an aromatic core attached to two photo reactive polymerisable end groups using aliphatic spacers as illustrated in figure 1.29.
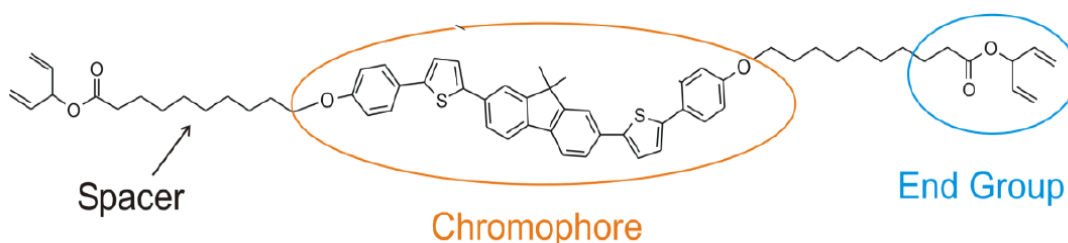


**Figure 1.29 – Chemical structure of a reactive mesogen with a polymerisable end group[57].**

By inducing polymerisation of the end groups of the MLC a polymer can be formed, which retains the liquid crystalline properties and hence become a PLC. This technique is useful for 'freezing' the liquid crystal ordering of the material into a glass phase, to ensure the desired morphology is retained for the intended application. A side chain polymer is formed, as shown in figure 1.30(a), when the reactive mesogen has only one polymerisable group. A polymer network can be formed, as shown in figure 1.30(b), when the monomers have two polymerisable end groups[56,58,62].

45
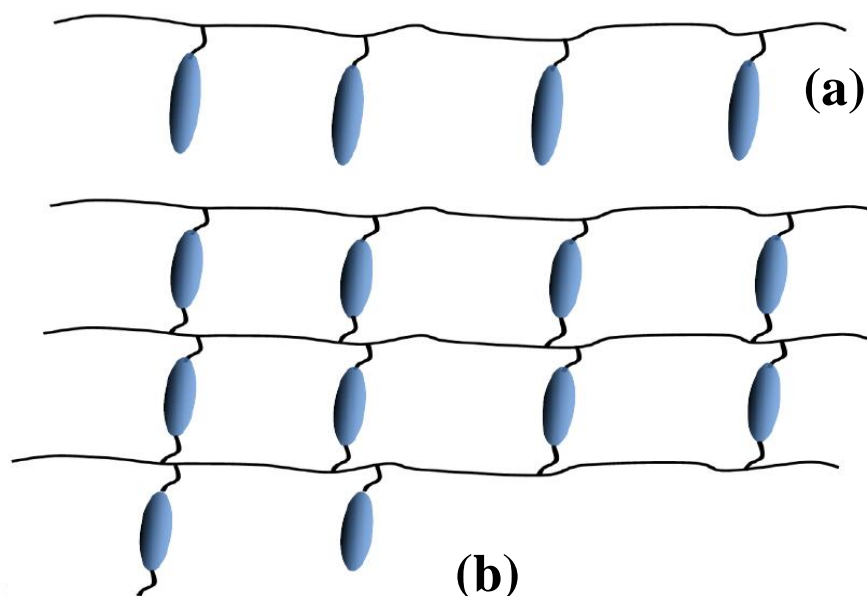
**Figure 1.30 – Two examples of polymer formation from monomers, (a) Side chain polymer and (b) Polymer network[57].**

A laser or UV lamp can be used to irradiate a thin film of the reactive mesogens, at the mesophase temperature, to induce polymerisation. This creates an insoluble polymer network which enables multi layer devices to be fabricated, such as bilayer organic PV devices and RGB pixelated OLEDs using wet processing techniques[43,65,66]. Some compounds form a nematic glass upon cooling from the nematic mesophase and can be photo polymerised at room temperature. Polymerisation can also be induced thermally[58,67,68].

Polymerisation occurs by the generation of free radicals, either thermally or photo induced. For (meth)acrylate groups polymerisation takes place via linear radical polymerisation reaction, to form a relatively flexible poly(meth)acrylate backbone. Light is absorbed by the aromatic core of the reactive mesogen and it is suggested that thermally assisted energy transfer takes place from the core to the (meth)acrylate end group to initiate the polymerisation. The energy barrier for dissociating the C=C of the reactive group is reduced by the same value as the absorption energy of the aromatic core[64].

For the diene end groups, shown in figure 1.29, free radical cyclopolymerisation occurs where the two end groups form a ring. This involves a sequential intra-molecular and inter-molecular propagation to provide a rigid backbone. This reaction is generally slower than that for the (meth)acrylate groups and diene groups do not undergo thermal polymerisation. Oxetane groups are polymerised by a photocationic mechanism upon irradiation of the monomer doped with an appropriate photosensitive catalyst. Protons (H+) are released from the catalyst, which attack the electron-rich oxygen atom in the oxetane ring to open it to form a linear poly(oxypropyl) polymer backbone. Free radical polymerisation can only occur in the absence of oxygen, whilst the cationic polymerisation has the disadvantage of residual ionic impurities remaining in the polymerised thin film[64,69].

Liquids crystal molecules can align with their long axes either normal or parallel to a substrate surface, referred to as homeotropic and homogeneous (planar) alignment respectively. This can be influenced using an alignment layer composed of hexamethyldisilazane (HMDS), or rubbed polyimide[70,71,65]. Figure 1.31 illustrates the two types alignment on a substrate surface. For OLEDs and PVs planar alignment is preferred since, as discussed in chapter 2.2, intermolecular charge transport is faster between closely spaced molecules.
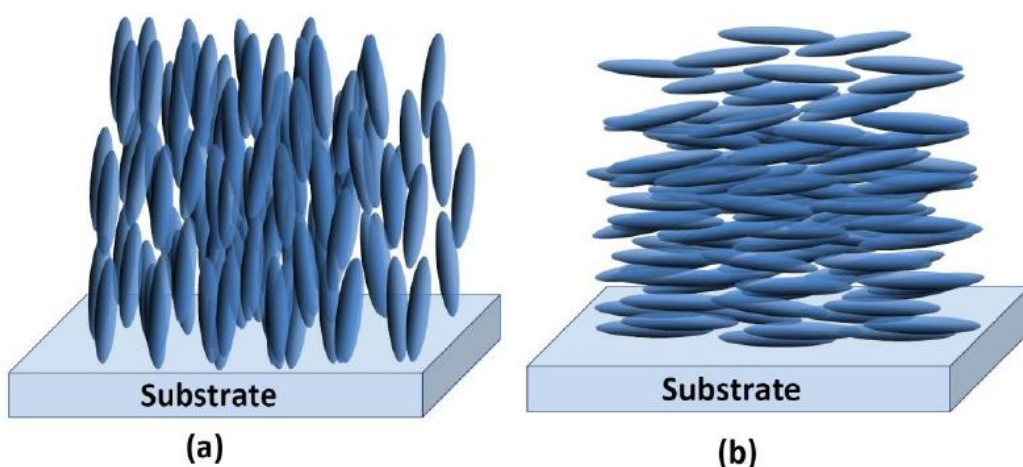


**Figure 1.31 – (a) Homeotropic and (b) Planar liquid crystal alignment[57].**

## 1.8.4 Liquid Crystal Charge Transport

A key benefit of the liquid crystal orientational order is a significant improvement in the charge carrier mobility of the material[58]. This is a particular important property as the mobility of organic semiconductors is generally much lower than that for inorganics, around $10^{-3}$ cm$^2$V$^{-1}$S$^{-1}$ or less[58,67]. The low mobility values are due to the molecular disorder inherent in amorphous organic materials. In 2004 Adam et al reported an increase in mobility by a factor of 10 for hexa-hexyl-thio tripheny-lene (HTTP) when in the hexagonal discotic phase[72], whilst mobility values of $10^{-3}$ cm$^2$V$^{-1}$s$^{-1}$ to 0.1 cm$^2$V$^{-1}$s$^{-1}$ have been reported for calamitic liquid crystals[73].

This improvement in mobility is achieved via enhanced molecular order. In the case of discotic mesogens, the molecules self-organise into 1D columns which effectively act as molecular wires with relatively high mobility. For calamitic mesogens in the nematic or smectic phases the molecules form a 2D conductor. In both cases the liquid crystal mesophases produce self organised domains with highly ordered and tightly packed structures, which in turn improves the overlap of the aromatic cores and intermolecular $\pi$ orbitals. This promotes anisotropic charge transport and supports the hopping mechanism of charge transport between the closely packed molecules[58,74].

The liquid crystal transition temperature is usually above room temperature for semiconducting organic materials. During cooling of a thin film from the liquid crystal mesophase the self organised domains can fragment into small polycrystalline domains separated by grain boundaries. This can lead to charge trapping and hence reduce the charge carrier mobility. As mentioned earlier, polymerisation of reactive mesogens can be carried out at the liquid crystal mesophase temperature, in order to retain the desired LC morphology. We discuss charge transport mechanisms at more length in section 2.6.

# 1.9 Thesis Outline

The overall purpose of this thesis is to identify novel organic semiconductors suitable for photovoltaic device fabrication. Chapter 2 provides the background to the areas we will investigate in the subsequent chapters, including the generic methods of measurement available for each area. Chapter 3 details the actual experimental methods and equipment used for the experimental chapters $4 - 8$.

In chapter 4 we investigate the energy levels of newly synthesised organic materials, in order to identify good donor/acceptor combinations. The energy levels are measured using a combination of cyclic voltammetry and a uv-visible spectrometer. We will consider how the chemical structure of an organic compound can affect the energy levels and the energy band gap. In total we investigate 28 organic compounds synthesized by the chemistry department of the University of Hull.

Charge mobility is investigated in chapter 5. Here we use the time of flight measurement technique to investigate the charge mobility in pure donor materials, before comparing this to the mobility for donor/acceptor blends.

Photovoltaic devices are fabricated and characterised in chapter 6, using seven different donor materials with our standard acceptor to make bulk heterojunction devices. We will investigate how the molecular structure of the donor influences the efficiency and other performance parameters related to PV device performance. We also consider how the donor to acceptor blend ratio affects performance, before investigating the effect of various electrode materials and deposition processes.

In chapter 7 we focus on how the liquid crystal phase of a donor material influences PV device performance. The transition temperatures of four different ratios of the same donor/acceptor blend will be investigated using differential scanning calorimetry and a polarised microscope. PV devices were fabricated and characterised for each blend ratio, each one annealed above and below the mesophase temperature for comparison. We investigate the morphology of all eight devices using an atomic force microscope. Finally, in chapter 8 we summarise and conclude the findings from the experimental work carried out in chapters 4 to 7. Potential improvements are highlighted along with how these can be realised through future work.

# 2. Areas of Investigation

## 2.1 Electrical and Optical Properties of Organic Semiconductors

The energy levels of an organic semiconductor are crucial when considering their suitability as an electron donor or acceptor within a photovoltaic device. As discussed in chapter 1, the relevant energy levels are represented by the highest occupied molecular orbit (HOMO) and the lowest unoccupied molecular orbit (LUMO). Here we investigate the energy levels of organic materials in general beginning with an overview of how the energy levels of a material affect the performance of a photovoltaic device. Cyclic Voltammetry (CV), the technique for measuring the HOMO and/or LUMO energy levels of a material will be introduced. It will be shown that the absorption spectrum of an organic semiconductor can be used to find the energy band gap ($E_g$) of the material. These two measurements provide the energy level data needed to fully evaluate a compound's suitability for use in photovoltaic devices, as either an electron donor or acceptor material.

## 2.1.1 The Effect of HOMO/LUMO on PV Device Performance

As discussed in chapter 1, the first stage of the photovoltaic process is the absorption of light photons. The absorbance of a material ($A_\lambda$) is a quantitative measure which is expressed as the logarithm of the ratio between the intensity of light incident on the material ($I_0$) and the intensity of light which is transmitted through the material ($I_t$),

$$A_\lambda = \log\left(\frac{I_0}{I_t}\right) = 0.434\alpha d \qquad \textbf{(2.1)}$$

$$\text{where } \alpha = \frac{4\pi k}{\lambda}$$

It is important for the material to absorb as much as possible across the solar spectrum as shown in figure 2.1. The maximum wavelength of light which can be absorbed is determined by the energy difference between the HOMO and LUMO energy levels. It therefore follows that a smaller band gap would lead to more photon absorption and a greater photo generated current. However, the energy of charge carriers generated by longer wavelengths is low and this limits the built in electric field of the device. The optimum energy band gap is said to be around 1.4eV for PV devices and the materials absorption spectrum should ideally go beyond 600nm[75]. Organic materials with an energy band gap lower than 2eV, corresponding to a wavelength of 620nm, are classed as a low band gap organic semiconductors[76].
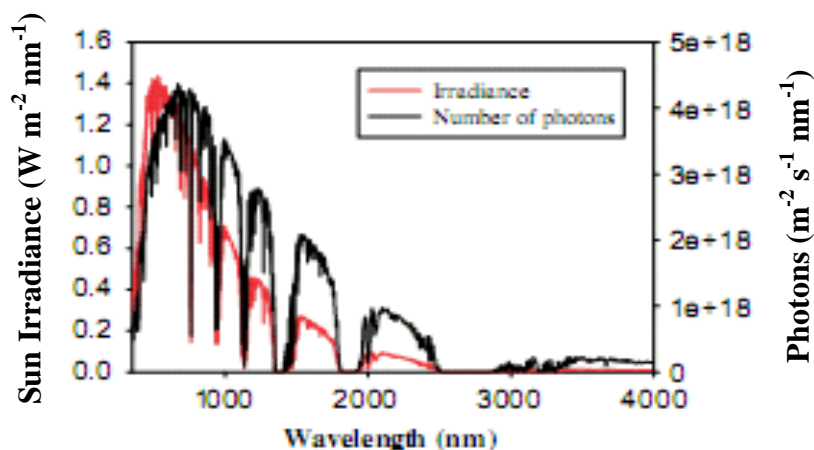
**Figure 2.1 – Sun irradiance (red) and number of photons (black) as a function of wavelength[75].**

The second stage of the photovoltaic process is charge separation, which requires an offset between the donor and acceptor energy levels. Figure 2.2 shows the relative energy levels of a typical donor/acceptor pair, in this case the donor is on the left and the acceptor on the right. As explained in chapter 1 the smaller of the donor or acceptor energy gap ($E_g$) minus the binding energy ($E_B$) needs to be greater than the difference between the donor HOMO energy ($E_{D\text{-}HOMO}$) and the acceptor LUMO energy ($E_{A\text{-}LUMO}$) in order to achieve charge separation at the donor acceptor interface. This condition can be expressed as,

$$E_{ex} = E_g - E_B > |E_{D-HOMO}| - |E_{A-LUMO}| \qquad (2.2)$$

where $E_{ex}$ is the exciton energy. The value of $E_B$ for organic semiconductors is controversial, and is estimated to be between 0.2-0.4 eV[26,27]. The difference between the donor HOMO and the acceptor LUMO has been found to be related to the maximum open circuit voltage ($V_{oc}$) of a solar cell[75,77,78]. Scharber et al[78] found that for conjugated polymer:PCBM bulk heterojunction cells the $V_{oc}$ could be estimated as,

$$V_{oc} = \left(\frac{1}{e}\right)(|E_{D-HOMO}| - |E_{A-LUMO}|) - 0.3V \qquad \textbf{(2.3)}$$

Rand et al[26] determined that the maximum $V_{oc}$ in an organic solar cell is equal to the difference between $E_{D\text{-}HOMO}$ and $E_{A\text{-}LUMO}$. However, this maximum is rarely observed in practice due to variations in the nano scale morphology, temperature and incident light intensity.
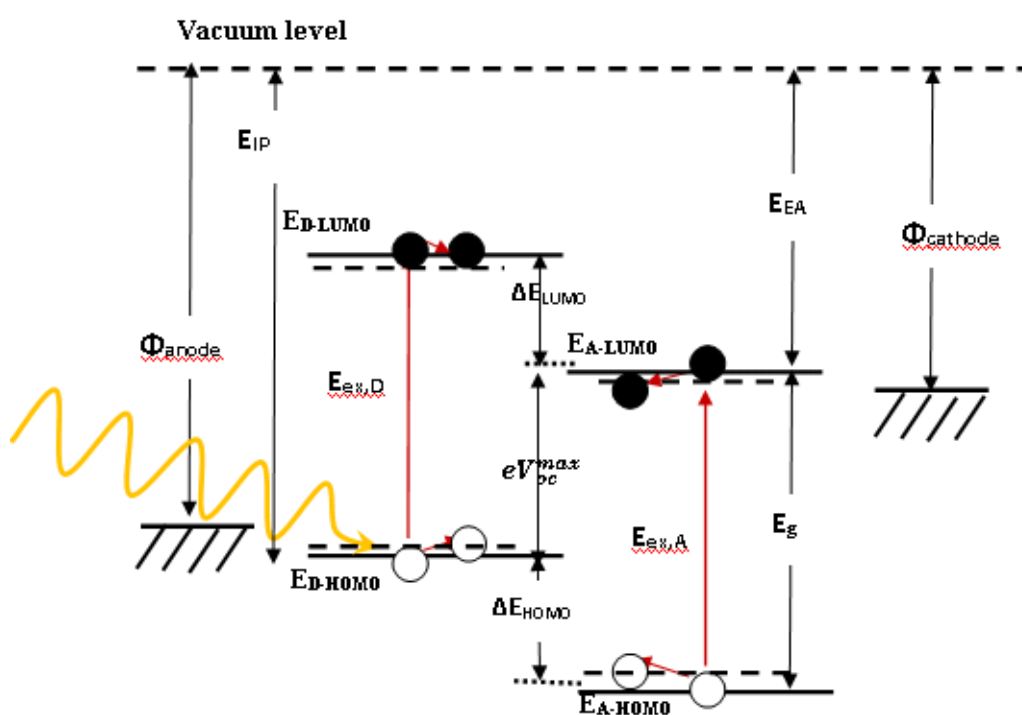


**Figure 2.2 - Schematic diagram of the energy levels of the materials and electrodes for a typical photovoltaic device[57].**

The $E_{D\text{-}HOMO}$ should ideally be below -5.27eV as this is the threshold at which air oxidation occurs[27]. This makes the material air stable for ease of processing. The HOMO energy of the donor must be higher than that of the acceptor to ensure efficient hole charge transfer from the acceptor to the donor. Similarly, the donor LUMO energy must also be higher than the acceptor LUMO energy to ensure efficient electron charge transfer from the donor to acceptor.

The difference between the HOMO (LUMO) energy of the donor and the HOMO (LUMO) energy of the acceptor is referred to as the frontier orbital energy offset[79], $\Delta E_{HOMO}$ ($\Delta E_{LUMO}$), as illustrated in figure 2.2. It is important to have a balanced value for both of these energy offsets, which need to be large enough to allow charge separation whilst not too large that they would significantly reduce the value for the $V_{oc}$[79, 80]. Dennler et al[6] recently reported that the ideal energy offset for $\Delta E_{LUMO}$ would be 0.3eV with a donor energy band gap of 1.2 – 1.7eV. Figure 2.3 shows the calculated PV device efficiency as a function of both the donor band gap and the difference between the LUMO energies of the donor and acceptor.
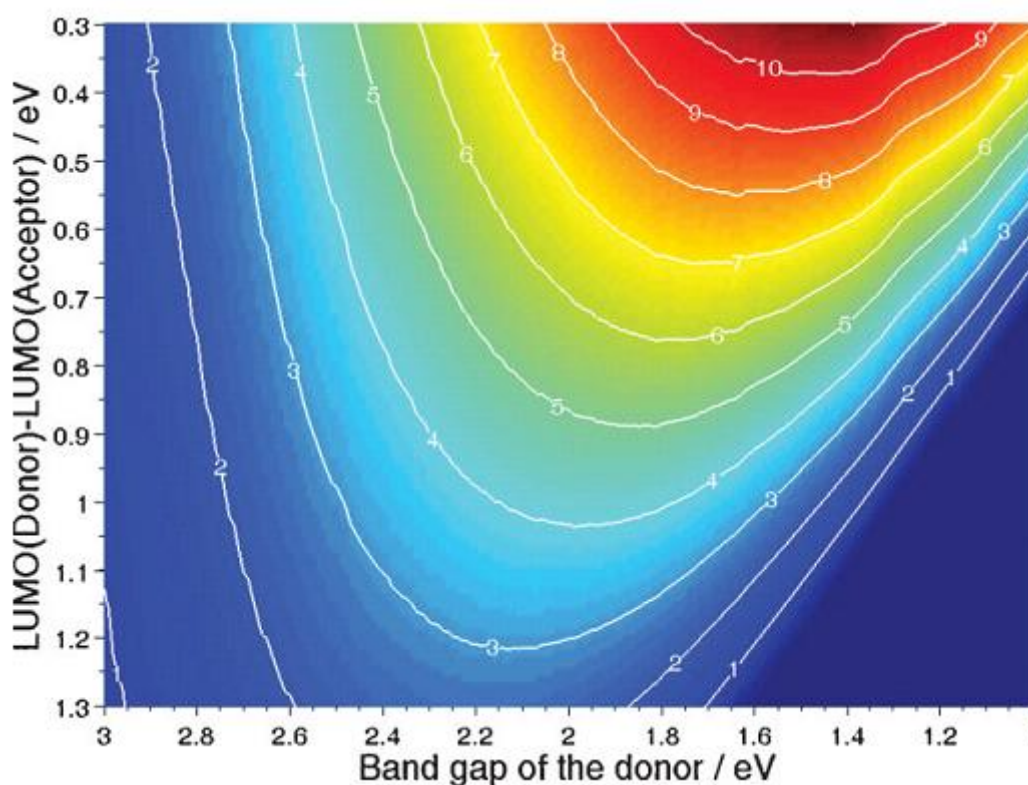


**Figure 2.3 – Calculated efficiency under AM1.5G illumination for bulk heterojunction devices based on composites that consist of a donor with a variable band gap and LUMO level and an acceptor with a variable LUMO level[6].**

Finally the holes and electrons need to be collected at their respective electrodes, having been transported through the donor/acceptor material respectively. Here the energy levels of the electrodes and how they align with the donor/acceptor energy levels has a direct impact on the efficiency of charge collection. Ideally the work function of the

anode (cathode) should be aligned as close as possible just above (below) the HOMO (LUMO) of the donor (Acceptor)[81,82,33] as shown in figure 2.2. The charge transport within the donor and acceptor also needs to be as balanced as possible. That is, the mobility values need to be similar for the electrons within the acceptor and the holes within the donor. If there is a significant difference in these mobility values then charge accumulation can take place near the electrodes, which we discuss further in chapter 5.

## 2.1.2 Ionisation Potential and Electron Affinity

The electron affinity ($\chi$) is chemically defined as the energy gained by an originally neutral molecule as a result of an electron being added to its LUMO. Similarly, the Ionisation Potential (*IP*) is defined as the energy needed to remove an electron from a neutral molecule's HOMO to the local vacuum level[83]. Figure 2.4 illustrates these definitions, where the valence band and conduction band are analogous to the HOMO and LUMO respectively.
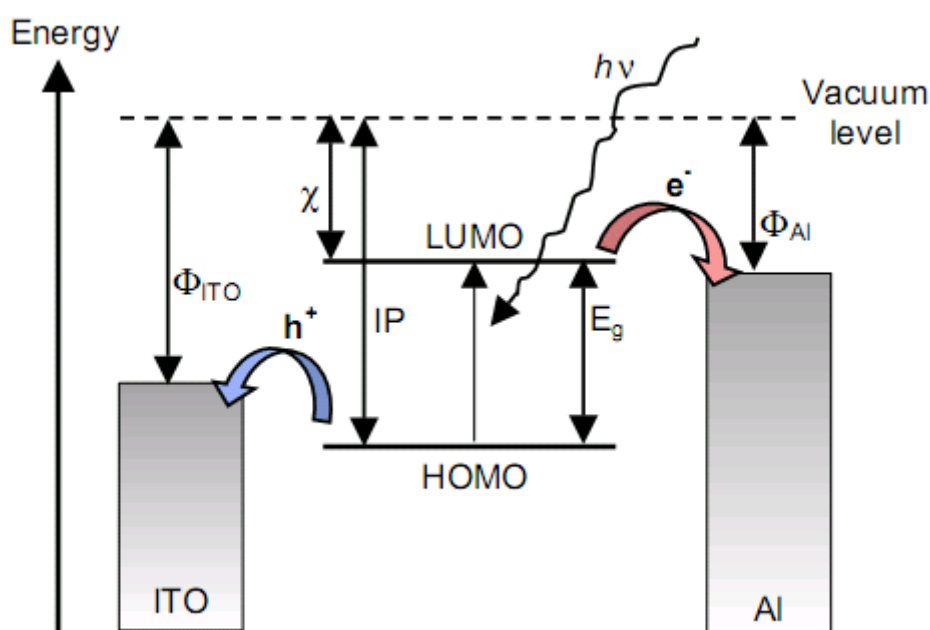


**Figure 2.4 – Energy level diagram illustrating the energy levels with respect to the local vacuum level. $\Phi$ is the work function, $\chi$ is the electron affinity, *IP* is the ionisation potential and $E_g$ is the optical band gap[33].**

Koopmans theorem links the *IP* and $\chi$ to the HOMO and LUMO energy levels respectively as simply the negative value of the former, i.e.[20,84,85]

$$IP = -E_{HOMO} \tag{2.4}$$

$$\chi = -E_{LUMO} \tag{2.5}$$

This theorem makes the assumption that the orbitals of the ion are identical to those of the neutral molecule, referred to as the frozen orbital approximation. There are several techniques available to measure the *IP* and $\chi$ of an organic semiconductor, such as ultraviolet photoemission spectroscopy (UPS), inverse photoemission spectroscopy (IPES), electrochemical voltage spectroscopy (EVS) and cyclic voltammetry (CV)[83,84]. The latter technique is used to measure energy levels in this thesis, as discussed in the next section.

## 2.1.3 Cyclic Voltammetry (CV)

All compounds used here were developed by the Organophotonics group at Hull University. These compounds are based on small molecules but with the addition of side chains to make them soluble and hence allow wet processing techniques.

The CV technique uses an electrochemical cell, which consists of three electrodes submerged in an electrolyte solution containing the material to be studied. The three electrodes are defined as the working (WE), reference (RE) and counter (CE) electrodes. Generally noble metals (platinum or gold) or glassy carbon are used for the WE, silver/silver chloride or saturated calomel for the RE and platinum wire for the CE.

A potential is applied between the working and reference electrodes whilst the current response is measured between the working and counter electrodes. Figure 2.5 illustrates the waveform used for CV measurements. The applied voltage is swept from an initial potential, $E_{initial}$, to a switching potential, point *b*, at which point the direction of the voltage scan is reversed. A reverse scan (line C) returns the voltage to its initial value before the scan is repeated for a second cycle and ends at the final potential, $E_{final}$, [86,87,88,89].
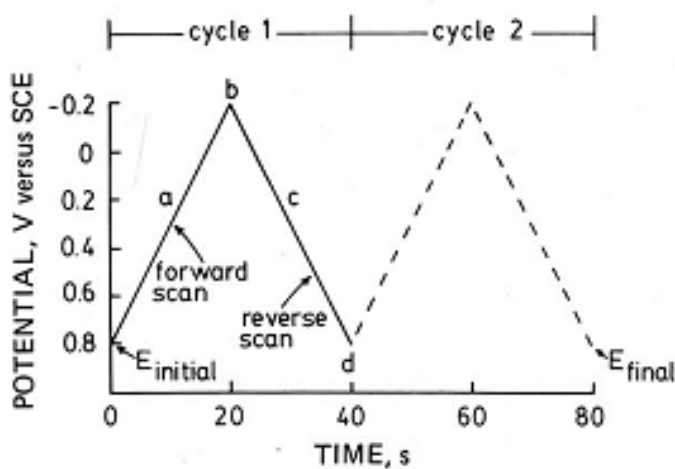


**Fig 2.5 - Cyclic Voltammetry waveform[89]**

Essentially CV measures the current at the working electrode against the voltage applied to give a cyclic trace similar to that shown in figure 2.6. This electrode facilitates the exchange of electrons with the compound being tested in order to measure its electrolysis properties[86,88,89]. The peaks produced relate to the electrolysis properties of the chemical compound being tested, referred to as oxidation and reduction. The oxidation of a compound relates to the loss of electrons or gain of oxygen by a molecule, hence the term oxidation, whilst reduction describes the opposite effect [86,87]. Electrolysis occurs when the solution is in contact with the working electrode surface which has reached a sufficient voltage, positive or negative depending on the reaction.

The current is then measured when the solution either loses or gains electrons to the surface of the working electrode, known as the anodic and cathodic current respectively[88,89]. The rise in anodic or cathodic current hence indicates oxidation and reduction reactions respectively. Figure 2.6 also demonstrates a reversible redox reaction, whereby the compound is oxidised on the forward scan and gives away an electron before being reduced and regaining the electron on the return scan.
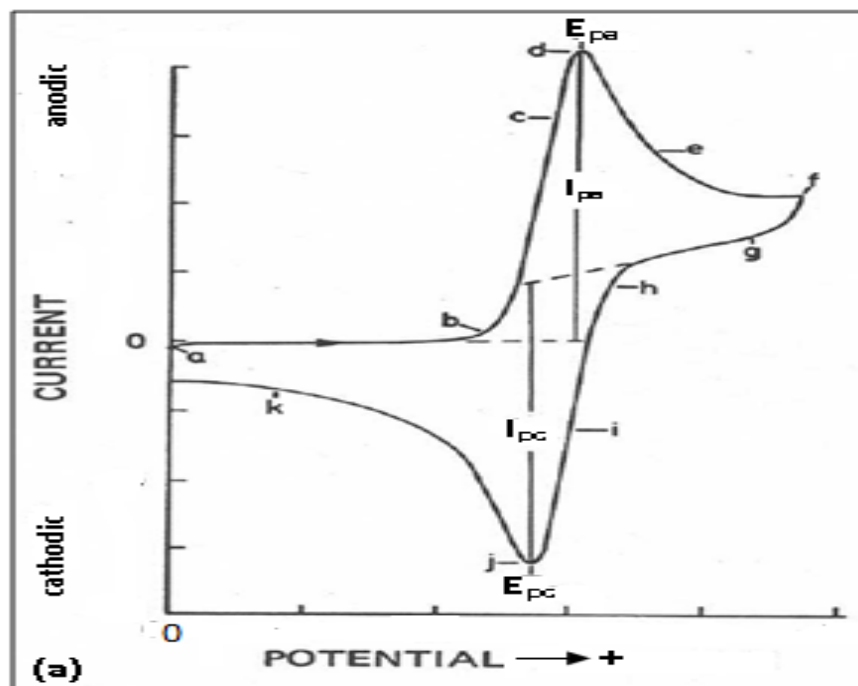


**Fig 2.6 - Typical Cyclic Voltammogram, $I_{PA}$ and $I_{PC}$ are the anodic and cathodic current respectively, $E_{PA}$ and $E_{PC}$ and are the voltage values at which the anodic and cathodic current reach a peak[89].**

In the case of an oxidation reaction the forward scan, for a material $X$, begins at point *a* in figure 2.6 and the potential is increased as the scan moves to the right. At point *b* the positive potential is large enough to start an oxidation reaction and the anodic current begins to rise, to give:

$$X \rightarrow X^+ + e \qquad\qquad (2.6)$$

The anodic current continues to rise steeply until it peaks at **d**, at which point the $X$ concentration near the electrode surface becomes depleted and the concentration of $X^+$ at the electrode surface becomes large. The anodic current then falls as it reaches the potential switching point at $f$, and continues to fall as the scan direction reverses. At point $h$ the potential has decreased enough for a reduction reaction to occur, which effectively reverses the oxidation reaction seen on the forward scan. This time a cathodic current increases until point $j$ when the $X^+$ concentration has decreased as:

$$X^+ + e \rightarrow X \qquad (2.7)$$

The cathodic current then falls as the potential continues to decrease to point $k$, at which point the original material $X$ has been restored to its initial condition and the $X^+$ have been depleted. Having returned to the initial potential the cycle is complete and a second cycle can then be run to check for reproducibility[88,89]. The reverse of the above process, with the voltage scan in the negative direction, begins with a reduction on the forward scan and oxidation on the return as:

$$X + e \rightarrow X^- \qquad (2.8)$$

$$X^- \rightarrow X + e \qquad (2.9)$$

Figure 2.7 illustrates a typical cyclic voltammetry trace for an organic semiconductor showing both oxidation and reduction reaction.

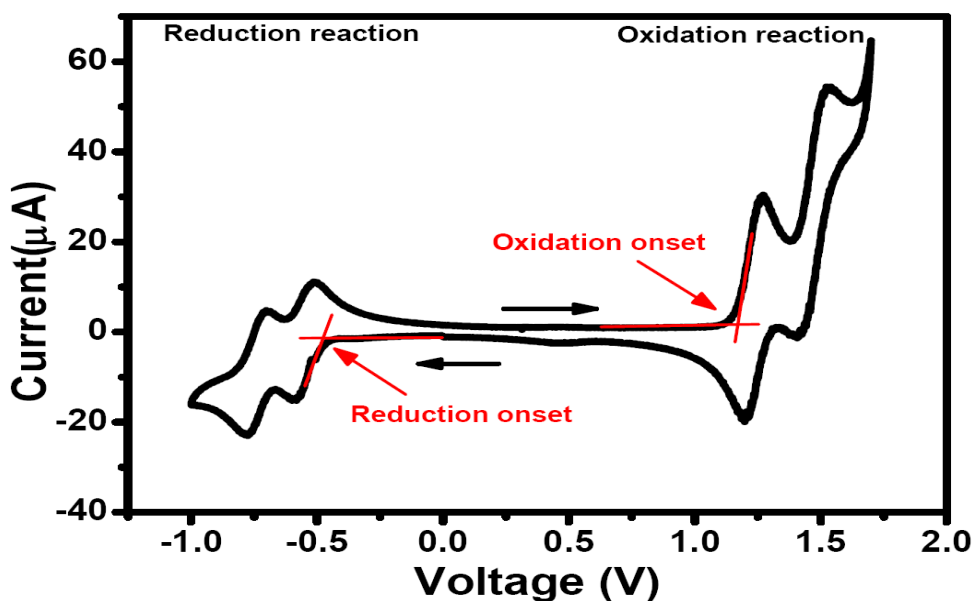**Figure 2.7 – A typical cyclic voltammetry trace showing oxidation and reduction reactions[57].**

The oxidation ($E_{ox}^{onset}$) and reduction ($E_{red}^{onset}$) onsets are determined by the intersection of the two tangents drawn where the anodic or cathodic current begins to rise, as shown in figure 2.7. These values are used to find the ionisation potential and electron affinity of the material, which in turn give us the value for the HOMO and LUMO energies respectively. The experimentally recorded potentials are relative to the reference electrode, but in order to find the *IP* and $\chi$, the potential needs to be correlated to the local vacuum level. This is achieved by relating a normal hydrogen electrode (NHE) to our reference electrode. The potential of the NHE is given as 4.5V ($\pm$0.1V)[90,91] with respect to the vacuum level, whilst for the Silver/Silver Chloride (Ag/AgCl) reference electrode the potential is 0.197V[90,92] with respect to the NHE.

Figure 2.8 illustrates the potential of the NHE with respect to the vacuum level and also shows the relative potentials of typical reference electrodes Ag/AgCl and saturated calomel (SCE). The result is that all potentials measured using CV can be related to the vacuum level by adding 4.7eV for a Ag/AgCl reference electrode or 4.74eV for a SCE.
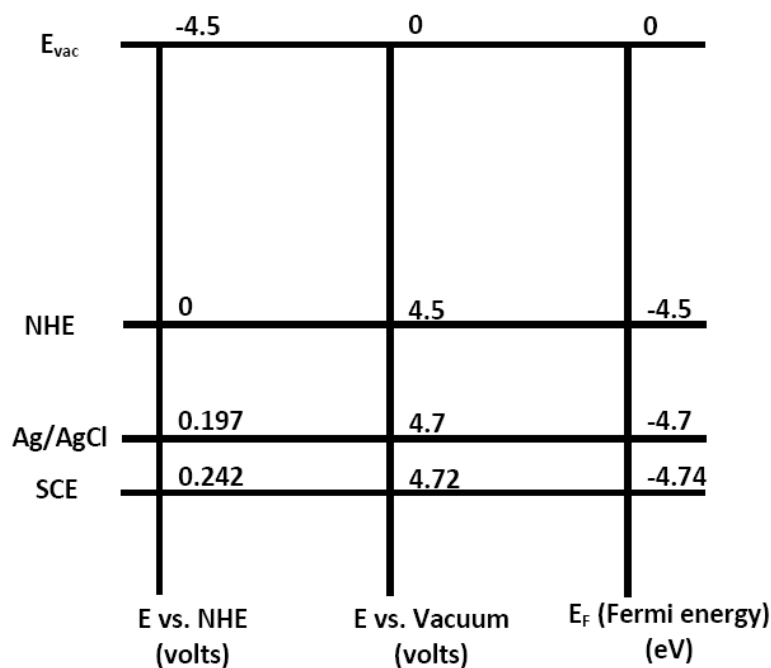
**Figure 2.8 – Illustration of the potential for the NHE with respect to vacuum and the potentials for Ag/AgCl and SCE with respect to the NHE[90]**

Hence it is now possible to relate the oxidation and reduction onsets experimentally recorded to the vacuum level, for the Ag/AgCl electrode this gives us:

$$E_{ox} = E_{ox}^{onset} + E_{Ag/AgCl} = E_{ox}^{onset} + 4.7 \tag{2.10}$$

$$E_{red} = E_{red}^{onset} + E_{Ag/AgCl} = E_{red}^{onset} + 4.7 \tag{2.11}$$

Now, having related the oxidation and reduction onsets to the vacuum level the final step is to calibrate these values against a known reference material. A popular choice for this task is ferrocene/ferrocenium (Fc/Fc$^+$) for which the oxidation has been shown to be a simple chemically reversible one electron process in organic solvents[90,93]. However, the reported half wave potential for ferrocene $\left(E_{Fc}^{1/2}\right)$ can vary[94,95]. Pavlishchuk et al[94] summarised a wide range of experimental values found for the $E_{Fc}^{1/2}$ of Fc/Fc$^+$ for various reference electrodes such as SCE, NHE and Ag/AgCl.

**Figure 2.9 – Cyclic Voltammetry of M Ru(acac)₃ in CH₃CN using RE Ag/Ag⁺ (a), with addition of ferrocene (b), RE SCE (c), RE copper wire[95].**
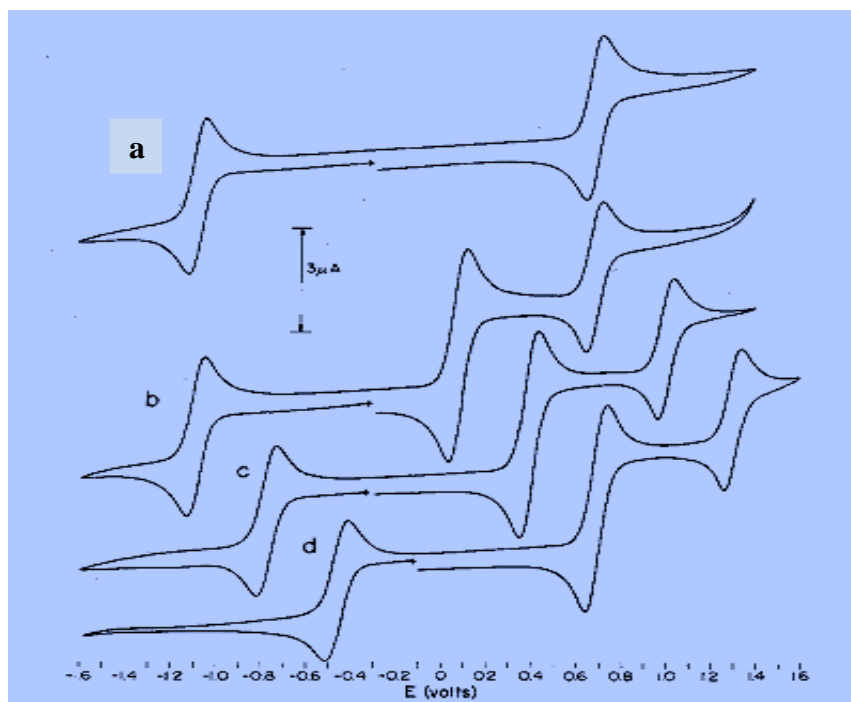
Figure 2.9 (a) shows the CV cycle for tris(acetylacetonato)ruthenium(III) in CH₃CN using a Ag/Ag⁺ reference electrode, and (b) shows the effect of adding ferrocene. It can be seen that the reduction and onset curves for the material being studied do not change with the addition of ferrocene, which shows its own oxidation peak in between.

Figure 2.9 (c) and (d) show how the CV curves are shifted along the x-axis when a different reference electrode material is used, in this case SCE and copper wire respectively. However, the formal potential of the material relative to the Fc/Fc⁺ are unchanged, which means that results for a material are reproducible relative to ferrocene even if the RE material is changed.

The addition of a correction factor, the difference between the reference value for $E_{Fc}^{1/2}$ and the experimentally measured value for $E_{Fc}^{1/2}$, to equations 2.8 and 2.9 takes the RE into account. For Ag/Ag⁺ we use the average of the values found from the study by Pavilishchuk et al as our reference for the half wave potential of Fc/Fc⁺, which is 0.425V[94].

63

$$E_{ox} = E_{ox}^{onset} + 4.7 + 0.425 - E_{Fc}^{1/2} \qquad (2.12)$$

$$E_{red} = E_{red}^{onset} + 4.7 + 0.425 - E_{Fc}^{1/2} \qquad (2.13)$$

Now we can relate the ionization potential and electron affinity to the oxidation and reduction onset of a material respectively.

$$E_{IP} = eE_{ox} \qquad (2.14)$$

$$E_{EA} = eE_{red} \qquad (2.15)$$

When both oxidation and reduction reactions are produced, the difference between the measured IP and EA values is the electrical energy band gap ($E_{g,ec}$). However, it is often the case that a cyclic voltammetry measurement of a material will only produce one redox reaction, either oxidation or reduction, because of the limited operating range of the experiment. In this event the optically measured energy gap ($E_{g,op}$) of a material can be used to estimate the unknown value as,

$$E_{IP} = E_{EA} + E_{g,op} \qquad (2.16)$$

$$E_{EA} = E_{IP} - E_{g,op} \qquad (2.17)$$

Note, however, that this does not take the binding energy of the exciton into account. The energy band gap of an organic semiconductor can be estimated from its absorption spectrum[96]. The onset of absorption indicates the longest wavelength photon that can be absorbed, and hence the minimum energy needed to excite an electron across the semiconductor band gap. A UV/visible spectrometer can be used to determine the absorption spectrum of a compound by measuring the intensity of light transmitted through a sample in comparison to a blank reference sample. The spectrometer steps through a chosen range of wavelengths measuring the transmission through the sample over the desired spectrum.

By comparing this to the transmission of light through a blank reference sample the absorption spectrum of the semiconductor is obtained.
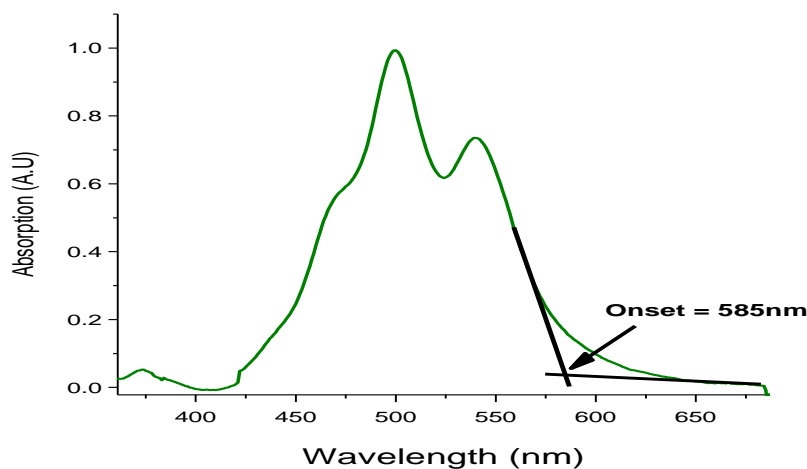


**Figure 2.10 – A typical absorption spectrum for an organic semiconductor.**

Figure 2.10 illustrates how the absorption onset is determined by the intersection of the two tangents drawn along the rise and background absorption. Using the relation $E=h\upsilon$ the energy gap, in eV, can then be determined by:

$$E_{g,op} = {hc}/{\lambda e} \qquad \textbf{(2.18)}$$

where $h$ is Planck's constant, $c$ is the speed of light, $\lambda$ is the wavelength and $e$ is the elementary charge. The cathodic and anodic peak potentials ($E_{pc}$, $E_{pa}$) and peak currents ($i_{pc}$, $i_{pa}$) determined during CV measurements, labelled in figure 2.6, can provide an indication of the stability of a compound and the reversibility of the redox reactions. An electro-chemically reversible couple is a redox couple in which electrons are rapidly exchanged between the material and the working electrode. This process needs to be fast enough to maintain the concentrations of the oxidised and reduced forms in equilibrium near to the electrode surface. The material is supplied to the electrode by diffusion, which in turn controls the rate of electron transfer, so the exchange of electrons needs to be fast in comparison to the rate of diffusion. A slower rate of electron exchange leads to an electrochemically irreversible reaction[88,89].
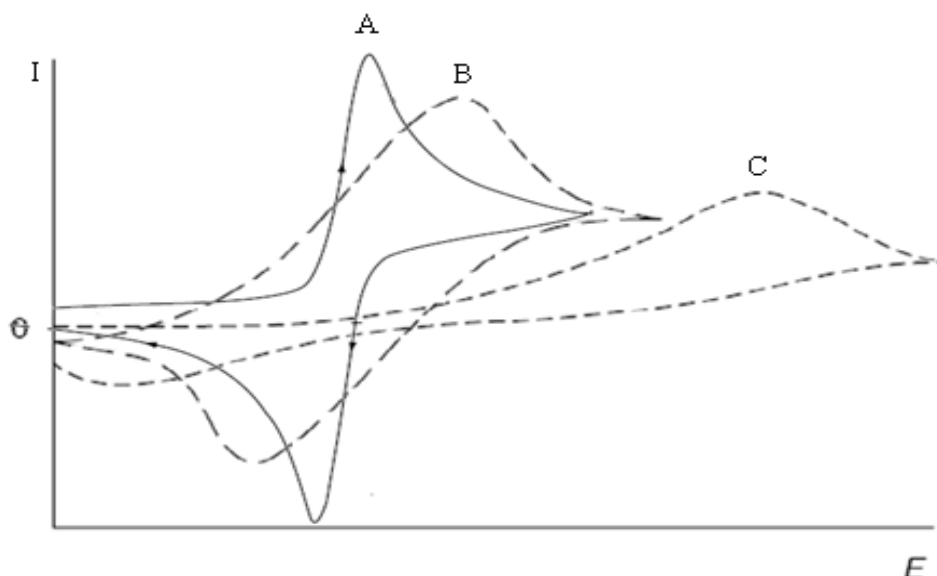
**Figure 2.11 – Cyclic Voltammetry scan for (A) reversible, (B) quasi-reversible and (C) totally irreversible redox reactions[97].**

Figure 2.11 (A) illustrates the CV wave for a typical reversible redox reaction. Here the original material depleted by the forward reaction is reproduced by the reverse reaction, with no side chemical products produced.

The electrochemical reversibility of a compound then can be evaluated by measurement of the potential difference between the two redox peaks produced by the CV cycle. In an ideal system the difference in potential for the anodic and cathodic current peaks shown in figure 2.5, $E_{pc}$ and $E_{pa}$, for a reversible reaction is given by:[86-89]

$$\Delta E_p = \left| E_{pc} - E_{pa} \right| = \frac{0.059}{n} \qquad (2.19)$$

where $n$ is the number of electrons transferred in the electrode reaction. So a value of 59mV for $\Delta E_p$, for one electron transfer, is generally a sign of a reversible redox reaction. However, the electron transfer rate is reduced by the cell resistance which leads to an increase in $\Delta E_p$, meaning a measured value of 60 – 80mV would still be considered to be reversible reaction[98].

Slow electron transfer at the electrode surface causes the peak separation to increase, as can be seen in figure 2.11 (B) and (C). The quasi reversible reaction has broader peaks, as shown for (B), which separate further apart with increasing scan rate. When the peaks are spread so widely that no parts of the two peaks overlap on the potential axis, as seen for (C), then this is referred to as a totally irreversible redox reaction[88,89].

The peak current for a reversible reaction during the forward sweep of the first cycle is given by the Randles-Sevcik equation[89],

$$I_p = (2.69 \text{X} 10^5)n^{3/2}AD^{1/2}Cv^{1/2} \qquad \textbf{(2.20)}$$

where $I_p$ is the peak current (amps), $n$ is the electron stoichiometry, $A$ is the electrode area (cm$^2$), $D$ is the diffusion coefficient (cm$^2$s$^{-1}$), $C$ is concentration (mol cm$^{-3}$) and $v$ is the scan rate (Vs$^{-1}$). This equation shows that $I_p$ increases with $v^{1/2}$ and is directly proportional to concentration. For a fast exchange of electrons, and hence a reversible reaction, the values $I_{pa}$ of and $I_{pc}$ should be equivalent[89],

$$\frac{I_{pa}}{I_{pc}} \approx 1 \qquad \textbf{(2.21)}$$

Chemical reactions coupled to the electrode process can significantly affect the ratio of peak currents, so a ratio of 1 is a good sign of chemical reversibility. A redox reaction is considered to be chemically reversible if the original material depleted by the forward scan is reproduced by the reverse electrochemical reaction, without a new electrode reaction or production of side products. The reaction is chemically irreversible when side products are produced by the reverse scan reaction[99].

To summarise, an electrochemically reversible reaction (R) shows that the forward and reverse redox reactions are fast enough to maintain the concentration of the oxidised and reduced forms in equilibrium at the electrode surface. A quasi-reversible reaction (QR) is too slow to retain the equilibrium conditions near to the electrode, but the anodic and cathodic peaks still overlap on the potential axis. An irreversible reaction (IR) is so slow that the anodic and cathodic peaks do not overlap at all on the potential axis. A different peak current during the reverse scan indicates a chemically irreversible reaction.

## 2.2 Charge Transport in Organic Semiconductors

The mobility of charge carriers within a semiconductor has a significant impact on the overall device efficiency of a solar cell. As previously explained, once the exciton has separated at the interface between the donor and acceptor materials the hole and electron charge carriers need to travel to their respective electrodes. The mobility values for the two types of charge carrier give an indication as to how efficient this stage of the process is for a given material. Here we investigate charge transport in general, beginning with a brief review of the transport mechanism within both organic and inorganic materials. The difference in how charge carriers move within these two types of materials is highlighted, along with the challenges created by the lower mobility values generally seen for organic materials. An overview of the various experimental techniques used to measure charge mobility is given, followed by an in depth look at the technique used in this thesis, the Time of Flight measurement. The actual experimental set up used is detailed along with the challenges faced in both the sample preparation and the measurements taken. Results are then presented with analysis of how the chemical structure of donor molecules affects the charge mobility measured. Blends of donor/acceptor are then investigated to see how the charge carrier transport differs from that of the pristine donor and acceptor compounds.

## 2.2.1 Charge Mobility

In the absence of an applied electrical field, or a concentration gradient, electrons and holes move randomly but without any overall net motion (i.e. the net change in momentum is zero over time). When an electric field is applied the charge carriers accelerate, the direction being dependent on the carrier charge in relation to the electric field. In a vacuum this linear acceleration would continue unabated, but within a solid material this acceleration is hampered by collisions with crystal defects, phonons and impurities. These scattering events effectively limit the average velocity of the charge carriers and is generally referred to as the 'drift velocity' $(v)$[100]. The change in momentum $(p)$ for a charged particle of mass $(m)$ in an electric field $(E)$ is given by[20],

$$\langle\frac{dp}{dt}\rangle = eE = \frac{m\langle v\rangle}{\tau} \tag{2.22}$$

Where $\tau$ is the mean time between collisions. Therefore,

$$\langle v\rangle = \frac{e}{m}\tau E \tag{2.23}$$

The mobility $(\mu)$ is defined as the average velocity gained per unit field[20,100],

$$\mu = \frac{\langle v\rangle}{E} = \frac{e}{m}\tau \tag{2.24}$$

This mobility value indicates how efficiently electron and hole charge carriers can travel through a particular material, or blend of materials. It is related to the conductivity '$\sigma$' of the material by[100,101],

$$\sigma_e = ne\mu_e \quad , \quad \sigma_h = pe\mu_h \tag{2.25}$$

where the concentration of electrons and holes are denoted by $n$ and $p$ respectively, $\mu_h$ and $\mu_e$ denote hole and electron mobility respectively. Whilst a high mobility does not necessarily equate to a good photovoltaic material, it is certainly a key parameter to consider when evaluating the overall performance of a solar cell device. It is also desirable that $\mu_h$ and $\mu_e$ are approximately equal to provide balanced charge transport.

## 2.2.2 Charge Transport Mechanisms

In semiconductors there are two main mechanisms of charge transport, referred to as band transport in delocalised states and hopping between localised states. Here we examine how these states arise, before specifically considering charge transport in organic materials.

## 2.2.2.1 Origin of Bands

When atoms are widely spaced, as in a gas, the electrons within the attractive potential of each atom occupy bound states separated by forbidden energy gaps. Within an ideal crystalline semiconductor the atoms are regularly packed together close enough to interact with each other. This causes each energy level to split into a large number of levels equal to the number of atoms. Due to the very small difference in energy between the individual levels they can be viewed as energy bands rather than discrete levels for each atom. Each energy band has a band width, with a quasi-continuous energy level distribution when the number of atoms is large. These bands are separated by 'forbidden zones' generally referred to as the energy gaps, which represent energy intervals containing no allowed states. Inorganic semiconductors tend to have large bandwidth energy bands and small band gaps due to their strong covalent bonds[100]. Figure 2.12 illustrates how these energy bands are formed by closely packed particles. It can be seen that the delocalised bands are quasi continuous throughout the crystal[102].
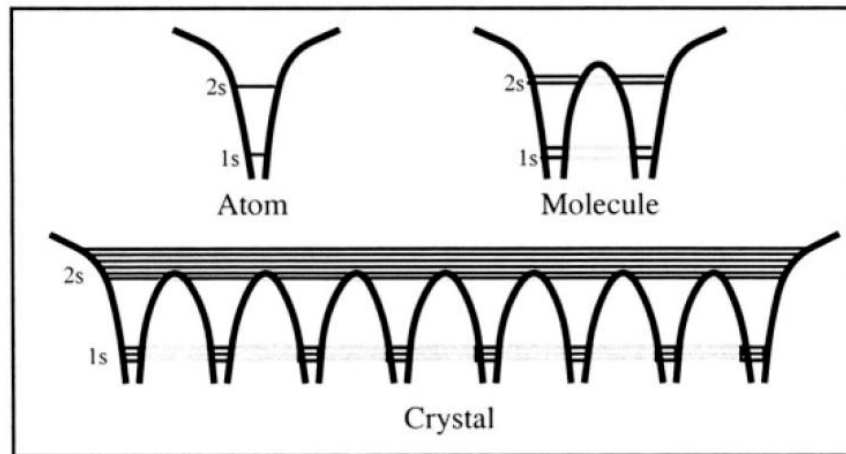
**Figure 2.12 - Allowed energy levels of an atom, hypothetical molecule and crystal[102]**

For the example given in figure 2.12, electrons in the 1s energy level, close to the nucleus, are tightly bound, whilst those in the higher 2s level can move throughout the crystal. Materials with some weak disorder, such as inorganic semiconductors, can be modelled this way as their density of states varies only slightly from the ideal crystal. These materials use the concept of almost free quasi-particles (Bloch waves) travelling within the energy bands[101]. When a charge carrier is moving in a solid material the force between other atoms will affect its movement. Hence an effective mass is used to describe the movement of the charge carrier, which varies from the actual mass and can even be negative depending on the circumstances. The charge carriers move as a delocalised plane wave through the energy band with a relatively large mean free path. This generally gives high mobility values for inorganic semiconductors, with Germanium and Silicon showing mobility in the order of $10^3 cm^2/V.s$[103].
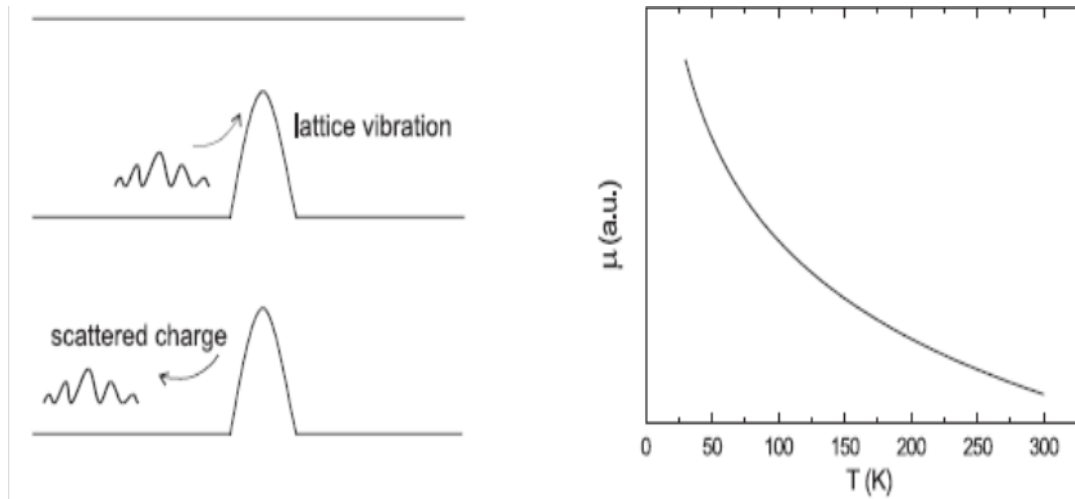
**Figure 2.13 - Band transport in an ideal crystal and thermal vibration scattering (left), schematic graph showing the decrease of the mobility as a function of increasing temperature (right)[104].**

At room temperature the thermal energy causes the atoms to collectively vibrate in the lattice, generating phonons, which leads to scattering of charges as illustrated in figure 2.13 (left). This in turn attenuates the movement of the charge carriers. As the temperature increases more phonons are generated due to additional thermal energy, which in turn causes more scattering of electrons and hence a reduction in the overall charge mobility. This can be seen in figure 2.13 (right), which illustrates the relationship between mobility and temperature given by[20],

$$\mu \propto T^{-n} \tag{2.26}$$

where n>1.

## 2.2.2.2 Localised States and Hopping Transport

In contrast to the strong covalent bonds holding together molecules within an inorganic semiconductor, the molecules within organic semiconductors are held together mostly by weak van der Waals forces and some local coulombic interaction. The crystalline quality of most thin film organic materials is very poor compared to inorganic semiconductors. The intermolecular bond interaction energy is low, comparable to that of the vibrational energy of the molecules at room temperature. Charge excitations and interactions are localised on individual molecules and hopping becomes the dominant charge transport mechanism[20,103].

Defects within the crystals lead to small crystalline domains forming, surrounded by grain boundaries, which when small enough lead to an amorphous material. The defects lead to more scattering of charge carriers, reducing the mean free path significantly in comparison to weakly disordered inorganic crystals. When the mean free path is less than the inter-atomic distance the charge carrier becomes localised on a few atoms. Charge carriers can become trapped in strongly localised state and become immobile for a period of time before becoming free and hopping to the next trapped state. Hence 'hopping' transport takes place between strongly localised states as illustrated in figure 2.14. Overall this leads to much lower mobility values, e.g. $1cm^2/V.s$ for amorphous silicon and from $10^{-7}$ to $10^{-3}cm^2/V.s$[103] for thin film organic semiconductors.
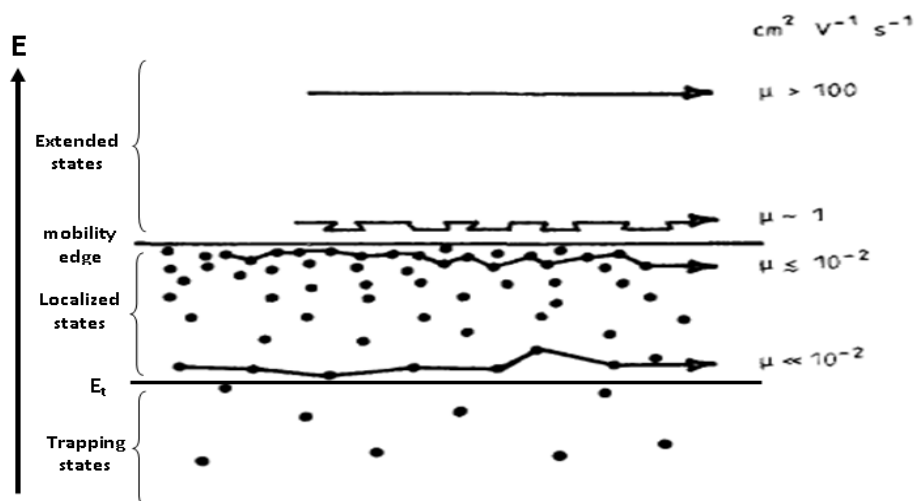
**Figure 2.14 - The variation of charge carrier mobility with the energy distribution of traps and an expectation of the mobility values according to energetic disorder[105].**

Whilst crystalline inorganic semiconductors have clearly defined energy bands and forbidden areas, as discussed earlier, organic semiconductors have discrete energy states. This is due to the weak interactions between the molecules, which produces a continuous spread of energy levels that include trap states as illustrated in figure 2.15.
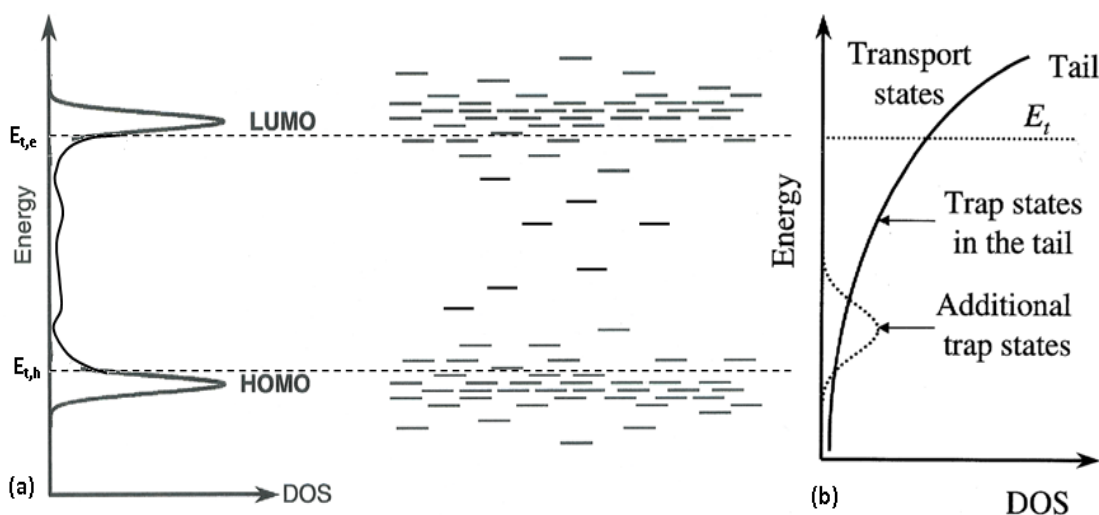


**Figure 2.15 - (a) Density of states distribution of HOMO/LUMO levels in disordered organic semiconductors, (b) Enhancement of the tail region showing the trap states in the tail and the additional trap states and the transport states[106].**

Figure 2.15 shows that the energy regions with high density of states are referred to as the lowest unoccupied molecular orbit (LUMO) and the highest unoccupied molecular orbit (HOMO). The energy regions with low density of states, between the HOMO and LUMO are the 'trap states'. These traps states are seen to be most concentrated just above and below the HOMO and LUMO levels respectively with progressively fewer trap states as we approach the centre. The charge transport sites exist as discrete states within the HOMO and LUMO levels for organic materials, shown as a series of short lines in figure 2.15. Charge transport within an organic material involves hopping between these states along the LUMO for electrons and along the HOMO for holes. The trap states just below the LUMO and just above the HOMO are referred to as electron and hole traps respectively. The HOMO and LUMO states in the tail of the density of states distribution can act as traps, as discussed later.

The defects found within organic semiconductors fall into two main categories, chemical (extrinsic) and Physical (intrinsic). Chemical defects are generally caused by impurities introduced whilst processing the material, for example during synthesis of the compound or whilst processing a thin film device. The energy levels (HOMO/LUMO) of a foreign molecule may lay within the energy gap of the host material, hence creating the energetic trap states seen between the HOMO and LUMO. Physical defects can occur in chemically pure materials as a distortion of the lattice structure of the composing molecules. There are different types of physical defects, such as a vacant lattice site, grain boundaries or a molecule occupying an interstitial position. Physical defects can also be caused by chemical defects distorting their neighbourhood[20,107,108,109].

An activation energy facilitates hopping from one localised state to another. Here an increase in temperature provides thermal energy which overcomes the activation energy required for the charge carrier to hop from one state to another. Thermal energy can actually transform a trap state into a transport state[20,108,110]. Figure 2.16 illustrates the relationship between temperature and mobility for a disordered organic semiconductor, in contrast to the relationship seen for inorganic semiconductors in figure 2.13.
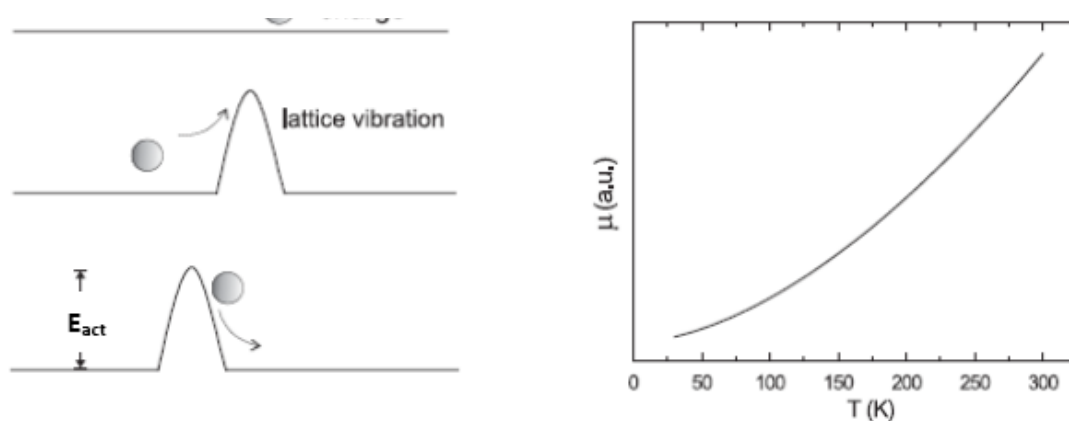


**Figure 2.16 - Hopping transport in disordered materials with localized carriers. Thermal vibration helps to overcome the activation barrier of energy $E_b$ (left), schematic graph showing the increase of the mobility as a function of increasing temperature (right)[104].**

## 2.2.2.3 Charge Transport in Disordered Organic Materials

Here we discuss models that have been developed to describe charge carrier transport within organic materials. For conventional insulators the field-assisted thermal ionisation model, also referred to as the Poole Frenkel effect, is used to explain the electric field and temperature dependence of carrier mobility[111,112,113]. Specifically, this model was used to explain charge carriers escaping from trapping centres into the conduction band when an electrical field is applied. The field reduces the coulomb potential barrier, and the field dependence of the mobility is[111],

$$\mu = \mu_o \exp\left(\frac{\beta_{PF}E^{1/2}}{k_B T}\right) \tag{2.27}$$

where $\beta_{PF} = (e^3/\pi\varepsilon\varepsilon_o)^{1/2}$ is the Poole-Frenkel coefficient, $k_B$ is the Boltzmann constant, $\varepsilon$ is the dielectric constant of the material and $\varepsilon_o$ is the permittivity of free space. Similar results were found by Gill for molecular doped polymer TNF:PVK, who produced the following empirical relation for $\mu$,[114]

$$\mu = \mu_o \exp\left(-\frac{E_o - \beta_{PF}E^{1/2}}{k_B T_{eff}}\right) \tag{2.28}$$

where $\frac{1}{T_{eff}} = \frac{1}{T} - \frac{1}{T_o}$ , $T$ is the sample temperature, $T_o$ is the temperature at which mobility values are constant for all field strengths and $E_o$ is the zero field activation energy. Whilst this model has been widely used it fails to take into account the disordered structure of organic semiconducting materials, with respect to the field and temperature dependence of charge mobility.

Liquid crystals are relatively disordered so a thermal activated, disorder based model is used to describe charge transport. The intersite hopping of carriers occurs via π-π interactions between sites, which are usually the aromatic cores of the molecules. The hopping rate depends on the strength of the intermolecular coupling between the HOMOs and LUMOs of adjacent molecules. Disorder or polaron models describe the field and temperature dependence of mobility. We assume here that charge carrier transport takes place via incoherent hopping between localised states randomly distributed in space with a concentration, $N$. Further, we assume that the energy of the charge carriers on these states have a Gaussian distribution, $g(E)$, so that the density of states (DOS) can be described by[101],

$$g(E) = \frac{N}{\sigma\sqrt{2\pi}}\exp\left(-\frac{E^2}{2\sigma^2}\right) \tag{2.29}$$

where $\sigma$ is the width of the Gaussian energy distribution and $E$ is the energy measured relative to the centre of the DOS. The energetic disorder originates from fluctuations in the lattice polarisation energies and the distribution of the effective segment length for the main chain polymer. The value for $\sigma$ is of the order of -0.1eV for most random organic materials[115].

The transition rate of a charge carrier from a localised state $(i)$ to a localised state of lower energy $(j)$ is dependent on the spatial separation $(R_{ij})$ between the two sites as[101],

$$v_{ij} = v_o\exp\left(\frac{-2R_{ij}}{a}\right) \tag{2.30}$$

where $a$ is the localisation length, which is assumed to be equal for sites $(i)$ and $(j)$.
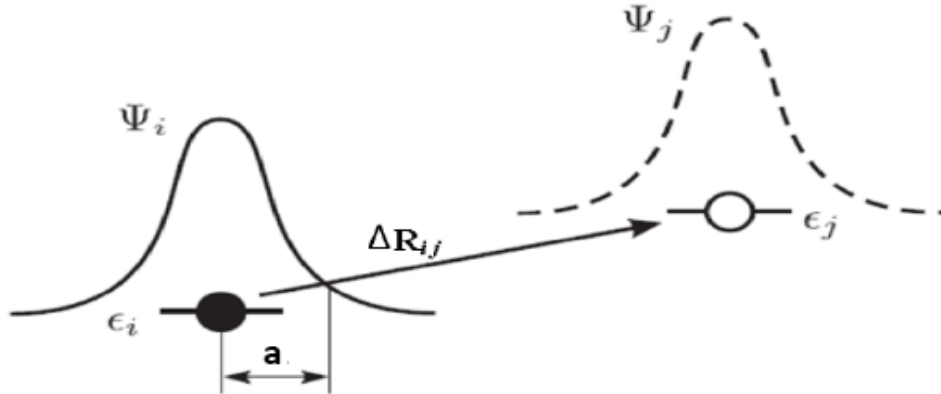


**Figure 2.17 – Hopping transition between two localised states i and j.**[101]

The exponential decay of the charge carrier wave function in the localised state is determined by $a$. The factor $v_o$ is dependent on the carrier interaction mechanism that causes the charge transition.

When the above transition from $(i)$ is to a localised state of higher energy $(j)$, the energy difference between the two states will also influence the transition rate. This energy difference can be compensated for by the absorption of a phonon of similar energy[116]. The addition of a further exponential term to equation 2.30 takes the energy increase into account as[101],

$$v_{ij} = v_o \exp\left(\frac{-2R_{ij}}{a}\right) \exp\left(-\frac{E_j - E_i + |E_j - E_i|}{2kT}\right) \tag{2.31}$$

Charge carriers in the DOS relax down from high energy states until they reach the equilibrium energy $(E_\infty)$ [103,115]. As shown in figure 2.18 (left) the equilibrium energy is at $-\sigma^2/k_B T$, and this forms the energetic centre of the occupied density of states (ODOS).
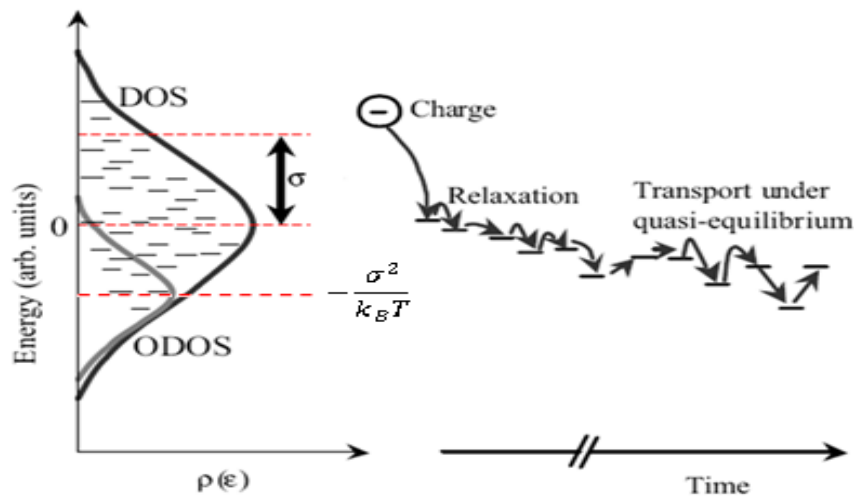


**Figure 2.18 – Schematic of a Gaussian energy distribution of the localised states (left) and the charge transitions between localised states as the carrier relaxes from the density of states DOS to the equilibrium energy of the occupied density of state ODOS (right)[23].**

The time taken for the charge carrier to relax to equilibrium is referred to as the relaxation time $(T_{rel})$. During the relaxation time charge transport is dispersive due to the random distribution of charge carrier states as they relax downward energetically.

Once the energy distribution of the charge carriers has stabilised around $E_\infty$, at a time $T > T_{rel}$, transport becomes nondispersive (Gaussian)[115]. Then hopping resembles a multiple trapping process, where the carrier hops to a state below $E_\infty$ and then back up in energy to a state near to $E_\infty$. Figure 2.18 (right) illustrates this process after the initial relaxation time marked by the break in the x-axis.

It has been shown that there are two main factors affecting the mobility within a material, positional and energetic disorder, which are characterised by the two exponential terms in equation 2.31. We now investigate these parameters further. The positional disorder originates from variations in the intersite distance, $a$, which in turn determines the so called overlap parameter $(\Gamma)$ as $\Gamma = 2\gamma a$. $\gamma$ is the charge carrier localisation constant, also known as the inverse wave function decay constant, where greater values correspond to greater charge localisation and a sharper decay of electron density with distance[101]. $\Gamma$ quantifies the degree of electronic coupling between localised sites due to the wave function overlap.

The positional disorder $(\Sigma)$ is determined by the sum of $\Gamma$ for each site, $\Gamma_i$ and $\Gamma_j$, each of which can vary randomly within a Gaussian probability density of standard deviation $\delta\Gamma$. The variation of $\Gamma_{ij}$ gives us the positional disorder parameter as $\Sigma = (2\delta\Gamma)^{1/2}$. The energetic disorder is described by the parameter $\sigma/k_B T$. Monte Carlo simulations, using a zero applied field, have shown that the mobility varies with temperature according to[117,118],

$$\mu(E = 0, T) = \mu_o \, \exp\left[-\left(\frac{2\sigma}{3K_B T}\right)^2\right] \qquad \textbf{(2.32)}$$

where $\mu_o$ is the value of the zero field mobility projected to infinite temperature. Figure 2.19 illustrates this relationship using the Monte Carlo simulation results.
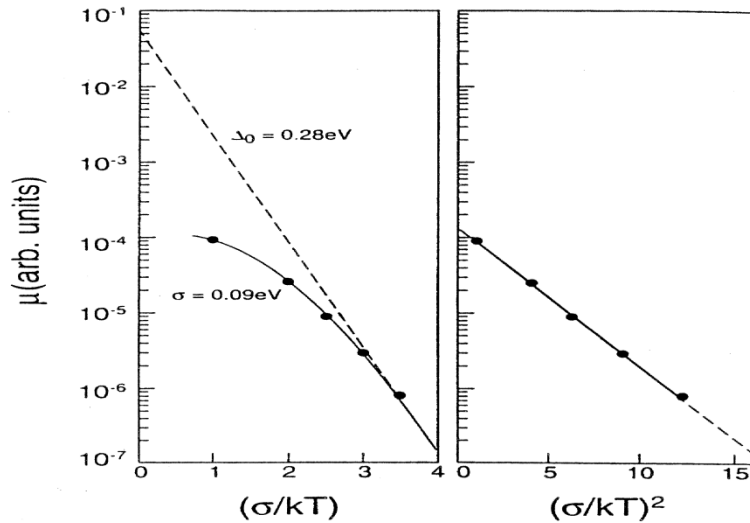
**Figure 2.19 – Plot of mobility on a log scale as a function of the disorder parameter (left) and the square of the disorder parameter (right) from Monte Carlo simulation results[118].**

Analysis of the effect of the applied electric field was carried out by running simulations with a variable value for the energetic disorder whilst holding the value for the positional disorder parameter at zero. The variation of the mobility as a function of the applied field is shown in figure 2.20 for various values of $\sigma/k_BT$.
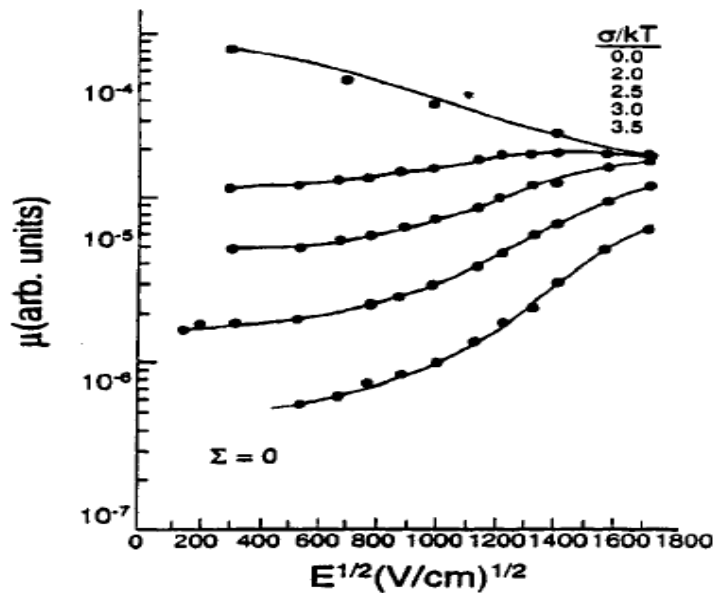


**Figure 2.20 – Monte Carlo simulation plot of mobility on a log scale as a function of the applied electric field for various value of $\sigma/k_BT$ and $\Sigma$ held at zero.[118]**

Figure 2.20 shows that at high fields the mobility increases with field strength, following the Poole-Frenkel relation $\left(\ln \mu \, \alpha \, E^{1/2}\right)$. The gradient is shown to decrease with the disorder parameter until it becomes negative as $\sigma/k_B T$ tends to zero. At low field strength the mobility is almost saturated, with only small increase shown relative to the high field regime as the field strength increases.
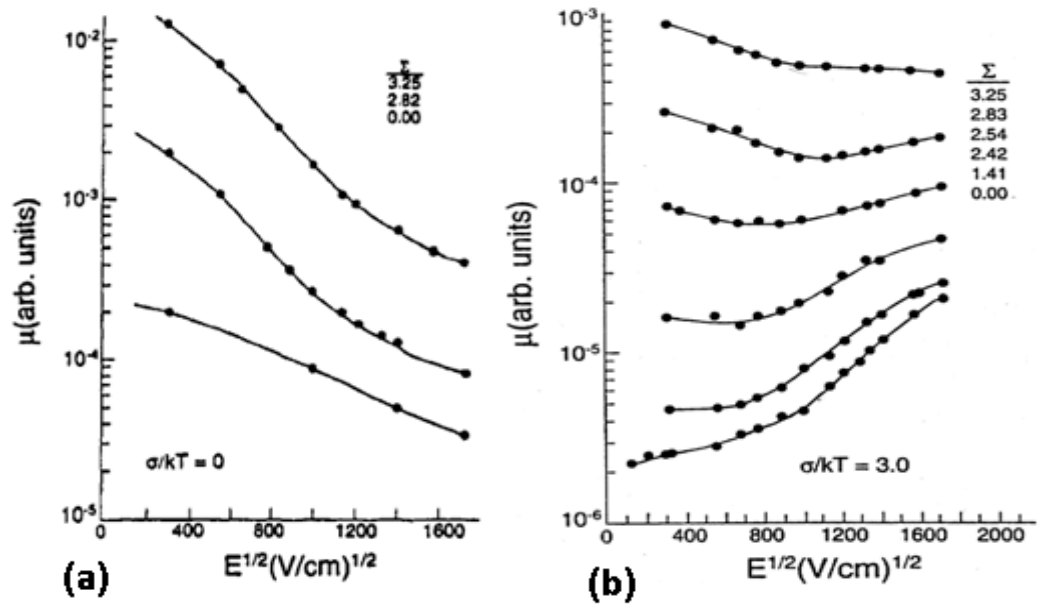


**Figure 2.21 – Plot of Monte Carlo simulation results for ln ($\mu$) as a function of the applied electric field strength for various values of $\Sigma$, with $\sigma/k_B T$ held at zero (a) and 3 (b)[118].**

Figure 2.21(a) shows the effect of varying the positional disorder parameter with the energetic disorder held at zero. Here we can see that mobility decreases with field strength. Figure 2.21(b) shows the effect of both energetic and positional disorder superimposed, the former being fixed at a value of 3 whilst the latter is varied. It is shown that as the positional disorder increases, the gradient of the plot decreases until it becomes negative. At high fields the gradient becomes negative when $\Sigma$ becomes larger than $\sigma/k_B T$, whilst at low fields a negative gradient is seen when $\Sigma \sim 0.8(\sigma/k_B T)$.

The increase of positional disorder increases the fluctuations in the electronic coupling between localised sites, which leads to the negative field dependence shown for the carrier mobility[117]. The fluctuations block some direct charge transport routes due to unfavourable coupling between sites, but also creates other faster routes with favourable coupling as shown in figure 2.22. Here the charge carriers following the indicated route need to hop against the field at some point, and have to overcome increasingly high barriers as the field increases. This in turn results in lower mobility values.
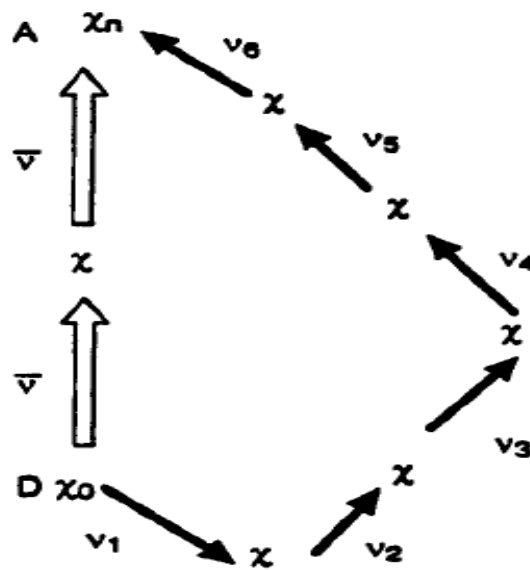


**Figure 2.22 – Illustration of charge transport route for a carrier under the influence of an applied electrical field in the A-D direction.**

In order to relate the mobility to both temperature and the electric field it is necessary to determine the dependence of the slope $\beta = \partial \ln \mu / \partial E^{1/2}$ with both the positional and energetic disorder. Figure 2.23 shows simulation results for $\beta$ as a function of $(\sigma / K_B T)^2$ for various values of $\Sigma$.
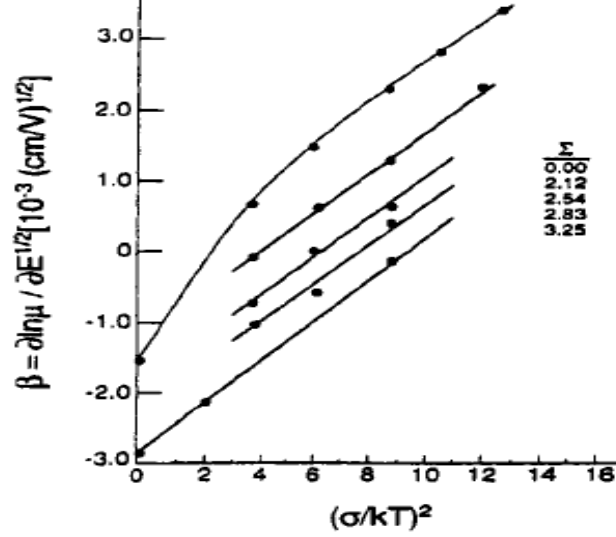
**Figure 2.23 – The variation of $\beta$ as a function of $(\sigma/K_B T)^2$ for various values of $\Sigma$ [118].**

Figure 2.23 shows a set of almost parallel lines for the different values of $\Sigma$, with a gradient of $C$. Using this result with equation 2.32 the mobility can now be expressed in terms of both energetic and positional disorder as[118],

$$\mu(E,T) = \mu_o \, \exp\left[-\left(\frac{2\sigma}{3k_B T}\right)^2\right] \exp\left[C\left\{\left(\frac{\sigma}{k_B T}\right)^2 - \Sigma^2\right\}\sqrt{E}\right] \; ; \Sigma \geq 1.5 \quad \textbf{(2.33)}$$

And

$$\mu(E,T) = \mu_o \, \exp\left[-\left(\frac{2\sigma}{3k_B T}\right)^2\right] \exp\left[C\left\{\left(\frac{\sigma}{k_B T}\right)^2 - 2.25\right\}\sqrt{E}\right] \; ; \Sigma < 1.5 \; \textbf{(2.34)}$$

where $C$ is an empirical constant which is dependent on the intersite hopping distance. These two equations can be used with mobility and temperature dependence data to determine values for $\sigma$, $\mu_o$, $\Sigma$ and $C$.

86

## 2.2.2.4 Polaron Hopping Transport

When the disorder is low, an alternative polaron model is used to describe charge transport in organic semiconductors. Self-trapping occurs where an excess charge carrier is present on an organic molecule. This causes molecular deformation which in turn leads to a reduction in energy for the excess charge carrier. The carrier and its produced molecular deformation is classed as a new quasi-particle referred to as a polaron, denoted $P^+$ or $P^-$ according to the charge carrier sign. Two charge carriers sharing the same molecular deformation form a bipolaron[106,119,20].

Whilst polarons and bipolarons are not traps in the usual sense, as they remain mobile, their mobility values are one or two orders of magnitude lower than that for the free charge carrier. If the carrier energy is only lowered by a small amount, in the order of $10^{-4}$eV, then the effect can be neglected compared to other trap states. However, in some polymers this energy reduction is more than 0.1eV, which creates a trap state on the polymer chain and is referred to as self-trapping[106].

The polaron can only move when accompanied by the molecular distortion, which holds the charge carrier in its potential well. Holstein[119] proposed the polaron hopping model as a possible charge transport mechanism for polarons. Here it is assumed that, in the presence of strong electron-phonon interactions, charge transition between sites occurs when the energies of the initial and final states coincide due to thermal fluctuations of the atomic configuration. More recently this model was amended to assume that energy levels of local states fluctuate due to lattice vibrations or a fluctuating coulomb potential created by hopping charge carriers. It was suggested that tunnelling transitions occur between localised states when the localised energy levels are in resonance[101].

The total mobility of polarons can be expressed to a good approximation as the sum of two contributions, from tunnelling transport $(\mu_{tun})$ and hopping transport $(\mu_{hop})$[120]. The first term relates to coherent electron transfer, which is the dominant transport mechanism at low temperatures. The second term relates to incoherent electron transfer and this becomes the dominant transport mechanism at high temperatures. The relative contributions from each of these mechanisms is dependent on microscopic parameters, such as the electron-phonon coupling constant $(g)$. Figure 2.24 shows the relationship between the transport mechanism and temperature for strong $(g^2 \gg 1)$ and weak $(g^2 \ll 1)$ electron-phonon coupling.
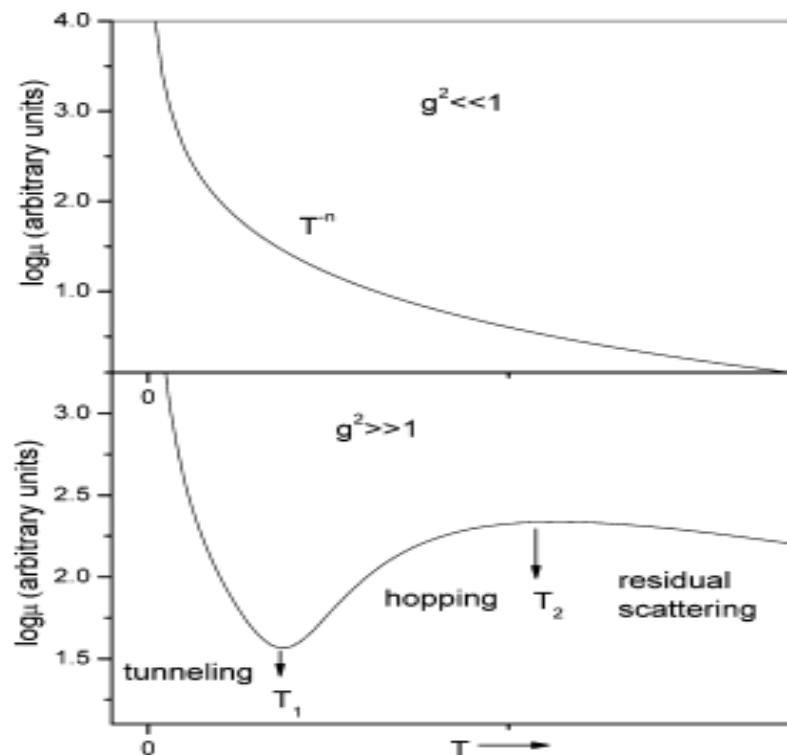


**Figure 2.24 – Temperature dependence of the mobility predicted by the Holstein polaron model for the limiting case of strong and weak electron-phonon couplings[120].**

Figure 2.24 (top) shows that for weak electron-phonon coupling the dominant transport mechanism is tunnelling and the mobility displays a band like temperature dependence across the whole range of temperatures. For strong electron-phonon coupling, figure 2.24 (bottom) shows three distinct temperature regimes.

At low temperatures $(T < T_1)$ the mobility is band like, as the temperature increases $(T_1 < T < T_2)$ hopping transport starts to dominate as mobility switches from coherent to an incoherent, temperature activated transport. At very high temperatures $(T > T_2)$ the thermal energy is sufficient to dissociate the polaron and the residual electron is scattered by thermal phonons, which results in a decrease in mobility with increasing temperature. The temperatures $T_1$ and $T_2$ are defined by a combination of microscopic parameters, and for a particular system only one or two transport mechanisms may be accessible[120].

The transition rate for polarons is given by[121],

$$\nu_{ij} \propto \frac{1}{\sqrt{E_r T}} \exp\left(-\frac{\left(E_j - E_i + E_r\right)^2}{4E_r k_B T}\right) \qquad (2.35)$$

where $E_r$ is the intramolecular reorganisation energy. $E_r$ is the energy cost due to geometric modifications to go from a neutral to a charged molecule and vice versa. The charge carriers move by thermally activated hops between adjacent sites and have a temperature and electric field dependent mobility as[121,122],

$$\mu(E,T) = \mu_o \exp\left[-\frac{E_r}{4k_B T} - \frac{(aE)^2}{4E_r kT}\right] \frac{sinh(aE/2k_B T)}{aE/2k_B T} \qquad (2.36)$$

## 2.2.3 Techniques for Measurement of Mobility

There are several experimental techniques that have been developed for measuring the charge mobility of organic semiconductors, either directly or indirectly. Here we give a brief overview of some of these techniques before focussing on the Time of Flight technique (TOF), the method used in this thesis.

### 2.2.3.1 The Acousto-electric Travelling Wave Method (SAW)

A running surface acoustic wave (SAW) is resonantly generated on a piezoelectric wafer using a high frequency driving voltage to a suitably spaced interdigital electrode structure. The mechanical Rayleigh wave is accompanied by an electric field wave, due to the piezoelectric properties of the wafer, and this wave decays exponentially into free space. A thin slice of semiconductor material is positioned parallel to the wafer surface, causing the charge-carriers to experience an alternating electrical field force as shown in figure 2.25[20,123].
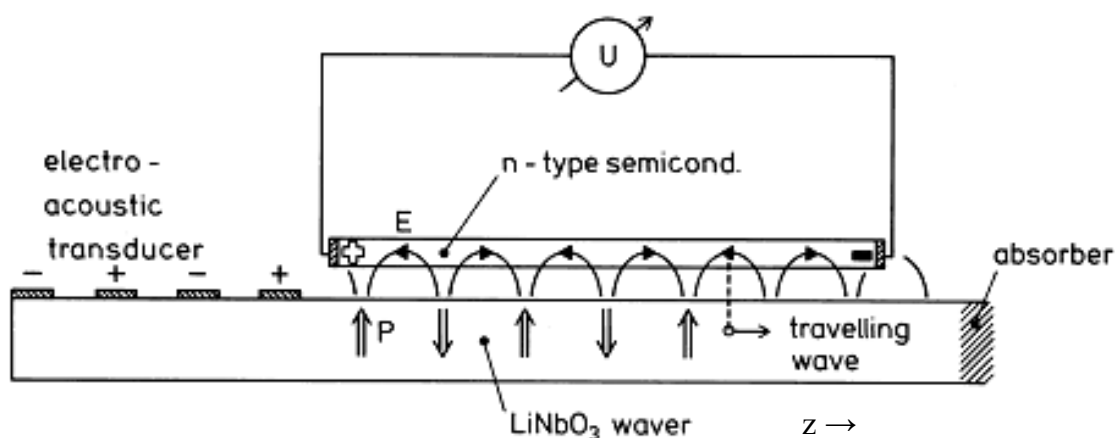


**Figure 2.25 – Principle of the SAW method for measuring charge carrier mobility[123].**

The z-component of the field pulls the charge carriers periodically along and against the propagation direction of the wave. The wave generally moves across the charge carriers faster than they can follow which results in an asymmetric forced motion containing a dc component. The semiconductor slice is short circuited between its ends to generate a dc current, as a result of the dc component of the field. An open circuit configuration leads to a corresponding dc counter voltage building up as[20],

$$V_L = -\frac{\mu E_w^2 L}{v_r} \tag{2.37}$$

where $L$ is the sample length, $E_w^2$ is the square of the average amplitude of the electric field wave in the z-direction, $\mu$ is the mobility and $v_r$ is the propagation velocity of the surface wave. The voltage ($V_L$) can be measured can be measured using an electrometer whilst the value for $v_r$ is known for common transducer materials and orientations[20]. If conductivity is based on a single sign then these signals provide a direct measurement of the charge carrier mobility, although if mobile holes and electrons are both present their signals will partially cancel each other out[20,123].

This technique has been shown by Karl et al[123] to be successful at measuring charge carrier mobility in organic thin films, for mobility values as low as $10^{-4}$cm$^2$/Vs. However, this technique can only accurately measure materials transporting one charge sign, i.e. either electrons or holes. As such this method would be unsuitable for measuring the charge mobility in donor/acceptor blends.

## 2.2.3.2 The Field Effect Transistor Method (FET/TFT)

Field effect mobility is the average charge carrier drift velocity per unit field, and is generally used as a measure to determine the processing speed of field effect transistors (FET). The electrical characteristics measured in a FET configuration can be used to determine the charge carrier mobility. The mobility is determined in a narrow space-charge accumulation layer within a semiconducting thin film, capacitively induced by a perpendicular gate field applied across an insulating layer. The extra contribution of charge carriers to the conductivity is used to obtain the charge carrier mobility within the linear regime (transconductance) or saturation regime of the current-voltage (I-V) of the device[20,101,110].

It has been shown that the I-V expressions derived for inorganic transistors can be applied to organic transistors, giving in the linear regime[110],

$$I_{SD} \ = \ \frac{W}{L}\mu C(V_G - V_T)V_{SD} \tag{2.38}$$

and in the saturated regime,

$$I_{SD} \ = \ \frac{W}{2L}\mu C(V_G - V_T)^2 \tag{2.39}$$

where $I_{SD}$ and $V_{SD}$ are the current and voltage bias between the source and drain, $V_G$ is the gate voltage, $V_T$ the threshold voltage (at which the current begins to increase), $C$ is the capacitance of the gate dielectric, $W$ and $L$ are the width and length of the conducting channel. At the interface between the dielectric and the organic

semiconductor the charge carriers migrate within a very narrow channel, in the order of a few nm[20,101,110,124].

There are a number of factors which affect charge carrier transport when using this measurement technique. Structural defects or impurities can lead to traps at the interface which must be filled with injected charges before a current is generated. This in turn causes the mobility to become dependent on the gate voltage. The dielectric gate insulator causes polarisation effects across the interface and it has been shown that charge mobility reduces as the gate dielectric constant increases. Further, contact resistance at the source and drain metal/organic interfaces has an increasing effect on mobility as the length of the channel is reduced and the transistor operates at low field. However, this effect can be accounted for by using four-probe measurements. Mobility values tend to be higher in the saturated regime than the linear due to their different electric field distribution[20,101,110,124,125,126].

## 2.2.3.3 Charge Extraction by Linearly Increasing Voltage

Charge extraction by linearly increasing voltage (CELIV) is a technique which can be used to directly measure the charge carrier mobility in semiconductors with dispersive transport. A linearly increasing electric field is applied at one electrode and the resulting current transient is used to determine the mobility that arises from doping induced charged carriers. In comparison to the time of flight technique (TOF) used in this thesis, CELIV has two main advantages. Firstly, neither electrode needs to be transparent and secondly the organic film can be much thinner than that needed for TOF, as it is not necessary to have a carrier transit time significantly longer than the carrier's energetic relaxation time[101,110]. This suggests that the CELIV technique would be suitable for direct mobility measurements of reverse biased solar cells. However, there is no way to

distinguish between holes and electrons which is a major limitation, particularly for donor/acceptor blends.

Further, a sufficient number of free charge carriers is needed within the semiconductor, which would require some sort of doping for a wide band gap organic semiconductor[101,110].
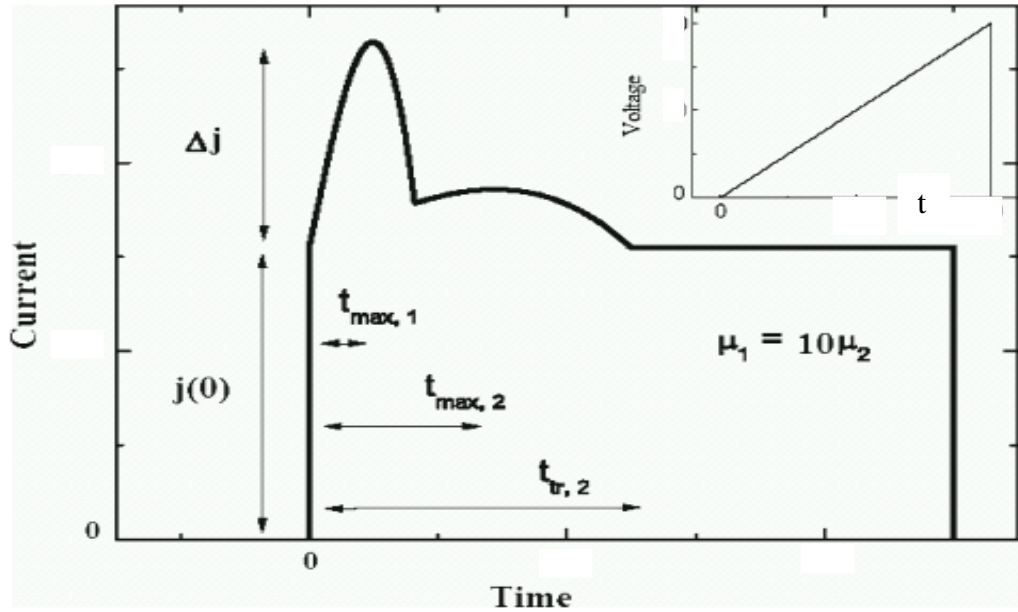


**Fig 2.26 – Calculated CELIV transient with extraction voltage (inset)[110]**

Figure 2.26 shows a calculated CELIV transient with both holes and electrons present, and the extraction voltage is shown in the inset. One charge sign mobility is ten times larger than its counterpart, as shown by the double peak in figure 2.26, but there is no way of determining which way around this is from the CELIV measurement alone. The mobility value is calculated from the current peak maximums seen in figure 2.26, given by[110],

$$t_{max} = d\sqrt{2/3\mu A}$$ (2.40)

Where $t_{max}$ is the time corresponding to the current peak, $d$ the sample thickness, µ the mobility and $A$ the voltage rise speed.

94

All free carriers are extracted after the slowest carrier's transit time, shown in figure 2.26 as $t_{tr}$. The electric field and temperature dependence of the charge mobility found using CELIV agrees with TOF mobility measurements, which demonstrates that using doping induced carrier generation rather than photo-generation does not have a major effect. This technique can be used to measure mobility values as low as $10^{-5}$ to $10^{-6}$ cm$^2$/Vs. Mobility values below this would give an extraction maximum after the end of the extraction pulse and hence cannot be measured[101,110].

## 2.2.3.4 Photo CELIV

This technique is a modified version of the CELIV method just described, with the addition of a light pulse to increase charge carrier concentration prior to extraction. Photo CELIV can be used to probe the energetic relaxation of the photo generated charge carriers, whilst CELIV can only probe equilibrium carriers[110]. Here, the organic layer is illuminated by a short light pulse which is absorbed in the bulk, and after a predetermined delay time $(t_d)$ the triangle voltage pulse is applied to the sample[127,128,129], as illustrated in figure 8.16. The mobility can then be determined from the extraction current maximum time, given by[128,130] ,

$$\mu = \frac{2d^2}{3At_{max}^2\left(1+0.36\frac{\Delta j}{j_0}\right)} \qquad \text{if } \Delta j \leq j(0) \tag{2.41}$$

where $A$ is the voltage increase rate, $d$ is the sample thickness, $j(0)$ is the capacitive displacement current and $\varDelta j$ is the change in current at time $t_{max}$, as shown in figure 2.27.
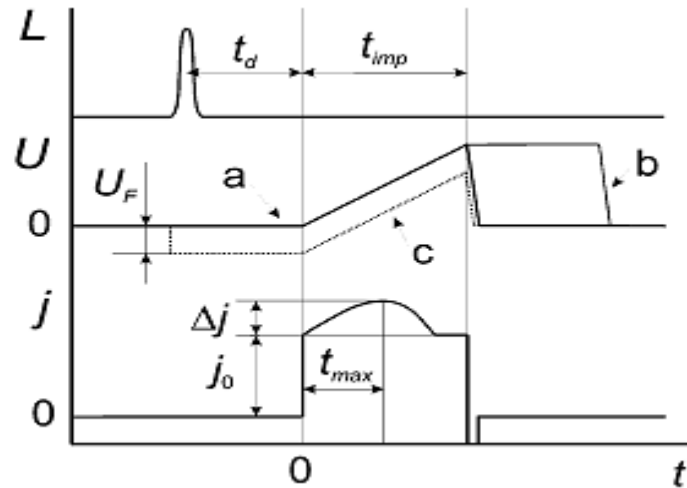
**Figure 2.27 – Schematic illustration of Photo CELIV method, where U is the voltage applied on sample electrodes, L is the light pulse and j is the corresponding current transient[130].**

The relaxation process can be observed by varying the delay time between light and extraction voltage for samples where the transit time is less than, or comparable to, the extraction time. The carrier life time can be estimated by calculating the number of extracted charge carriers as a function of the delay time between the light pulse and extraction. Charge loss generally results from deep trapping or recombination and for materials where the latter is the dominant loss mechanism it is possible to calculate a recombination constant[110].

## 2.2.4 Time of Flight (TOF) Measurement Technique

### 2.2.4.1 Introduction

The Time of Flight (TOF) method was first used for measuring the charge mobility of an organic material by Kepler and Le Blanc in 1960[131]. The mobility of holes and electrons in Anthracene crystals was successfully measured by Kepler, by recording the short circuit current. Le Blanc independently recorded the time evolution of the charge as the open circuit voltage on an integrating capacitor. These two methods are equivalent but Kepler's method provided a clearer pulse shape, where the charge arrival time can be difficult to see. Since that time TOF has become a well established technique for mobility measurements in organic disordered systems and is considered to be one of the most successful methods for this task. TOF is a direct and general measurement technique for determining charge carrier mobility as it directly visualises their field induced motion through a sample from its generation near one electrode to the arrival at the opposite one[20,101,106,110].

### 2.2.4.2 Experimental Theory and Limitations

The TOF measurement technique is based on the carrier transit time ($t_{tr}$), i.e. the time taken for a sheet of photo-generated charge carriers to drift from the electrode at which they were generated across the sample to the opposite electrode under an applied electric field. The organic semiconductor layer is sandwiched between two electrodes, one of which needs to be transparent to allow for photo-excitation of the charge carriers with a short pulse laser. The photon energy of the laser needs to exceed the band gap of the semiconducting layer, to enable charge generation[20,101,106,110].
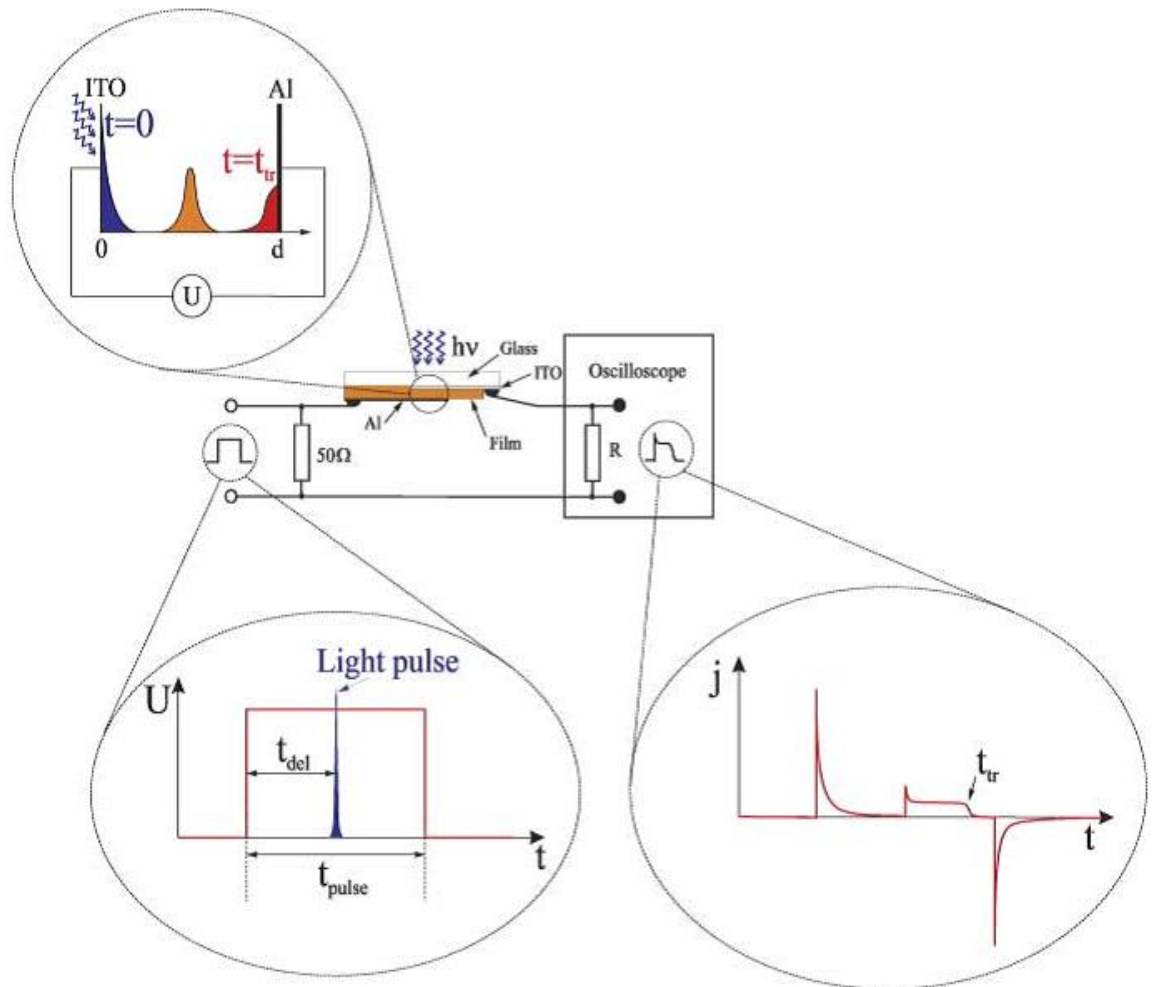
**Figure 2.28 – Typical TOF setup, where the capacitance of the sample and the load resistance R in the oscilloscope form a differentiating RC circuit. The top magnified picture shows the transport dynamics of charge carriers photo-generated at the surface of the film under applied voltage U. The bottom left picture shows the timing of light and voltage pulses and the right picture shows the current transient response in the oscilloscope with the characteristic transit time $t_{tr}$ noting the arrival of charge carriers to an opposite contact.**[132]

A typical experimental set up for the TOF technique is shown in figure 2.28 for a sample of thickness, $d$. The potential difference $U$ applied between the two electrodes creates a capacitor effect with the build up of a charge $Q$ giving a capacitance of[110],

$$C = \frac{Q}{U} = \frac{\varepsilon_r \varepsilon_o A}{d} \tag{2.42}$$

Prior to laser illumination of the sample, the charge on each electrode is equal and opposite creating a uniform electric field between them, i.e. $Q_2 = -Q_1$. When the laser irradiates the sample surface through the transparent electrode (ITO electrode in figure 2.28) charge pairs of holes and electrons are generated within a penetration depth of the surface, $\delta$, also known as the absorption depth of the semiconducting material. It is important that the sample thickness is significantly larger than the material absorption depth ($\delta \ll d$), to ensure that most of the charge carriers are generated close to the surface of the sample rather than throughout the bulk[20,110].

The duration of the laser pulse, $t_{pulse}$, needs to be much shorter than the transit time, $t_{tr}$, of the charge carriers across the sample film. This is to ensure that the most of the charge is generated before any significant transit across the sample occurs, and hence provide a clearer charge transit time during measurement. It is also an important condition that the capacitance charge, $Q$, is much larger than the photo-generated charge, $q$, in order to maintain a uniform electric field across the sample and minimise space charge effects from the photo-generated carriers. A large value of $q$ can slow down the charge transit, creating a longer tail in the drift current, and hence lead to an error, $\Delta t$, in the measured transit time given by[103],

$$\frac{\Delta t}{t_{tr}} = \frac{q}{CV}$$
(2.43)

One of the advantages of the TOF method is that hole and electron mobility can be studied separately, which is a particularly desirable trait when investigating blends of donor/acceptor material. The electric field applied across the sample will cause either the holes or electrons to drift through the film to the opposite electrode (Al electrode in figure 2.28), depending on the field polarity chosen, whilst the opposite charge carriers are extracted immediately at the transparent electrode. A resistance ($R$), which is much smaller than the sample resistance, is applied to the external circuit[20,101,133].

The drifting charge carriers generate a current equal to $Nev/d$, where $N$ is the number of charge carriers, $e$ is the elementary charge, $v$ is the velocity and $d$ is the film thickness. A further condition, $RC \ll t_{tr}$ ($C$ is the total capacitance across resistance $R$), is needed for current measurements to ensure that the carrier transit time is longer than the rising time of the signal[110]. This is the most commonly used mode of TOF, referred to as the differential low light intensity TOF[132]. This mode ensures that the applied electric field inside the film is disturbed only fractionally, which simplifies the interpretation of the current transients. High light intensity TOF can be used to study charge carrier recombination, where the photo-generated charge is greater than the capacitance charge, but this is not suitable for mobility measurements[132].

## 2.2.4.3 Measurement of Transient current and Transit time

As discussed in the previous section, charge carrier pairs are generated by the short laser pulse close to the transparent ITO electrode, which are then separated by the applied electric field into holes and electrons. When set up to measure hole mobility the ITO electrode is held at a positive potential $Q$ with respect to the ground, whilst the opposite electrode is grounded through a resistance $R$, which creates an applied potential in the sample. This means that the electrons are extracted immediately into the ITO electrode, hence changing its charge from $Q$ to $Q - q$. The holes then drift as a sheet across the sample, thickness $d$, to the Al electrode as a result of the applied potential with a constant drift velocity of $v_d$. The time taken for the holes to reach the opposite electrode is the transit time, $t_{tr}$, which gives us[110],

$$v_d = \frac{d}{t_{tr}} \tag{2.44}$$

Upon excitation of the sample the transient current increases as a result of the two electrodes trying to reach equilibrium. In the case where holes are travelling through the sample, the electrons collected at the ITO electrode move through the external circuit creating a constant current. In an ideal case the current would show a flat plateau to indicate that the charge carriers travel together. Upon reaching the Al electrode, at a time $t_{tr}$, the holes would meet and recombine with the electrons which have also reached the Al electrode via the external circuit[20,101,106]. At this point the transient current drops to zero, giving a time for $t_{tr}$ as shown in figure 2.29 (a).
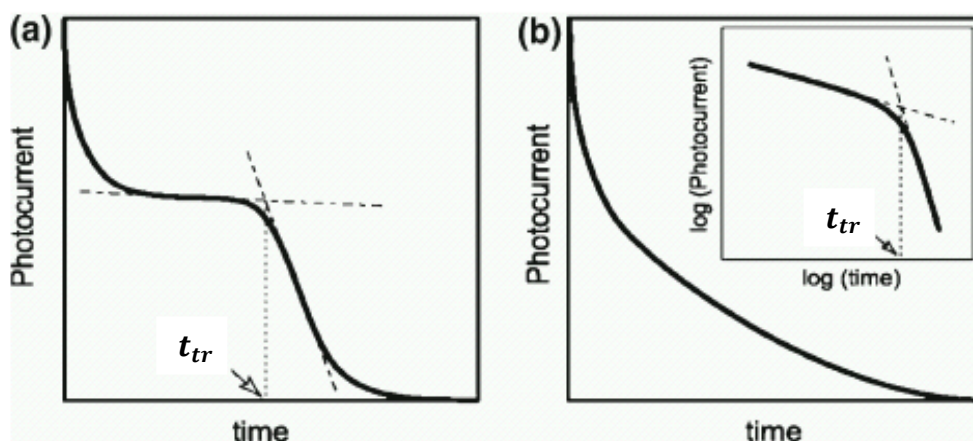


**Figure 2.29 – Typical transient photocurrents. (a) shows non-dispersive (b) dispersive with double logarithmic plot inset[110].**

To achieve a clear transient signal as shown in figure 2.29 (a) the charge carriers travelling through the sample should not be dispersed. Ensuring that the laser pulse is much shorter than the transit time and that the material absorption depth is much smaller than the sample thickness helps to avoid dispersion. However, even when meeting these conditions many organic semiconductors still experience dispersion due to charge traps within the material. Figure 2.30 shows a typical current transient for an amorphous organic semiconductor due to charge traps, where some of the charge carriers occupy lower energy levels than the transporting level for a time during transit.

Figure 2.29 (b) shows the case for even more dispersive charge transport where the transit time can no longer be determined from the linear plot, and hence the transient needs to be examined in a double logarithmic plot, as shown inset[20,101,110,134].
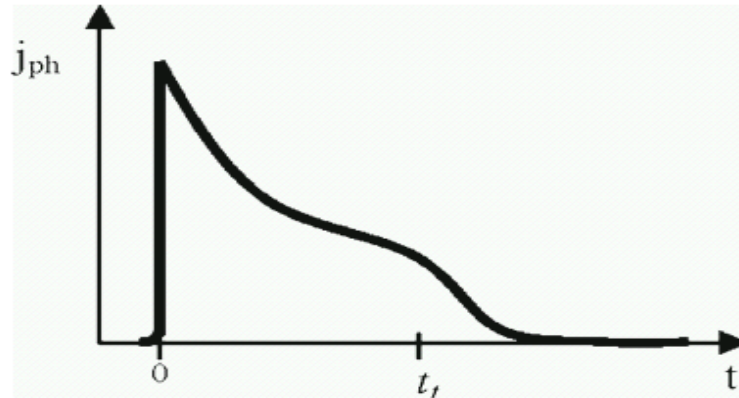


**Figure 2.30 - Transient current pulse shape due to deep traps[110].**

In the case of both linear and double logarithmic plots, the transit time is determined by the intersection between two straight lines along the two main slopes, as illustrated by the dotted lines in figure 2.29 (a) and (b). The double logarithmic method of analysis for dispersed charge transport was developed by Scher and Montroll in 1975[135], where it was found that the inflection point was an indication of the arrival time of the first charge carriers. The transit time obtained can be used with equations 2.24 and 2.44 to give the mobility as,

$$\mu = \frac{d^2}{U.t_{tr}} \qquad (2.45)$$

For TOF measurements relatively thick samples are needed, ideally in the region of 1μm or more, in order to meet the requirement of the absorption depth being significantly less than the film thickness. High charge carrier density within a material can also cause measurement difficulties due to diffusive charge carriers affecting the drift of photo-generated charge carriers under an applied field.

Further, problems are encountered when measuring high mobility values for organic materials, especially for relatively thin films. This is due to noise which originates from the $N_2$ laser pulse used to excite the sample, which can overlap with the transient signal as shown in figure 2.31 (left). The noise can be reduced by employing the 3 methods devised by Kashima et al[136] with a Nitrogen excitation laser, firstly by increasing the distance between the $N_2$ laser and the sample, since the noise passes through the air. Second, a photocoupler is used between the laser and pulse generator, to reduce the noise travelling along the electro-circuit. Finally a digital filter is used to remove characteristic oscillations caused by the laser[110,136].
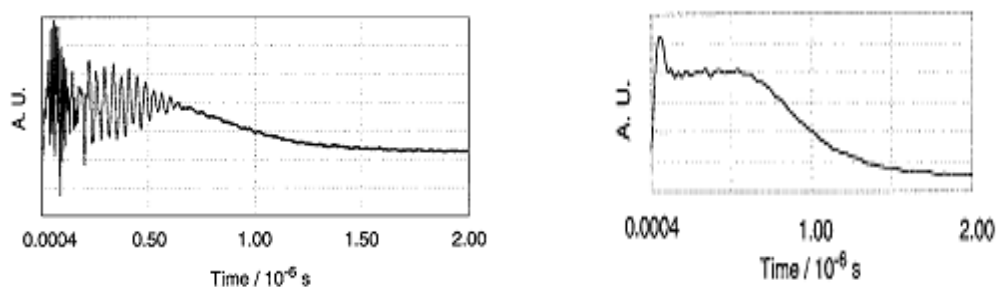


**Figure 2.31 – The current signal for a TPD thin film, 500nm thickness, irradiation pulse 337nm ($N_2$ Laser) with no noise reduction (left) and all 3 noise reduction methods employed (right)[136].**

Figure 2.31 illustrates the extent of noise reduction using these 3 methods. The signal on the left does not give us a clear transit time for the charge carriers, whilst the noise reduced signal on the right shows a clear inflection to allow the transit time to be determined.

# 2.3 Nano Morphology of Organic Semiconductors

## 2.3.1 Introduction

As briefly alluded to in chapter 1, the nano morphology of the active layer of a photovoltaic device is crucial to the overall device efficiency. The two steps of the photovoltaic process affected by the morphology are the exciton diffusion/charge separation and the charge transport before collection at the electrodes. Bilayer devices provide good charge pathways for collection but provide a very limited interface between the donor and acceptor for charge separation. This is limited to around 10nm either side of the interface, meaning only around 20nm of the total device thickness is useful. Bulk heterojunction devices can improve the interfacial area, but clear charge pathways become more of a challenge.

Here we investigate how the nano morphology of the active layer can be influenced, using the measured properties of the donor/acceptor materials to guide the thin film processing conditions. We will begin with a introduction to the phase transition temperatures of organic materials and how the Differential Scanning Calorimetry (DSC) technique can be used to measure and identify the phase of the material over a temperature range. It will then be shown how a polarised microscope can be used to view liquid crystal phase transitions, which in turn can confirm and further identify the phase transitions found using the DSC. Different methods of influencing the morphology of the photoactive blend layer will be considered, followed by an introduction to the Atomic Force Microscope (AFM), which can be used to study the nano morphology in detail.

## 2.3.2 Phase Transition Temperatures

As discussed in chapter 1, liquid crystalline organic semiconductors have been shown to improve the overall photovoltaic performance. The liquid crystal phase is an intermediate state of matter, halfway between isotropic liquid and solid crystal. Thermotropic liquid crystals have molecules as their basic units and phase transitions depend on temperature and pressure. The main feature of these molecules is their shape anisotropy, such as disk or rod shape, which gives rise to the thermotropic mesophase. In addition to individual molecules, thermotropic properties can also be achieved by mixtures of different molecules[137].

By using materials within their liquid crystal state the respective donor and acceptor molecules are free to move and self organise. During the photoactive layer annealing process the material's liquid crystal transition temperature can be exceeded in order to provide this freedom of movement. It is hoped that the self organised domains formed will provide both a good interface area and clear pathways for the charge carriers to their respective electrodes. Further, the ordered molecules should provide for better overlapping of the $\pi$ bonds and hence provide better charge transport as discussed in chapter 1. It has been shown in previous studies that using liquid crystalline materials can improve the mobility and overall device efficiency, due to the improved morphology of the active layer [43,138,139,140,42,58,141,72,142,143,73].

The organic materials used in this thesis have been synthesised by the chemistry department at Hull University. These materials have various phase transition temperatures which need to be measured and identified in order to guide our thin film processing conditions, particularly in respect to device annealing. To this end thermal analysis is needed to allow further study of the various phase transitions for both individual materials and donor/acceptor blends.

Liquid crystals may exhibit many mesophases between crystalline solid and isotropic liquid states, which may have either first or second order phase transitions. First order transitions involve a latent heat, where the system absorbs or releases a fixed amount of energy. The temperature of the system will remain constant as heat is added during the transition, during which the system is in a mixed-phase regime where some parts of the system have completed the transition and others have not. The melting of ice or the boiling of water are common examples of first order transitions. Second order phase transitions are also referred to as continuous phase transitions, where the old phase transforms into the new phase in a smooth, continuous manner. Ferromagnetic transitions, super conductor and the super fluid transitions are examples of second order phase transitions[144].

Calorimetric experiments can be used to obtain the temperature dependency of the energy or enthalpy $H(T)$ for a material. This is often achieved by measuring the heat capacity, which is related to the rate of change in enthalpy as a function of temperature. However, for first order phase transitions a direct measurement of the enthalpy is needed as the latent heat information cannot be obtained from the measurement of the heat capacity. There are several techniques which can be used for this purpose such as differential scanning calorimetry (DSC), adiabatic calorimetry (both scanning and non scanning) ,ac calorimetry, photo acoustic and photo pyroelectric methods[145,146,147]. Here we focus on the DSC measurement technique which will be used to investigate materials within this thesis.

## 2.3.3 Differential Scanning Calorimetry

Differential scanning calorimetry (DSC) is viewed as the standard technique for measuring transition temperatures and the enthalpy changes that occur at these transitions. This technique is widely used to investigate phase transitions and thermal properties of liquid crystals [147,63,148,149]. The principles of this measurement are quite straight forward. The sample is compared to a reference material over a pre-determined temperature range. Two small aluminium pans are used to contain the sample and reference materials, with just a few milligrams of the material under study required. A fixed rate of heating (or cooling) is chosen to be applied to the sample and reference pans over the predetermined temperature range. A servo system then ensures that the sample material tracks the temperature of the reference sample throughout the heating and cooling cycles selected [147,63].

By keeping the temperature of the sample and reference equal to each other during heating and cooling, the required heating power is varied. This differential power input is recorded throughout the heating/cooling cycle as a plot of the rate of change of enthalpy, $\frac{dH}{dT}$ , against temperature. Hence it is possible to observe enthalpy change, including the latent heat for a first order phase transition. Figure 2.32 illustrates a typical DSC pan set up.
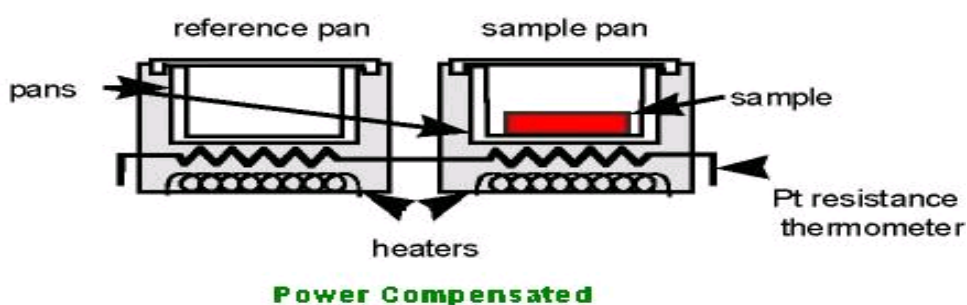


**Figure 2.32 – Schematic for typical DSC pan set up**[150]

When the heating power required by the sample increases to maintain its temperature with respect to the reference pan this indicates that an endothermic reaction is taking place, such as melting. When the reverse of this happens an exothermic reaction is taking place, such as crystallisation, as shown in figure 2.33.
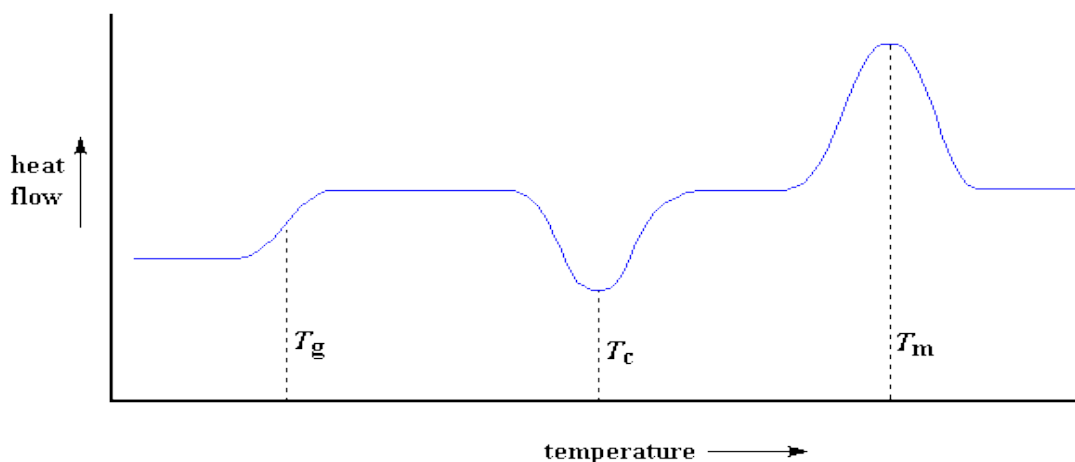


**Figure 2.33 – A typical DSC trace showing a glass transition ($T_g$), crystallisation ($T_c$) and melting point ($T_m$)[151]. Endothermic reactions are shown to have a positive heat flow (peak) whilst exothermic reactions have a negative heat flow (trough).**

Liquid crystal phase transitions such as crystal → nematic or nematic → isotropic need additional heat energy and hence show up as endothermic peaks on the DSC trace. It is possible to determine a value for the enthalpy change, $\Delta H(T)$, by integrating the area under the endothermic peak. The phase transition temperature is generally obtained from the position of the peak on the temperature x-axis, although the heating rate can affect this. Upon cooling, the reverse of the phase transitions seen on heating will produce opposite peaks. That is, for a phase transition showing an endothermic peak on heating an exothermic peak will be seen upon cooling. However, the peak during cooling is often shifted to the left relative to the peak on heating. This can be caused by either supercooling of the phase transition or machine hysteresis, which can be negated by calibration. Phase transitions which do not reach equilibrium quickly can cause significant errors in the measurement, although most liquid crystal transitions do tend to be rapid[63,146,147].

In addition to the above phase changes discussed, the glass transition ($T_g$) of a material can also be determined. Whilst most liquids crystallise on cooling, a lack of molecular symmetry or a fast rate of cooling can inhibit crystallisation and cause a glass to form instead. Whilst crystallisation is a first order phase transition, a glass transition simply comprises of a steady increase in viscosity leading to a frozen version of the liquid from which it formed. The temperature at which glass transition occurs is dependent on the rate of cooling as it is not a thermodynamic transition, lacking any true equilibrium state. As shown in figure 2.33, the glass transition is seen as a step on the DSC trace rather than a peak[63,146]. Many of the liquid crystals investigated in this thesis form a glass on cooling.

## 2.3.4 Polarised Microscopy

Whilst the DSC can provide us with the phase transition temperatures for a material, it is not immediately clear what type of transition has taken place. The magnitude of the enthalpy change, $\Delta H$, can be used to identify some phases, but further investigation is often necessary. This is particularly the case for liquid crystal phase transitions. A polarised microscope can be used to view the texture of a material as it is heated through a desired temperature range. Phase transitions can be seen during heating due to the anisotropic properties of the liquid crystalline material. A polarised microscope is simply an optical microscope which incorporates two polarising plates, referred to as the polariser and analyser as illustrated in figure 2.34.
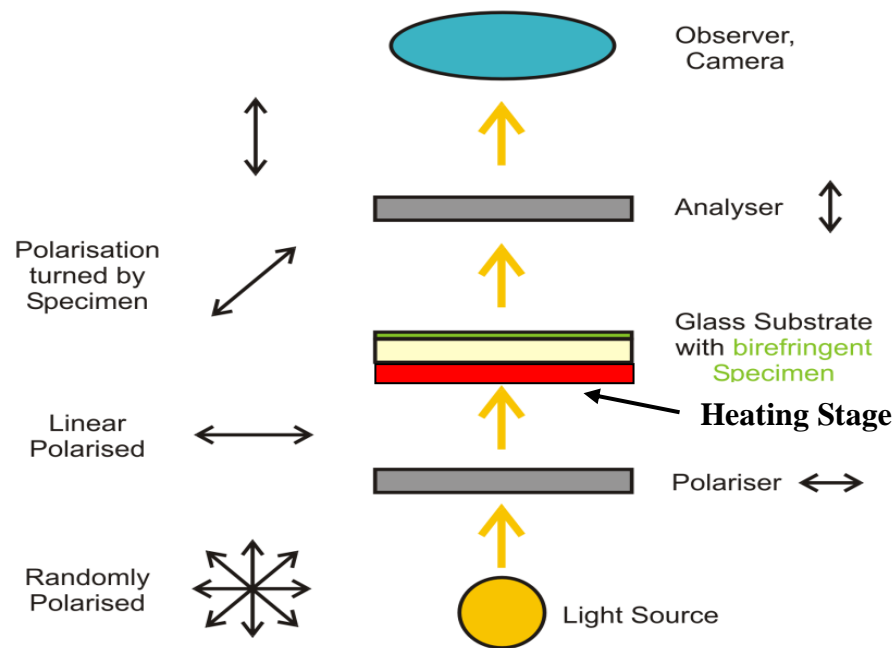
**Figure 2.34 – Schematic of light path within a typical polarised microscope. The polarisation is in the x-y direction whilst the light ray is in the z direction[69].**

As shown in figure 2.34 we begin with randomly polarised light passing through the linear polariser. The resulting linear polarised light then passes through the sample under study, which is generally a small amount of liquid crystalline compound on a glass microscope slide. If the sample material is in a liquid crystal phase then the incident polarised light will experience retardation as it passes through. This alters the polarisation direction of the light. Conversely, an isotropic state does not affect the polarisation of the light passing through the sample.

After passing through the sample the light travels to the analyser, which is aligned at right angles to the first polariser. If the sample does not have any effect on the plane of polarisation of the incident light then it will be completely blocked by the analyser and the resulting image will be completely dark. However, if the sample does change the plane of polarisation then the light can pass through the analyser and an image can be seen. Hence, a dark image indicates that the sample is in an isotropic phase, whilst a visible image indicates a liquid crystalline phase.

Crystal structures which exhibit cubic symmetry and amorphous materials, which have no crystal structure, are optically isotropic with respect to the transmitted light[152]. Other crystal structures can also show birefringence.
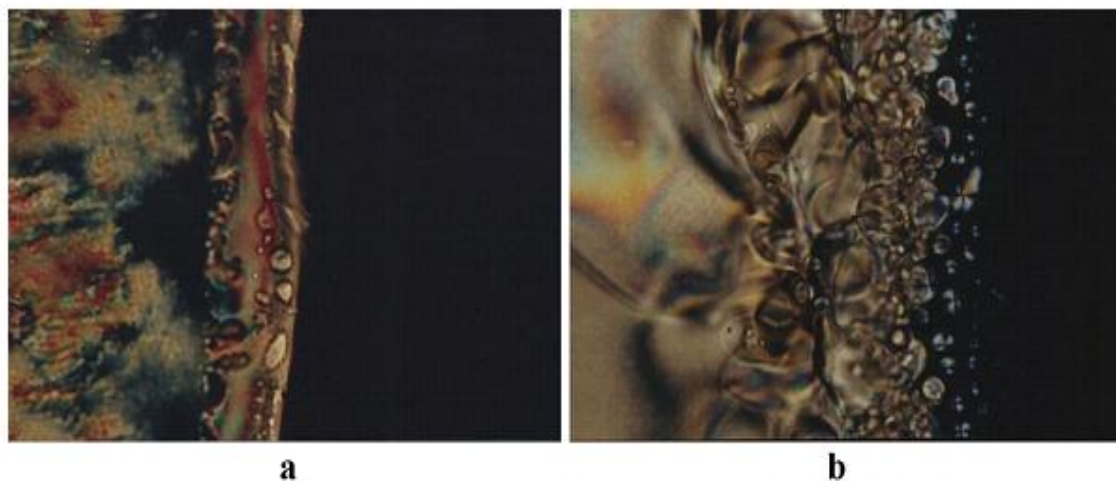


**Figure 2.35 – (a) Nematic to isotropic and (b) isotropic to nematic phase transitions observed through a polarised microscope (non orientated texture)[153].**

An example of a nematic liquid crystal phase is shown in figure 2.35, the nematic to isotropic transition (a) and isotropic to nematic transition (b). The sample stage of the polarised microscope incorporates a heating stage which heats the sample being viewed over the selected temperature range and rate. The phase transitions identified using DSC can now be viewed and identified by their texture, as the sample is heated through these transition points.

## 2.3.5 Influence of Thin Film Processing on Morphology

There are several other factors which can affect the morphology of a blended thin film device in addition to the phase of a material, liquid crystalline or otherwise. These factors are mainly related to the device processing conditions, which need to be optimised in order to produce the morphology we need.

Whilst we want a good interface area between the donor and acceptor materials, it is also important to have connected charge pathways for charge carriers to reach their respective electrode. An important configuration is to have the donor material phase separated at the bottom of the active layer, in contact with the ITO electrode, and the acceptor at the top connecting to the Aluminium electrode.
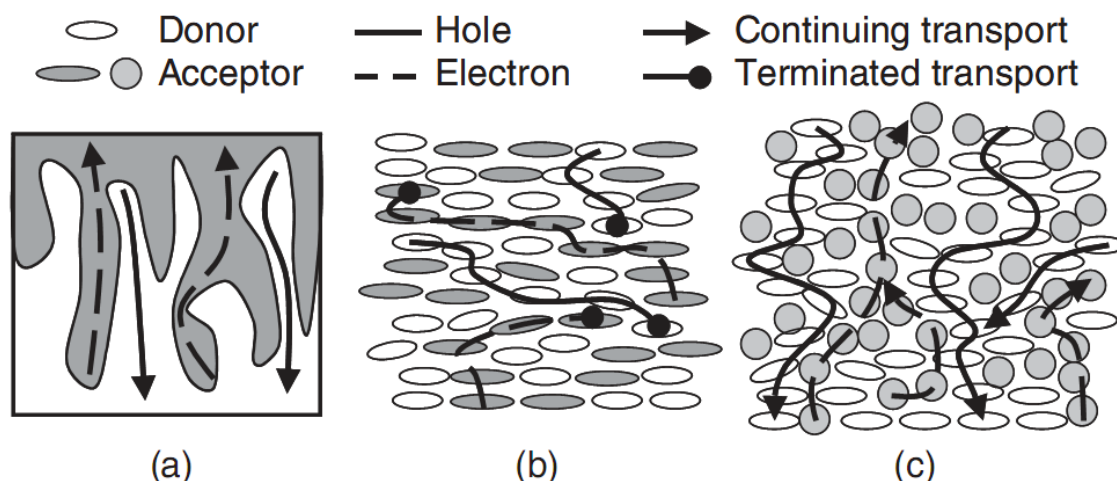


**Figure 2.36 – Illustration of potential morphologies for BHJ active layer, (a) Idealised, (b) Interrupted charge pathways, (c) Percolating pathways[154].**

An idealised bulk heterojunction morphology for an organic PV device is illustrated in figure 2.36 (a), where vertical phase separation has occurred. This structure provides us with a large donor/acceptor interface whilst retaining clear charge pathways. Charge recombination can take place near the electrodes where the donor material touches the wrong surface, as shown in figure 2.36 (b) and (c), which reduces the PV device efficiency. Charge collection at the wrong electrode reduces the parallel (shunt) resistance of the device.

The charge pathways shown in (b) are discontinuous, which leads to charge trapping and subsequent recombination. The morphology shown in (c) provides clear pathways and is perhaps a more realistic achievement than that shown in (a). Current blocking layers can be used either side of the active layer to prevent the charge carriers from reaching the wrong electrode.

The morphology of the donor/acceptor blend can be influenced before, during and after the thin film processing. The substrate preparation is key to providing a suitable surface for the organic blend to attach to whilst minimising the possibility of dewetting. The substrate surface energy plays an important role[155,156]. It is crucial therefore to thoroughly clean the substrates prior to film deposition, and plasma treatment can further improve the surface conditions[18].

When two organic materials are blended together phase separation occurs as it is thermodynamically favourable. The difference in solubility of the compounds also leads to phase separation, as one of the materials becomes insoluble before the other as the solvent evaporates following spin casting[156,157]. The solvent chosen for spin casting influences the film morphology, as shown by Hoppe et al[158]. Here a significant increase in device efficiency was achieved as a result of the different morphology produced by using chlorobenzene as casting solvent instead of toluene. The relative molecular weights of the donor/acceptor materials have also been shown to have a considerable effect on photovoltaic device performance[157]. In addition, the ratio of donor to acceptor used to make a blend impacts on the morphology[156]. The spin casting conditions, such as spin speed and duration, together with the solution concentration determine the active layer thickness.

Following the film formation, annealing conditions can have a significant effect on the final active layer morphology. The temperature chosen for annealing must be high enough to allow for demixing, which occurs above the glass transition temperature of the components[156]. Exceeding the transition temperature of the liquid crystal phase would also have a significant effect on morphology as discussed earlier. However, care must be taken not to exceed the boiling point of the casting solvent used, and this should be a major consideration when selecting the solvent.

## 2.3.6 Atomic Force Microscopy (AFM)

There are several techniques available to study the morphology and surface topography of organic thin films, such as transmission electron microscopy (TEM) and scanning electron microscopy (SEM)[156,158]. More recently scanning probe microscopy (SPM) has been developed, which includes a complete family of techniques such as scanning tunnelling microscopy (STM), scanning near-field optical microscopy (SNOM) and atomic force microscopy (AFM)[159,160]. Each of these SPM techniques measures a specific interaction between a probe with an ultra-sharp tip and the sample surface. This enables sub-nanometer resolution images of the topography to be produced, and also provides the means to measure, analyse and quantify properties of matter on the nanometer scale. Data for adhesion, elasticity, conductivity and capacitance can be obtained for a material by using specific probes and measuring conditions[159,160].

Here, we focus on the AFM technique from the SPM family which is discussed to investigate the thin film morphology of our materials in this thesis. This technique provides us with near atomic resolution and can provide both two and three dimensional images of the thin film surface. Conductors and insulators can both be imaged using mechanical based tip interaction with the surface, something which is not possible with the STM. The material can also be imaged in various environments such as normal atmosphere (air), in liquids, at elevated temperatures and even under the influence of external forces. This provides much more flexibility than the SEM and an added advantage is that the sample is directly measurable without any complex preparation procedures[159,160].

.

## 2.3.6.1 Measurement Modes and Operating Principles of the AFM

The atomic force microscope (AFM) measures the inter-atomic force between the atoms of the sample and the probe. The probe used for measurements consists of a flexible cantilever with a small sharp tip attached to the end, as shown in figure 2.37 (a). As the tip approaches the sample surface it experiences the inter-atomic force, which can be repulsive or attractive depending on the tip distance from the sample, and this causes the cantilever to deflect. Figure 2.37 (b) illustrates the cantilever tip in close proximity to the sample surface whilst (c) shows how the inter-atomic varies from repulsive to attractive as a function of the distance between the probe and sample.
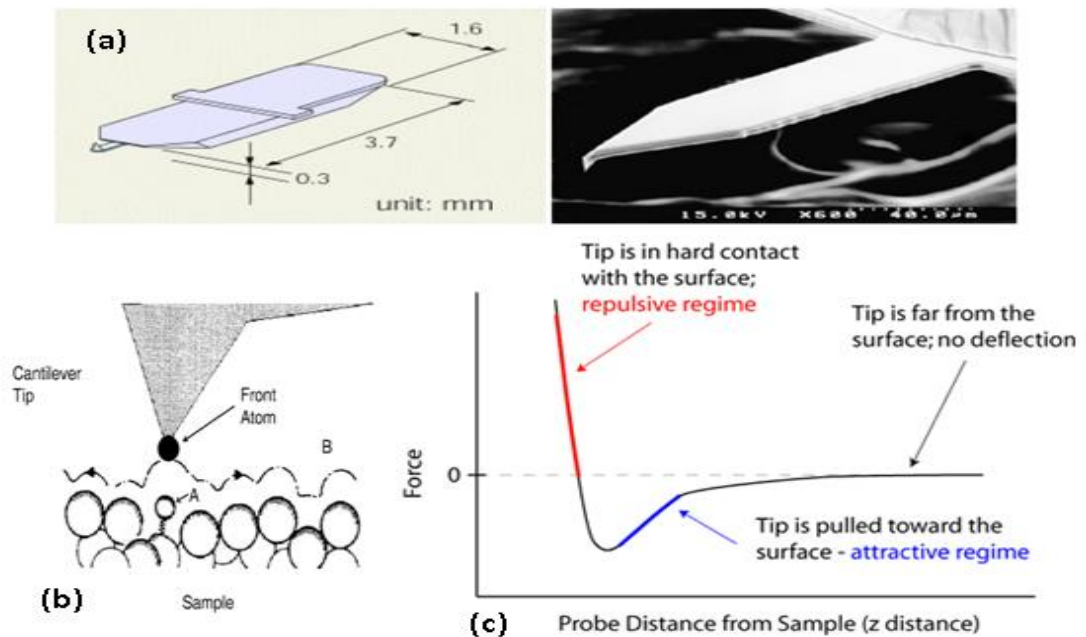


**Figure 2.37 – (a) Schematic of an AFM cantilever tip (left) and the tip magnified 600 times (right) (b) Schematic of cantilever tip scanning surface in atomic scale (c) The variation of inter atomic force as a function of the probe distance from the sample[161].**

The cantilever is generally mounted onto a three axis piezo arrangement, which in turn controls the cantilever movement in the x, y and z planes. The tip scans the sample in the x-y plane whilst changes in the z direction, caused by the cantilever deflection, are monitored and used to produce the topographic measurements and provide a surface image.

Based on the tip to surface distance there are three main measurement modes for the AFM. These are referred to as tapping mode (TM-AFM), non-contact mode (NC-AFM) and contact mode (C-AFM)[159,160,162].

The TM-AFM mode uses a stiff cantilever which oscillates close to the sample and, as the name suggests, the probe taps the surface. The oscillation is set to a fixed frequency near resonance with a large amplitude, which is monitored as the sample surface is scanned in the x-y plane. Here the repulsive regime exerts a force on the probe tip, changing its position in the z direction. This is measured via the change in the oscillation amplitude of the cantilever. A feedback system reports this change in amplitude, as illustrated in figure 2.38. This causes the piezo to alter the z position of the cantilever in order to maintain the preset oscillation amplitude and hence the tip to sample spacing. In this way a surface topographic profile is obtained, based on the movement of the tip relative to the sample surface. This technique is generally used for soft materials, as the limited surface contact help reduce damage to the sample whilst providing a high resolution image.
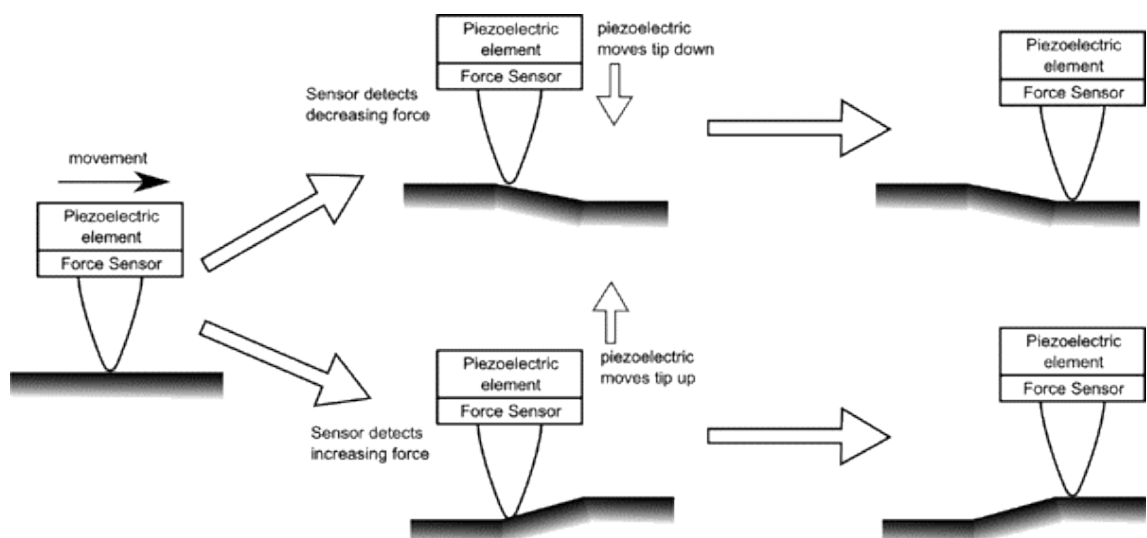


**Figure 2.38 – Schematic of feedback control; when the force sensor detects a change in sample height the piezo moves to maintain the same tip-sample force[162].**

The C-AFM mode uses a probe which is in constant contact with the sample surface during measurements. Here the cantilever is bent according to changes in the surface topography as the probe tip scans across the x-y plane. As with TM-AFM the tip experiences force from the repulsive regime, which provides high resolution images. However, the dragging motion of the cantilever tip can cause damage to the sample and the tip itself, making this technique unsuitable for soft organic materials.

The NC-AFM mode uses a cantilever held within $5-10$nm of the surface, but with no actual contact being made. This positions the probe tip within the attractive force regime of the sample surface. Here the cantilever is connected to a piezo crystal which causes the probe tip to oscillate at a fixed frequency in the range $50-500$KHz. The tip is maintained at a pre-determined distance from the sample surface using a feedback system. Changes in the oscillation amplitude or resonant frequency of the cantilever cause the piezo to move the probe tip in the z direction, back to the pre-determined distance from the sample surface. As with the TM-AFM, a surface topographic profile is obtained as the probe scans the sample across the x-y plane. The attractive force exploited here is weaker than the repulsive force, several orders of magnitude less than the C-AFM, and as such the image resolution is not as high. However, the non contact feature makes this technique ideal for soft materials like organic semiconductors, as it minimises damage to the probe tip and sample.

## 2.3.6.2 AFM Instrumentation

The AFM set up consists of the microscope stage itself along with the control electronics and a computer. The microscope stage is shown in detail in figure 2.39 (a) along with a schematic of the piezoelectric scanner (b).
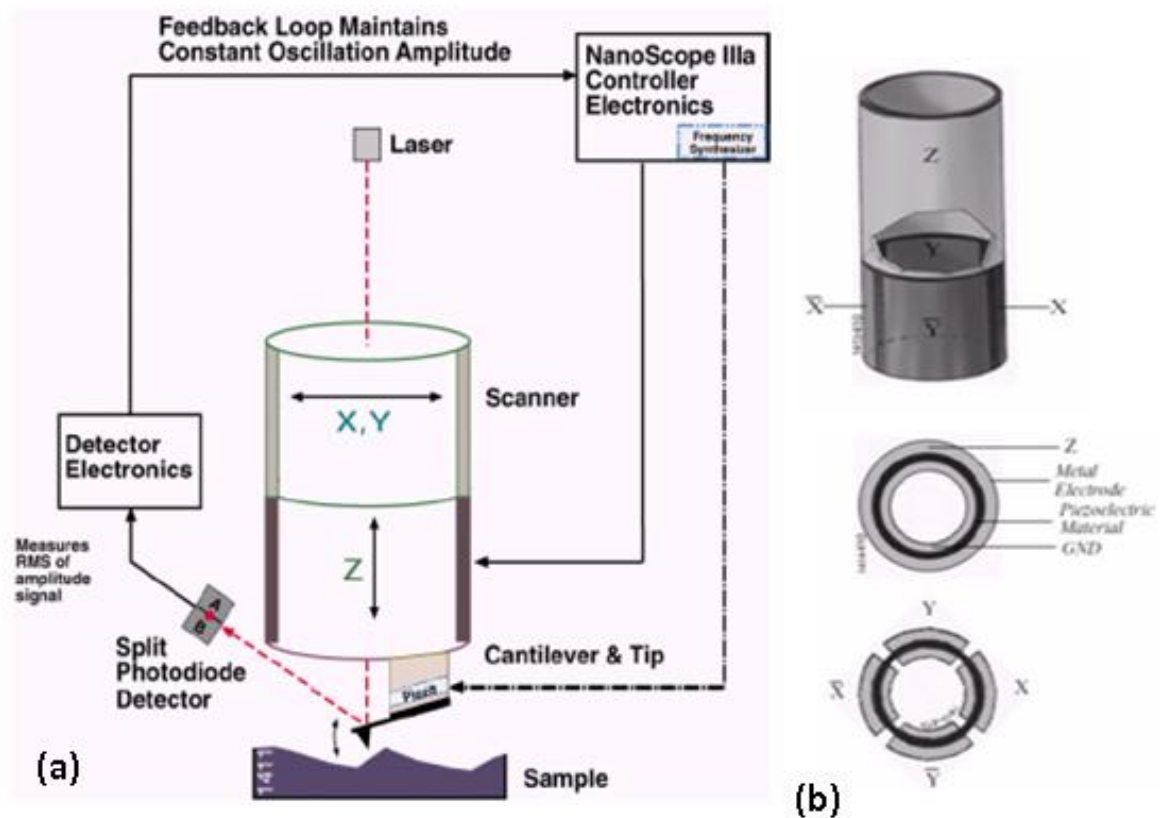
**Figure2.39 – (a) Schematic of the main AFM components and (b) schematic of the piezoelectric scanner [163].**

The cantilever tip scans across the sample surface, rising and falling relative to changes in the surface topography. The piezoelectric scanner controls the movement of the cantilever in the x, y and z directions. The scan over the x-y plane is performed in parallel lines across the sample surface whilst the z direction is influenced according to the topography of the line being scanned. A laser beam is reflected from the cantilever towards the split photodiode sensor, as shown in figure 2.39 (a), thus providing data on the oscillation amplitude of the cantilever to the detector electronics. The signal is then fed back to the piezo scanner to alter the z position of the cantilever accordingly. Finally the attached computer records the data produced by the scan and produces 2d and 3d images of the sample surface topography, based on the z position of the probe tip as a function of the x-y position.

There are two methods used to cause the cantilever to oscillate, when in TM-AFM or NC-AFM mode, one of which is using a quartz piezo as shown in figure 2.39 (a). The second method uses a cantilever coated with a magnetic material. A coil positioned either underneath the sample or above the cantilever generates an alternating magnetic field which causes the cantilever to oscillate[159,160,162].

## 2.3.6.3 Surface Topography Characterisation

The AFM measurement provides a wealth of information which requires further processing and analysis to get the most detailed picture of the sample morphology. The AFM software usually has two main functions, image acquisition and image processing[162]. The former is used to save the measurement data as a file containing all the height and other data recorded by the AFM. The latter provides the means to carry out the processing described in the rest of this section.
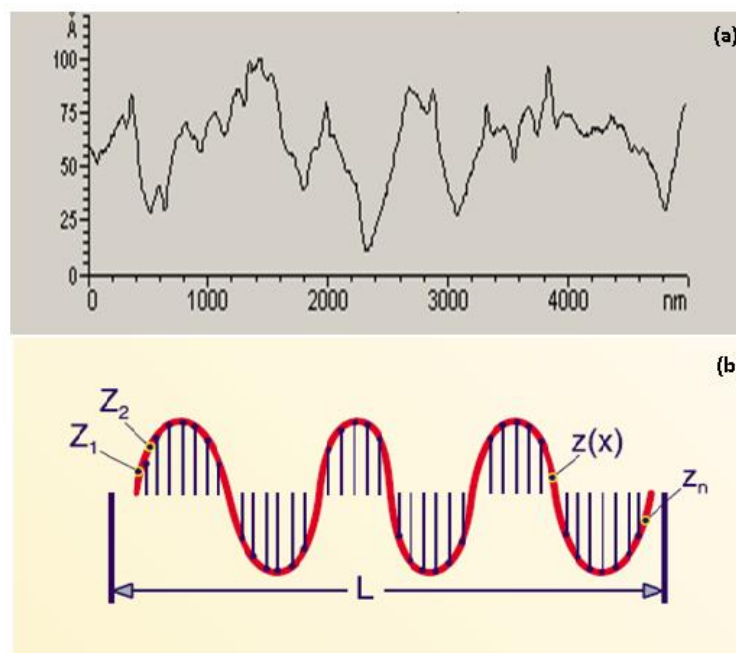


**Figure 2.40 – (a) Surface profile in the x-direction (b) Roughness profile approximated digitally[164]**

Surface roughness is an important property for many applications and particularly so for photovoltaic blends. There are several techniques which can be used to measure the roughness. The surface roughness profile recorded by an AFM provides 2D traces of the sample surface, as shown in figure 2.40 (a) for the x-direction. These line profiles are stacked in the y-direction to produce the full surface image. Any one of the 2D line profiles can be selected for further analysis of the surface roughness. It is useful to regard the roughness profile as shown in figure 2.40 (b) as a waveform comprising amplitude (height), wavelengths, peaks, troughs and spacing features[165]. The amplitude can be represented by the roughness average ($R_a$), the root mean square roughness ($R_q$) or the maximum profile peak height ($R_p$).

The roughness average, also referred to as the arithmetic roughness[162], is the basic parameter for specifying the surface roughness. This is derived from the average of the absolute values of the surface deviations from the mean plane, given by,[162,165]

$$R_a = \frac{1}{MN}\sum_{i=1}^{M}\sum_{j=1}^{N}|Z_{ij}| \qquad (2.46)$$

Where M and N are the number of data points in the X and Y direction respectively and Z is the surface height relative to the mean plane reference. This value has a positive correlation, i.e. a larger value indicates a greater topographical variation in the image. However, the roughness average does not give any information about the shape of the surface profile or on the spacing between the features.

The root mean squared roughness always produces a larger value than $R_a$ and is said to be more sensitive to outlying points[162]. Consequently $R_q$ is used more widely than $R_a$ as a parameter for evaluating the surface roughness. It is calculated by taking the average of the squares of each height value in the dataset, given by[162,164]

$$R_q = \sqrt{\frac{1}{MN} \sum_{i=1}^{M} \sum_{j=1}^{N} Z_{ij}^2} \qquad (2.47)$$

The squaring of the height values in this calculation makes $R_q$ more sensitive to the peaks and troughs of the surface roughness compared to $R_a$. However, $R_q$ is still unable to detect differences in spacing.

The peak height parameter, $R_p$ , provides data on the height distribution of the surface roughness peaks and troughs. This gives us a range for the height of the roughness features on a sample surface, including the number of data points for each height. Plotting these values provides a graphical way to compare surface roughness features.

### 2.3.6.4  Fourier Analysis and Power Spectral Density (PSD)

It is possible to convert the AFM image from the spatial domain into the frequency, or wavelength, domain. This is achieved by performing a two-dimensional Fourier transform on the surface topography dataset. The mathematical operation, referred to as a fast Fourier transform (FFT),  decomposes the data into frequency components, which is very useful for indentifying any repeating patterns in the  image. One benefit of FFT analysis is that it enables us to identify the frequency of any noise in the image, the source of which tends to have a characteristic frequency, and hence eliminate it[162].

The main use for FFT analysis is to extract more useful data about the sample morphology. This data has been used for roughness analysis, identification of frequency characteristics for large features and to analyse atomic lattice parameters[162]. The Fourier transform is based on the principle that any periodic function can be decomposed into the sum of a set of sine and cosine waves.

The periodic function $f(x)$ is given by,[166,167]

$$f(x) = \frac{a_o}{2} + \sum_{n=1}^{\infty} a_n \cos nkx + \sum_{n=1}^{\infty} b_n \sin nkx \qquad \text{(2.48)}$$

Where $a_o, a_n, b_n$ are referred to as the Fourier coefficients of the function $f(x)$, which are determined by Fourier analysis. These coefficients are given by, [166,167]

$$a_o = \frac{2}{\lambda} \int_0^{\lambda} f(x) dx \qquad \text{(2.49)}$$

$$a_n = \frac{1}{\lambda} \int_0^{\lambda} f(x) \cos(nx) dx \qquad n \geq 0 \qquad \text{(2.50)}$$

$$b_n = \frac{2}{\lambda} \int_0^{\lambda} f(x) \sin(nx) dx \qquad n \geq 1 \qquad \text{(2.51)}$$

Where $\lambda$ is the interval, or wavelength, of the periodic function $f(x)$. Figure 2.41 illustrates a periodic function broken down into its constituent sine and cosine wave functions. The Fourier transform can be applied to continuous or discrete and periodic or aperiodic functions. Consequently, there are four categories of Fourier analysis: Fourier Series (periodic-continuous), Fourier Transform (aperiodic-continuous), Discrete Time Fourier Transform (aperiodic-discrete) and Discrete Fourier Transform (periodic-discrete)[166,167,168].

122
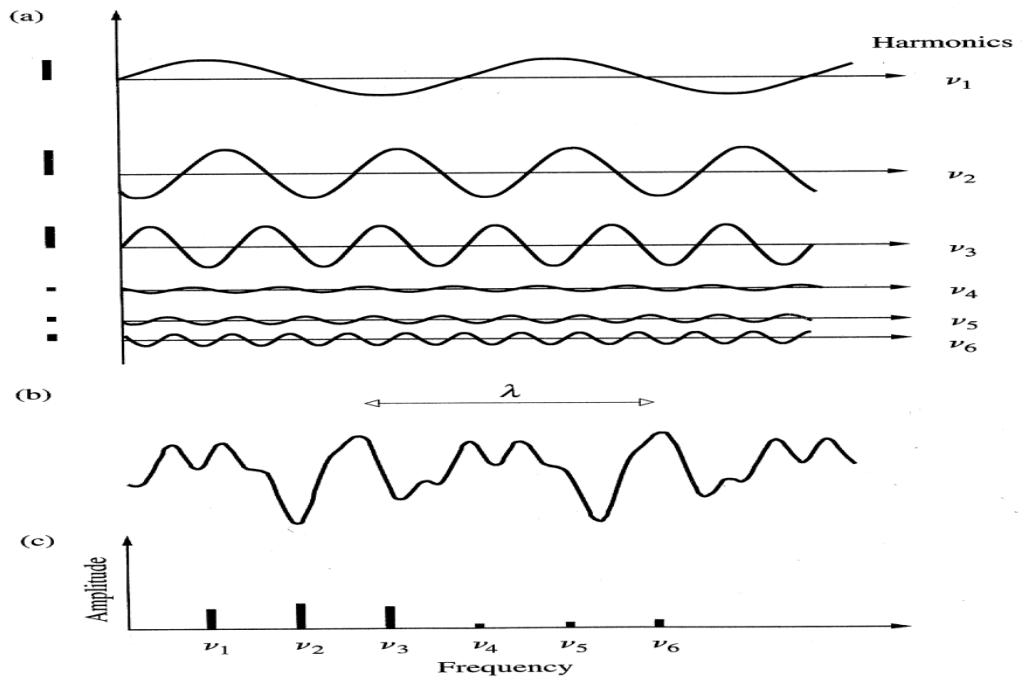
**Figure 2.41 – A periodic function over an interval $\lambda$ broken down into sine and cosine waves[166].**

Figure 2.42 illustrates the four different types of Fourier transform with an example signal. This enables the correct transform to be chosen with respect to the type of function or data being analysed.



**Figure 2.42 – Illustration of the four types of Fourier transforms[168].**

The surface topography of a sample imaged using an AFM consists of a finite set of discrete data points which synthesise an aperiodic signal. Hence the Discrete Time Fourier Transform (DTFT) would best represent this data. However, the Fourier transform can only be calculated using a computer algorithm if the function is periodical. It is possible to use digital signal processing to synthesis the AFM data into a periodic signal, which then allows the Discrete Fourier Transform (DFT) to be used[168]. For further ease of data processing, Fast Fourier Transform (FFT) is generally used which is a modified version of (DFT). The number of arithmetic operations involved in the calculations for large data sets is significantly reduced by (FFT) in comparison to (DFT). The DFT is given by, [166,167]

$$F(k) = \frac{1}{N} \sum_{n=0}^{N-1} f(n) exp\left(\frac{-2\pi i}{N} nk\right) \quad n = 0, \dots, N-1 \qquad (2.52)$$

As discussed in the previous section the root mean square (RMS) roughness, whilst useful, does not provide any information on the spacing of the roughness features and makes no distinction between peaks and troughs. The power spectral density (PSD) of the surface topography provides a more complete description. Here, the surface profile is broken into spatial wavelengths which allows comparison of roughness measurements over various spatial frequency ranges, i.e. the lateral distance over which the height variation occurs. The PSD is the square of the Fourier transform as a function of the spatial frequency, which is calculated for each horizontal or vertical line in the data and then averaged over all of the x/y profile[169,170]. The one dimensional (1D) PSD is given by,[170]

$$PSD(f_x) = L\left[\frac{1}{N} \sum_{m=1}^{N} Z(x_m). exp\left(-2\pi i. x_m f_x\right)\right]^2 \qquad (2.53)$$

The two dimensional (2D) PSD is given by,[170]

$$PSD(f_x, f_y) = L^2 \left[ \frac{1}{N^2} \sum_{n=0}^{N} \sum_{m=0}^{N} Z(x_m, y_n) \, exp\left\{-2\pi i\left[(x_m \cdot f_x) + (y_n \cdot f_y)\right]\right\} \right]^2$$

(2.54)

Where $L$ is the scan length, assumed to be equal in the x and y direction, $f_x, f_y$ are the spatial frequency's in the x and y directions, $N$ is the number of measured data points assumed to be equidistantly spaced in the x and y directions so that $\Delta x, \Delta y = L/N$, $x_m = m \cdot \frac{L}{N}$ , $y_n = n \cdot \frac{L}{N}$ and the spatial frequencies take the discrete range of values $f_x, f_y = \frac{1}{L}, \frac{2}{L}, \ldots \frac{N}{2L}$ and $i = \sqrt{-1}$.

The PSD explains a surface much better than RMS roughness, providing useful information on fractals and superstructures that may co-exist in the microstructures. It was recently realised that the fractal geometry and scaling concepts can concisely describe the rough surface morphology[169]. When analysing the PSD data as a function of spatial frequency, the frequency scale may be used to represent domain sizes. This is of particular interest in relation to the morphology of the active layer in a bulk heterojunction photovoltaic device. As discussed earlier, the ideal domain size is around 20nm for efficient charge separation. We will use the PSD data to analyse the variation of domain size due to changes in processing conditions for our PV devices within the experimental chapters.

# 3. Experimental Techniques

## 3.1 Cyclic Voltammetry

The experimental set up used for cyclic voltammetry (CV) measurements is shown in figure 3.1. A Solartron 1285 potentiostat is interfaced with the computer, which controls this hardware using a Corrware Software package. The potentiostat consists of three primary components: A control amplifier, an electrometer and a current to voltage converter. The control amplifier (CA) maintains the voltage between the current carrying working electrode (WE) and the current free reference electrode (RE), as closely as possible to predetermined control voltage. This control is achieved by injecting current into the cell through an auxiliary, or counter electrode (CE). The voltage between the RE and the WE is measured by the electrometer and adjusted accordingly by the potentiostat. This prevents the WE from being influenced by the electrochemical reactions which take place. The resulting current between the CE and WE is measured at the WE by the current to voltage converter. This data is then transferred to the computer for analysis.
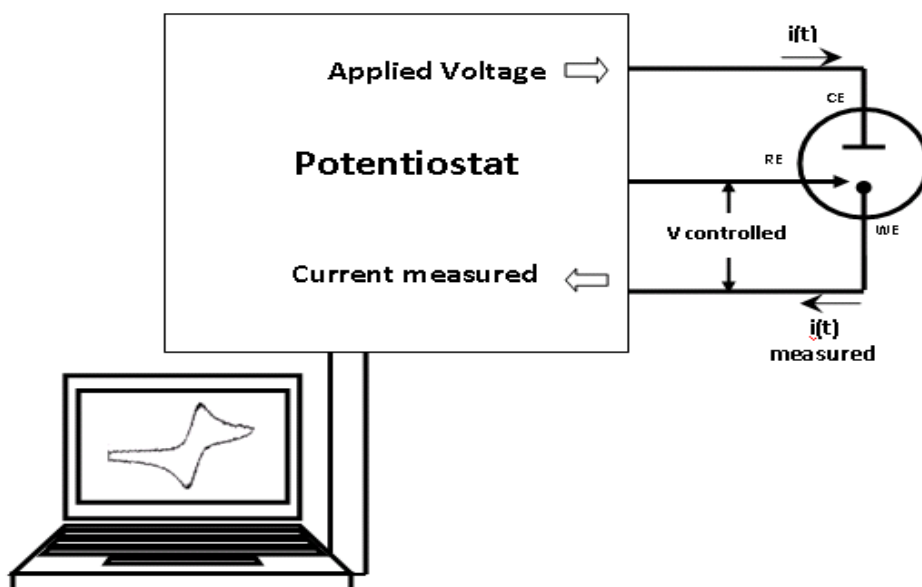
**Figure 3.1 – Experimental set up for cyclic voltammetry measurements[57].**

The electrochemical cell is shown enlarged in figure 3.2. The cell is constructed from a standard glass sample tube with a PTFE lid, chosen for its resistance to the solvent and materials which will be used. There are four holes in the lid to allow the three electrodes and a nitrogen line to be inserted. Here we use a silver/silver chloride (Ag/AgCl) RE, a glassy carbon WE (area $0.07cm^2$) and a platinum thin wire CE. The Ag/AgCl electrode was stored in a salt/deionised water solution (175 g/l concentration) when not being used.
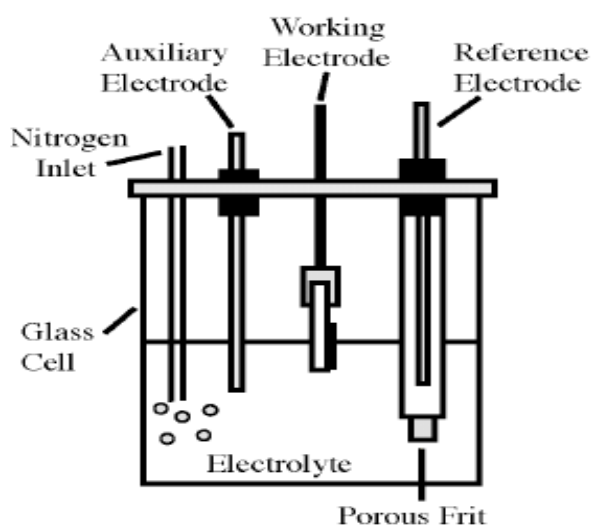


**Figure 3.2 – The electrochemical cell [171]**

The sample tubes were prepared by cleaning with Dichloromethane (DCM) followed by Iso-Proponal and then dried using a nitrogen blower. Dichloromethane (DCM) (purity>99%, water content<0.05%) was used to dissolve the compounds being tested. The electrolyte used was Tetrabutylammonium hexafluorophosphate (TBAHFP$_6$) (purity>98%), which had been recrystalised twice to improve the purity. First 0.3M (~581mg) of the electrolyte was added to the clean sample tube and dissolved with 5ml of DCM. 1mM of the material to be tested was then added followed by 1mM (~0.9mg) of ferocene. The electrodes were cleaned using DCM and dried with a nitrogen blower before being immersed into the solution via the holes in the cell lid. Finally the nitrogen line was connected to the inlet hole.

The nitrogen inlet was used to purge the cell for 3 minutes prior to making each measurement in order to remove oxygen from the solution. The potential scanning range was set using the Corrware software from -1.5 to 1.5V at a rate of 20 mVs$^{-1}$. Initially the experiment was run with only the electrolyte solution for one cycle as a check to ensure the cell was not contaminated and that the required flat current response was produced. The measurement was then taken with the material added, followed by a final measurement with the Ferrocene included.

## 3.2 Thin Film Absorption Spectrum

A glass substrate, measuring 12mm x 12mm, was spin-coated with the material to be studied in order to investigate its absorption spectrum. The substrates were cleaned using a standard process in order to provide a good surface for the compound to be coated on and remove surface contaminants. The substrates were placed into a clean Pyrex crystallisation dish and SVC 175 photo resist stripper was added. The dish was then placed into a heated sonicator (60˚C) and sonicated for 30 minutes after which the substrates were transferred to a new dish to which de-ionised water was added. Heated sonication again took place at 60˚C, this time for 10 minutes, after which the substrates were transferred to another clean dish with fresh de-ionised water and sonicated for a further 10 minutes. The substrates were then sonicated in acetone for 10 minutes followed by 10 minutes sonication in Iso-Proponal for 10 minutes. A nitrogen blower was used to individually dry each substrate, which were then placed into a glass Petri dish ensuring that there was no overlap of the slides. The Petri dish was placed into an oven at 100˚C for 1 hour in order to complete the drying process.



**Figure 3.3 – Typical spin coating machine** [172]

The compound to be investigated was first weighed using electronic scales within the glove box and placed into a sample tube. 3.75mg of a compound was typically needed together with 0.15ml of solvent in order to make a solution of concentration 2.5% by weight. This was needed to provide a layer thick enough to enable the spectroscopy to be effective. Chlorobenzene was used to dissolve the compound within the sample tube and was then drawn into a metal syringe. A 0.02 µm filter was attached to the syringe to prevent any un-dissolved 'lumps' from being applied to the substrate.

The substrate was held by vacuum on the spinning chuck whilst the dissolved compound was applied evenly over the full surface. The spin speed was 2000 rpm, acceleration 2000 r/min$^2$, for 30 seconds after which the sample was annealed at 120˚C for 1 hour, in order to evaporate all of the solvent.

A UV/Visible Spectrometer (Lambda 40, Perkin Elmer ) was used to make all absorption spectrum measurements. The wavelength range was set from 800nm to 300nm, with a step size of 1nm between measurements. A clean substrate was scanned first as the blank reference sample after which the compound coated substrate was scanned. The spectrometer measures transmittance or absorbance versus wavelength across the selected range, automatically correcting for the glass substrate.

# 3.3 Time of Flight (TOF)

## 3.3.1 Sample preparation (cell technique)

There are two primary methods for sample preparation suitable for TOF measurements, the LC cell technique and spin coating. The cell technique uses two glass-ITO substrates, which are etched to provide small area electrodes which overlap when the substrates are placed together face to face as shown in figure 3.4.
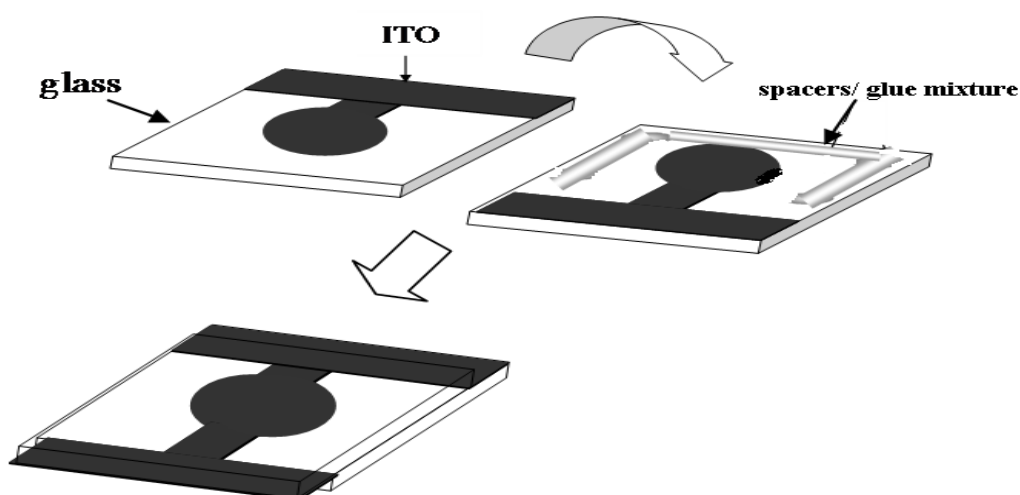


**Figure 3.4 – The cell technique[57].**

The two substrates are glued together at three sides, leaving one side open for the LC organic semiconductor to enter and fill the cell. This is achieved by placing the cell on a controllable hot stage within a vacuum chamber and the organic material next to the cell opening. By heating the material above its clearing point an isotropic liquid is formed, which upon filling the chamber with $N_2$ then spreads throughout the cell opening and flows into the cell due to the capillary effect[57]. However, in practice this technique does not reproduce device film conditions and was not used for any experimental work carried out in this thesis.

## 3.3.2 Sample preparation (spin coat technique)

### 3.3.2.1 Preparation of substrate

All TOF samples were prepared using a 12mm x 12mm glass substrate with 100nm ITO coating of resistance ≤ 20 ohms square supplied by UQG Optics. Positive photo resist was applied to the substrate, covering all but a narrow strip along one side of the substrate, approximately 2mm wide. Acid etching was then performed, as described in section 3.7, to remove the ITO coating along this 2mm strip as shown in figure 3.5. This was done to reduce the possibility of short circuiting the device due to the top Aluminium electrode, added later in the process, making contact with the bottom ITO electrode. This also reduced the overlap between the top and bottom electrodes, which in turn reduced the capacitance of the sample to help meet the condition $RC \ll t_{tr}$ described earlier.
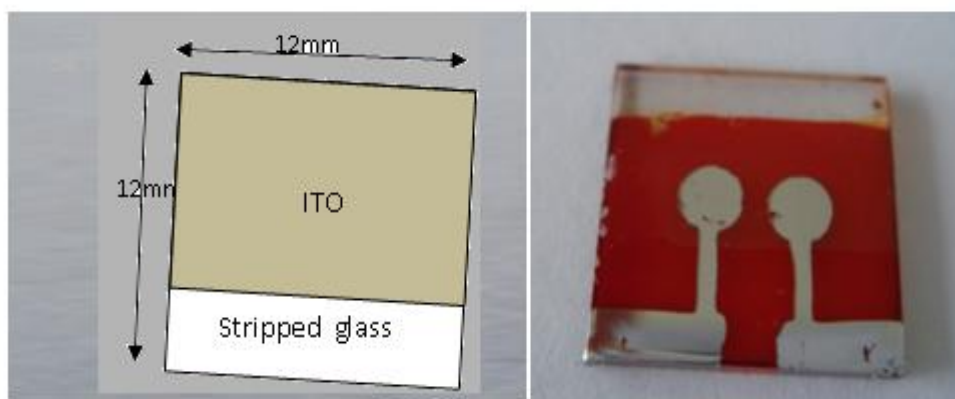


**Figure 3.5 – Illustration of substrate following acid etching (left) and Photograph of TOF sample with organic film and top Al electrode(right)[57].**

After acid etching the substrate was sonicated in acetone twice, to remove the photo resist, before being cleaned using the standard substrate cleaning process described in section 3.3. Oxygen plasma treatment was then applied to the substrate, as described in section 3.7, before being introduced to the nitrogen purged glove box ready for spin coating of the organic semiconductor.

## 3.3.2.2 Spin Coating a Thick Film

As discussed earlier, a relatively thick film of ideally 1µm or more is required for TOF measurements. This is significantly thicker than the thin films used for photovoltaic devices of around 80nm, so the spin coating technique used for those devices needs to be amended to provide a thicker film, whilst still providing a uniform smooth surface. Here three main factors influencing film thickness are taken into account; solution concentration, spin speed and evaporation time.

Whilst a drop cast technique, which allows the solvent to evaporate without spinning the sample, produces a thick film it also produces a high level of surface roughness. Spin coating provides a smooth and uniform film but limits the film thickness. The concentration of the solution can be increased up to a point, beyond which the filter becomes blocked. This constraint was in part overcome by allowing an evaporation time after the organic solution was applied to the substrate, before spinning, which increased the remaining solution concentration. The film morphology is also improved by controlling the evaporation time, as this gives the molecules more time to arrange freely on the substrate.

If evaporation occurs too quickly the organic material accumulates around the edge of the substrate and creates an uneven surface. The evaporation rate was reduced by placing an inverted glass beaker over the sample during evaporation, which also prevented dust molecules from falling onto the sample during this time. A solvent rich environment was created to further extend the evaporation time. During the evaporation time the spin coater itself was tilted gently in each direction to prevent the accumulation of the organic material on the edges of the substrate, as shown in figure 3.6.
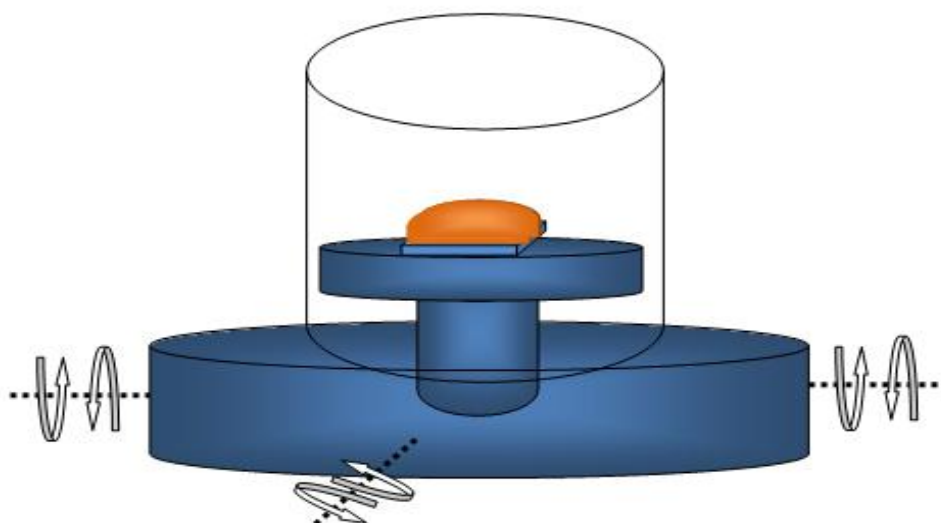
**Figure 3.6 – An illustration of the spin casting stage with the sample under a glass beaker lined with solvent to extend the evaporation time. The stage was tilted as illustrated to prevent material build up around the edges[57].**

In some cases several attempts were made with various concentrations and evaporation times before producing a film thick enough for TOF measurements, whilst still retaining a smooth enough surface to allow the top electrodes to be added. The compounds were dissolved in chlorobenzene, at a concentration of about 20mg per 0.2ml of solvent, before being applied to the substrate on the spin coater stage through a 0.2 µm filter. The 250ml glass beaker was lined with a small amount of solvent and placed over the sample during evaporation which varied from 20 – 35mins depending on the material or blend. The actual solvent concentrations and evaporation times used for each material measured are given in the results section. After evaporation the samples were spun at 900rpm at an acceleration of 590 $r/m^2$ for 35s. The film would crack and become very rough on annealing with a hotplate, so samples were placed within a vacuum overnight, to remove the remaining solvent from the organic material.

### 3.3.2.3 Deposition of Top Aluminium Electrode and LiF Buffer

Once fully dried under vacuum, the sample was placed onto a shadow mask which exposed the bottom 4mm of the substrate and then placed into the vacuum chamber ($<10^{-5}$mbar). A lithium fluoride insulating layer, 25nm thick, was thermally evaporated onto the substrate as shown in figure 3.7 (middle). The sample was then transferred to another shadow mask of two electrodes as shown in figure 3.7 (right) and previously shown as a photograph in figure 3.5 (right). Aluminium was then thermally evaporated to form the top electrodes, with a thickness of around 100nm.
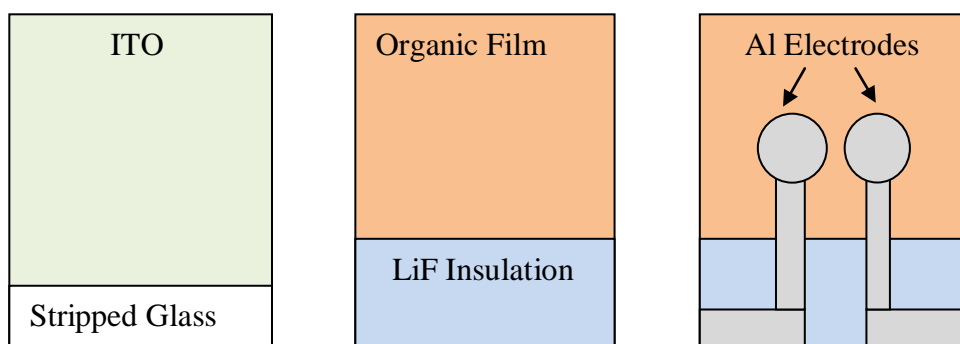


**Figure 3.7 – Substrate before spin coating (left), with organic film and addition of LiF insulation layer (middle) and Al electrodes (right).**

When the organic film is spun onto the glass/ITO substrate, it is possible that a corner of the ITO would remain exposed at the glass/ITO junction. If this is the case then the addition of the aluminium electrode directly on top would cause the device to short circuit. The addition of the LiF insulating layer ensures that the ITO is completely covered and insulated from the Al electrode. The active areas of the device are located where the two Al discs have been evaporated. All evaporation was carried out within the nitrogen purged glove box, which houses the vacuum dome and evaporator therein. After electrode deposition a thin strip of film at the top of the device was removed, around 2mm wide, to expose the ITO electrode. This allows the electrical contact to be made for the TOF measurements.

## 3.3.2.4 Determining the thickness and surface profile of the film

A white light interferometer (Wyko NT1100) was used to determine the thickness of the organic film after TOF measurements had been made. The Wyko is a non-contact optical profiler which has two modes of operation, Vertical Scanning Interferometer (VSI) and Phase-Shift Interferometer (PSI). The VSI mode is generally used to measure steps greater than 200nm and rough surface profiles, whilst the PSI mode is used for small steps below 200nm and general surface profiling for relatively smooth films. The film was scratched using a fine needle in a number of places around each electrode as shown in figure 3.8 (b).
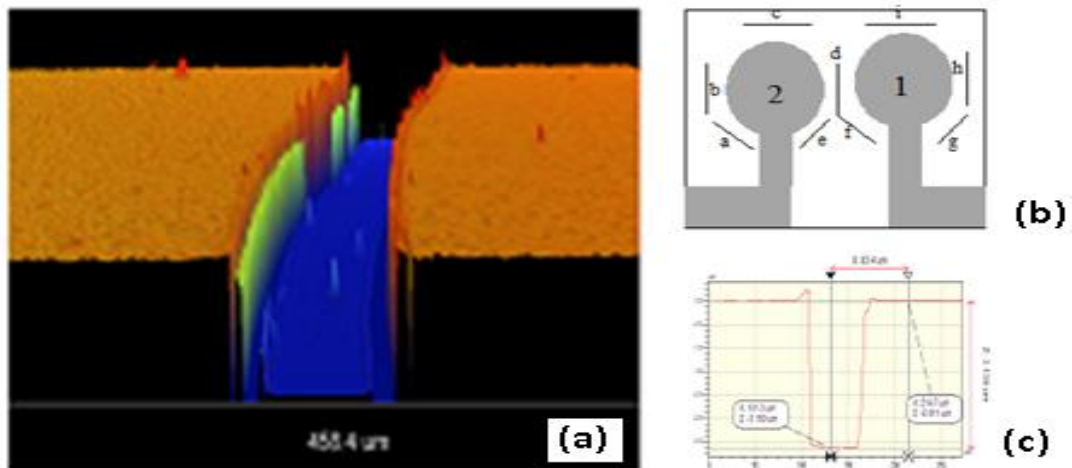


**Figure 3.8 – Example of a 3D white light interferometer profile of a thin film with a scratch mark to find the thickness (a), the positions of the scratch marks around the electrodes (b) and a 2d profile of a scratch (c) [57].**

The VSI mode was used to measure the film thickness, as it was expected to be significantly thicker than 200nm, and the PSI mode was used for a general surface profile of the film as roughness features should be less than 200nm. Several measurements were taken along each of the scratches made in order to provide an average thickness around each electrode and a standard deviation as an indication of the film roughness. A typical 3D and 2D profile of a scratch is shown in figure 3.8 (a) and (c) respectively.

### 3.3.3 TOF Measurement Experimental Setup

The prepared sample is placed within a gas tight chamber, as shown in figure 3.9 (i), whilst still within the nitrogen purged glove box. An electrode contact is connected to the exposed ITO strip at the top of the device, whilst a second contact is connected to one of the two aluminium electrodes. The sample is positioned on a heating stage over a small hole, to allow the excitation laser to reach the device, ensuring that the round active area of the connected Al electrode is directly over this hole. The chamber is then sealed, removed from the glove box and transferred to the TOF measurement set up shown in figure 3.9 (ii) (a).
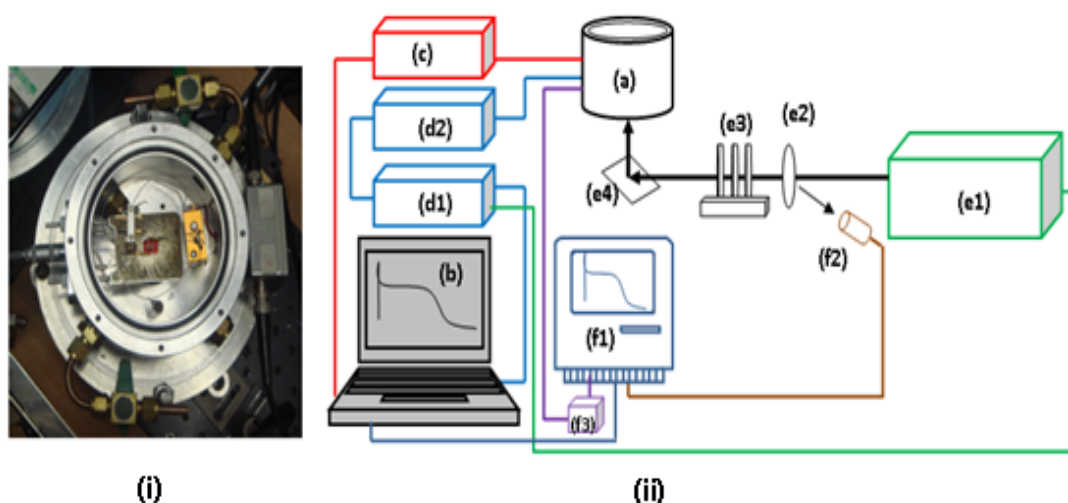


**Figure 3.9 - (i) Photograph of the chamber showing the sample position on the hot stage. (ii) schematic diagram of the TOF experimental setup showing the chamber (a), the computer with controlling program (b), the temperature controller (c), the function generator(d1), the amplifier (d2), the Nitrogen UV pulsed laser (e1), the laser beam alignment system of lens, neutral density filters and mirror (e2,e3,e4), the oscilloscope (f1), the avalanche photodiode (f2), the load resistance (f3)[57].**

A computer (b) is used to control the instruments and record the data for each measurement, using a Labview program. The Linkam TP4 temperature controller (c) is used to maintain a constant temperature for the sample, via the heating stage within the chamber, whilst measurements are made. The bias voltage controller consists of an Agilent 33120A waveform generator (d1) and an amplifier (d2). A Laser Science Inc.

VSL-337ND Nitrogen laser (e1) is used to excite the sample with a 337nm wavelength pulse of 6ns duration. Lenses (e2) focus and guide the laser beam through the neutral density filters (e3) which control the intensity of the beam. The mirror (e4) reflects the laser beam into the sample chamber via a quartz window, where it then passes through a $0.049\text{cm}^2$ hole in the heating stage onto the sample. The Tektronix TDS2012 oscilloscope (f1) is connected to the sample via switched load resistance (set to $100\Omega$) and is triggered by an avalanche photodiode (APD) (f2), which in turn is positioned to collect part of the reflected laser beam. This trigger set up removes the uncertainty of the time lapse between the laser receiving a firing pulse and the sample being excited by the beam.

The Labview program first sets the desired sample temperature via the heating stage in the chamber and holds this constant. The waveform generator-amplifier then produces a positive bias voltage pulse which is applied to the sample. After a short delay, for the voltage across the sample to stabilize, a firing pulse is sent to the laser. The laser then emits a pulse and triggers the oscilloscope which collects current waveform generated by the sample. Several voltage and laser pulses are generated for each measurement, in order to produce a number of current waveforms. An average waveform is calculated by the Labview software in order to improve the accuracy of the data set for each measurement. The data is then recorded, for electron charge carriers, and the process repeated with negative biased voltage pulses to generate the hole current waveform data. The voltage is varied and the process repeated to generate current waveforms as a function of the applied electric field. The data range for both time (horizontal) and current (vertical) settings can be altered manually in order to take a wide range of data for the current waveforms.

# 3.4 Differential Scanning Calorimetry

The materials to be studied were weighed, in the relevant ratio for the required blend, using digital scales and standard sample tubes. A small amount of dichloromethane was used to dissolve the acceptor material which was then added to the donor and agitated within the sample tube to mix the blend components. The blend solution was then drop cast into a standard aluminium DSC pan using a pipette, within a fume cupboard. As the DSC pan is very small, this process had to be repeated, with intervals to allow the solvent to evaporate and thus allow more solution to be added to the pan.

Once a sufficient amount of blended material had been added to the pan, and all of the solvent had evaporated, the pan was weighed to determine the amount of material in the sample. Around 4 – 5mg of material is needed to produce reliable DSC results. The pan was prepared in this way in order to produce a similar blend to that produced for thin film processing. Finally, the pan lid was pressed into place to complete the sample preparation ready for measurement. It is crucial that the aluminium pan is firmly sealed by the lid in order to prevent any material leakage during heating within the DSC furnace.



**Figure 3.10 – Photograph of Perkin Elmer DSC.**

Figure 3.10 shows the Perkin Elmer DSC 7 used for measurements. As can be seen, there is a mini glove box enclosing the sample chamber, which allows for a nitrogen purged environment whilst measurements are being made. The sample chamber contains two furnace pans, as shown in figure 3.11, one for the sample under study and the other for the known reference. The DSC is calibrated using a known indium sample before any sample measurements are made. The sample is then scanned according to the parameters chosen..
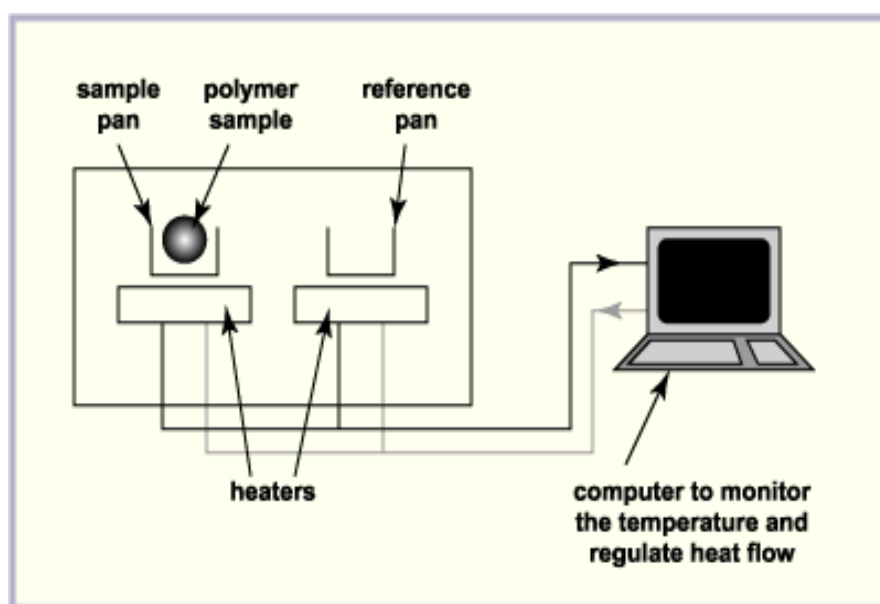


**Figure 3.11 – Schematic of the DSC experimental set up.**[173]

For each blend measured the scan rate chosen was 10°C/min, whilst the temperature range was generally over 0°C to 300°C depending on the materials under study. Two full heating and cooling cycles are run to check for reproducibility of the phase transition temperatures. Further, the first cycle generally provides the transition temperatures for the individual blend components whilst the second cycle produces transition temperatures for the blend. Each cycle begins at room temperature (25°C) rising to 300°C, then down to 0°C and back to room temperature.

The maximum temperature was normally chosen in order to exceed the highest melting point of the individual blend components by at least 20°C, which ensures that the

materials mix homogeneously. However, it is also important not to exceed the melting point by more than that necessarily needed as higher temperatures increase the risk of material leakage from the sample pan.

## 3.5 Polarised Microscopy

A small quantity of the blend solution prepared in section 3.4 for the DSC sample is applied to a blank microscope slide using a pipette. A glass cover slip was pressed onto the blend sample and the solvent allowed to evaporate. The slide was then inserted into a heating stage, whilst ensuring that the sample area could be seen through the hot stage window. The heating stage was then placed onto the sample stage of the polarisation microscope, to enable the sample to be viewed between crossed polarisers whilst heating and cooling took place. This allows the phase change transitions to be viewed in real time.
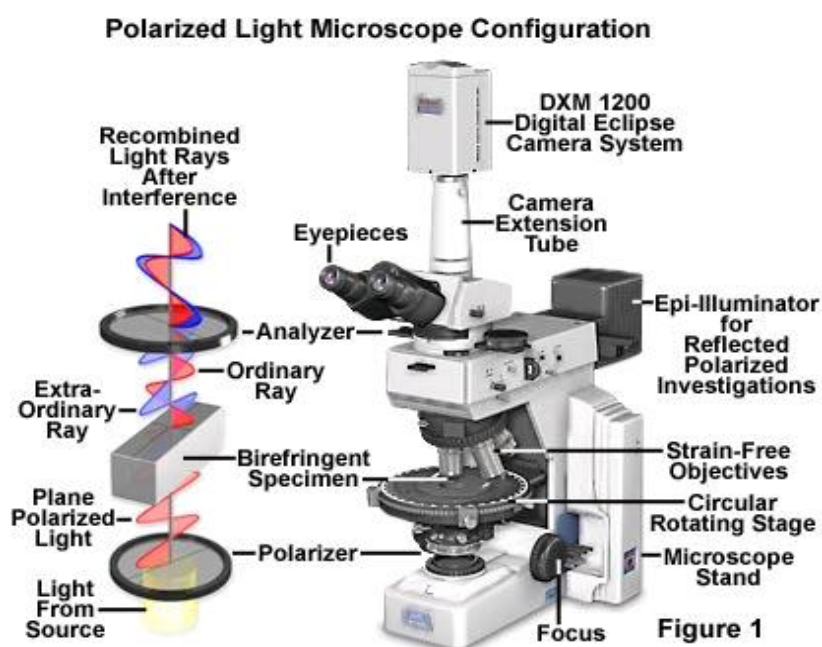


**Figure 3.12 – A typical polarisation microscope.**[174]

Figure 3.12 shows a typical polarisation microscope, which has a digital camera incorporated into the eye piece. The camera is connected to a computer with image processing software, where the images can be saved and processed. The sample was heated and cooled at a rate of 10°C/min over the same temperature range as that used for the DSC. The blend was closely observed before, during and after the phase transition temperatures identified using the DSC, and relevant images were captured for further study.

## 3.6 Atomic Force Microscopy

The surface morphology of the active layer was investigated for various photovoltaic devices using an atomic force microscope (AFM) developed by Molecular Imaging (Agilent). The AFM set up is similar to that shown earlier in figure 2.39. The thin film was positioned on the viewing stage so that an active layer portion was imaged towards the centre of the device. Each image was scanned over three sizes, 5x5µm, 1x1µm and 500x500nm. MAC Levers Type II cantilevers (Agilent) were used for all measurements made. These cantilevers are made from silicon, including the tip, and have a thin magnetic coating which enables oscillation to be induced by the alternating magnetic field produced by the AFM.

The image processing software, Picoscan V.5.2, was also provided by Molecular Imaging. This software was used to produce all the AFM images shown in this thesis and also to obtain the RMS roughness and height distribution data  The fast Fourier transform (FFT)  and the power spectral density (PSD) data was processed using Gwyddion freeware software. Origin7 was used to plot all data produced for roughness, height distribution and PSD data for further investigation and presentation within this thesis.

# 3.7 Photovoltaic Device Fabrication and Characterisation

Figure 3.13 illustrates the dimensions of the multiple layers which comprise our completed photovoltaic device.
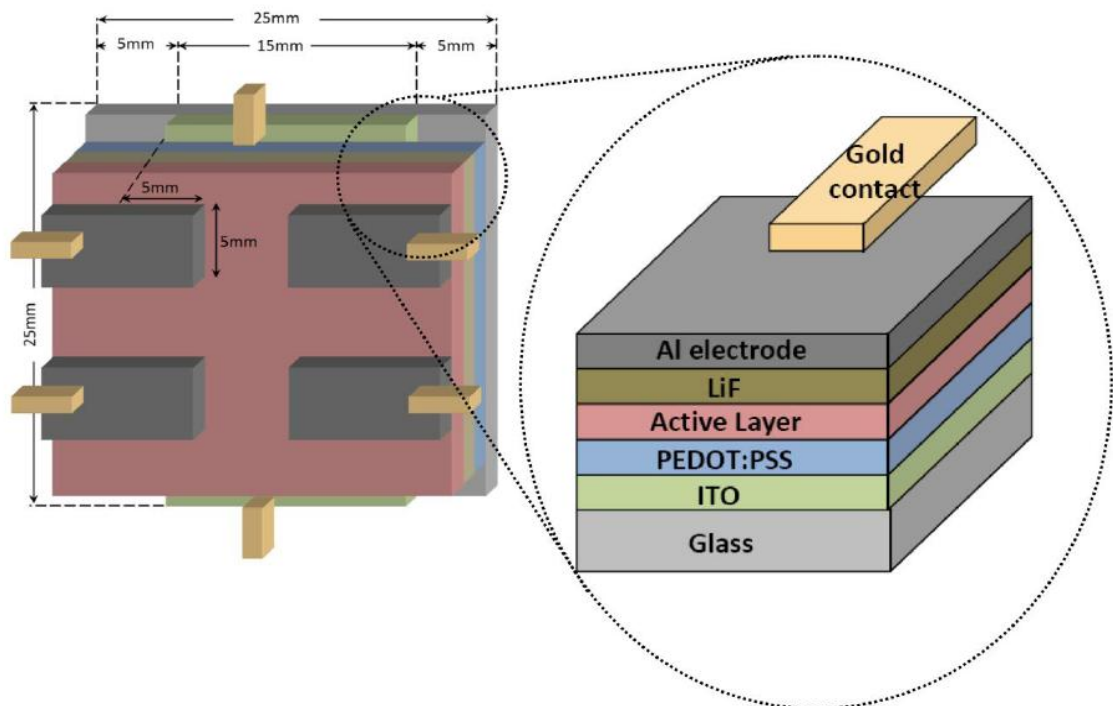


**Figure 3.13 – Schematic of photovoltaic device fabrication[57].**

There are several steps involved in the fabrication of our PV devices, and we will investigate each of these steps in turn. First the substrate preparation will be explained, which comprises of cleaning, plasma treatment and the PEDOT:PSS layer. Then we will consider the application and annealing of the bulk heterojunction active layer and finally the deposition of the top electrode. The method and types of measurements made to characterise the device are then discussed.

## 3.7.1 Substrate Preparation

The substrate surface, which constitutes the anode of the PV device, is a key factor for the optimisation of device performance. The basic soda lime glass substrates were provided by UQG optics, of 1.1mm thickness and pre cut into 25x25mm squares. The substrates were supplied pre-coated with a 100nm thick indium tin oxide (ITO) layer, which has a sheet resistance of ≤20 ohms square. The first step in our device processing is to remove a 5mm strip of ITO from two sides of the substrate as shown in figure 3.14. This is done to prevent accidental contact between the top and bottom electrode once the device is complete.
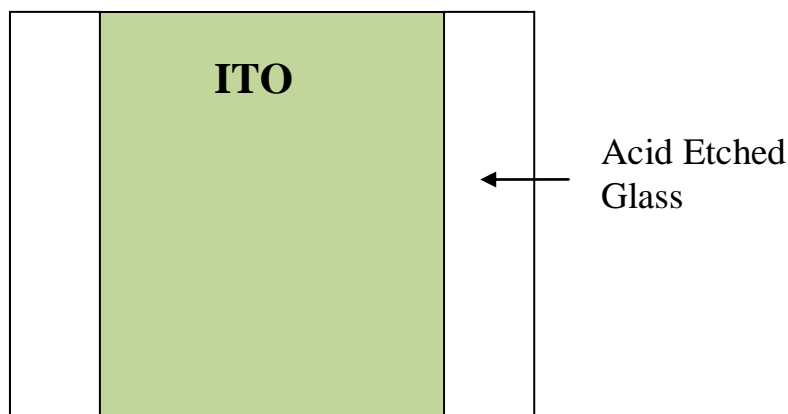


**Figure 3.14 – ITO substrate with strip removed either side.**

Positive photo resist was used to cover the central area of the substrate, the green shaded area in figure 3.14, and left to dry overnight. The substrates were then placed into an ferric chloride acid bath, preheated to 70 ˚C, ensuring that the ITO side of the substrate was facing upwards. After being submerged for 30 minutes the substrates were removed and rinsed with de-ionised water. A multi meter was used to ensure that the ITO had been fully removed from the uncovered side strips. The substrates were then sonicated in acetone for 10 minutes twice, in order to remove the positive photo resist, and dried using a nitrogen blower. The substrates were then cleaned using the standard cleaning procedure described in section 3.2.

The interface between the ITO and active layer of the PV device can create a barrier which inhibits hole transport from the active layer to the collecting electrode. The barrier height, which is further increased by surface contaminants on the ITO, can have an adverse effect on the device current/voltage (I-V) characteristics[175]. Various studies have shown that the work function of the ITO can be influenced through treatment and modification of the surface[176,81,177,178,179]. Further, trapping centres can be created as a result of ITO induced degradation mechanisms releasing oxygen from the electrode. The adverse effects of surface contaminants and the interface morphology can be reduced by modifying the ITO surface using oxygen plasma treatment[180].

The plasma treatment was carried out within an evacuated dome containing two plate electrodes. The substrates were placed within the dome between the two electrodes after which the dome was fully evacuated. Oxygen was allowed to fill the dome which was then fully evacuated again to remove airborne contaminants. This process was repeated 5 times to fully purge the dome with oxygen, before admitting the desired pressure of oxygen needed for the plasma treatment.

A voltage of 300V was applied to the electrodes which bombards the ITO surface with large ions, smoothing the surface by eroding peak features. The vacuum was then disengaged and the substrates removed. During plasma treatment surface contaminants are released and afterwards the substrates were cleaned once more, by sonication in de-ionised water for 10 minutes followed by 10 minutes sonication in Iso-Proponal. The substrates were then individually dried using the nitrogen blower and admitted to a nitrogen purged glove box ready for spin coating. As previously discussed the organic materials are subject to degradation in oxygen and moisture, which can also create charge trapping sites. This is particularly the case during heating (annealing) and as such all device processing was carried out in a nitrogen purged glove box.

The final step of the substrate preparation is to spin coat a layer of poly(3,4-ethylenedioxythiophene) (PEDOT) doped with poly(styrenesulfonate) (PSS). This polymer is water soluble and has good electronic conductivity, optical clarity and environmental stability. It is used to increase the work function of the ITO electrode and act as a physical barrier to known defect sites present within the ITO[181,182,183,184]. Here we use commercially prepared PEDOT:PSS (Baytron P VP. AI 4083) which is supplied in a water based solution. Immediately prior to use the PEDOT:PSS is sonicated for 5 minutes in order to dissolve any clumps within the solution.

The PEDOT:PSS was spin-cast onto the ITO surface of a plasma treated substrate using the spin coater described in section 3.2. A spin speed of 4000 rpm was used with an acceleration of 2000 $rpm^2$ and a spin duration of 30 seconds. These spin conditions have been shown by Dr. C. H. Lei at the University of Hull to produce a uniform layer approximately 20nm thick. A lint free tissue was used to remove the PEDOT from two sides of the substrate, to enable electrical contact to be made with the ITO electrode for subsequent measurements. The substrate was then annealed on a hot stage at 120°C for 30 minutes to evaporate the water, followed by 5 minutes at 220°C to thermally polymerise the PEDOT:PSS. The substrate was then cooled to room temperature ready for the active layer to be applied. All heating and cooling steps were carried out at a rate of 10°C/min.

## 3.7.2 Application of Bulk Heterojunction Active Layer

The donor and acceptor materials were weighed into standard sample tubes within the nitrogen purged glove box using digital scales. For each device a total of around 4mg of donor/acceptor material is required, split into the desired blend ratio. An organic solvent, 0.6ml chlorobenzene, was used to dissolve the two materials and blend them together to produce a blend solution concentration of 1.5%wt. The solution was applied to the substrate, on top of the annealed PEDOT:PSS layer, using a 0.2µm filter to remove any large un-dissolved particles.

The solution was spin cast at 2000 rpm at an acceleration of 2000 $rpm^2$ for a duration of 30 seconds. The spin conditions and solution concentration used here have been shown by Dr. C. H. Lei at the University of Hull to produce a uniform layer of around 80nm thickness for our materials. A lint free tissue was used, with a small amount of chlorobenzene, to remove the active layer from two sides of the substrate to expose the underlying ITO contacts. This allows electrical contact to be made with the bottom electrode as shown in figure 3.13. The substrate was then annealed using the hot stage, generally at 120°C for one hour, in order to evaporate the solvent and improve the morphology of the active layer. The sample was then cooled to room temperature and transferred to the evaporation dome ready for the addition of the top electrodes. The heating and cooling rate was 10°C/min. It will be specified when the annealing conditions are varied in the subsequent experimental chapters.

## 3.7.3 Deposition of the Top Aluminium Electrode

Within the nitrogen purged glove box a vacuum vapour deposition unit is used to deposit the top aluminium electrodes. The substrate was mounted upside down on a shadow mask, as shown in figure 3.15, and then placed inside the vacuum chamber.
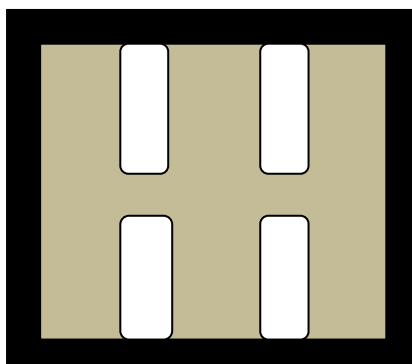


**Figure 3.15 – Shadow mask for top Aluminium electrode.**

The vacuum chamber was evacuated to around $3 \times 10^{-7}$ Torr before evaporation could take place. The rotary pump was used to initially reduce the pressure to around $10^{-5}$ Torr, after which the diffusion pump was used to further evacuate. Liquid nitrogen was used to keep the diffusion pump cool and working efficiently throughout the vapour deposition process. The dome is equipped with a quartz crystal thickness monitor, which was used to determine the thickness of the vapour deposited films.

A 0.6nm thick layer of lithium fluoride (LiF) was vapour deposited followed by 100nm of aluminium (Al) to produce the top electrode. The LiF was used as a buffer between the active layer and the top aluminium electrodes in order to reduce the height of the electron barrier between the active layer and Al electrode. This in turn improves the extraction of electron charge to the external circuit. The completed PV device is removed from the vacuum dome and is now ready for characterisation.

## 3.7.4 The Test Chamber

It is necessary to remove the device from the protective environment of the nitrogen purged glove box in order to make measurements of the device characteristics. To this end a vacuum sealed test chamber was fabricated to house the PV device during measurements. Figure 3.16 shows the a photograph of the test chamber used.



**Figure 3.16 – The device test chamber.**

The test chamber contains a mounting frame with spring loaded clips to hold the PV device in place. There are four Al electrode contacts, one contacting each of the four electrodes deposited, and two ITO electrode contacts, one each side of the device contacting the exposed ITO strip. These contact points are illustrated in figure 3.13 by the gold contacts. Each electrode contact is fed through to the rear of the test chamber, where external electrical connections can be made for measurements. The chamber lid contains a quartz window to allow light to pass through and excite the active layer of the device. The completed PV device was mounted and sealed inside the test chamber and then removed from the glove box for measurements.

## 3.7.5 Photovoltaic Device Characterisation

The experimental set up for the photocurrent and J-V measurements used in this thesis is illustrated in figure 3.17.
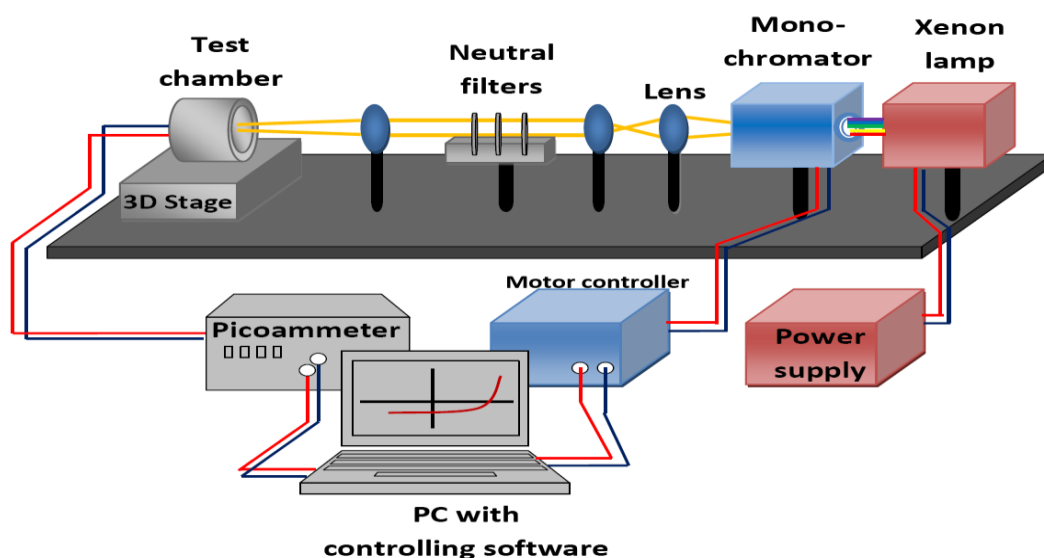


**Figure 3.17 – Schematic of experimental set up for photocurrent and J-V measurements[57].**

The Xenon lamp (Bausch & Lomb) provides illumination across the visible spectrum, from ultraviolet to infrared, at high intensity. Light is emitted from the lamp into the mechanical monochromator (Bausch & Lomb), which emits light at a chosen wavelength. The connected PC uses a software package (written by Gordon Sowersby) to select and control the light wavelength emitted from the monochromator. The light then passes through a set of lenses which collimates and focuses the light beam perpendicular to the test chamber.

The light is directed onto one of the four active areas of the device, where the bottom and top electrodes overlap. Each active device area is around 25mm$^2$ and the chamber is positioned so that the incident light beam covers most of this. The 3D stage is used to move the test chamber to enable to incident light to be focussed on each of the four active areas in turn.

The incident light intensity was measured using a power meter (Coherent Fieldmaster) which could then be varied using the neutral density filters, which are positioned between the collimating lenses. The connected PC incorporates a voltage waveform generator to apply an electrical field across the device and the resultant current is measured by the pico ammeter. The data is recorded and displayed using a home written software package produced by Gordon Sowersby.

The mechanical monochromator steps through a pre-determined wavelength range and the photo generated current is measured and recorded for each wavelength interval used. During this wavelength scan the applied field is zero. A single wavelength, generally that which provided the peak current in the first measurement, is then used to produce all light J-V measurements. With a constant incident light wavelength, the applied field is varied and the photocurrent for each voltage interval is recorded. A light shield is placed across the quartz window of the test chamber for dark J-V measurements to be made.
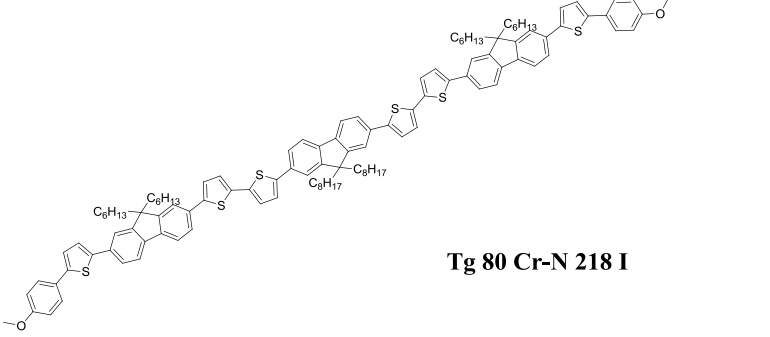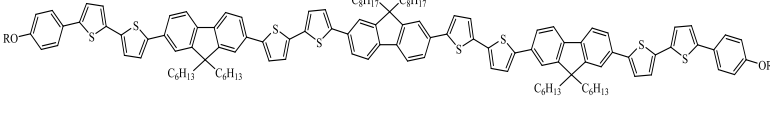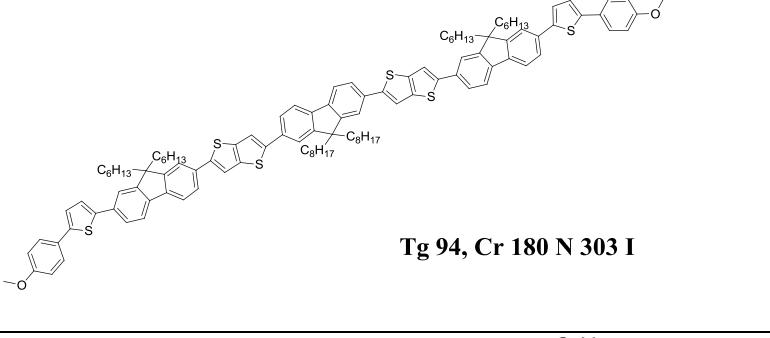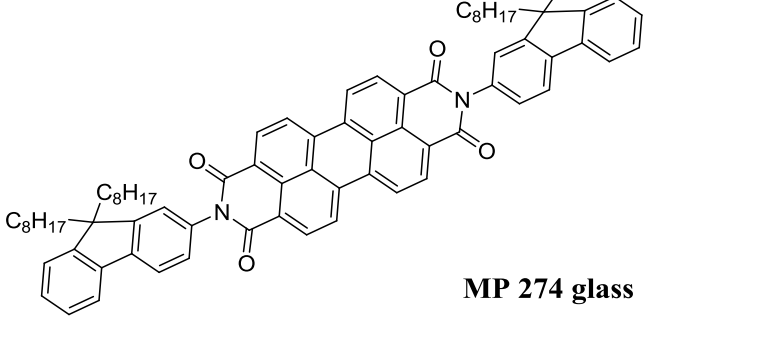
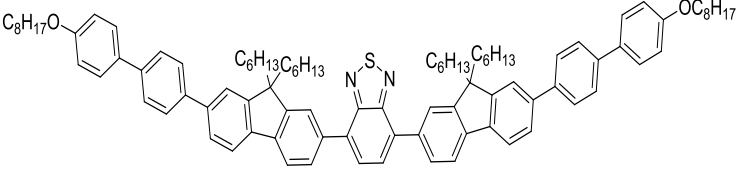# 4. Investigation of the Energy Levels of Organic Semiconductors
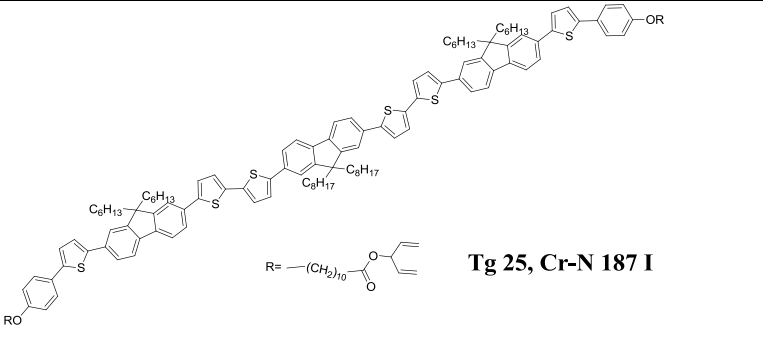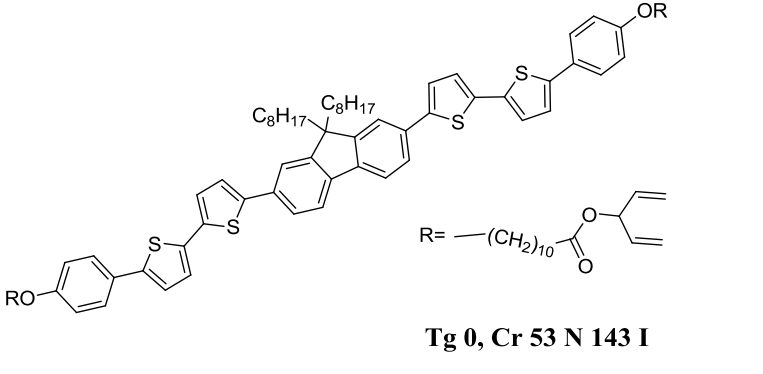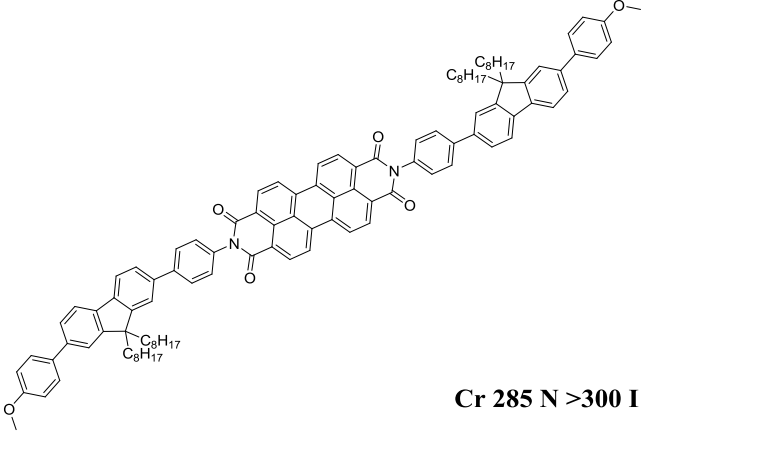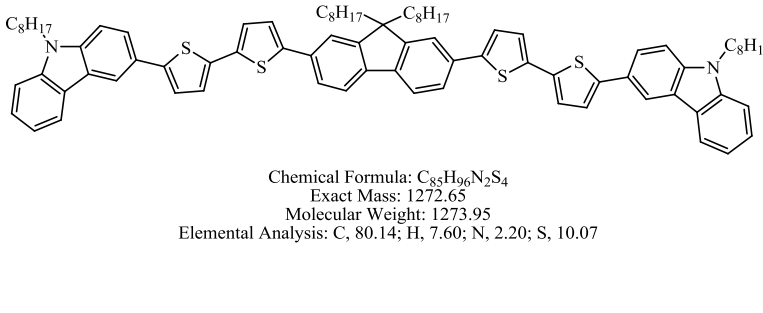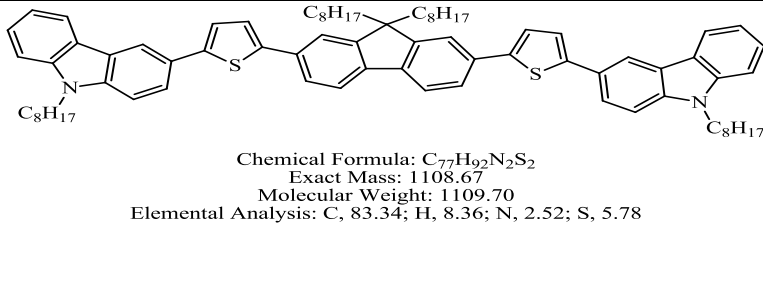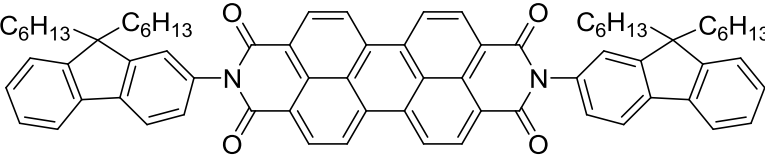
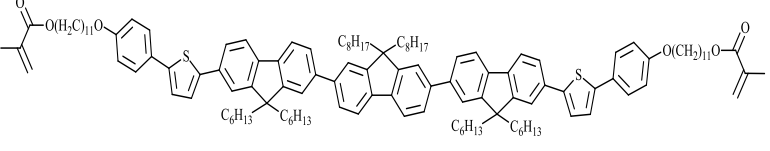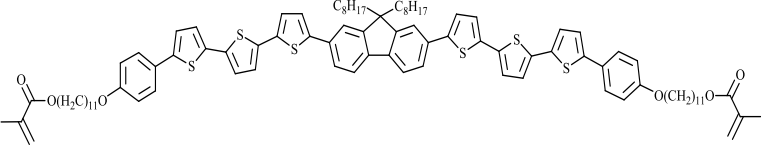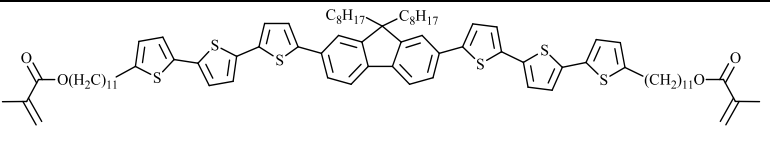## 4.1 Chemical Structure of Materials Studied
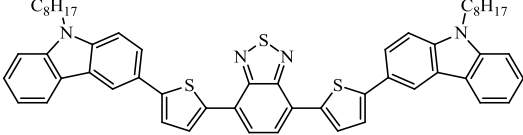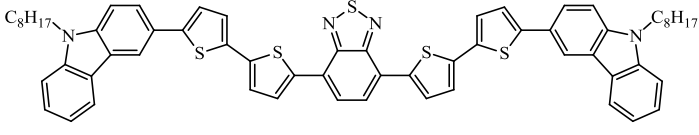
The Materials studied in this thesis are listed in table 4.1 with an illustration of their chemical structures. In the right hand column is a summary of the energy levels found for these compounds using cyclic voltammetry and the absorption spectrum. Values found from oxidation reactions are prefixed $^O$ whilst reduction reactions are marked $^R$. After the listed values the type of reaction is indicated by (R) for reversible, (QR) for quasi-reversible or (IR) for irreversible. Some measurements were previously made by M. Alkhalifah[57] as indicated by * to the left of the compound. All other measurements were made by the author of this thesis. The oxidation, reduction and ferocene peaks measurements were made with a precision of ± 0.01eV, which gives a precision of ±0.02eV for the measured HOMO/LUMO energy level. The absorption spectrum onset was measured with a precision of ± 2nm, which gives a precision of ±0.01eV for the measured energy gap. Where the absorption spectrum is used with the measured HOMO (LUMO) energy level to estimate the LUMO (HOMO) energy level the precision is ± 0.03eV. However, the systematic errors are expected to be significantly higher so that absolute values for the IP and EA are unreliable. For example, the absorption spectrum was measured in solid state, as a thin film, whilst the CV measurements were carried out in solution. As previously discussed there are also different electrode materials which can be used. Whilst calibration using the standard ferocene value is intended to compensate for this, it does present a further potential source for error.
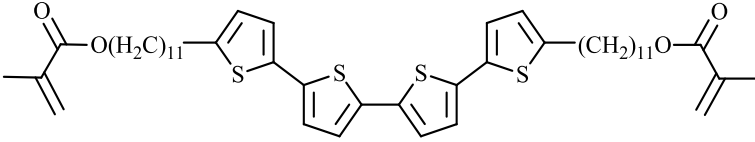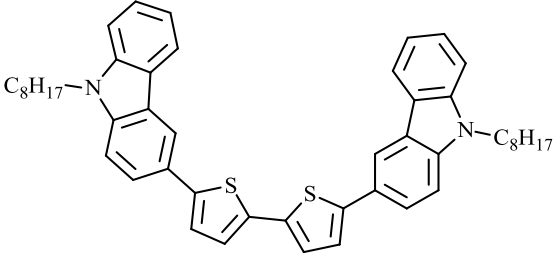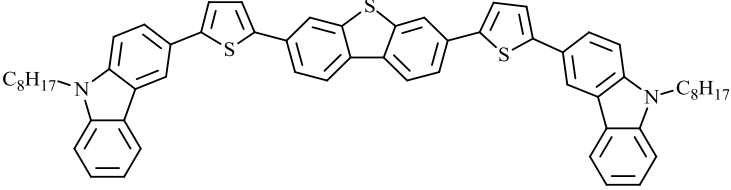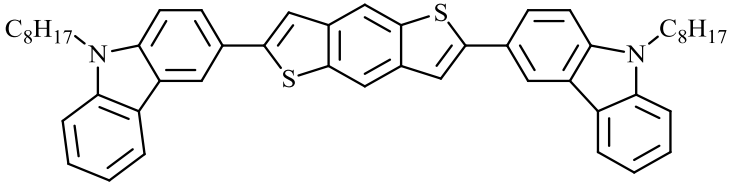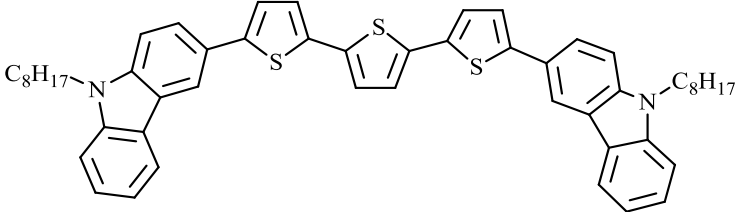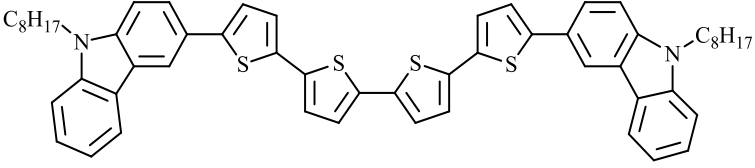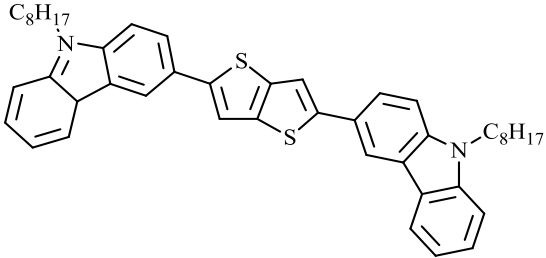
The absorption spectrum can vary due to a difference in background levels, although the impact of this is reduced as we measure the onset rather than the peak. Overall, relative measurements are reliable when measuring trends.
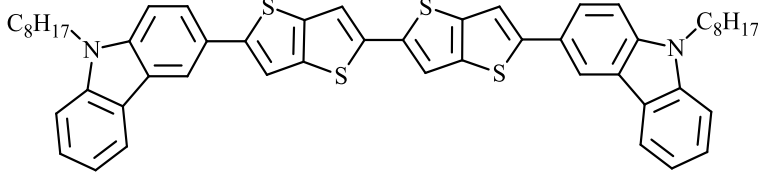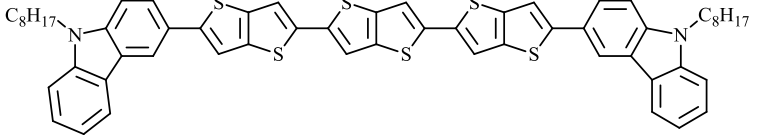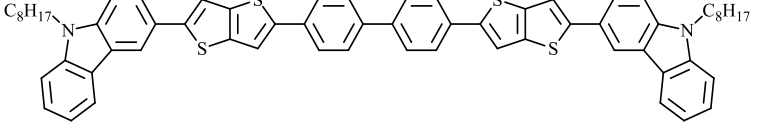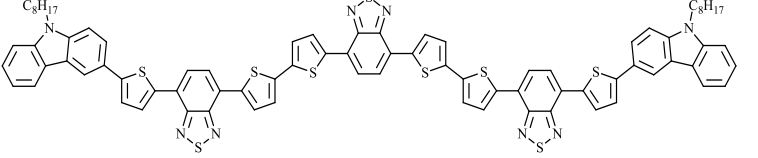
**Table 4.1 - Compounds studied in this thesis with illustrations of molecular structure, ionisation potential IP, electron affinity EA, optical energy gap and electrical energy gap. Prefix $^O$ means oxidation reaction, $^R$ reduction reaction, R means reversible reaction, QR quasi reversible reaction and IR means irreversible reaction. The Hull compound name is also given.**

| Mat. | Structure | Energy Levels (±0.03eV) |
|------|-----------|-------------------------|
| 1 |  **Tg 80 Cr-N 218 I** | **IP  EA  $E_{g,op}$ (eV)** <br><br> $^O$ **5.52 , 3.15, 2.37 (R)** <br><br> **SPK516** |
| 2 |  | **IP  EA  $E_{g,op}$ (eV)** <br><br> $^O$ **5.52 , 3.11, 2.41 (R)** <br><br> **SPK620** |
| 3* |  **Tg 94, Cr 180 N 303 I** | **IP  EA  $E_{g,op}$ (eV)** <br><br> $^O$ **5.53 , 3.1 , 2.43 (R)** <br><br> **SPK523** |
| 4* |  **MP 274 glass** | **IP  EA  $E_{g,op}$ (eV)** <br><br> $^R$ **6.31, 4.19, 2.12 (QR)** <br><br> **MPA340** |

| | | |
|---|---|---|
| 5* | <br>**Tg 25, Cr-N 187 I** | **IP  EA  E$_{g,op}$** (eV)<br><br>$^O$ 5.52 , 3.15 , 2.37 (R)<br><br>**PV318** |
| 6* | <br>**Tg 0, Cr 53 N 143 I** | **IP  EA  E$_{g,op}$** (eV)<br><br>$^O$ 5.5 , 3.07 , 2.43 (IR)<br><br>**PV237** |
| 7* | <br>**Cr 285 N >300 I** | **IP  EA  E$_{g,op}$** (eV)<br><br>$^O$ 5.89 , 3.77, 2.12 (R)<br><br>$^R$ 6.37 , 4.25 , 2.12 (R)<br><br>**E$_{g,ec}$ 1.64**<br><br>**SPK309** |
| 8 | <br>Chemical Formula: C$_{85}$H$_{96}$N$_2$S$_4$<br>Exact Mass: 1272.65<br>Molecular Weight: 1273.95<br>Elemental Analysis: C, 80.14; H, 7.60; N, 2.20; S, 10.07 | **IP  EA  E$_{g,op}$** (eV)  $^O$<br><br>5.38 , 2.93, 2.45  (R)<br><br>**SK433** |
| 9 | <br>Chemical Formula: C$_{77}$H$_{92}$N$_2$S$_2$<br>Exact Mass: 1108.67<br>Molecular Weight: 1109.70<br>Elemental Analysis: C, 83.34; H, 8.36; N, 2.52; S, 5.78 | **IP  EA  E$_{g,op}$** (eV)<br><br>$^O$ 5.50 , 3.21 , 2.29 (R)<br><br>**SK435** |

154

| | | |
|---|---|---|
| 10 |  | **IP   EA   E$_{g,op}$** (eV) [O] <br><br> 5.31 , 3.52 , 1.79  (R) <br><br> [R] 5.42 , 3.63, 1.79  (R) <br><br> E$_{g,ec}$ **1.68** <br><br> **SK451** |
| 11 |  | **IP   EA   E$_{g,op}$** (eV) <br><br> [O] 5.25 , 3.48 , 1.77 (IR)    [R] <br><br> 5.34 , 3.57 , 1.77 (R) <br><br> E$_{g,ec}$ **1.68** <br><br> **SK452** |
| 12 |  | **IP   EA   E$_{g,op}$** (eV) <br><br> [O] 5.89, 3.51 , 2.38 (QR) <br><br> **SPK411** |
| 13 | SPK536 <br>  | **IP   EA   E$_{g,op}$** (eV) <br><br> [R] 6.34 , 4.21 , 2.13 (R) <br><br> **SPK536** |
| 14 |  | **IP   EA   E$_{g,op}$** (eV) <br><br> [O] 5.58  2.83  2.75  (R) <br><br> **SK407** |
| 15 |  | **IP   EA   E$_{g,op}$** (eV) <br><br> [O] 5.44 , 3.12 , 2.32 (R) <br><br> **SK415** |
| 16 |  | **IP   EA   E$_{g,op}$** (eV) [O] <br><br> 5.45 , 3.22 , 2.23 (QR) <br><br> **SK425** |

| 17 |  | **IP** **EA** **E$_{g,op}$** **(eV)** |
|----|----|----|
| | | $^o$ **5.47** **(R)** |
| | | **SK427** |
| 18 |  | **IP** **EA** **E$_{g,op}$** **(eV)** |
| | | $^o$ **5.30 , 3.27 , 2.03 (R)** |
| | | **SK441** |
| 19 |  | **IP** **EA** **E$_{g,op}$** **(eV)** |
| | | $^o$ **5.69** **(R)** |
| | | **SK443** |
| 20 |  | **IP** **EA** **E$_{g,op}$** **(eV)** |
| | | $^o$ **5.41 , 3.31 , 2.10 (R)** |
| | | **SK446** |
| 21 |  | **IP** **EA** **E$_{g,op}$** **(eV)** |
| | | $^o$ **5.28 , 3.15 , 2.13 (R)** |
| | | **SK449** |
| 22 |  | **IP** **EA** **E$_{g,op}$** **(eV)** |
| | | $^o$ **5.27** **(R)** |
| | | **SK459** |
| 23 |  | **IP** **EA** **E$_{g,op}$** **(eV)** |
| | | $^o$ **5.31** **(R)** |
| | | **SK460** |

| 24 |  | **IP** **EA** **E<sub>g,op</sub> (eV)** |
|----|----|----|

| # | Structure | Data |
|---|-----------|------|
| 24 |  | **IP** **EA** **$E_{g,op}$ (eV)**<br>**$^O$ 5.31** **(R)**<br>**SK465** |
| 25 |  | **IP** **EA** **$E_{g,op}$ (eV)**<br>**$^O$ 5.27** **(R)**<br>**SK470** |
| 26 |  | **IP** **EA** **$E_{g,op}$ (eV)**<br>**$^O$ 5.40** **(R)**<br>**SK472** |
| 27 |  | **IP** **EA** **$E_{g,op}$ (eV)**<br>**$^O$ 5.21** **(IR)**<br>**$^R$ 3.57** **(R)**<br>**$E_{g,ec}$ 1.64**<br>**SK473** |

\* Indicates that experimental measurements were made by Dr. M. Alkhalifah.

We now discuss the materials separated into groups based on their chemical structures. The influence of chemical structure on energy levels can be thus be investigated. We will then evaluate some potential donor/acceptor pairs for use in photovoltaic devices, based on their respective energy levels.

## 4.2 Fluorene Structures with Thiophene and Phenyl groups

As explained in section 3.1, three cyclic voltammetry measurements were taken for each experiment. Figure 4.1 shows the three CV waves starting with an electrolyte only solution, with compound **1** and ferocene added sequentially. The desired flat current response is seen for the electrolyte only solution, which confirms the cell is not contaminated. Compound **1** shows a reversible oxidation reaction, as the difference between the first set of oxidation peaks is within 80mV meeting the condition described in section 2.13. The second and third set of oxidation peaks shown for **1** relate to further oxidation states, but it is only the first peak onset which is used to calculate the value for the IP. Clear oxidation peaks are also seen for the ferocene when added for calibration, alongside the oxidation peaks for **1**.

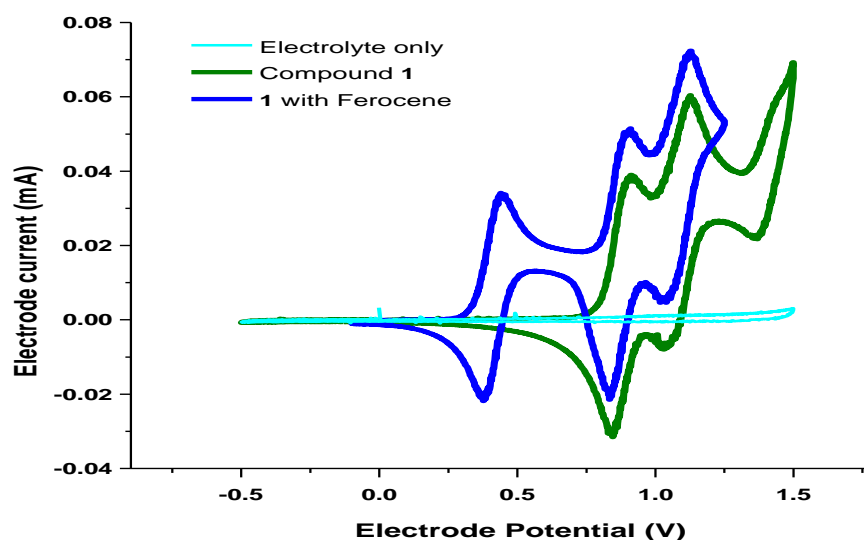

**Figure 4.1 – CV Waves for compound 1, showing the 3 measurement steps**

Figure 4.2 shows the oxidation onset from the CV wave (left) and the onset of absorption (right) for compound **1**. This enabled values to be calculated for the HOMO

and the energy gap respectively, from which a value for the LUMO could be subsequently determined.
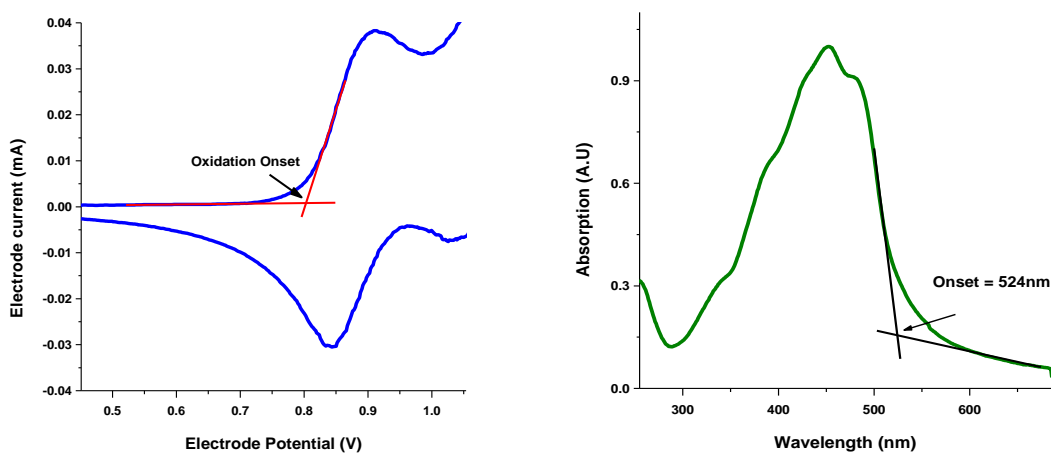


**Figure 4.2 – Oxidation onset (left) and absorption onset (right) for compound 1.**

Compound **3** and **14** were measured similarly, each producing a reversible oxidation reaction. Figure 4.3 and table 4.2 show the structure of **1**, **3** and **14** where $R_1$ is the aliphatic end group, which does not affect the HOMO/LUMO energy levels. **R** is given in table 4.2 for each compound along with the measured energy levels.

Thiophenes are an important active group in organic semiconductors and have been shown to be one of the most environmentally and thermally stable materials[75,185,186,187,188]. Table 4.2 shows that the fusing the bithiophene group does not affect the IP, which is the same for **1** and **3** within error limits. The complete removal of the bithiophene groups in **14** leads to an increase of more than 0.3eV in the energy band gap and a 0.27eV reduction in the EA. This is in agreement with the work of Lim et al[189]. Liedtke et al[190] recently showed that the atomic transition densities for compound **1** are delocalised over the backbone with a higher concentration on the thiophene groups within the central 6 ring unit, as shown in figure 4.4. It is clear from figure 4.4 that the absence of the central electron rich thiophenes will have a significant impact on the energy levels, as this is where the atomic transitions are most concentrated.
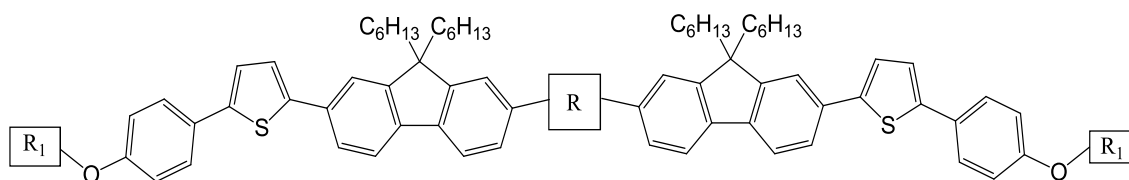
**Figure 4.3 – Shared chemical structure of 1, 3 and 14. R is given in table 4.2 and R$_1$ is the aliphatic end group.**

**Table 4.2 – Chemical structure of R and measured energy levels for 1, 3 and 14.**

| Compound | R Structure | IP (eV) | EA (eV) | E$_{g,op}$ (eV) |
|---|---|---|---|---|
| 1 |  | 5.52 | 3.15 | 2.37 |
| 3 |  | 5.53 | 3.10 | 2.43 |
| 14 |  | 5.58 | 2.83 | 2.75 |
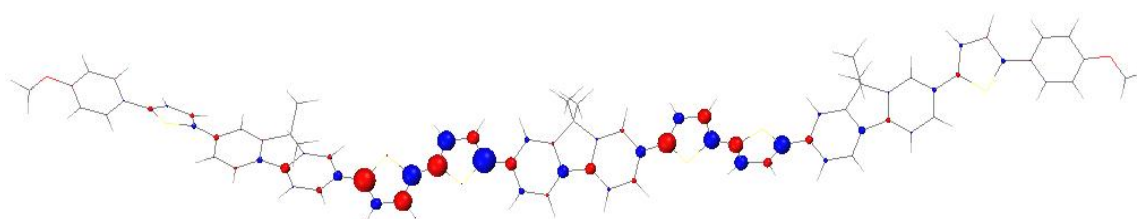


**Figure 4.4 – Atomic transition densities associated with the lowest absorption band for compound 1. The size and colour of the spheres represent the sign and amplitude of the atomic transition desnsities[190].**

Figure 4.5 shows a reversible oxidation reaction for **15** and an electrochemically quasi reversible reaction for **16**. The potential difference between the anodic and cathodic current peaks was 117mV, which exceeds the maximum difference to be considered reversible, as discussed in section 2.13.

160
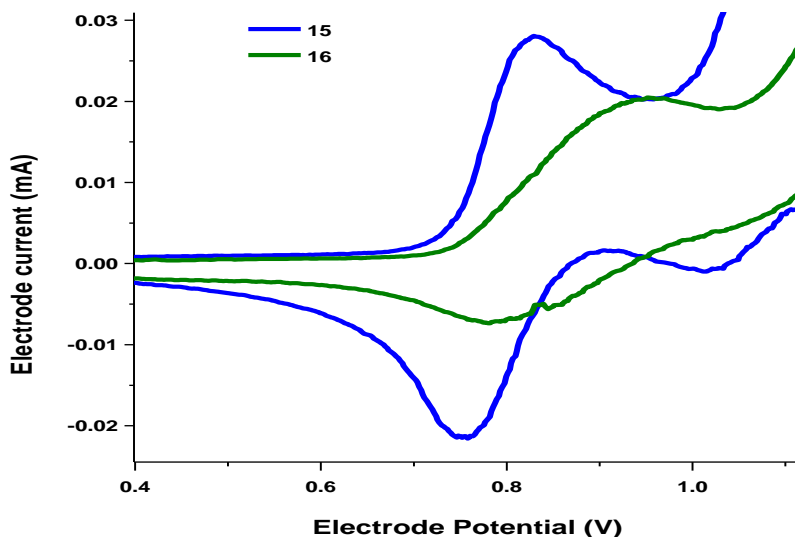
**Figure 4.5 – Oxidation peaks showing reversible and quasi-reversible reaction for compounds 15 and 16 respectively.**

There is still some overlap of the oxidation peaks for **16** on the potential axis so this is not classed as a totally irreversible reaction. Figure 4.6 shows the shared structure of **1**, **2, 6, 8, 15** and **16**, with the structure of **R** given in table 4.3 along with the measured energy levels. All compounds produced reversible oxidation reactions, except for **16** as described above.

Table 4.3 shows that there is no significant change in the measured energy levels between **1** and **2**. This indicates that the central shared structure determines the energy levels for these compounds, as discussed earlier. However, a comparison of **6**, **15** and **16** shows that changes in the outer structure can have a small effect on the energy levels. Here the addition of a thiophene from **6** to **15** leads to reductions in the IP of 0.06eV and an increase in the EA of 0.05eV. The substitution of a phenoxy for a thiophene from **6** to **16** leads to an increase of 0.15eV in the EA and a small reduction of the IP.
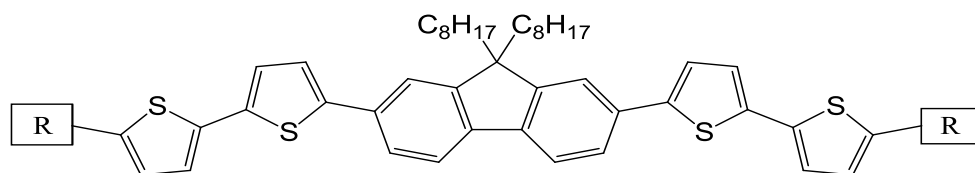
**Figure 4.6 – Shared chemical structure for 1, 2, 6, 8, 15, and 16. R is given in table 4.3 and R₁ is the aliphatic end group.**

**Table 4.3 – Variation in R structure and measured energy levels for 1, 2, 6, 8, 15 and 16.**

| Compound | R Structure | IP (eV) | EA (eV) | $E_{g,op}$ (eV) |
|---|---|---|---|---|
| 1 |  | 5.52 | 3.15 | 2.37 |
| 2 |  | 5.52 | 3.11 | 2.41 |
| 6 |  | 5.50 | 3.07 | 2.43 |
| 15 |  | 5.44 | 3.12 | 2.32 |
| 16 |  | 5.45 | 3.22 | 2.23 |
| 8 |  | 5.38 | 2.93 | 2.45 |

162

Replacing a phenoxy with a carbazole group from **6** to **8** leads to a reduction in the IP and the energy band gap of 0.12eV and 0.14eV respectively. Replacing thiophene with carbazole from **16** to **8** leads to a reduction in the EA of 0.29eV and an increase in the energy band gap of 0.22eV.

The lowest IP and EA values are found when **R** is carbazole as a result of its electron withdrawing nature[75]. The nitrogen atom in carbazole lowers the oxidation potential and hence raises the HOMO energy level[191]. Furthermore, the nitrogen atom also changes the reactivity of the positions around the benzene rings. Compared to fluorene, the addition of a nitrogen bridge to form carbazole changes the favoured sites for electrophilic substitution from the 2- and 7- positions to the 3- and 6- positions[191]. It was recently shown by Kato et al[192] that changing the position of thiophene substituents of a carbazole moiety from 2- and -7 to 3- and 6- raised the HOMO and the LUMO energy levels. This was attributed to an enhancement of the electron-donating ability of the carbazole moiety by the increased influence of the electron-rich thiophene groups.

## 4.3 Fluorene Vs Benzothiadiazole Core

Here we investigate the effect of using a benzothiadiazole centre group and compare to fluorene. Three of the materials here, **10**, **11** and **27** produced both oxidation and reduction reactions. The absorption spectrum, as shown previously, provides a value for the optical band gap whilst the difference between the oxidation and reduction provides a value for the electrical energy gap. The reduction reactions for **10**, **11** and **27** were all reversible, whilst the oxidation reactions were reversible for **10** and irreversible for **11** and **27**.
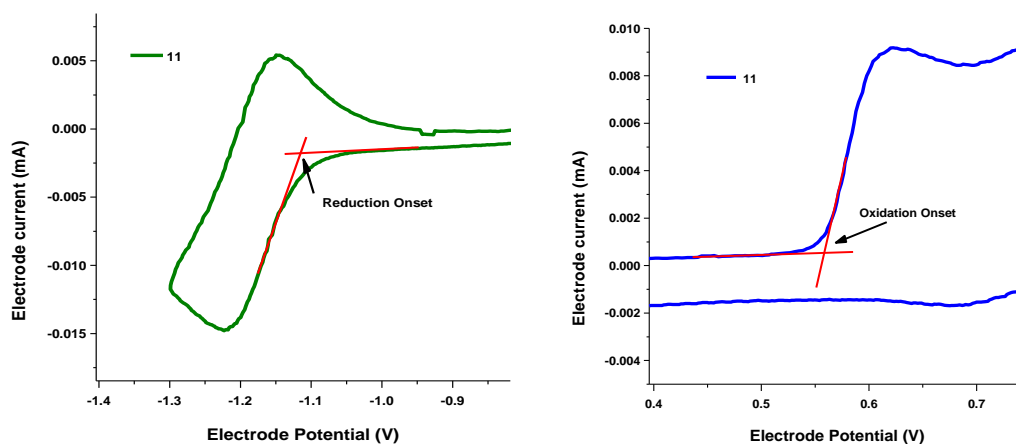
**Figure 4.7 – Reversible reduction reaction (left) and Irreversible oxidation reaction (right) for compound 11.**

Figure 4.7 shows a reversible reduction reaction (left) and an irreversible oxidation reaction (right) for compound **11**. The anodic current peak for the oxidation reaction does not have a corresponding cathodic current peak overlapping on the potential axis and therefore signals a totally irreversible reaction. **10** produced reversible reactions for both oxidation and reduction, suggesting that the addition of the electron-rich thiophene pair in **11** may have contributed to the irreversible oxidation. Li et al[193] recently reported that an increase in the electron-donating ability of copolymers caused irreversible oxidation reactions, which agrees with our findings here.

Figure 4.8 shows the shared carbazole outer group of the materials studied in this section, with the chemical structure and measured energy levels show in table 4.4.
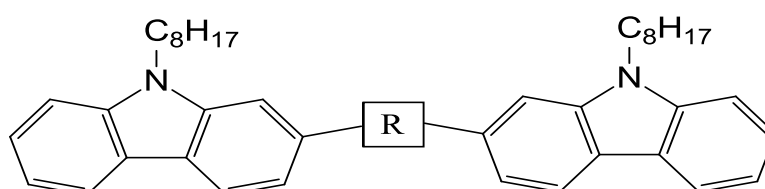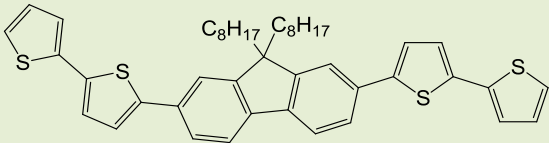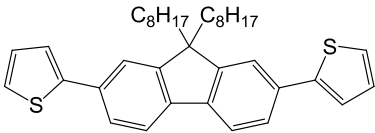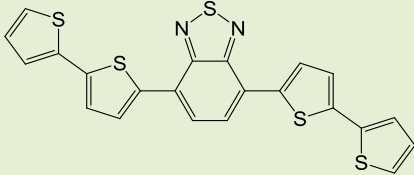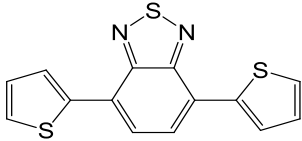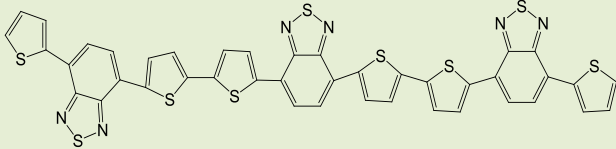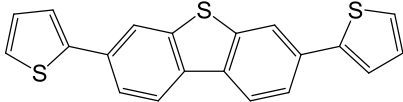


**Figure 4.8 – Shared chemical structure for 8-11, 19 and 27. R is given in table 4.6**

**Table 4.4 – Variation in R structure and measured energy levels for 8-11, 19 and 27.**
**Measurements made using the reduction reaction are shown in brackets.**

| Compound | R Structure | IP (eV) | EA (eV) | $E_{g,op}$ (eV) |
|---|---|---|---|---|
| 8 | | 5.38 | 2.93 | 2.45 |
| 9 | | 5.50 | 3.21 | 2.29 |
| 11 | | 5.25 (5.34) | 3.48 (3.57) | 1.77 — 1.77 $E_{g,ec}$ 1.68 |
| 10 | | 5.31 (5.42) | 3.52 (3.63) | 1.79 — 1.79 $E_{g,ec}$ 1.68 |
| 27 | | 5.21 | (3.57) | $E_{g,ec}$ 1.64 |
| 19 | | 5.69 | | |

The removal of an electron-rich thiophene from each end of the central group from **8** to **9** leads to an increase of 0.12eV in the IP and an increase of 0.28eV in the EA, giving an reduction in the optical energy band gap of 0.16eV. However, the removal of a thiophene from **11** to **10** has far less influence on the energy levels. This suggests that the atomic transitions may be more concentrated within the central benzothiadiazole group of **11** compared to the central fluorene group of **8**.

The substitution of the central fluorene group for an electron-accepting benzothiadiazole group is shown to have a significant impact on the energy levels. Comparing **8** to **11** there is a reduction in the IP of 0.19eV and a large increase in the EA of 0.55eV. The combined effect leads to an optical energy band gap reduction of 0.68eV, to create a low band gap donor. This is attributed to the electron-accepting benzothiadiazole centre group, which agrees with several recent studies [75,194,195,196]. Comparing **11** to **27** there is very little change in the measured IP and EA. This suggests that the atomic transitions are still concentrated within the central 6 ring unit for the benzothiadiazole core molecules.
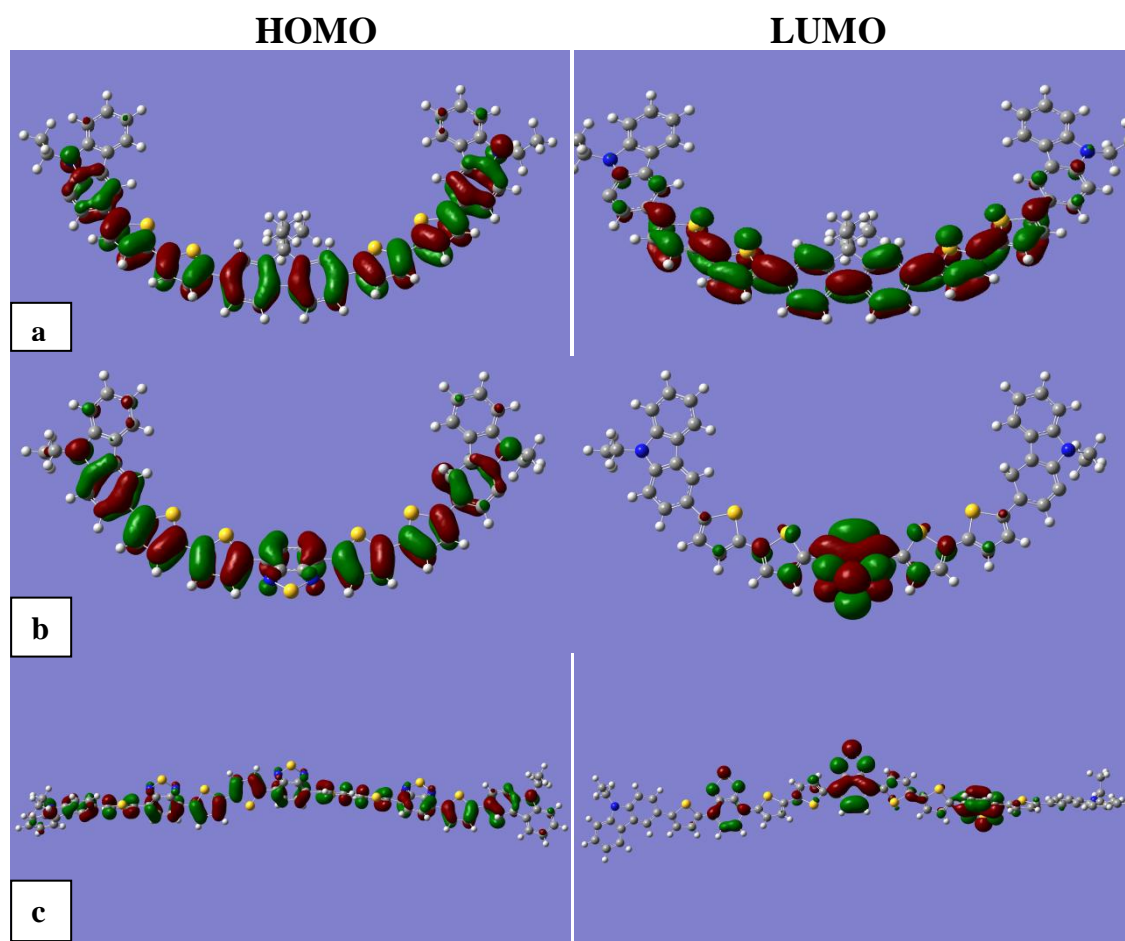


**Figure 4.9 - Molecular orbital contour plot for compounds (a) 8, (b) 11 and (c) 27. The HOMO is shown on the left and the LUMO on the right. Images were produced by Dr M. Wright at the University of Hull.**

Figure 4.9(a) shows that for compound **8** both the HOMO and LUMO are delocalised along the backbone. The HOMO extends into the outer carbazole group whilst the LUMO is concentrated within the central 6 ring unit. The change from fluorene to benzothiadiazole, from **8** to **11**, creates a donor/acceptor molecule which produces both reduction and oxidation reactions. This agrees with the work by Li et al[193]. Figure 4.9 (b) shows that for **11** the HOMO is delocalised over the backbone, similar to **8**. However, the LUMO is now concentrated within the benzothiadiazole core. The oxidation takes place on the electron rich thiophene groups along the backbone (donor) whilst reduction occurs on the central benzothiadiazole group (acceptor). Figure 4.9 (c) shows that for **27** the LUMO is concentrated on the three benzothiadiazole groups, whilst the HOMO is once again delocalised across the backbone.

Figure 4.10 illustrates the different energy levels for **10**, **11** and **27**, measured from oxidation and reduction of the donor and acceptor part of the molecule respectively. There is reasonable agreement between $E_{g,op}$ and $E_{g,ec}$.
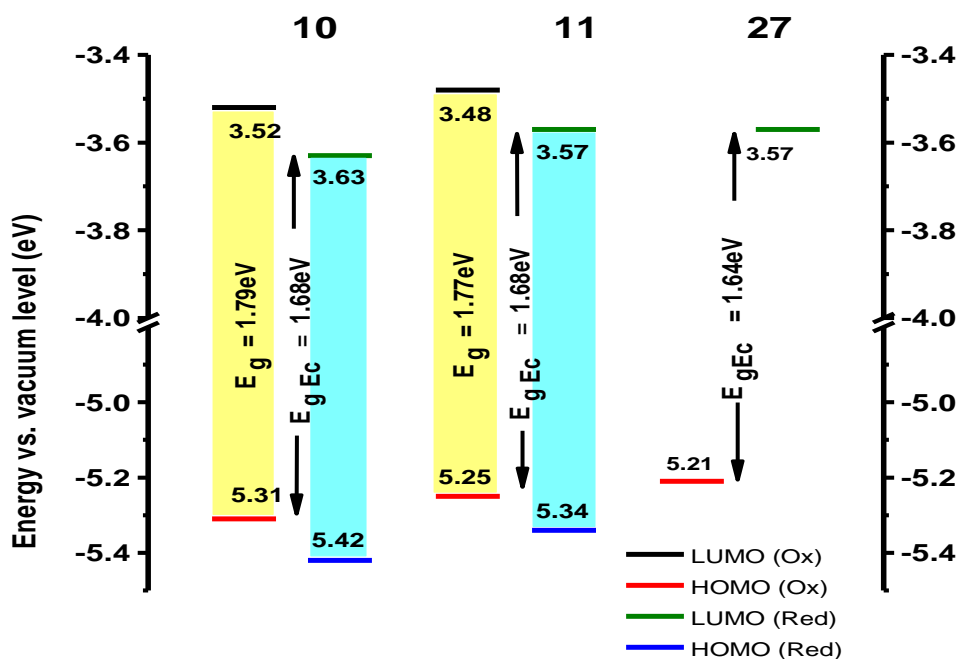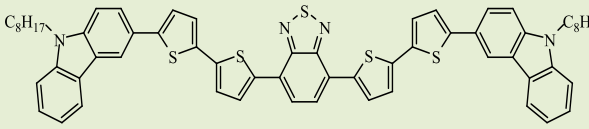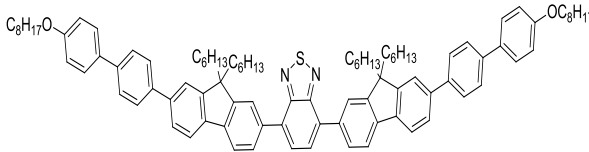


**Figure 4.10 – HOMO and LUMO energy levels for compounds 10, 11 and 27 measured from oxidation and reduction. Absorption onset is also used for 10 and 11 to highlight the two different energy gaps.**

Table 4.5 shows the structures and measured energy levels for **11** and **12**. Here we see that the lack of thiophenes within the central 6 unit core in **12** has led to a large increase in the IP and the energy band gap. This shows the influence of the electron-rich thiophene group in raising the HOMO energy level.

**Table 4.5 – Variation in chemical structure and measured energy levels for 11 and 12.**

| Compound | Structure | IP (eV) | EA (eV) | $E_{g,op}$ (eV) |
|---|---|---|---|---|
| **11** |  | 5.25 | 3.48 | 1.77 |
| **12** |  | 5.89 | 3.51 | 2.38 |

## 4.4 Perylene Bisimide with Fluorene Structures

Compounds **4**, **7** and **13** all have an electron accepting perylene bisimide central group, which is known to be an efficient electron acceptor. Perylene based materials have been shown to be air stable and can have high mobility values[197]. **7** and **13** produced reversible reduction reactions as shown in figure 4.11, whilst **4** produced a quasi-reversible reduction reaction. The shared perylene structure is shown in figure 4.12 with the structure of the **R** group and measured energy levels given in table 4.6.
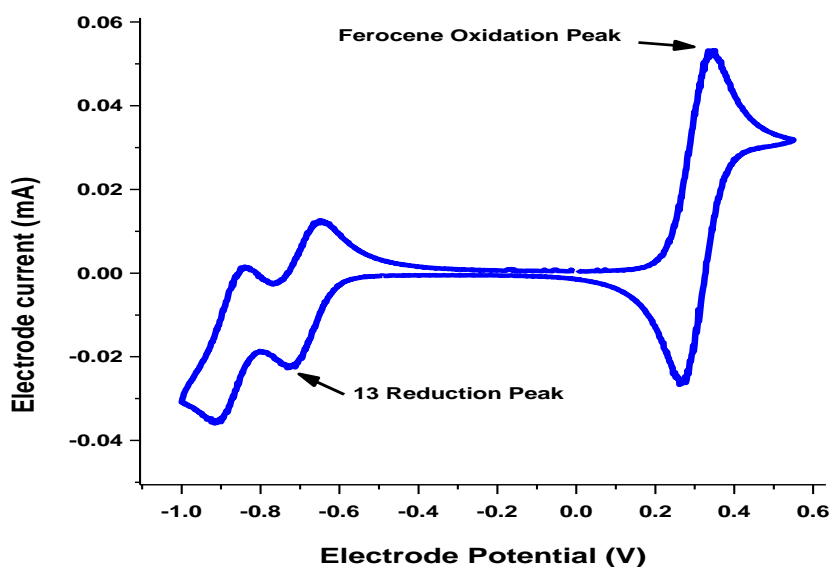


**Figure 4.11 – Reversible reduction reaction for compound 13  calibrated with ferocene oxidation.**
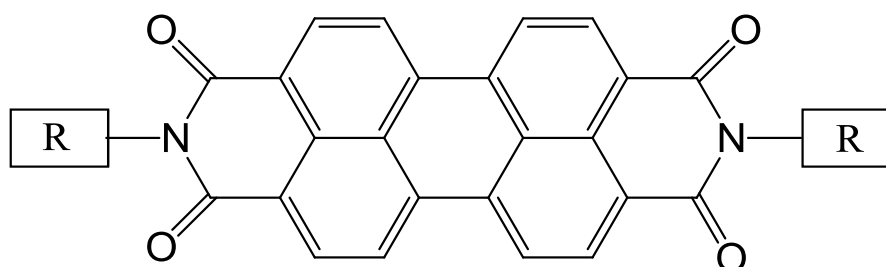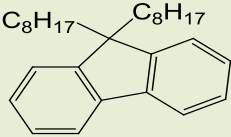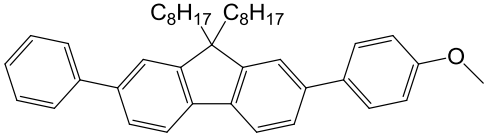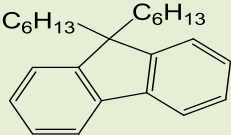


**Figure 4.12 – Shared chemical structure for 4, 7 and 13. R is given in table 4.8**

**Table 4.6 – Variation in R structure and measured energy levels for 4, 7 and 13. Measurements from reduction reaction are shown in brackets.**

| Compound | R Structure | IP (eV) | EA (eV) | $E_{g,op}$ (eV) |
|---|---|---|---|---|
| 4 | C$_8$H$_{17}$  C$_8$H$_{17}$ (fluorene structure) | (6.31) | (4.19) | 2.12 |
| 7 | C$_8$H$_{17}$  C$_8$H$_{17}$ (phenyl–fluorene–methoxyphenyl structure) | 5.89 (6.37) | 3.77 (4.25) | 2.12  2.12  $E_{g,ec}$ 1.64 |
| 13 | C$_6$H$_{13}$  C$_6$H$_{13}$ (fluorene structure) | (6.34) | (4.21) | 2.13 |

There is little variation in the LUMO energy of the 3 materials. This is because the reduction reaction takes place on the central perylene bisimide group common to all three compounds. Compound **7** produced an oxidation reaction in addition to the reduction, as shown for **10**, **11** and **27** earlier. The oxidation reaction takes place on the outer fluorene and phenyl groups, rather than on the perylene. Figure 4.13, produced by Alkhalifah[57], shows that the HOMO is localised on the fluorene and phenyl groups (a) and the LUMO is localised on the perylene bisimide core. Note that for **7** the HOMO measured via reduction and absorption is much lower than that directly measured by oxidation using CV. This is because the former method gives the 'HOMO' localised on the perylene moiety.
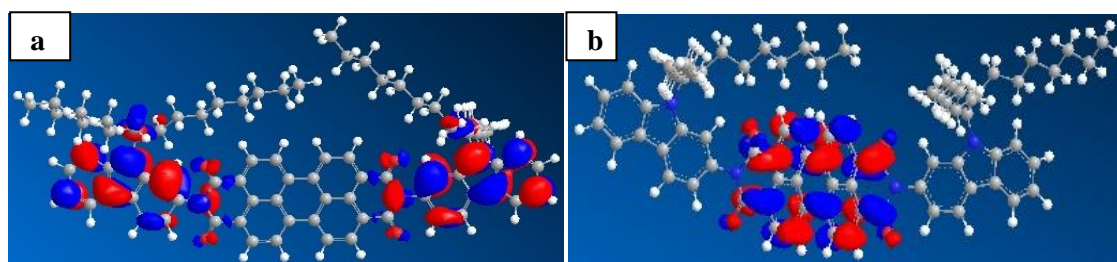


**Figure 4.13 – Molecular orbital contour plot for compound 7 (a) HOMO and (b) LUMO[57]**

# 4.5 Potential Donor/Acceptor Pairs

Figure 4.14 illustrates the energy levels of three donor/acceptor pairs which are used in as the active layer in photovoltaic devices, investigated in chapter 6. All three blends shown meet the main criteria discussed in section 2.11. As discussed earlier, the maximum open circuit voltage ($V_{oc}$) for a PV device is proportional to the difference between the donor HOMO energy level and the acceptor LUMO energy level. This value is highest for blend **1:4**, which means that this blend should have the highest potential $V_{oc}$.
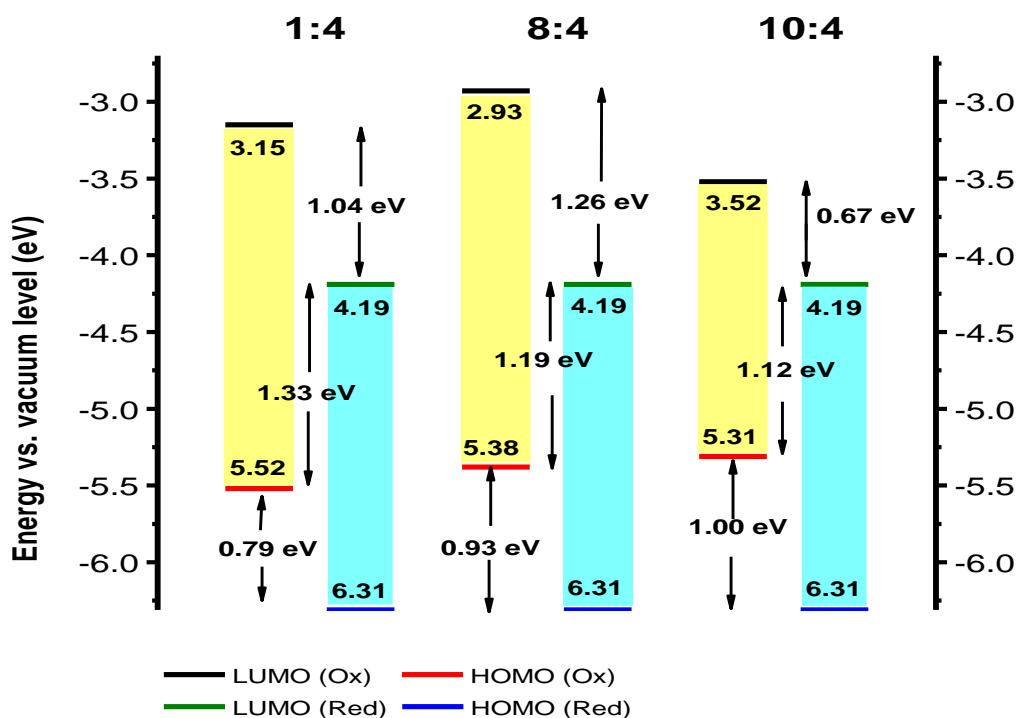


**Figure 4.14 – HOMO and LUMO energy levels for three potential donor/acceptor combinations.**

In order to achieve efficient charge separation within a donor/acceptor blend we need a certain offset between the HOMO energy levels ($\Delta E_{HOMO}$) and the LUMO energy levels ($\Delta E_{LUMO}$) of the two materials. Ideally these offsets needs to be 0.3eV for high device efficiency[6].

Figure 4.14 shows that the values for $\Delta E_{HOMO}$ and $\Delta E_{LUMO}$ are all larger than the ideal requirement of 0.3eV. It has been shown by Dennler et al[6] that as $\Delta E_{LUMO}$ increases above 0.3eV the PV device efficiency drops significantly, as shown earlier in figure 2.3. For the **1:4** blend around 50% of the optical energy is lost by relaxation. Ideally these energy offsets need to be reduced significantly. This could be achieved by synthesising donors with lowered energy levels and/or acceptors with raised energy levels. The absolute position of the HOMO and LUMO energy levels do not determine the maximum device efficiency, rather it is the energy offsets and energy band gap that are crucial.

Donor **12** has relatively low lying HOMO and LUMO energy levels, which would produce much lower energy offsets than the other donors when blended with **4**. A blend of **12**:**4** would have energy offsets of 0.42eV and 0.68eV for $\Delta E_{LUMO}$ and $\Delta E_{HOMO}$ respectively. However, despite these favourable energy offsets the PV device performance of this blend was very poor and is not included in chapter 6.

The minimum absorption energy is determined by the smaller optical band gap of the donor or acceptor. For the **1:4** and **8:4** blends this is the band gap of the acceptor material. However, for the **10:4** blend the donor has a smaller band gap. Donor **10** provides absorption across more of the visible spectrum than the other potential donors.
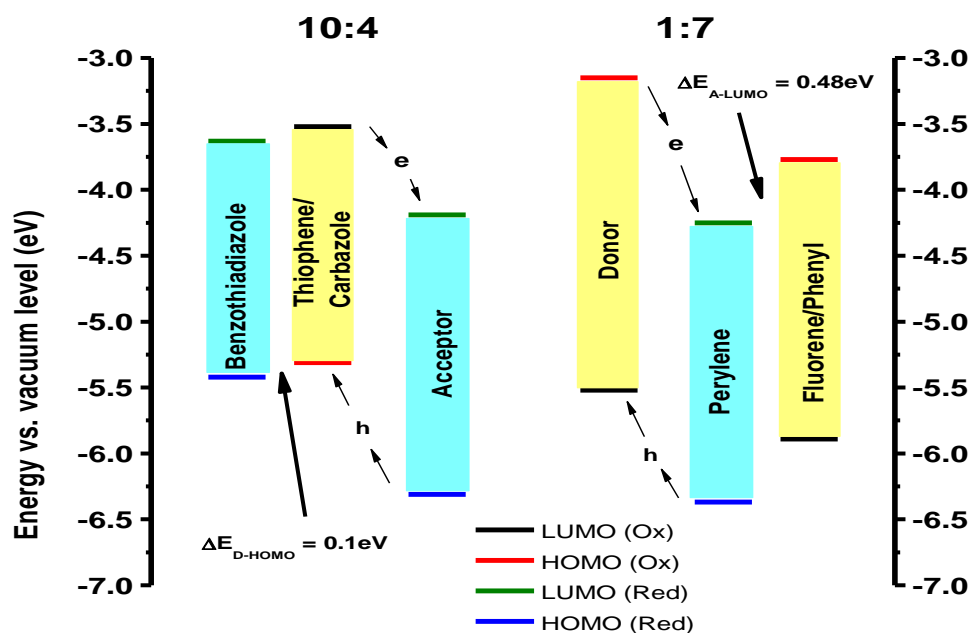
**Figure 4.15 – HOMO and LUMO energy levels for 10:4 and 1:7 blends. Energy levels for donor and acceptor components of compounds 10 and 7 are shown. The blue highlighted energy gaps relate to the LUMO measured via the reduction reaction using CV and the optical band gap from absorption. The yellow highlighted energy gap relates to the HOMO measured via the oxidation reaction using CV and the optical energy band gap.**

Figure 4.15 shows the energy levels for the **10**:**4** blend and **1**:**7** blend, which highlights

the donor/acceptor nature of **10** and **7**. The difference in energy between the HOMO

levels of the D/A components of **10** ($\Delta E_{D\text{-}HOMO}$) is small, 0.1eV, so hole transport could

take place along both parts of the molecule. Figure 4.9 (b) showed that the HOMO was

delocalised along the backbone of the molecule.

The energy difference between the LUMO levels of the D/A components of **7**

($\Delta E_{A\text{-}LUMO}$) is large, 0.48eV, which means that electron transport may be restricted to the

perylene core. Whilst no oxidation reaction was seen for compounds **4** and **13**, the side

fluorene groups may act as a donor component with similar energy levels to that of the

phenyl/fluorene groups of **7**. The outer fluorene and phenyl rings of the acceptors may

also act to shield the perylene core from the donor material and hence inhibit charge

separation.

# 4.6 Conclusion

A total of 27 organic compounds, synthesised within the chemistry department at Hull University, have been investigated. The oxidation (reduction) reactions recorded from cyclic voltammetry were used to estimate the HOMO (LUMO) of the material whilst the absorption onset measured using the spectrometer was used to estimate the optical energy band gap. It was shown that molecular changes within the central 6 ring unit of a molecule had the largest impact on energy levels. The influence on energy levels lessened with distance from the central unit, with changes in end groups not having any significant impact.

In general electron-rich thiophene groups raise the HOMO energy level. The effect on the LUMO level was different for carbazole based materials. The addition of phenyl groups was shown to lower the HOMO and/or raise the LUMO energy level, leading to an increased energy band gap. Carbazole was shown to raise the HOMO energy level and also raise the LUMO level in some cases.

The use of a benzothiadiazole centre group was shown to be the most significant molecular change studied as a large reduction in the energy band gap was seen. This was the result of the benzothiadiazole core raising the HOMO level and lowering the LUMO level. This group can therefore be used as a core for low band gap semiconductors.

The final group studied, based around perylene bisimide cores, was shown to have HOMO/LUMO values around 1eV higher on average than the other materials. The offsets were found to be far higher than that needed for charge separation, which causes loss of PV device efficiency. Electron transport is restricted to the perylene core, due to the much higher LUMO of the fluorene and phenyl outer groups. Modifications should be made to the outer donor component to lower the LUMO level to more closely match

that of the perylene. Based on our findings here, the substitution of the phenyl groups with thiophene may result in a lower LUMO level for the donor component. This would allow more efficient charge transport along the whole molecule, rather than restricting it to the perylene core. Alternatively the end groups could be left out, leaving just the perylene core.

The fluorene based compounds (**1**, **2**, **3, 5, 6**) with carbazole (**8**, **9**) and the benzothiadiazole/thiophene/carbazole structures (**10**, **11**) will all be used as donor materials with the perylene bisimide core materials (**4**, **7**) as acceptors in the subsequent chapters.

# 5. Investigation of Charge Mobility

## 5.1 The Effect of Molecular Structure on Charge Mobility
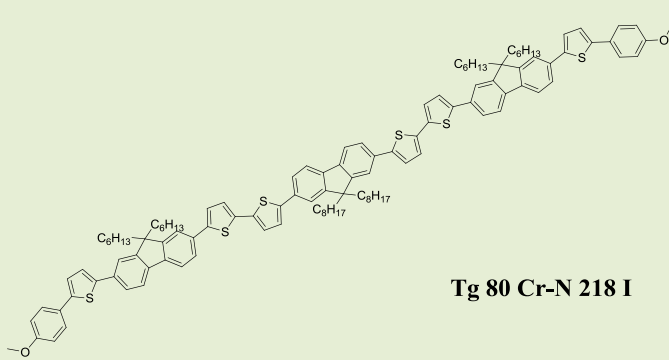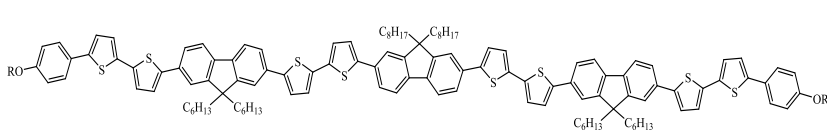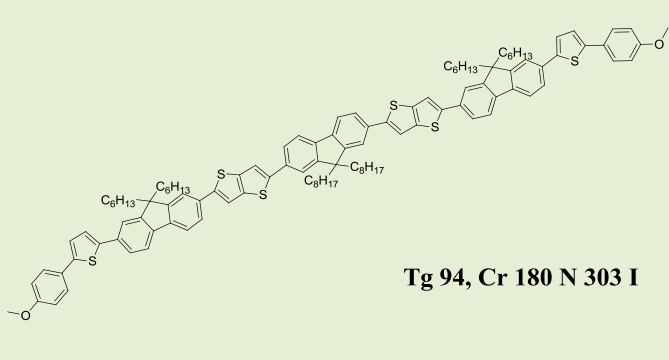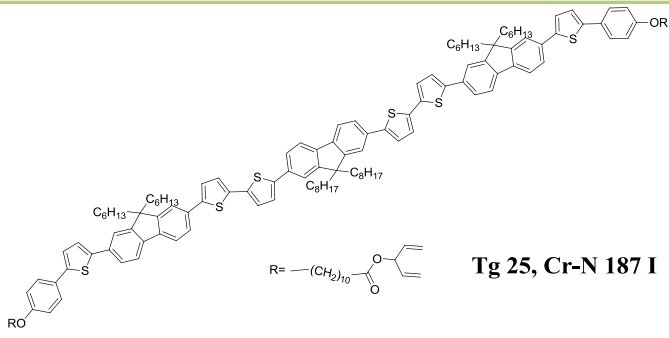
Here we investigate the mobility of four organic semiconductors which have been synthesised within the chemistry department at Hull University. All 4 materials have been used as electron donors to fabricate bulk heterojunction photovoltaic devices. These donors are labelled as compounds **1**, **2**, **3** and **5** and their molecular structures are shown in table 5.1. **5** has the same aromatic core as **1** but has a photo-reactive end groups, which enable photochemical polymerisation. We investigate how small changes to the molecular structure impact on the charge carrier mobility.

The TOF films for **2** and **3** were prepared as described in section 3.3 using 20mg of material with 0.2ml of chlorobenzene and evaporation times of 25 and 30 minutes respectively. The film thickness was measured using the WYKO, for **2** this was $956 \pm 24$nm and $994 \pm 54$nm around the left and right electrodes respectively. The thickness of **3** was $760 \pm 28$nm around the right electrode (no results were obtained from the left electrode for this material). The laser fluence incident on the samples was $350 \ \mu Jcm^{-2}$ /pulse and all measurements were made with the samples at room temperature, 25°C. Current transients obtained from **2** are shown in figure 5.1 for both electrons (a) and holes (b), the transient time was determined as discussed in section 2.2.4.

As can be seen in figure 5.1, the hole transit time is far clearer than that for the electron charge carriers. Transit time measurements were made for a range of applied electric fields, but at higher fields (above $4 \times 10^{-5} \ Vcm^{-1}$) the electron transit time became unclear and could not be determined accurately. Hence only hole data was available at higher fields. Figure 5.1 also shows that the measured hole current is around ten times

that shown for electrons, which indicates significantly greater trapping of electrons compared to holes.

**Table 5.1 – Chemical structures for compounds 1, 2, 3 and 5**

| Compound | Structure |
|---|---|
| 1 |  **Tg 80 Cr-N 218 I** |
| 2 |  |
| 3 |  **Tg 94, Cr 180 N 303 I** |
| 5 |  **Tg 25, Cr-N 187 I** |

**Figure 5.1 – Current transient for compound 2 showing charge carrier transit time for electrons (a) and holes (b) at an applied electric field of 3.02 x 10$^{-5}$ Vcm$^{-1}$.**
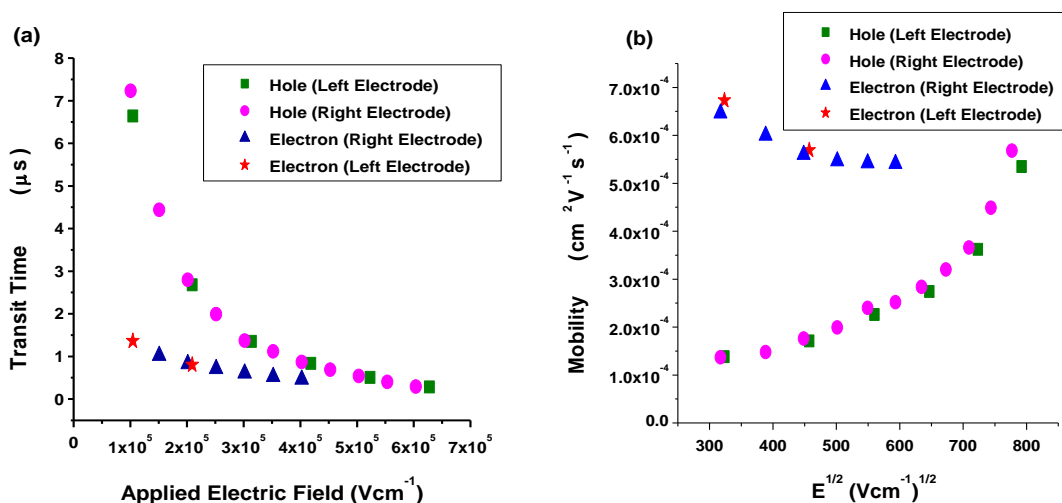


**Figure 5.2 – Transit times (a) and mobility's (b) for electrons and holes in compound 2.**

Figure 5.2 (a) shows how the transit times for both electrons and holes reduce as the applied electric field is increased. This reduction is far greater for the holes, which seem to 'catch up' with the electron transit times at higher fields. Figure 5.2 (b) shows the mobility values as a function of the square root of the applied electric field. It can be seen that whilst the hole mobility increases with applied electric field, the electron mobility shows the opposite relation and decreases as the applied field goes up.

The negative field dependence of the electrons, which initially seems counter-intuitive, is explained by the Gaussian Disorder Model[118]. This occurs when the charge carriers follow a looped route, as illustrated earlier in figure 2.22, which entails some hopping against the applied electric field during transit, creating higher activation barriers as the field increases.

Current transients obtained from **3** are shown in figure 5.3 for electrons (a) and holes (b), with the transient time determined as discussed in section 2.2.4.
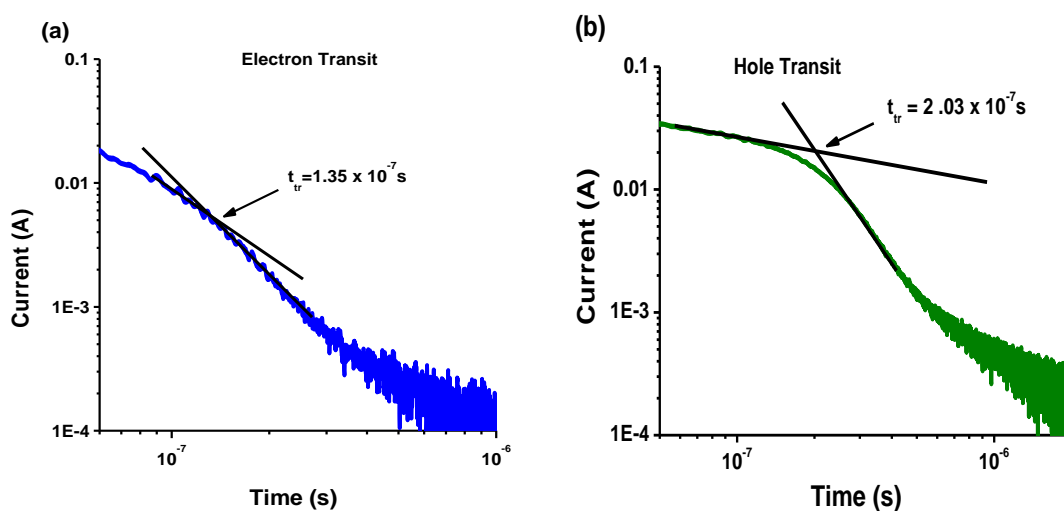


**Figure 5.3 – Current transient for compound 3 showing charge carrier transit time for electrons (a) and holes (b) at an applied electric field of 3.95 x 10$^{-5}$ Vcm$^{-1}$.**

Similarly to **2** the hole transit time for **3** is much clearer than that for the electrons, as can be seen in figure 5.3. However, on this occasion the transients remained clear enough to provide electron transit times at the highest applied electric field used here. It is also shown that the electron and hole currents for **3** are approximately equivalent to each other, and around the same magnitude as the hole current for **2**. This indicates far less electron trapping in **3** relative to **2**, although the current transients suggest more dispersive transport for electrons compared to holes in both donor materials[134].
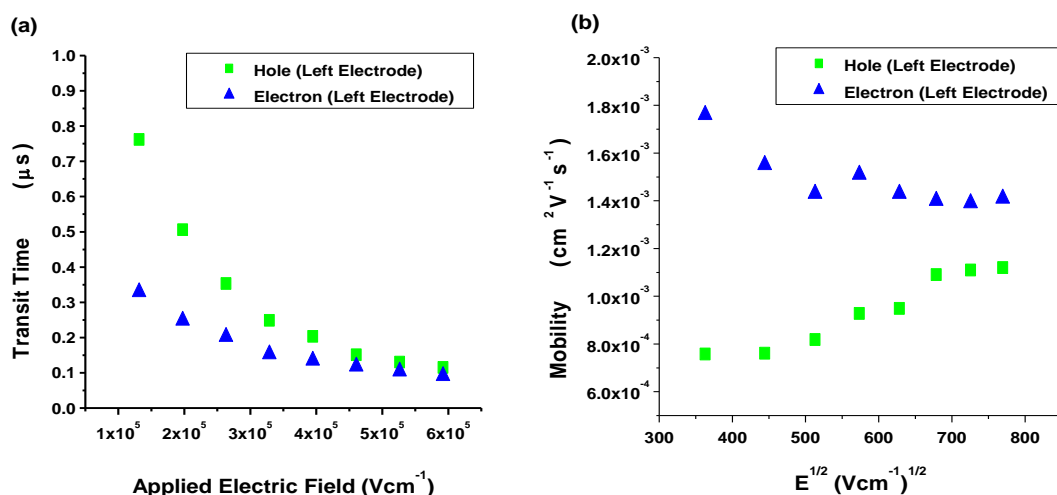
**Figure 5.4 – Transit times (a) and mobility's (b) for electrons and holes in compound 3.**

Figure 5.4 (a) again shows a similar response for **3** as that seen for **2**, with the charge transit times for holes and electrons reducing as the applied electric field strength is increased. Figure 5.4 (b) shows that the mobility increase for holes and reduces for electrons as the field is increased. At higher fields ($> 4 \times 10^5$ Vcm$^{-1}$) the mobility values for both charge carriers seem to level off, at which point hole and electron mobility values are closer together.

Figure 5.5 shows the mobility values of all 4 donor materials, **2** and **3** were measured as discussed above by me, whilst **1** and **5** were previously measured by Alkhalifah[57]. It can be seen that all donors show a positive relationship between hole mobility and applied electric field. The electron mobility, when measurable, shows a negative field dependence which occurs when the charge carriers follow a looped route as discussed earlier. Calculated values for the mobility, using equations 2.33 and 2.34, have been included in figure 5.5 for comparison where we use a value of $\Sigma = 2.5$ for the positional disorder parameter. The energetic disorder parameter is varied using $\sigma = 0.1$eV and 0.02eV for T1 and T2 respectively, so that we have greater energetic disorder for T1 and greater positional disorder for T2.
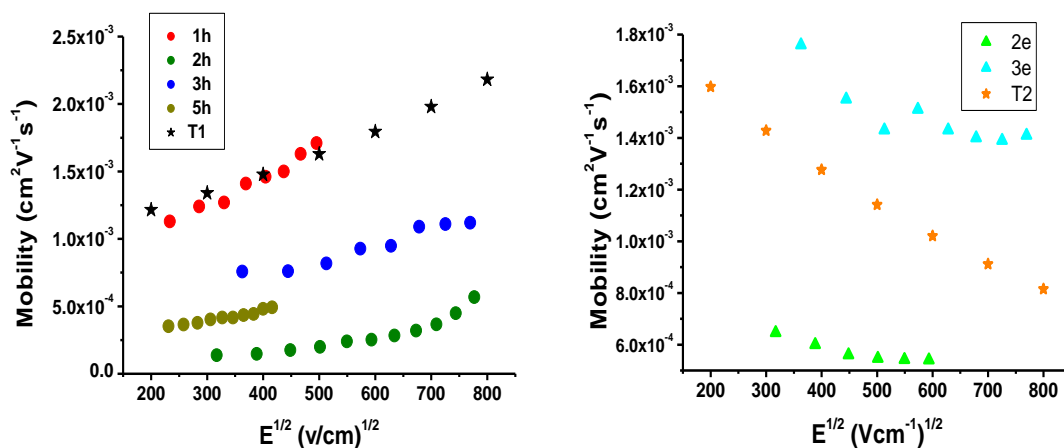
**Figure 5.5 – Mobility measurements for electrons and holes for donors 1, 2, 3 and 5. The compound no. and charge type, (h) hole and (e) electron, are shown inset. Theoretical mobilities have been calculated for $\left(\frac{\sigma}{k_BT}\right)^2 > \Sigma^2$ (T1) and $\left(\frac{\sigma}{k_BT}\right)^2 < \Sigma^2$ (T2).**

Figure 5.5 shows that the mobility dependence on the applied electric field for the donors agrees with the Gaussian disorder model (GDM). The positive dependence for the hole mobility is consistent with greater energetic disorder whilst the electron dependence is consistent with greater positional disorder. Whilst our data agrees with GDM, our data range is too limited to have confidence that the parameter values are unique.

**1** has the highest hole mobility and is also the best performing donor in a photovoltaic device as discussed in chapter 6. The next best performing PV device used **3** as a donor, which shows the second highest hole mobility. **2** is shown to have the lowest hole mobility and also produced the lowest PV device efficiency, so overall the mobility measurements correlate with the donor's PV device performance The effect of fusing the two thiophene molecules in **3** has had the effect of reducing the hole mobility from an average of $1.4 \times 10^{-3}$ cm$^2$V$^{-1}$s$^{-1}$ to $0.9 \times 10^{-3}$ cm$^2$V$^{-1}$s$^{-1}$, i.e. by a factor of around 35%.

The addition of the photo polymerisable end group on **5** gives us an average mobility of $4.2 \times 10^{-4}$ cm$^2$V$^{-1}$s$^{-1}$, a 70% reduction compared to **1**. Finally, the addition of two extra thiophenes before the end group of **2** leads to the largest reduction in mobility seen here, down to an average of $3.1 \times 10^{-4}$ cm$^2$V$^{-1}$s$^{-1}$, a reduction of almost 80% compared to the mobility of **1**.

The end chains of nematic liquid crystals interpenetrate the aromatic core, so that the bulkiness of the end group causes an increase in intermolecular separation. This in turn reduces the intermolecular $\pi$ orbital overlapping and hence reduces the overall charge carrier mobility. It has been shown that compounds with similar length and shaped end groups, but with large differences in polarisability, produce similar mobility values. However, compounds with different shaped end groups produce significantly different mobility values (almost 2 orders of magnitude)[73,67]. This indicates that the shape of the diene end group, rather than it's polarisable nature, accounts for the relatively large reduction of mobility seen by **5**.

The largest mobility reduction seen for **2** suggests that the addition of an extra thiophene into an already relatively long chained molecule has a negative impact on charge transport. The fused thiophene in **3** has a small reduction effect on mobility here, but as shown in chapter 7 this also affects the liquid crystalline phase transition. As shown in chapter 7, the performance of **3** as a donor material in a PV device improved significantly after being annealed above the liquid crystal transition temperature. Unfortunately, as discussed earlier, the TOF films used here were annealed within a vacuum as heating would cause cracks in the relatively thick film. This prevents us from investigating any potential improvement in mobility due to further liquid crystal ordering for **3**.

Generally the charge carrier mobility of amorphous organic materials is limited to values in the order of $10^{-3}$ cm$^2$V$^{-1}$s$^{-1}$ or less, due to molecular disorder[67,58], although liquid crystal ordering has been shown to increase mobility values to as high as 0.1 cm$^2$V$^{-1}$s$^{-1}$ for smectic and ordered discotic phases[198]. The improvement is due to the large self organised domains formed in the liquid crystal mesophase with highly ordered and close packed structures. This improves the intermolecular $\pi$-orbital overlapping, which supports the hopping mechanism of the charge carrier between sites of close separation.

The mobility values determined here range from 0.3 to 1.7 x $10^{-3}$ cm$^2$V$^{-1}$s$^{-1}$ overall, which is similar to the upper range quoted above for disordered organic materials. Hole mobilities above 0.2 cm$^2$/Vs have been achieved for some meso-morphic derivatives of hexabenzocoronene in the room temperature discotic phase[199]. Mesogens in the room temperature smectic phase have produced mobilities of 0.1 cm$^2$/Vs and 0.2 cm$^2$/Vs for holes and electrons respectively[199]. These high mobility values were attributed to close-packed structures as a result of the LC ordering.

The low mobility values measured for our materials do not seem to reflect the high mobility expected from liquid crystal ordering. As discussed earlier, all of the donors investigated here are nematic glasses at room temperature. It was shown in chapter 1 that nematic liquid crystals have orientational, but not positional order. Orientational order helps the mobility as the short intermolecular spacing is in the direction of charge transport. However, the ideal overlapping of $\pi$-orbitals required for efficient hopping charge transport relies on both the positional and orientational order of the rod like molecules.

# 5.2 Investigation of Charge Mobility in Blends

Whilst it is useful to know the charge mobility characteristic of individual donor and acceptor materials, it is the mobility within blends which is key to the performance of bulk heterojunction photovoltaic devices. Here we investigate the mobility of donor/acceptor blends and how this compares to the mobility of the two blend components. Compound **4** is used as the electron acceptor for three of the blends, this being the acceptor used for all of the photovoltaic devices studied in chapters 5, 6 and 7. The four donor materials discussed in the previous section are all used to make blends; **1**, **2** and **3** are blended with **4**, whilst **5** is blended with the acceptor **7**. All blend films were processed as described in section 3.3.

Each blend was prepared using 0.2ml of chlorobenzene to dissolve the material amount indicated in table 5.2. After 22 minutes evaporation time the **5:7** film degraded significantly and higher material concentration blocked the syringe filter, hence it was not possible to achieve a thicker film for this blend.. The film thickness was measured using the WYKO and the laser intensity incident on the sample was 350 µJ cm$^{-2}$/pulse and all measurements were made with the sample at room temperature, 25°C.

**Table 5.2 – Processing conditions for each blend investigated. Film thickness measured were made over different regions around the electrode and averaged**

| Blend Compounds | Material Quantity (mg) | D/A Ratio (Mol) | Evaporation Time (s) | Film Thickness (µm) |
|---|---|---|---|---|
| **1:4** | 20 | 1:2 | 30 | 1.04 ± 0.06 |
| **2:4** | 20 | 1:2 | 30 | 0.89 ± 0.02 |
| **3:4** | 20 | 1:2 | 30 | 0.99 ± 0.05 |
| **5:7** | 17 | 1:2 | 22 | 0.66 ± 0.02 |

Initial data taken did not show clear current transients for either electrons or holes. This was due to the larger photo generated charge relative to the individual compounds, as the blend would have much more efficient charge separation. As discussed in section 2.2 it is an important condition that the photo generated charge is much smaller than the capacitance charge of the sample. A high charge carrier concentration creates a non-uniform electric field and attenuates charge carrier transport via space-charge effects. Hence the neutral density filters were used to reduce the incident laser intensity to 22 $\mu Jcm^{-2}$/pulse and 9.4 $\mu Jcm^{-2}$/pulse and current transient data taken for each one.



**Figure 5.6 – Current transient for a blend of 2 and 4 (1:2 Mol. Ratio) showing charge carrier transit time for electrons (a) and holes (b) at an applied electric field of 3.03 x 10$^{-5}$ Vcm$^{-1}$ and laser incident intensity of 22 $\mu J$ cm$^{-2}$/pulse.**

Figure 5.6 shows the current transients for holes and electrons, which are now quite clear having reduced the laser intensity and hence the photo generated charge. Transients were clear enough to calculate transit times for electrons and holes over the full range of applied electric field values used. Whilst figure 5.6 shows current transients at 22 $\mu Jcm^{-2}$/pulse, the lower intensity 9.4 $\mu Jcm^{-2}$/pulse also produced clear transients. Note, electron hopping occurs between molecules of **4**, whilst the holes hop between the donor **2** molecules.
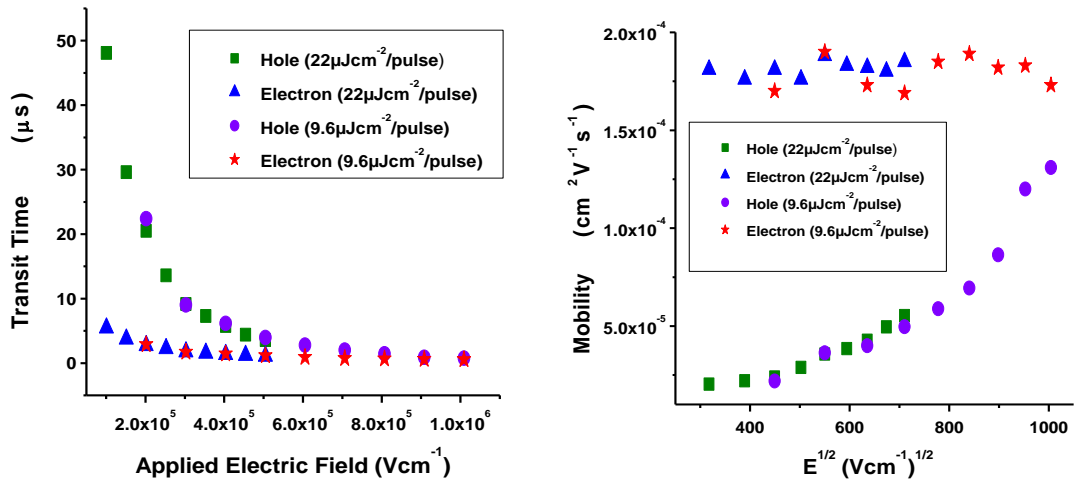
**Figure 5.7 – Transit times (a) and mobility's (b) for electrons and holes for a blend of 2 and 4 (1:2 Mol. Ratio).**

Figure 5.7 (a) shows that the transit time for both charge carrier types reduces as the applied electric field increases. This is far more pronounced for the holes which have much longer transit times than the electrons at low fields, but almost equal transit times at higher fields ($> 8 \times 10^5$ Vcm$^{-1}$). Figure 5.7 (b) shows that the hole mobility increases with the applied field, as was seen for the individual donors. The electron mobility remains fairly constant as the electric field increases. At the highest field applied the mobility values for the electrons and holes are close to parity, $1.7 \times 10^{-4}$cm$^2$V$^{-1}$s$^{-1}$ and $1.3 \times 10^{-4}$cm$^2$V$^{-1}$s$^{-1}$ respectively. It is important to have balanced transport of holes and electrons within the active layer of a PV device in order to avoid a build up of space charge. Kotlarski et al. showed that the FF of a fullerene bulk heterojunction solar cell fell from 50% to 40% as a result of charge transport unbalanced by one order of magnitude[200].

The laser intensity incident on the **5:7** blend was reduced to 22 μJcm$^{-2}$/pulse and 9.4 μJcm$^{-2}$/pulse using the neutral density filters and data was taken at each of these settings. Figure 5.8 shows the current transients for electrons and holes and the measured transit times. Whilst both laser intensity settings provided mostly clear transients, it was not possible to determine clear transit times for the electrons at higher fields. The higher laser intensity of 22 μJcm$^{-2}$/pulse provided the best transients for transit time measurement with less noise than those produced by the lower laser intensity. Note the significantly lower current at the transit time for the electrons, suggesting trapping.
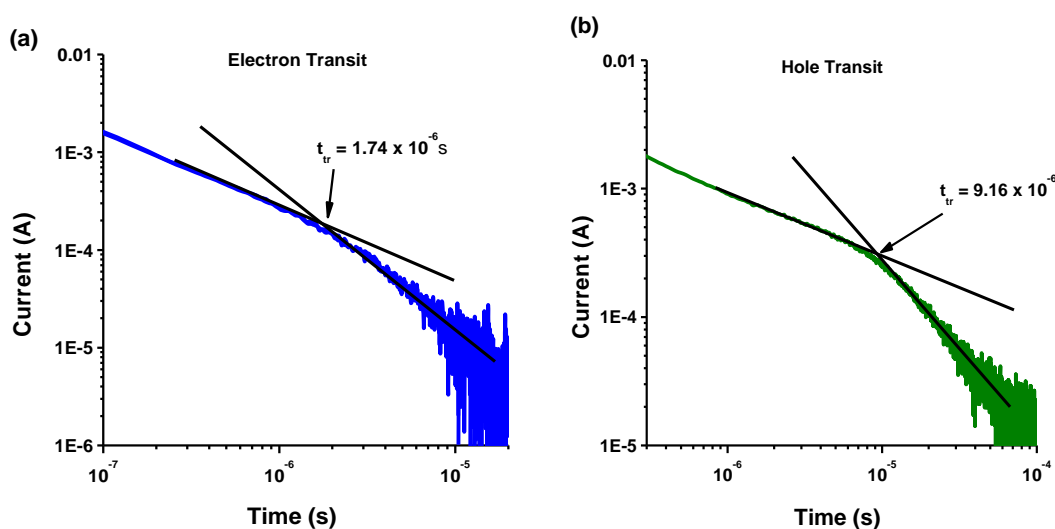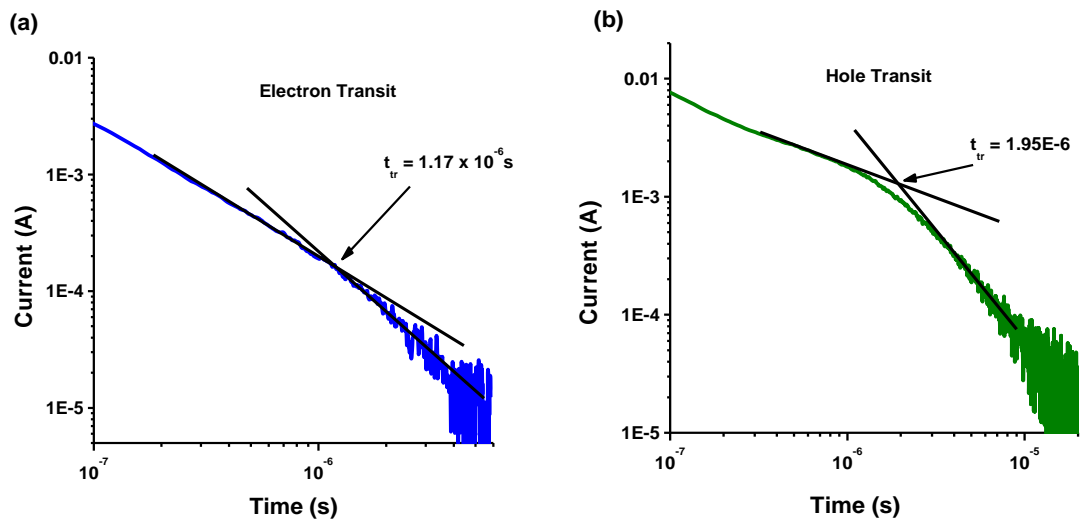


**Figure 5.8 – Current transient for blend of 5 and 7 (1:1 Wt. Ratio) showing charge carrier transit time for electrons (a) and holes (b) at an applied electric field of 3.01 x 10$^{-5}$ Vcm$^{-1}$ and laser incident intensity of 22 μj cm$^{-2}$/pulse.**

Figure 5.9 (a) shows that the charge carrier transit times reduce as the field increases and (b) the hole mobility rises and the electron mobility reduces as the applied field increases. The hole and electron mobility values and transit times reach equilibrium at a field strength of around 4.5 x 10$^5$ Vcm$^{-1}$. This would provide good balanced transport in a photovoltaic device, generally the range of the built in electric field of a photovoltaic is 10$^4$-10$^5$V/cm$^{-1}$ [18].
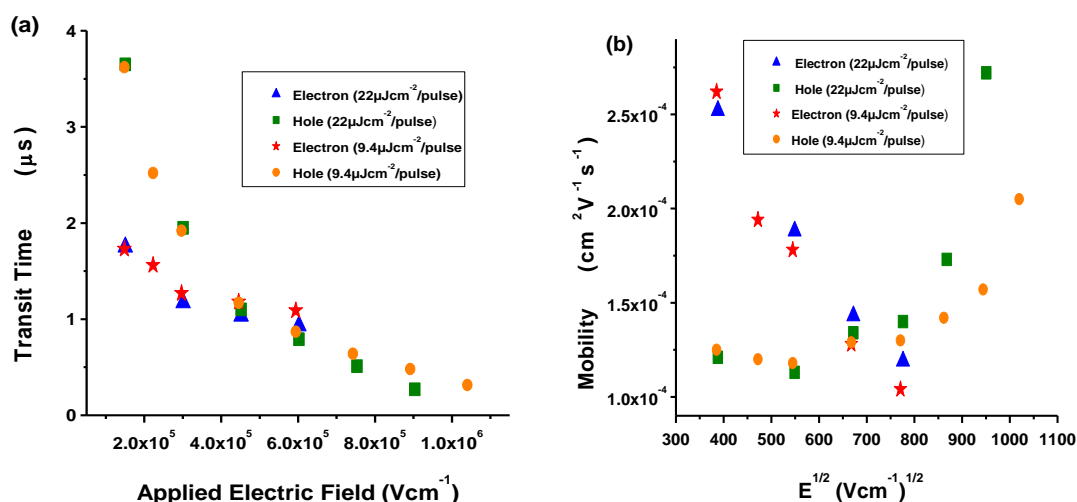
**Figure 5.9 – Transit times (a) and mobility (b) for electrons and holes for a blend of compounds 5 and 7 (1:1 Wt. Ratio).**

The laser intensity incident to the **1:4** and **3:4** blends was varied between 350, 67, 22, 9.4 and 5.1 µj cm$^{-2}$/pulse using the neutral density filters and data was taken at each of these settings. Both of these samples produced current transients which did not allow a clear transit time for either holes or electrons to be determined at any of the laser intensity settings used.
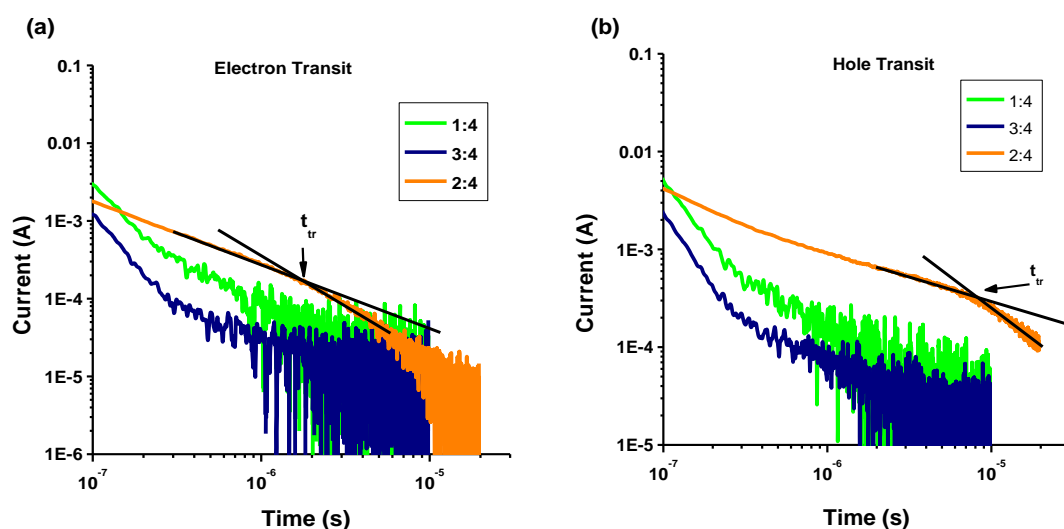


**Figure 5.10 – Current transient for blends of (1:4), (3:4) and (2:4) all 1:2 Mol. Ratio, for electrons (a) and holes (b). Only the 2:4 blend shows clear transit times for the charge carriers.**

Figure 5.10 shows the current transients for 3 blends, **1**:**4**, **3**:**4** and **2**:**4** with only the latter providing a transient from which the charge transit time could be determined. Out of the three donors used in the blends here **2** has the lowest mobility. It seems reasonable to expect the **1**:**4** and **3**:**4** blends to show higher charge mobility than the **2**:**4** blend, based on the higher mobility of the donor component. It can be difficult to measure the mobility of an organic semiconductor of low film thickness by TOF when the mobility value is high, as this reduces the carrier transit time which can lead to the transient signal being masked by the noise of the $N_2$ laser pulse[110,136]. Here, the shape of the transients suggests that trapping may have suppressed the photocurrent, causing it to quench immediately after photo generation[67]. It may be surprising that the **1**:**4** PV device has the best performance. This may be accounted for by the different sample preparation conditions. For TOF samples no annealing could be carried out, which is shown in chapter 7 to improve the organisation of the blend.
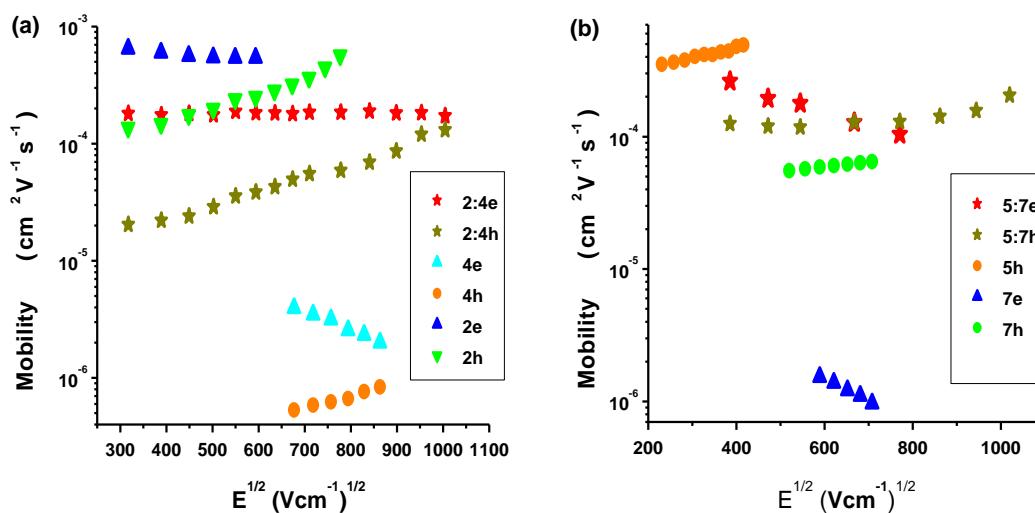


**Figure 5.11 – Mobility measurements for a blend of 2:4 (a) and 5:7 (b) compared to the mobility for the individual compounds.**

Figure 5.11 shows the mobility values for **2:4** (a) and **5:7** (b) along with the individual mobility value of the donors and acceptors within each blend. Compounds **4**, **5** and **7** were previously measured by Alkhalifah[57] using the same TOF set up as that used in this thesis. Within the blends electron transport is via hopping among the perylene, **4** and **7**, whilst hole transport is via hopping among the donors, **2** and **5**.

For each blend the hole mobility is lower than that of the pure donor material. This is particularly so for the **2:4** blend, which produced hole mobility values almost a whole order of magnitude lower than that seen for **2**. This difference is consistent across range of applied electric field strengths, as hole mobility in the blend exhibits the same field dependence as that shown for the pure donor. At low electric field strength the **5:7** blend produced hole mobility values around a quarter of that seen for **5**. Here the positive field dependence for the hole mobility is not evident at low fields, where the mobility values are fairly constant. However, the positive field dependence is seen at high fields, as shown in figure 5.11 (b). This change in field dependence is consistent with an increase in positional disorder for the **5:7** blend relative to the pure acceptor **7**, as shown earlier in figure 2.21(b). The drop in hole mobility shown for both blends, relative to the pure donors, could be a consequence of different organisation of charge transport pathways in the blend rather than the clear paths available in the pure donor.

The electron mobility of the **2:4** and **5:7** blends are around two orders of magnitude higher than that of the individual acceptors **4** and **7**. Possibly the large end groups of **4** and **7** impede intermolecular transport between the perylene end groups. The organisation is significantly different in the blend, improving transport. Alternatively, an increased photo generated charge is produced compared to pure materials as a result of more efficient charge separation with the donor/acceptor blend. The resulting higher density of electron charge carriers may have saturated the charge traps within the acceptor, resulting in the higher mobility seen for the blend electrons.

As discussed earlier, balanced charge transport is needed to prevent space charge build up around the collecting electrodes, and hence provide a more efficient PV device. Blend **5:7** provides reasonably well balanced charge transport across the range of applied electric fields and the best balance is found at an electric field strength of around 4.5 x $10^5$ Vcm$^{-1}$. For **2:4** the electron and hole mobility are one order of magnitude apart at low fields, but this gap narrows as the applied field increases. At the highest field applied here parity between the hole and electron mobility's is almost reached. A PV device using the **2:4** blend should be more efficient at higher fields, whilst using the **5:7** blend should show less variation of efficiency over a range of electric fields.

Tan et al recently measured the mobility of a new hole transporting polymer (PBTDTT-15) blended with (PC$_{70}$BM) using the TOF measurement technique. The blend mobility was calculated to be 3 x $10^{-3}$cm$^2$V$^{-1}$s$^{-1}$ for electrons and 7.8 x $10^{-5}$cm$^2$V$^{-1}$s$^{-1}$ for holes respectively[129]. This compares to 1.7 x $10^{-4}$cm$^2$V$^{-1}$s$^{-1}$ and 1.3 x $10^{-4}$cm$^2$V$^{-1}$s$^{-1}$ for the maximum electron and hole mobility in the measured in **2:4**, and the most balanced mobility of blend **5:7** of 1.28 x $10^{-4}$cm$^2$V$^{-1}$s$^{-1}$ and 1.29 x $10^{-4}$cm$^2$V$^{-1}$s$^{-1}$ for electrons and holes respectively. Whilst the blends studied here have a lower electron mobility than the Tan et al blend they do have a higher hole mobility and well balanced charge transport, almost at unity. It was also seen by Tan et al that the hole mobility of their blend was five times slower than that measured for the individual electron donor material (PBTDTT-15)[129], which confirms our findings here. Tan attributed this drop in mobility to the change in film morphology with the addition of the acceptor. Whilst compound 5 shows promise as a donor device, this material has already been used elsewhere[57] with acceptors **4** and **7** in PV devices and hence will not be included in chapter 6.

## 5.3 Conclusion

The two donor materials **2** and **3** both showed an increase in hole mobility and a decrease in electron mobility with applied electric field. In each case the electron mobility was found to be higher than that of the holes, but the difference between these values reduced as the electric field increased. The electron transients were significantly more dispersive and showed greater trapping.

The positive field dependence of hole mobility for **2** and **3** also applies to compounds **1** and **5** (measured previously by Alkhalifah) consistent with the Gaussian disorder model where energetic disorder dominates. The negative field dependence of electron mobility in **2** and **3** is consistent with the Gaussian Disorder Model where positional disorder dominates. Compound **1** was seen to have the highest hole mobility and was also the best performing PV device donor in chapter 6.

The **2**:**4** and **5**:**7** blends showed significantly higher mobility, two orders of magnitude, for electrons when compared to the pure electron acceptors **4** and **7**. It was suggested that this may be due to a reduction in trapping within the blend, due to significantly improved morphology. When compared to the pure donors **2** and **5** the blends showed a reduction in hole mobility. This can be attributed to the change of morphology when blended with the acceptor.

Generally, the electron mobility in the blends was higher than that for holes, but this difference reduced as the electric field increased. One of the most promising aspects of the TOF results for the two blends was the ratio between hole and electron mobility values which was almost at unity for certain electrical field values. This provides well balanced charge transport, making these blends suitable for photovoltaic devices.

# 6. Photovoltaic Device Performance

## 6.1 Introduction

Here we investigate the photovoltaic device performance of some of the materials identified as good potential electron donor materials in chapter 4. These will each be blended with compound **4**, which is the standard acceptor material used for the work in this thesis. Previous work by Alkhalifah[57] has shown this to be our best acceptor material and hence the focus here is on the newly synthesised donor materials. We investigate compounds **1**, **2**, **3**, **8**, **9**, **10** and **11**, whose energy levels are summarised in figure 6.1 alongside the work function for ITO, PEDOT and LiF/Al.
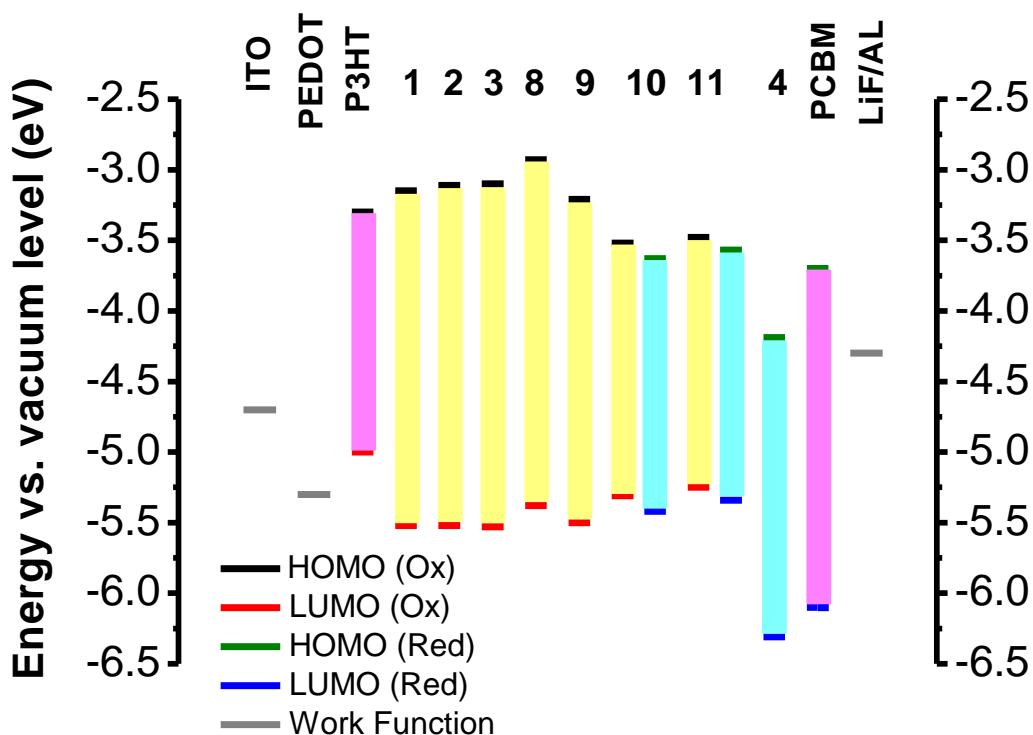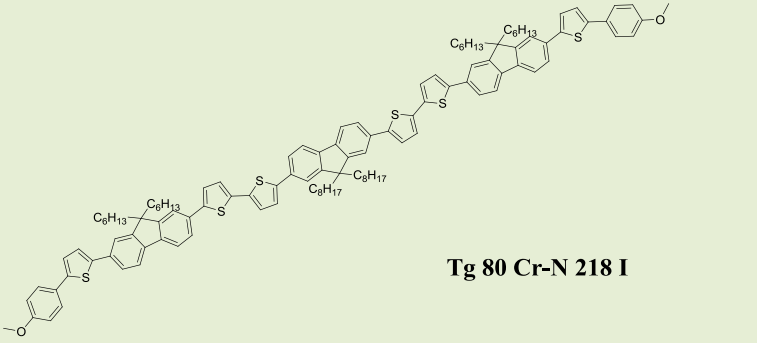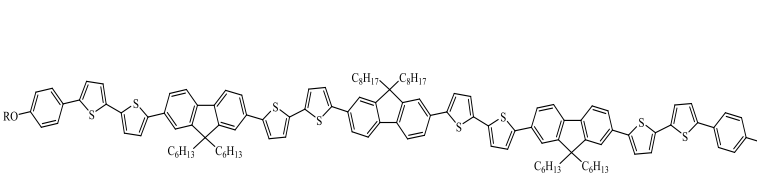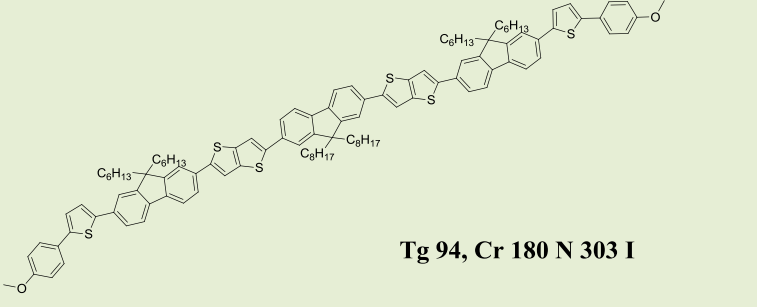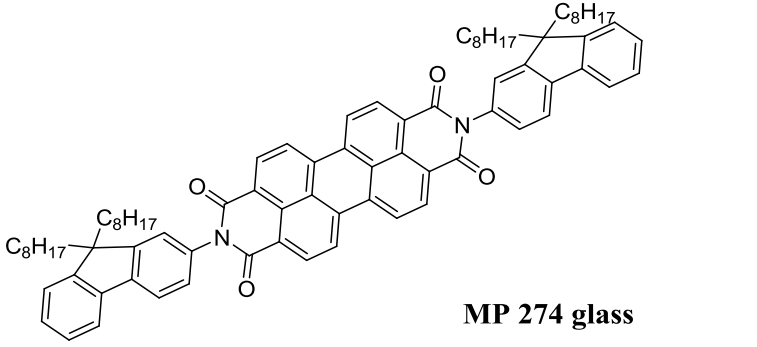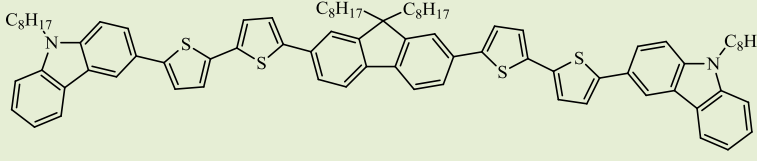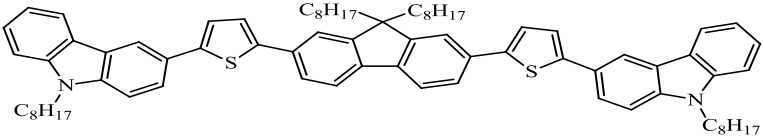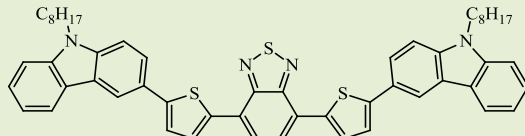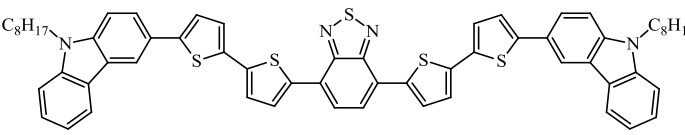


**Figure 6.1 – Energy levels for compounds 1,2,3,4,8,9,10,11 with P3HT and PCBM shown for reference. Also shown is the work function for ITO, PEDOT:PSS and LiF/AL. (Ox) and (Red) refer to the measurement of the oxidation and reduction transitions respectively by cyclic voltammetry. For compounds 10 and 11 two energy levels are shown, which relate to the oxidation and reduction reactions respectively as discussed in chapter 4.**

**Table 6.1 – Chemical structure for all materials used in this chapter.**

| Mat. | Structure | Energy Levels (±0.03eV) |
|---|---|---|
| 1 |  Tg 80 Cr-N 218 I | IP EA E$_{g,op}$ (eV) <br> $^O$ 5.52 , 3.15, 2.37 (R) <br> SPK516 |
| 2 |  | IP EA E$_{g,op}$ (eV) <br> $^O$ 5.52 , 3.11, 2.41 (R) <br> SPK620 |
| 3* |  Tg 94, Cr 180 N 303 I | IP EA E$_{g,op}$ (eV) <br> $^O$ 5.53 , 3.1 , 2.43 (R) <br> SPK523 |
| 4* |  MP 274 glass | IP EA E$_{g,op}$ (eV) <br> $^R$ 6.31, 4.19, 2.12 (QR) <br> MPA340 |
| 8 |  Chemical Formula: $C_{85}H_{96}N_2S_4$ <br> Exact Mass: 1272.65 <br> Molecular Weight: 1273.95 <br> Elemental Analysis: C, 80.14; H, 7.60; N, 2.20; S, 10.07 | IP EA E$_{g,op}$ (eV) $^O$ <br> 5.38 , 2.93, 2.45 (R) <br> SK433 |

| 9 |  Chemical Formula: $C_{77}H_{92}N_2S_2$<br>Exact Mass: 1108.67<br>Molecular Weight: 1109.70<br>Elemental Analysis: C, 83.34; H, 8.36; N, 2.52; S, 5.78 | **IP  EA  $E_{g,op}$ (eV)**<br><br>$^O$ **5.50 , 3.21 , 2.29 (R)**<br><br>**SK435** |
|---|---|---|
| 10 |  | **IP  EA  $E_{g,op}$ (eV)** $^O$<br><br>**5.31 , 3.52 , 1.79  (R)**<br><br>$^R$ **5.42 , 3.63, 1.79  (R)**<br><br>$E_{g,ec}$ **1.68**<br><br>**SK451** |
| 11 |  | **IP  EA  $E_{g,op}$ (eV)**<br><br>$^O$ **5.25 , 3.48 , 1.77 (IR)**   $^R$<br><br>**5.34 , 3.57 , 1.77 (R)**<br><br>$E_{g,ec}$ **1.68**<br><br>**SK452** |

The chemical structure for each material used in this chapter is shown in table 6.1. Compounds **1**, **2** and **3** have very similar structures of 3 fluorene groups interspaced with thiophenes and methoxy end groups. **1** and **2** are nematic liquid crystals with no detectable melting point, whilst **3** has a clear liquid crystal transition point around 180°C. All three materials form a long lived nematic glass at room temperature when cooled rapidly following annealing of a thin film. The liquid crystal transition temperature of **3** will be investigated further in chapter 7. Compounds **8** and **9** have a fluorene centre group and carbazole end groups separated by thiophenes. **8** has a smectic liquid crystal phase transition around 107°C, a relatively low clearing point of 143°C and a glass transition at 18°C. **9** does not have an observable liquid crystal phase and has a melting point of 158°C and glass transition of 19°C.

Compounds **10** and **11** have a benzothiadiazole centre group and carbazole end groups separated by thiophenes. These materials have the lowest band gaps of our donor materials and are classed as low band gap semiconductors, as discussed in chapter 2. Neither material exhibits a liquid crystal phase and have high melting points of 307°C and 343°C respectively. Glass transition temperatures are 56°C and 74°C respectively, which means that an amorphous glass is produced by both materials when cooled to room temperature. Compound **4**, our electron acceptor material, has a perylene bisimide core with two fluorene end groups. This material does not exhibit an observable liquid crystal phase and has a high melting point of 274°C.

The experimental results are split into three sections. First we compare all of the donor materials using the standard processing conditions. Different donor/acceptor blend ratios are then be investigated using donor material **1**. Finally we vary the top electrode material and compare electrode deposition pre and post film annealing using donor **1**.

# 6.2 Results and Discussion

## 6.2.1 Effect of molecular structure on PV device performance

Each donor material was used to fabricate a bulk heterojunction photovoltaic device as described in section 3.7, blended with **4** as the electron acceptor. The molecular weight of **4** is 1167.6 g/mol and the donor molecular weights range from 2373.6 g/mol for **2** down to 855.23 g/mol for **10**. Different ratios of donor to acceptor moles were chosen for each of the sub groups of donor used, based on their molecular weight relative to the acceptor molecule. Standard processing and annealing conditions were used and the donor/acceptor ratio is specified for each of the blends in table 6.2.
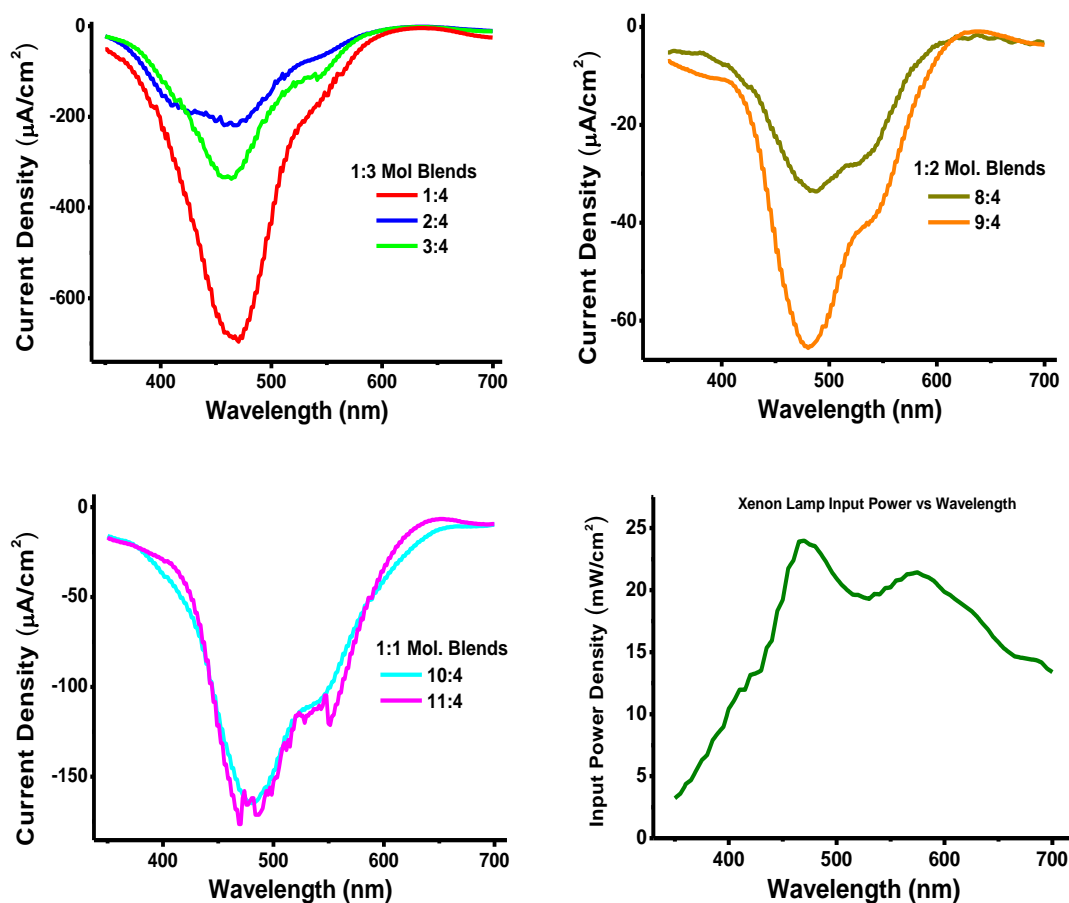


**Figure 6.2 – Photocurrent density spectrum for all donor blends where the incident light intensity is 24mWcm$^{-2}$ at 470nm. The input power vs. wavelength for the xenon lamp is also shown.**

Figure 6.2 shows the photocurrent produced over the visible spectrum, using the Xenon lamp for excitation of the samples as explained in section 3.7, with a measured incident intensity of 24mWcm$^{-2}$ at 470nm. The highest photocurrents are produced by **1:4**, **3:4** and **2:4**, which have very similar structures and nematic liquid crystalline properties. The addition of an extra thiophene pair for **2** significantly reduces the photo generated current relative to **1**, and the fusion of two thiophene pairs for **3** also resulted in a reduction in photocurrent. Donor **2** is the bulkiest molecule and this may have impacted the morphology. The morphology of **3** may be improved by annealing above the liquid crystal transition temperature and this will be investigated in the next chapter.

The next highest photocurrents were produced by **10:4** and **11:4** which gave almost identical values. Whilst these benzothiadiazole/carbazole based structures produce a lower photocurrent peak than the fluorene based structures, the lower band gap of the former absorbs across a wider spectrum overall. The lack of liquid crystalline properties may be responsible for the lower overall photocurrent due to an inferior thin film morphology. On this occasion the addition of two thiophenes for **11** relative to **10** did not seem to have any significant effect on the photo generated current produced.

The lowest photocurrent was produced by **8:4** and **9:4**, where the donors have a fluorene centre group rather than benzothiadiazole relative to **10** and **11**. Interestingly, the smectic liquid crystal phase of **8** shows a negative effect on the photocurrent produced relative to **9**. However, the solubility of **8** was not good which in turn had an adverse effect on the quality of the resultant thin film and this may be responsible for the drop in photocurrent. It was found by Blouin et al[27] that many of the polycarbazole derivatives that they produced were poorly soluble and showed a lack of organisation, which in turn led to poor PV device performance.
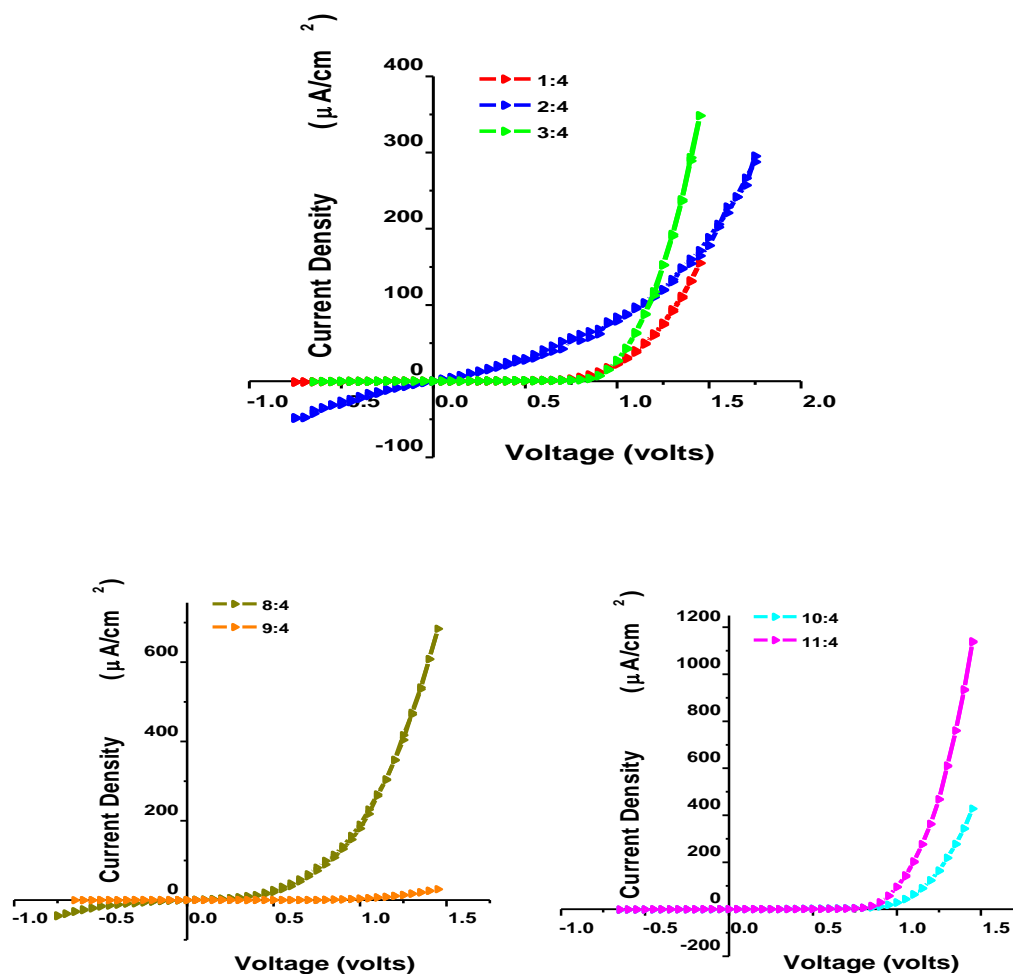
**Figure 6.3 – Dark JV Characteristics for all donor blends.**

Figure 6.3 shows the dark current JV characteristics for each blend, from which we can study the rectifying behaviour of each device. **1:4**, **3:4**, **10:4** and **11:4** all show good diode like characteristics, allowing current through in the forward bias and blocking current flow in reverse bias. **2:4** and **8:4** both show some current flow in reverse bias, which suggests a low shunt resistance and current leakage in the device. This is likely due to the morphology of the thin film and the resultant contact with the top electrode. Finally **9:4**, whilst blocking current in reverse bias, also seems to restrict current flow in the forward bias which may account for the lower photo generated current observed for this blend.
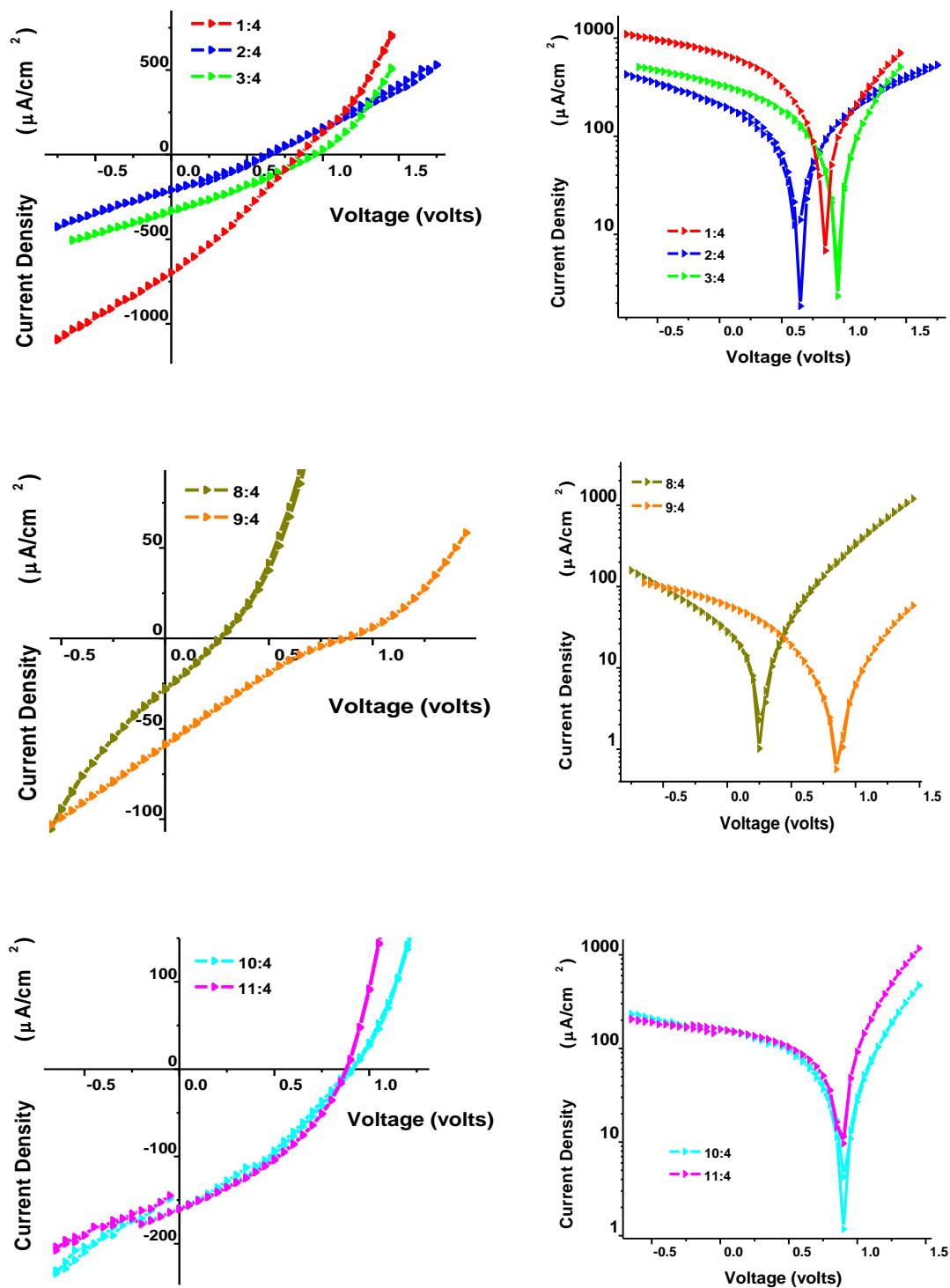
**Figure 6.4 – Light JV Characteristics for all donor blends, linear plot (left) and semi log (right) where the incident light intensity is 24mWcm$^{-2}$ at 470nm.**

Figure 6.4 shows the Light JV characteristics for each blend, from which we can determine the short circuit current density ($J_{sc}$) the open circuit voltage ($V_{oc}$) the fill factor ($FF$), power conversion efficiency ($\eta$), external quantum efficiency ($EQE$), series resistance ($R_s$) and shunt resistance ($R_{sh}$) as shown in table 6.2.

**Table 6.2 – PV device characteristics for all donor blends upon excitation with 24mWcm$^{-2}$ at a wavelength of 470nm.**

| Blend Materials | $J_{SC}$ (Acm-2) | $V_{OC}$ (V) | FF | $\eta$ (%) | EQE (%) | $R_s$ (kΩ) | $R_{sh}$ (kΩ) |
|---|---|---|---|---|---|---|---|
| **1:4** (1:3 Mol.) | 6.96 x 10$^{-4}$ | 0.84 | 0.29 | 0.70 | 7.65 | 1.1 | 1.8 |
| **2:4** (1:3 Mol.) | 2.08 x 10$^{-4}$ | 0.63 | 0.33 | 0.18 | 2.28 | 2.2 | 4.5 |
| **3:4** (1:3 Mol.) | 3.35 x 10$^{-4}$ | 0.94 | 0.30 | 0.39 | 3.73 | 1.8 | 3.65 |
| **8:4** (1:2 Mol.) | 2.84 x 10$^{-5}$ | 0.27 | 0.27 | 0.009 | 0.30 | 7.9 | 11.1 |
| **9:4** (1:2 Mol.) | 5.86 x 10$^{-5}$ | 0.87 | 0.21 | 0.045 | 0.63 | 21.4 | 12.4 |
| **10:4** (1:1 Mol.) | 1.6 x 10$^{-4}$ | 0.91 | 0.34 | 0.20 | 1.76 | 3.1 | 10.8 |
| **11:4** (1:1 Mol.) | 1.6 x 10$^{-4}$ | 0.88 | 0.37 | 0.22 | 1.72 | 1.3 | 10.9 |

Most devices show a relatively high $V_{oc}$ between 0.84 – 0.94V, with the exception of **2:4** at 0.63V and **8:4** at 0.27V. In both cases the actual energy levels are not the cause of the reduced $V_{oc}$ as they have similar energy levels, as shown in figure 6.1, to donors which produced higher $V_{oc}$ values. Hence the morphology and quality of the thin film itself is more likely to be responsible, particularly for **8:4** as previously explained.

The best power conversion efficiency was produced by **1:4**, which also has the highest external quantum efficiency. Overall the triple fluorene based donors achieved the best $\eta$ and EQE which indicates that these compounds provide the most efficient charge separation when blended with **4**. The carbazole/benzothiadiazole based donors produced lower EQE values, but both **10:4** and **11:4** achieved a higher $\eta$ than **2:4** due to their superior FF and $V_{oc}$. The carbazole/fluorene structured donors were disappointing, producing very low values for $\eta$ and EQE, indicating poor charge separation.

The highest fill factors were achieved by blends **11:4** and **10:4**, at 0.37 and 0.34 respectively, followed by **2:4**, **3:4**, **1:4**, **8:4** and **9:4** in descending order. Hence the benzothiadiazole based structures provide the highest FF, closely followed by the triple fluorene based structures, and the carbazole outer group structures producing the lowest.

However, all of the *FF* values produced by our blends are significantly lower than that produced by state of the art devices. Li et al[201] reported a *FF* of 0.68 for a P3HT:PCBM blend, whilst small molecule based solar cells are said to be capable of achieving a *FF* >0.50 [40]. However, it has also been seen for the latter category that this can be reduced to <0.25 due to charge carrier accumulation near one of the electrodes[40]. The charge carrier mobility within a blend has a strong influence on this; (i) low overall mobility can lead to strong field dependent exciton dissociation rate, which changes the curvature of the JV response. (ii) unbalanced charge transport can lead to space charge effects, which results in a square root dependence on *V* for the photo current. Under these space charge limited (SCL) conditions it is said that the *FF* is limited to 0.42 [40].

In chapter 5 it was shown that the hole mobility of donors **1**, **2** and **3** are two orders of magnitude higher than the electron mobility of the pure acceptor **4**. This degree of unbalanced charge transport would lead to SCL conditions. However it was also shown in chapter 5 that when the acceptor is blended with the donors, the electron mobility rises two orders of magnitude to provide balanced charge transport. This was also shown to be the case by Alkhalifah[57] for the same acceptor with similar donor materials. It is speculated that one reason for the increase in charge transport within **4** could be due to the larger photocurrent produced within the blend saturating the deep charge traps. If this is true, then the occupied traps may then contribute to SCL effects and hence be responsible for the relatively low *FF*s shown for our devices.

It has also been shown that poor contact between the top electrode and the active layer of the device can lead to reduced *FF*s[40]. A non uniform contact or incomplete coverage of the organic layer surface can lead to charge accumulation near the electrode, where a large number of sites form blind alleys which act as charge traps. The resultant field can facilitate the reverse injection of charge carriers from the electrode under reverse bias, observed as a high photocurrent in the reverse bias regime[40].

The series and shunt resistance determine the shape of the linear JV curves shown in figure 6.4 as previously explained, and hence define the *FF*. Both parameters are far from ideal. A high shunt resistance is desirable to prevent current leakage from the device, whilst a low series resistance is needed for photo generated charge to reach the external circuit. The lowest $R_s$ value of 1.1kΩ was produced by **1:4**, but a relatively low shunt resistance of 1.9kΩ in the same device reduced the overall *FF*. The highest $R_{sh}$ was achieved by **9:4** at 12.4kΩ but this blend also produced the highest $R_s$ of 21.4kΩ leading to the poor fill factor seen. Rather than look at absolute values it is perhaps more useful to consider the ratio of $R_s/R_{sh}$, with a desired value <<1. The best ratio was achieved by **11:4** where we see a $R_s$ of 1.3kΩ and a $R_{sh}$ of 10.9kΩ, giving a ratio of 0.12, which contrasts with the worst ratio seen for **9:4** of 1.92. These two blends have the highest and lowest *FF* respectively, which correlates inversely with the ratio $R_s/R_{sh}$.
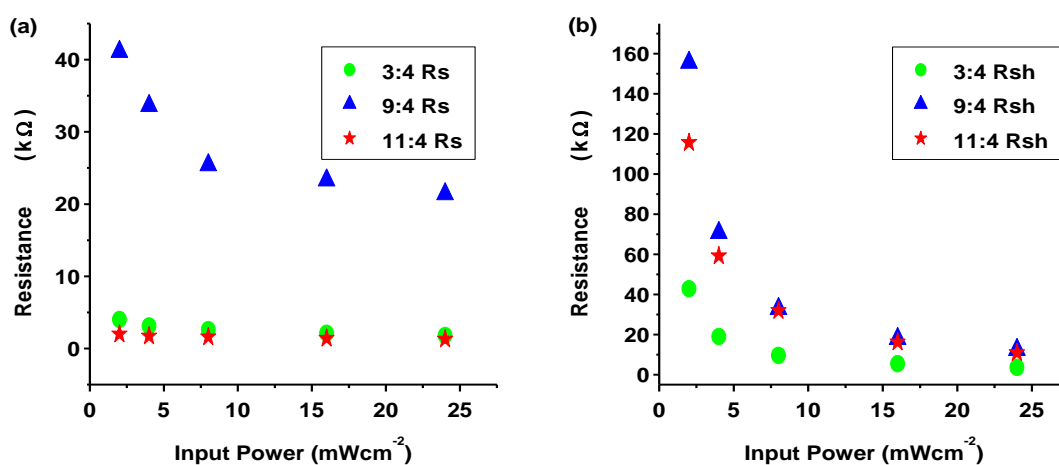


**Figure 6.5 – The variation of the series (a) and shunt (b) resistance with the incident light intensity for the 3:4, 9:4 and 11:4 blends.**

Figure 6.5 shows the $R_s$ (a) and the $R_{sh}$ (b) of blends **3:4**, **9:4** and **11:4** as a function of the incident light intensity. It is shown that the series resistance drops slightly with the incident intensity for the **9:4** blend, although the corresponding drop in shunt resistance is far greater. The **3:4** and **11:4** blends also show a significant drop in $R_{sh}$ with increasing incident intensity, which contributes to the poor *FF*s for our devices.
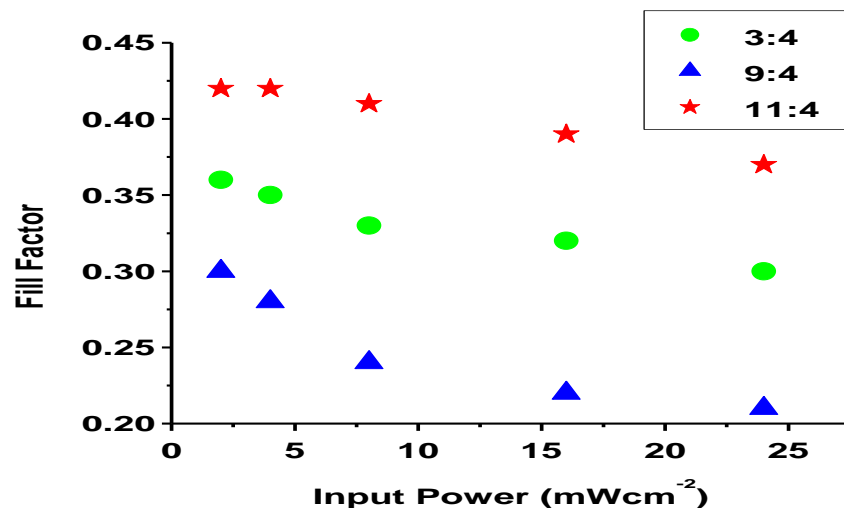
**Figure 6.6 – The variation of the fill factor a function of the incident light intensity for the 3:4, 9:4 and 11:4 blends.**

Figure 6.6 shows that the fill factor for each blend reduces with increasing incident intensity, which correlates with the large reduction in shunt resistance shown in figure 6.5 (b). This negative intensity dependence for *FF*, and for $R_{sh}$, agrees with the work of Riedel et al[202]. The **9:4** blend shows the largest drop in *FF* with input power, and was shown earlier to produce the lowest *FF* of all our devices. At low intensities, between 4 and 8mWcm[2], the highest fill factor was 0.42 for the **11:4** blend. The *FF* did not increase further as the intensity was furthered lowered to 2 mWcm[2], which indicates that this may be the maximum achievable for this blend. This correlates with the condition discussed earlier that the *FF* is limited to 0.42 for SCL cases.

In summary, the best performing donors here were the triple fluorene based group and our highest power conversion efficiency was 0.7% based on monochromatic illumination. This compares to the highest reported efficiency for a solar cell based on perylene diimide derivatives of 2.85% under AM1.5 conditions[203], significantly higher than our devices. However, a review of 21 different polyfluorene derivatives used to fabricate PV devices with PCBM, under AM1.5 conditions, show $\eta$ values in the range 0.17% to 2.84%[204], compared to our range of 0.18% to 0.7%. However, it should be

noted that comparing our efficiencies using monochromatic illumination against efficiencies achieved under AM1.5 conditions is not absolute.

It is claimed that the substitution of fluorene with carbazole can improve stability, as the nitrogen atom provides a lone electron pair that gives a fully aromatic structure[204]. However, our carbazole/fluorene based materials, **8** and **9**, produced very low efficiencies. The unusual shape of the Light JV curve for **8:4** and **9:4**, S shaped rather than J shaped, is thought to be caused by charge blocking[205,206]. It is thought that an energy barrier is formed due to poor charge carrier transport in one of the layers or interfaces, which prevents charge extraction. Lilliedal et al[207] recently demonstrated that an S shape JV curve can be transformed into the desired J shape by photo-annealing (repeated JV scans under illumination) for around 40 minutes. A corresponding increase in the $J_{sc}$, $V_{oc}$ and $FF$ were also shown. It has been hypothesised that mobile holes combine with adsorbed oxygen to form surface trap states, and upon desorption the concentration of mobile electrons increases. The photo-annealing process has been shown to encourage desorption via a favourable redistribution of oxygen within the cell, which improves the shape of the JV curve. It was also shown that increased temperatures during photo-annealing induced closer packing of polymer chains[207].

The substitution of the central fluorene group with benzothiadiazole, for **10** and **11** relative to **8** and **9** results in a significant increase in performance. A review of 17 polycarbazole derivatives blended with PCBM show a very wide range of power conversion efficiencies under AM1.5 conditions, from 0.2% to 6.1%[204]. The highest efficiencies in the review were obtained using materials with a benzothiadiazole centre group, which agrees with our findings here.
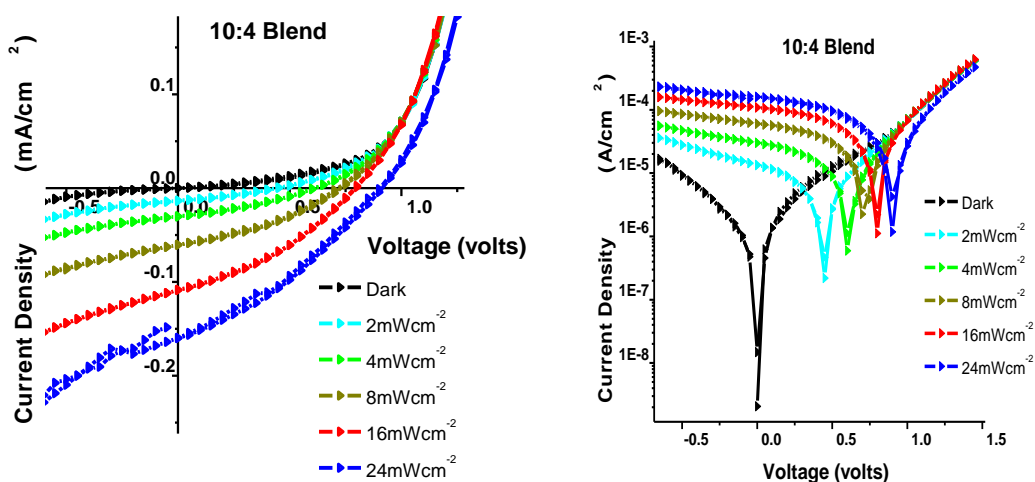
**Figure 6.7 – Light JV Characteristics for 10:4 Blend (1:1 Mol.) at various excitation intensities, linear plot (left) and semi log (right).**

Figure 6.7 shows the light JV curves for **10:4** with the variation of incident light intensity. The linear plot shows that both $J_{sc}$ and $V_{oc}$ increase with intensity. The semi log plot shows the intensity dependence of $V_{oc}$ more clearly. Blends **2:4** and **8:4** produced similar results for varying incident light intensities. Riedel et al[202] also found that the $V_{oc}$ value varied with incident intensity for a PPV:PCBM based blend, whilst Garcia-Belmonte produced simulations which predict this relationship[208]. One reason for this dependency of the $V_{oc}$ on the input light intensity may be the dark JV characteristics for these blends, a shown in figure 6.3. It was shown that both the **2:4** and **8:4** blends showed current leakage. As discussed in chapter 1, the $V_{oc}$ is reached when the photocurrent is equal to the dark current, hence producing a zero net current. The dark current flowing through a cell is often equated to the loss current of a cell[209]. Therefore the current leakage exhibited by the **2:4** and **8:4** blends will reduce the $V_{oc}$ of the device. At low incident light intensities, and hence lower photo generated current, these losses will have a larger impact on the $V_{oc}$ value of the device. Hence, the $V_{oc}$ is seen to drop as the input intensity is reduced for these blends.
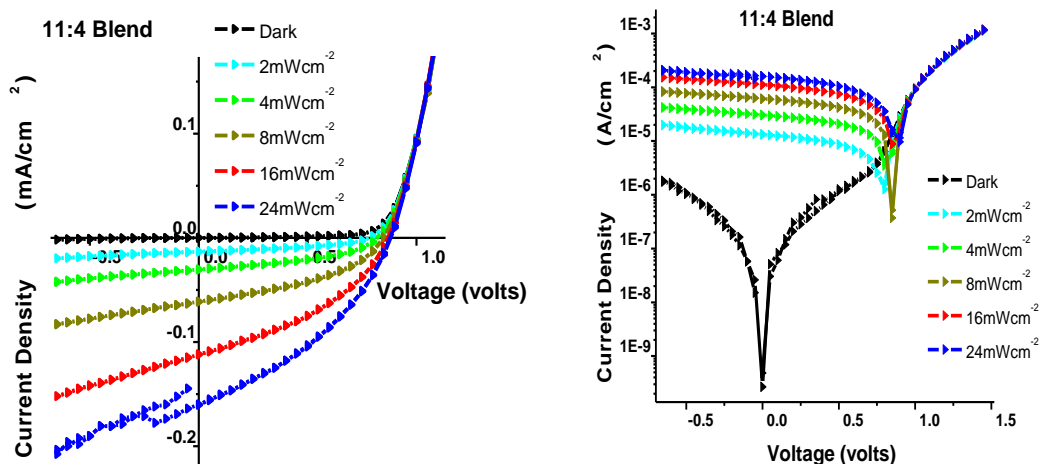
**Figure 6.8 – Light JV Characteristics for 11:4 Blend (1:1 Mol.) at various excitation intensities, linear plot (left) and semi log (right).**

Figure 6.8 shows the light JV curves for **11:4** as the incident light intensity is varied. Here we see the same relationship between the $J_{sc}$ and the incident light intensity as seen in figure 6.7 for **10:4**. However, the $V_{oc}$ does not change significantly as the intensity is varied. The semi log plot of figure 6.8 shows that the $V_{oc}$ value remains constant as the intensity is varied except for the lowest intensity used of 2mWcm$^{-2}$. Blends **1:4**, **3:4** and **9:4** were also seen to produce a constant $V_{oc}$ at varying incident light intensity. Li et al recently reported little effect on the $V_{oc}$ when the illumination intensity was varied for an organic heterojunction device[210]. The dark JV characteristics in figure 6.3 show no significant current leakage for the **1:4**, **3:4**, **9:4** and **11:4** blends, relative to the **2:4** and **8:4** blends. This further indicates that the current leakage is responsible for the $V_{oc}$ dependence on input light intensity. The exception to this is the **10:4** blend, which did not show current leakage in the dark JV characteristics but showed a $V_{oc}$ dependence on input light intensity.
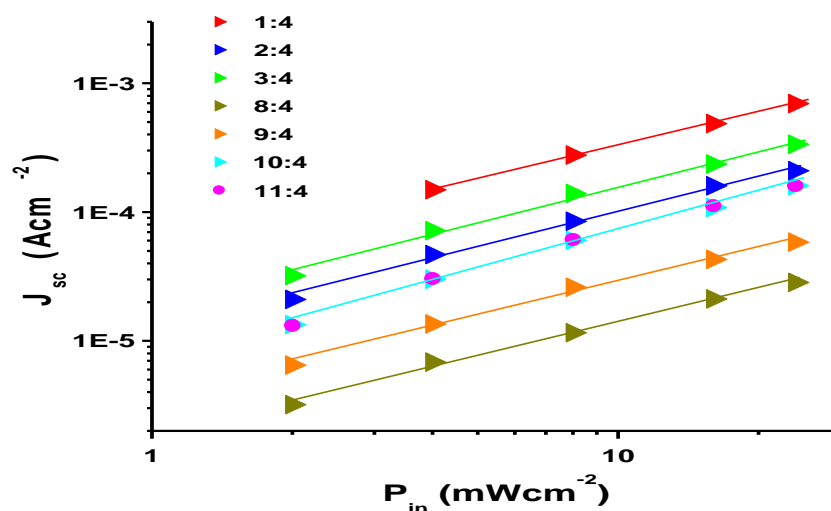
**Figure 6.9 –  Double logarithmic plot of $J_{sc}$ as a function of light intensity for all blends.**

Figure 6.9 shows a double logarithmic plot of the $J_{sc}$ as a function of incident light intensity, where $J_{sc}$ follows the power law $J_{sc} = P_{in}^{\alpha}$ [202]. Monomolecular recombination (geminate) is indicated by a linear dependence of the $J_{sc}$, i.e. a value of $\alpha = 1$, whilst bimolecular recombination (non-geminate) is indicated by a square root dependence where $\alpha = 0.5$. Geminate recombination is when an electron/hole pair generated together recombine, whilst non-geminate recombination involves separately generated electron and holes recombining. The value of $\alpha$ for each material can be determined from the gradient in figure 6.9 (using log values) to indicate the dominant charge recombination type.

The fluorene based donor blends, **1:4**, **2:4** and **3:4**, gave $\alpha$ values of 0.88, 0.91 and 0.90 respectively which indicates that monomolecular recombination is dominant, but with a small amount of bimolecular recombination. Blends **8:4** and **9:4** both produced an $\alpha$ value of 0.87, which indicates similar charge recombination to the three blends just discussed. All of these values are within the expected range for organic bulk heterojunction PV devices of around 0.8 to 1 [202,211].

Interestingly, the benzothiadiazole based donor blends, **10:4** and **11**:**4**, both produced values for $\alpha$ of 1.00 which indicates monomolecular recombination only. As bimolecular combination is thought to be due to accumulated space charge, in turn caused by low mobility, this may be an indication of high charge mobility within these two blends. However, monomolecular recombination may also be associated with poor charge separation, consistent with the relatively poor value of $J_{sc}$.

## 6.2.2 Effect of Donor/Acceptor Blend Ratio on PV device performance

Here we investigate blend **1:4** with various donor/acceptor blend ratios, all devices were prepared according to the standard procedure described in chapter 3.7. Figure 6.10 shows the photo current produced for each of the blend ratios studied.
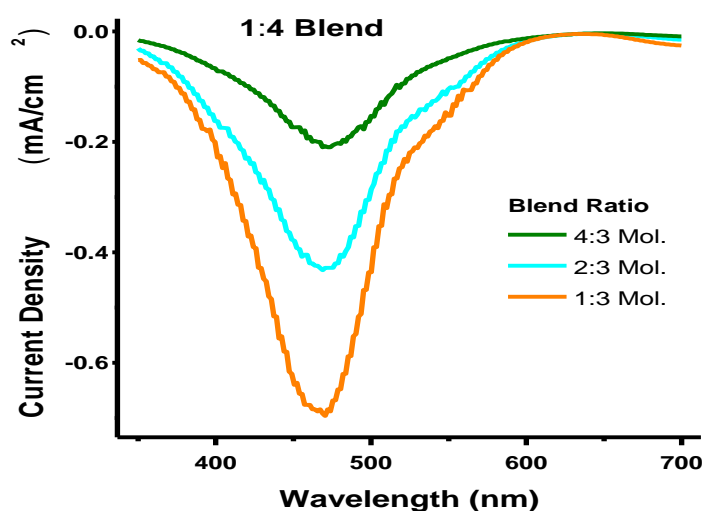


**Figure 6.10 – Photocurrent density generated over the visible light spectrum for compound 1 blended with 4 at various ratios.**

The highest photocurrent was produced by the blend with the smallest amount of donor material. As the ratio of donor material was increased, the photo current is seen to fall. This indicates that the ideal donor/acceptor morphology, for efficient charge separation, can be controlled via the blend ratio.

The overall trend suggests that more acceptor than donor material is desirable for higher photocurrents, though the ideal ratio can vary. This agrees with the findings of Hoppe et al[18] that increasing the fullerene (acceptor) component of a blend leads to higher electron mobility's and hence efficient electron transport. These findings indicate that a minimum grain size of the acceptor phase is needed to ensure percolated pathways for the electrons.
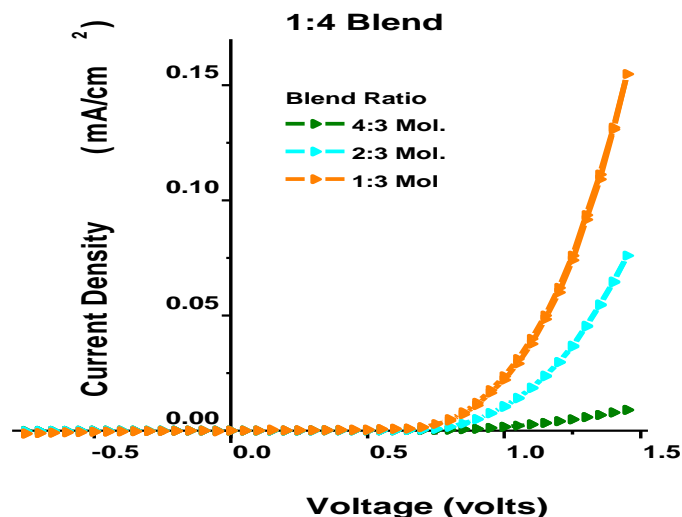
**Figure 6.11 – Dark JV Characteristics for compound 1 blended with 4 at various ratios.**

Figure 6.11 shows the dark current JV characteristics for the **1:4** blend at each blend ratio used. It can be seen that all ratios produce good diode characteristics, suppressing current in the reverse bias. The forward bias current is seen to be greatest for 1:3 mol blend and follows a similar pattern to the photo generated current in figure 6.10 as the donor concentration is increased.
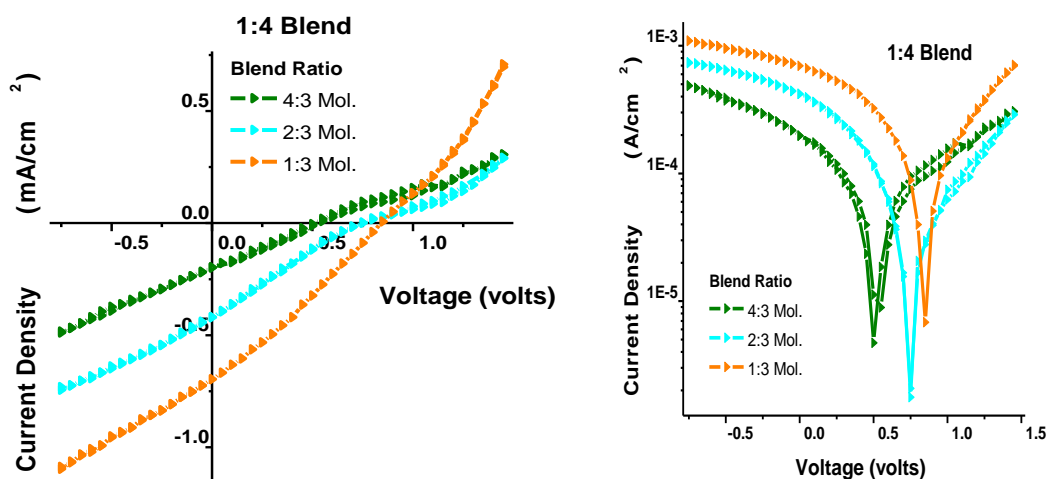


**Figure 6.12 – Light JV characteristics for 1:4 blends at various ratios, linear plot (left) and semi log plot (right).**

Figure 6.12 shows the light JV characteristics for **1:4** at each ratio used. It can be seen clearly in the semi log plot that the $V_{oc}$ reduces as the donor component of the blend increases. The key performance parameters have been extracted from these plots, as described previously, and are given in table 6.3.

**Table 6.3 – PV device characteristics for all blend ratios upon excitation with 24mWcm$^{-2}$ at a wavelength of 470nm.**

| Blend Materials | $J_{SC}$ (Acm-2) | $V_{OC}$ (V) | FF | $\eta$ (%) | EQE (%) | $R_s$ (k$\Omega$) | $R_{sh}$ (k$\Omega$) |
|---|---|---|---|---|---|---|---|
| **1:4** (1:3 Mol.) (1:2 Wt) | $6.96 \times 10^{-4}$ | 0.84 | 0.29 | 0.70 | 7.65 | 1.1 | 1.8 |
| **1:4** (2:3 Mol.) (1:1 Wt) | $4.2 \times 10^{-4}$ | 0.75 | 0.24 | 0.31 | 4.62 | 2.9 | 1.9 |
| **1:4** (4:3 Mol.) (2:1 Wt) | $1.98 \times 10^{-4}$ | 0.52 | 0.29 | 0.12 | 2.18 | 2.3 | 2.7 |

The best overall device efficiency for **1:4** was produced by the 1:3 D:A mol. ratio due to the relatively high $J_{sc}$ and $V_{oc}$. The consistent deterioration in performance with higher donor concentration has also been observed for the **3:4** blend, which is discussed in chapter 7. It is possible that more acceptor material is required in the blends because of the relatively low mobility of **4**.

The external quantum efficiency is seen to drop significantly as the donor concentration increases, suggesting that charge separation is less efficient with more donor material. However, the ideal donor/acceptor blend ratio can vary depending on the materials used. Li et al[212] showed that different donor molecular structures posses different interaction strengths with the acceptor, which in turn influences the final thin film morphology.

## 6.2.3 Effect of Cathode on PV device performance

The **1**:**4** blend (1:3mol.) was used to fabricate PV devices using the standard technique given in chapter 3.7, where the thin film was annealed prior to electrode deposition. We compare with a device annealed post electrode deposition (A.P.E). The latter device was annealed for one hour at 120°C, as standard, but this was done after the cathode had been deposited. The literature suggests that post-electrode annealing gives a less rough surface and enhanced performance.
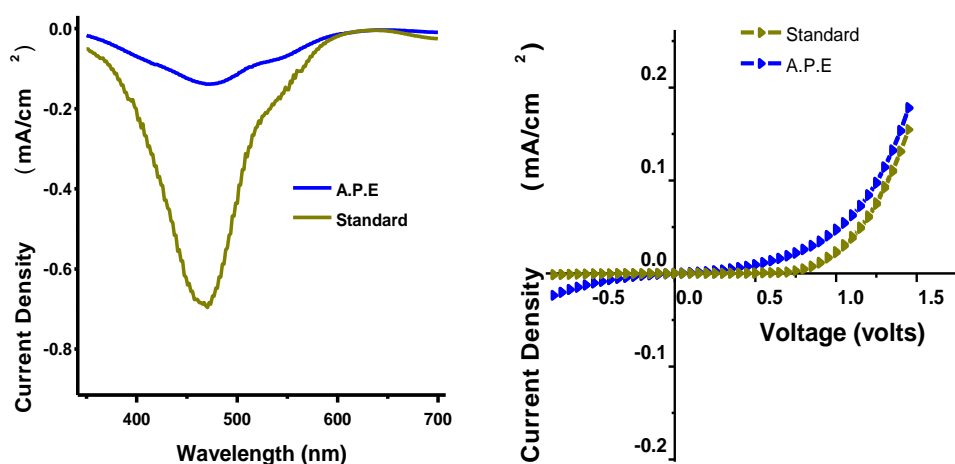


**Figure 6.13 – Photocurrent density (left) and dark IV characteristics (right) for 1:4 blend (1:3 Mol.) for devices annealed as standard and after electrode deposition.**

Figure 6.13 shows the photo current generated for each cathode type (left) and the dark IV characteristics (right). Here, annealing post electrode deposition causes a significant drop in photocurrent, possibly due to the electrode materials contaminating the bulk active layer whilst annealing. The standard device shows good diode characteristics while the A.P.E device shows some rectification, but some current flow is also evident in the negative bias.
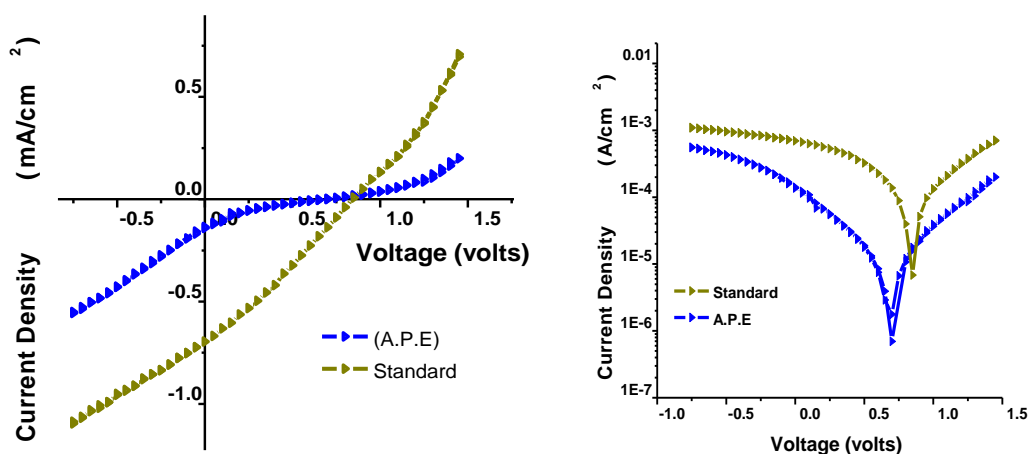
**Figure 6.14 – Light JV characteristics for 1:4 blends (1:3 Mol.) with different cathodes, linear plot (left) and semi log plot (right).**

Figure 6.14 shows the light JV characteristics for each electrode type, from which the PV device performance parameters have been extracted, shown in table 6.4.

**Table 6.4 – PV device characteristics for 1:4 Blend (1:3 Mol.) using different electrode deposition, upon excitation with 24mWcm$^{-2}$ at a wavelength of 470nm.**

| Top Electrode | $J_{SC}$ (Acm-2) | $V_{OC}$ (V) | FF | $\eta$ (%) | EQE (%) | $R_s$ (kΩ) | $R_{sh}$ (kΩ) |
|---|---|---|---|---|---|---|---|
| (A.P.E) | 1.39 x 10$^{-4}$ | 0.69 | 0.15 | 0.06 | 1.53 | 9.4 | 2.3 |
| Standard | 6.96 x 10$^{-4}$ | 0.84 | 0.29 | 0.70 | 7.65 | 1.1 | 1.8 |

It has previously been shown that the addition of a thin layer (5-10Å) of LiF improves the efficiency of an Al electrode by lowering the barrier for electron extraction[33]. The electron barrier is thought to be formed as Al atoms diffuse into the active layer, which is prevented by the LiF protective layer as it does not react chemically.

Annealing after the cathode deposition caused a large increase in the series resistance, which in turn led to a reduction in the $J_{sc}$ and *FF*. Overall this resulted in very poor overall device efficiency more than an order of magnitude lower relative to the standard device. This agrees with the recent work of Ismail et al[213] who reported on the effect of annealing after deposition of a 100nm thick Al cathode, for a C6:PCBM blend. It was

shown that the device efficiency reduced significantly with the rising temperature of post cathode annealing. This was attributed to deterioration in the interface between the active layer and Al cathode, which reduces charge carrier transport and collection at the electrode. A higher series resistance, and hence lower FF, were also attributed to the post annealing causing damage to the interface.

However, Li et al[214] reported an improved performance for a P3HT:PCBM blend for a device annealed post cathode deposition. Here the cathode consisted of 25nm calcium (Ca) and 100nm Al. The device annealed after the cathode deposition showed a 14% increase in efficiency relative to the device annealed prior to cathode deposition. It was suggested that the cathode acts as a barrier during thermal annealing, restricting the vertical movement of the polymer chains and hence result in better alignment. If the Ca layer acts as a barrier this may prevent damage to the Al interface, which as mentioned above is thought to be responsible for the reduction in device efficiency. The 0.6nm thick LiF layer used here may be too thin to have the same shielding effect as the Ca layer, hence the poor device performance.

A recent review also highlights an improved PV performance for a device annealed in the liquid crystal phase after deposition of the top electrode[199]. Elsewhere Ca has also been used as a buffer layer between the organic active layer and Al cathode. Theoretically it is thought that the relatively low work function of this metal would form a low resistance contact with the organic active layer. It was recently demonstrated by Tseng et al[215] that PV device efficiency was improved with the deposition of a 300Å layer of Ca between the active layer and Al cathode.

## 6.3 Conclusion

Photovoltaic devices were prepared using various donor materials blended with **4**. It was seen that the best device was produced by the **1:4** blend. The **3:4** blend also produced good results and the liquid crystal properties of this blend will be further investigated in the next chapter in order to optimise efficiency. **2:4** produced the worst performing PV device of the three triple fluorene based donors, the extra thiophene pair creating a bulkier molecule chain which seems to have negatively affected the thin film morphology. All three of these blends demonstrated mostly monomolecular recombination with a small amount of bimolecular recombination.

The benzothiadiazole/carbazole based donors produced relatively reasonable efficiency in the **10:4** and **11:4** blend devices, also shown to have shown to have the best $FF$'s. It was seen that the narrow band gap of these two donors allowed more of the visible spectrum to be absorbed without too much deterioration in $V_{oc}$. Further, these blends demonstrated monomolecular recombination only which may indicate high charge mobility. These qualities make **10** and **11** worthy of further investigation and optimisation as good potential donors.

The fluorene/carbazole based blends, **8:4** and **9:4**, produced disappointing efficiencies, particularly the former due to poor solubility. Comparing the molecular structure of these donors to **10** and **11**, the benzothiadiazole centre group produced much better PV devices than the fluorene centre group. It was suggested that the low $FF$s exhibited by our devices could be due to SCL effects. It was shown that the optimum donor/acceptor blend ratio for the **1:4** blend is 1:3 mol.(1:2 wt). The most efficient electrode configuration was found to be Al with a very thin (0.6nm) LiF buffer layer, deposited after annealing the active layer.

# 7. Annealing in the Liquid Crystal Phase

## 7.1 Introduction

As previously discussed, the nano-morphology of a solar cell can have a significant impact on its overall power conversion efficiency. It is possible to influence the morphology by annealing above the liquid crystalline phase of a material, which can give the donor and acceptor molecules freedom to move and self organise. It is hoped that the self organised domains formed will provide both a good interface area and clear pathways for the charge carriers to their respective electrodes. Further, the ordered molecules should provide for better overlap of the $\pi$ bonds and hence better charge transport as discussed in chapter 1. It has been shown in previous studies that using liquid crystalline materials can improve the mobility and overall device efficiency, due to the improved morphology of the active layer[43,138,139,140,42,58,141,72,142,143,73].

Here we investigate compound **3**, which has a crystal to nematic (Cr→N) transition at around 180°C. This material also has a glass transition temperature ($T_g$) of 94°C and a clearing point (N→I) of 303°C above which an isotropic liquid is formed. We will once again use **4** as the acceptor material, which does not have a liquid crystal phase and has a crystal to isotropic transition of 274°C, lower than the clearing point of **3**. Four different donor/acceptor blend ratios will be considered in the first part of this chapter in order to study the effect of donor concentration on the transition temperatures of the blend, and how this correlates with device performance and film morphology.

The experimental results will be split into four main sections. First we will study the phase transitions four blends of using donor **3** with acceptor **4**, mixed in the ratios 4:3, 1:1, 1:2 and 1:3 mol. The morphology of each blend will then be investigated using AFM microscopy. The photovoltaic device performance will then be discussed and correlated to the morphology. Finally we investigate the photovoltaic device results of Alkhalifah[57] for donor **1** blended with acceptor **4** in a 1:3 mol. ratio, annealed at various temperatures. We compare these to our results for the blend using donor **3**.

## 7.2 Phase Transitions

Here we investigate the phase transition temperatures for each blend ratio using differential scanning calorimetry (DSC) and an optical polarisation microscope. Four DSC pans were prepared by drop casting, as discussed in section 3.4, one for each blend ratio to be investigated. A standard indium sample was used to calibrate the DSC immediately prior to each blend measurement. Two heating/cooling cycles were run for each blend, beginning at room temperature, 25°C, heating to 300°C then cooling to 0°C before being heated back up to room temperature to complete the cycle. The heating and cooling rate was set at 10°C/minute.

Table 7.1 shows the chemical structure for compounds **3** and **4**, along with their respective phase transition temperatures and energy levels. The phase transition temperatures for both pure compounds were previously measured by Dr Stuart Kitney at the University of Hull, using DSC.

**Table 7.1 – Chemical Structure, phase transition temperatures and energy levels for compounds 3 and 4.**
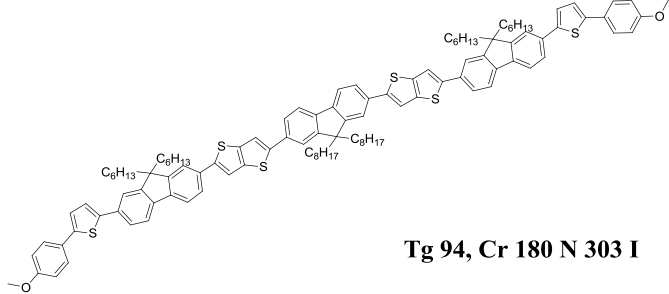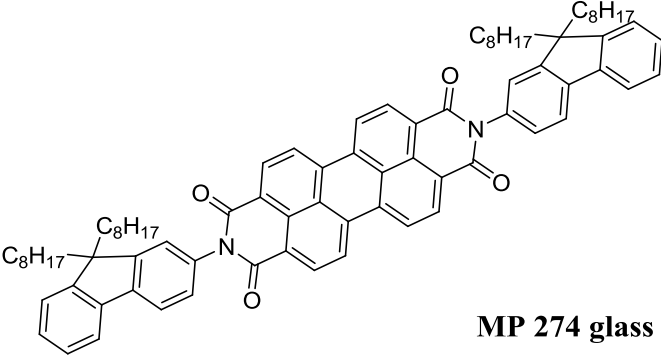
| Mate. | Structure | Energy Levels |
|---|---|---|
| 3 |  Tg 94, Cr 180 N 303 I | **IP  EA  E$_{g,op}$ (eV)** <br><br> $^O$ 5.53 , 3.1 , 2.43 (R) <br><br> **SPK523** |
| 4 |  MP 274 glass | **IP  EA  E$_{g,op}$ (eV)** <br><br> $^R$ 6.31, 4.19, 2.12 (QR) <br><br> **MPA340** |

Figure 7.1 shows the DSC trace for the pure compounds **3** and **4** and each of the four blend ratios used, with the phase transitions highlighted. Note the pure donor **3** is initially crystalline and on cooling from the isotropic a nematic glass. In the second cycle the glass melts to a mobile nematic phase at $T_g = 94°C$. It can be seen that each blend experiences three phase transitions during the first heating/cooling cycle. A crystal to nematic melting transition is seen first, due to the **3** component of the blend, a melting point is then observed followed by crystallisation during cooling. There is no liquid crystal melting transition during the 2nd heating cycle, but the melting point and crystallisation during cooling are still observed. We suggest that the donor component retains its LC phase during cooling, maybe forming a nematic glass, whilst the acceptor component crystallises out. This would explain the glass transition observed during the 2$^{nd}$ heating cycle and the crystallisation seen during both cooling cycles.
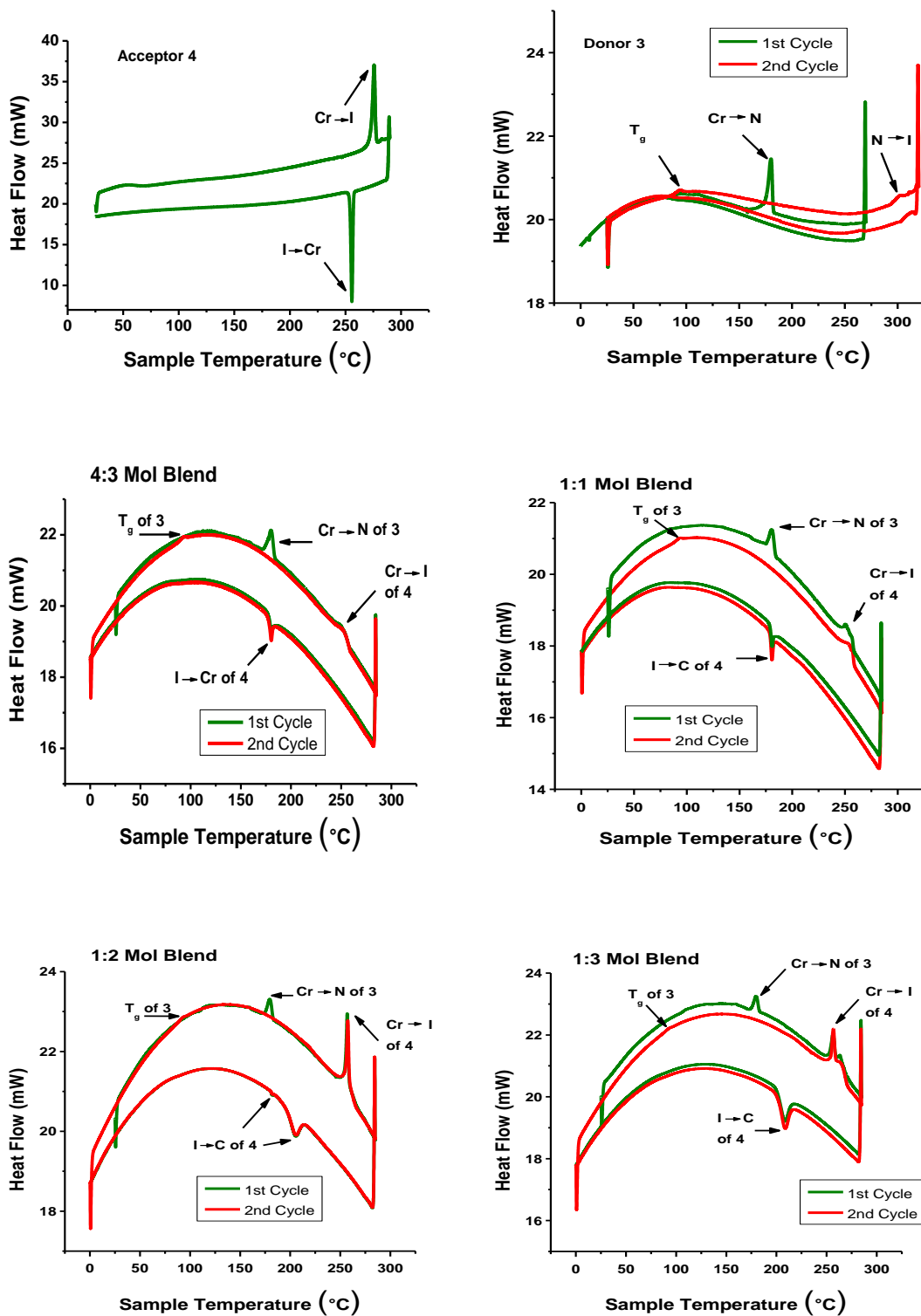
**Figure 7.1 – DSC trace for each pure compound and each donor/acceptor blend ratio, showing the various phase transition temperatures. DSC measurements of pure compounds 3 and 4 were made by Dr. Stuart Kitney, University of Hull.**

The actual temperatures for each of the highlighted transitions are summarised in table 7.2, with phase transitions from the $2^{nd}$ heating/cooling cycle shown in brackets. The baseline appears curved due to instrumental baseline susceptibility to long term drift.

However the calibration measurements made with the standard indium sample produced accurate peaks and enthalpy values, giving confidence in the accuracy of our results here.

**Table 7.2 – Phase transition temperatures for each of the four blend ratios studied. Phase transitions observed during the 2$^{nd}$ heating cycle are shown in brackets.**

| Blend Ratio | T$_g$ (°C) of 3 | Cr → N (°C) of 3 | Cr→I (°C) of 4 | I→Cr (°C) of 4 |
|---|---|---|---|---|
| Pure 3 | (94) | 180 | | |
| Pure 4 | | | 274 | 256 |
| 4:3 mol | (94) | 180 | 250 (254) | 180 (180) |
| 1:1 mol | (94) | 181 | 250 (253) | 181 (181) |
| 1:2 mol | (93) | 180 | 257 (257) | 206 (206) |
| 1:3 mol | (93) | 180 | 256 (257) | 209 (209) |

The values in table 7.2 show that the glass transition and Cr→N phase transition temperatures, during heating, are fairly constant for all blends, in the range 93 – 94°C and 180 to 181°C respectively. This correlates very closely with the phase transition temperatures for **3** of 94°C and 180°C respectively. The Cr→I transition temperature shows a small increase as more acceptor material is added to the blend, indicating that this transition applies to the acceptor component of the blend. The range of values, 250 – 257°C, are closer to that of the pure acceptor at 274°C compared to the higher clearing point (N→I) of the donor at 303°C. The shoulder of the melting peak for the 1:3 mol blend may signify the larger proportion of acceptor material taking longer to melt.

Upon cooling we see a supercooled I→Cr transition take place at around 180°C for the 4:3 and 1:1 mol. blends and between 205 - 208°C for the 1:2 and 1:3 mol blends. The 1:2 mol blend also shows a very small transition at 182°C, similar to the I→Cr transition temperature of the 4:3 and 1:1 blends. This may be an indication that the I→Cr shown by the 1:3 blend, and dominant in the 1:2 blend, is of a different nature to that of the higher donor concentrated blends. This is attributed primarily to **4** since the constant, albeit weakly defined, T$_g$ indicates that the donor cools to a glass.

**Table 7.3 – _ΔE_ for each phase transition observed for the four blend ratios studied. _ΔE_ values for phase transitions observed during the 2nd heating/cooling cycle are shown in brackets.**

| Blend Ratio | $T_g$ of 3 $\Delta E$ (J/g) | Cr→N of 3 $\Delta E$ (J/g) | Cr→I of 4 $\Delta E$ (J/g) | I→Cr of 4 $\Delta E$ (J/g) |
|---|---|---|---|---|
| **4:3 mol** | (0.37) | 5.99 | 3.02 (3.06) | -2.54 (-2.58) |
| **1:1 mol** | (0.41) | 3.81 | 4.15 (4.17) | -1.62 (-1.81) |
| **1:2 mol** | (0.19) | 2.69 | 6.57 (6.29) | -5.40 (-5.36) |
| **1:3 mol** | (0.133) | 2.69 | 8.06 (9.71) | -7.95 (-7.95) |

Table 7.3 shows the change in energy (_ΔE_) for each phase transition identified. Note that a positive value indicates an endothermic transition whilst a negative value indicates an exothermic transition. The errors are relatively large because of the poor background.

The _ΔE_ for the glass transition is shown to decrease with the donor content. This further indicates that the donor component forms a nematic glass when cooled to room temperature after the first heating/cooling cycle. For the Cr→N phase transition the value for _ΔE_ falls with donor content, as expected. There is an increase in the _ΔE_ for the Cr→I transition as more acceptor material is added, indicating that this transition applies primarily to the acceptor component. The I→Cr transition during cooling gives out more energy for the higher acceptor content blends. This suggests that it is primarily the acceptor material that is crystallising.

In order to confirm the nature of the phase transitions identified from the DSC measurements, a small amount of each of the blends was drop cast in solution to a standard microscope slide and a cover slip placed over the top as described in chapter 3.5. The same heating/cooling cycle used for the DSC measurements was used whilst observing changes in the phase of the material. Figure 7.2 shows images taken from the polarising microscope for each blend ratio at three temperatures; room temperature prior to heating, above the Cr→N transition temperature of **3** and finally room temperature after cooling.
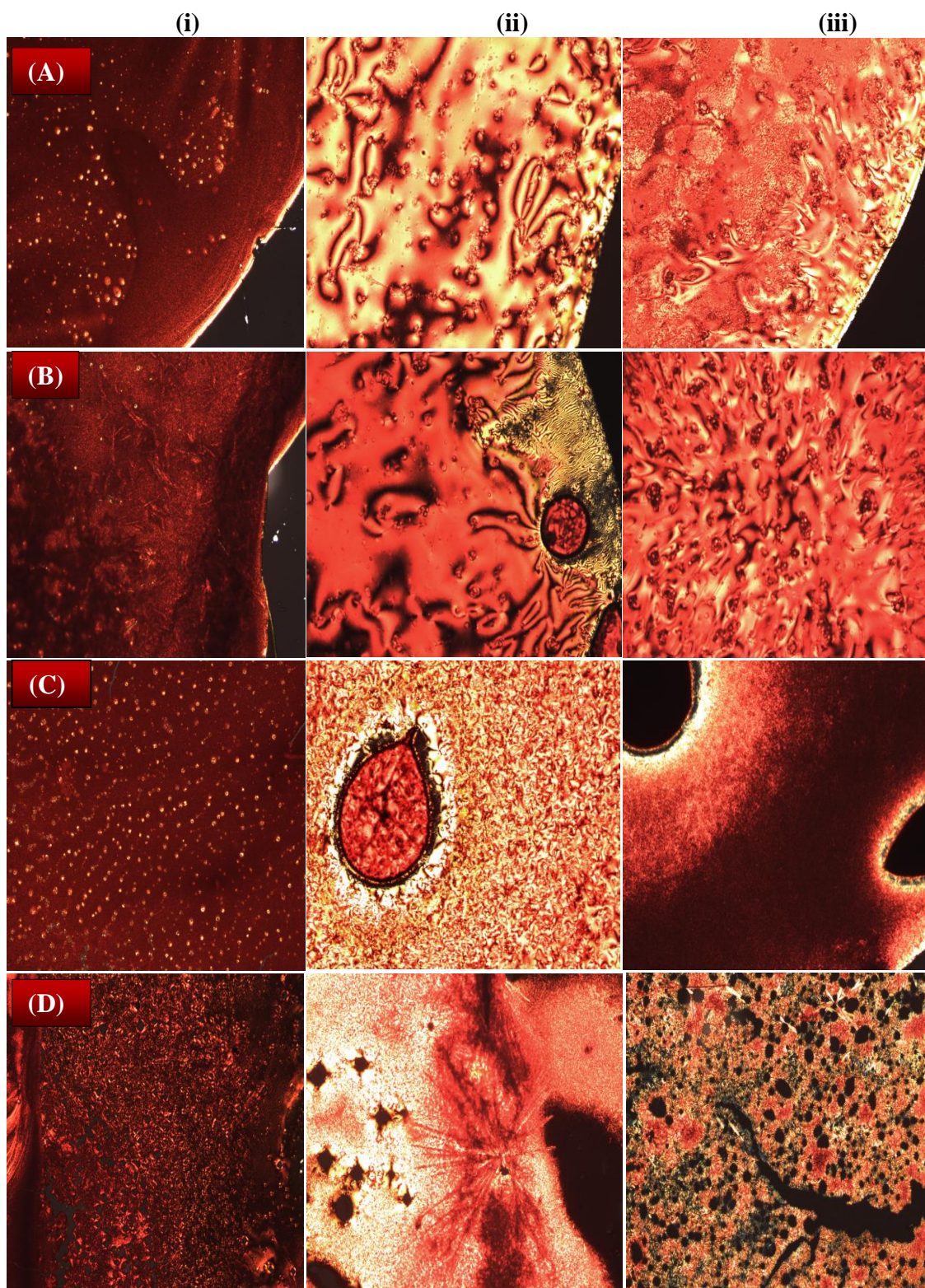
**Figure 7.2 – Polarised microscope images of all blend ratios; (A) 4:3 mol, (B) 1:1 mol, (C) 1:2 mol, (D) 1:3 mol, (i) at room temperature before heating, (ii) heated above Cr→N transition temperature of 3, (A) 250°C, (B) 230°C (C) 215°C and (D) 210°C , (iii) cooled back to room temperature, 25°C. Image sizes are 1mm x 1mm.**

Figure 7.2(i) shows a dark image for each of the blends at room temperature, before being heated. As discussed in chapter 2.3.4, a dark image indicates a lack of birefringence in the sample being viewed. The blends under study here appear to be in a crystalline state initially, and this is confirmed by the lack of an observed glass transition on the first cycle of the DSC shown in figure 7.1. Furthermore, the small bright areas in these images may represent small birefringent crystals. As the samples were heated there was no discernible change in the polarised image until the Cr→I transition temperature of **3**, 180°C, had been exceeded.

The images in figure 7.2 (ii) shows birefringent areas forming for each of the blends, which confirms that a Cr→N transition has taken place. Further, the schlieren texture shown indicates that this is a nematic liquid crystal state, as explained in chapter 1. This is particularly evident for the 4:3 and 1:1 mol blends, which show the characteristic features of the schlieren texture. The 4:3 blend shows more birefringence than the 1:1 blend, due to the higher concentration of donor material in the former. The 1:2 and 1:3 mol blends do not exhibit the detailed schlieren features, although both images show birefringence. The higher content of the acceptor material in these blends appears to have produced a mixture with isotropic and birefringent areas. This is particularly evident for the 1:3 blend, with an image comprised of bright and dark areas in figure 7.2 (D) (ii). However, the dark areas may represent groups of very small crystallites which appear dark due to the thickness of the material in these areas. A nucleated crystal can also be seen forming in this image.

When heated above the Cr→I transition identified by the DSC measurements, the polarised image became completely dark for the 1:2 and 1:3 mol blends, indicating an isotropic phase for both donor and acceptor. The DSC plots do not show a distinct clearing point N→I for the donor, possibly because of its low enthalpy in comparison to that of the Cr→I transition of **4**. We note a small shoulder at 265°C in the 1:3 scan.

However, for the 4:3 and 1:1 mol blends an image remained after the Cr→I transition, as shown in figure 7.3.
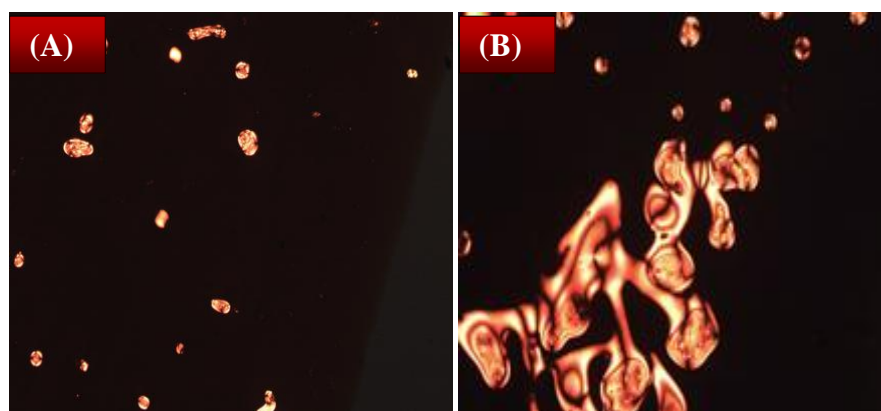


**Figure 7.3 - Polarised microscope images slightly below 300°C for (A) 4:3 mol and (B) 1:1 mol.**

Figure 7.3 shows that although the acceptor has become isotropic, according to the DSC measurements, some of the donor material remains in a nematic phase. This indicates phase separation of the donor and acceptor, leading to droplets of pure material. At 300°C these images became completely dark as the donor completed the nematic to isotropic transition.

Upon cooling the samples, the birefringence seen in figure 7.2 (ii) first appeared at around 285°C for the 4:3 and 1:1 mol blends. For the 1:2 and 1:3 mol blends the images in figure 7.2 (ii) did not appear until cooled to around 235°C and 210°C respectively. For the 1:3 mol blend this implies that the donor becomes nematic only when the acceptor crystallises out.

The images in figure 7.2 (iii) were taken after cooling the samples back to room temperature. It appears that the liquid crystal state has been 'frozen' into place as a glass is formed. Relatively bright schlieren features are still evident for blends 4:3 and 1:1, due to the larger donor concentration. The 1:2 and 1:3 blends have birefringent and isotropic areas, relating to the donor and acceptor regions respectively.

To summarise, the blends seem to mostly retain distinct donor and acceptor phases. The acceptor Cr→I transition is clearly defined by the DSC. Clearly the donor transitions occur at slightly higher temperatures for the 4:3 and 1:1 blends. The acceptor component crystallises during cooling and the donor component cools to a nematic glass.

# 7.3 Active Layer Morphology

Here we investigate the morphology of the thin film for each of the PV devices characterised in the next section. Photovoltaic devices were fabricated using **3** as the donor and **4** as the acceptor material, using each of the four blend ratios investigated in the previous section. The standard processing conditions described in chapter 3.7 were used and all devices were annealed for one hour at 120°C. For each blend ratio, one device was then annealed at 200°C for 5 minutes in order to exploit the self organisation of the liquid crystal phase. It was important to anneal at 120°C initially to ensure that all of the casting solvent had evaporated, before raising the temperature to 200°C which is well above the boiling point of chlorobenzene at 131°C. Each device fabricated has been assigned a number as shown in table 7.4, to aid in the analysis of the results.

**Table 7.4 – Blend ratio and maximum annealing temperature for devices 1 – 8.**

| Device No. | Blend Ratio | Max Annealing Temperature |
|---|---|---|
| 1 | 4:3 mol | 120°C |
| 2 | 4:3 mol | 200°C |
| 3 | 1:1 mol | 120°C |
| 4 | 1:1 mol | 200°C |
| 5 | 1:2 mol | 120°C |
| 6 | 1:2 mol | 200°C |
| 7 | 1:3 mol | 120°C |
| 8 | 1:3 mol | 200°C |
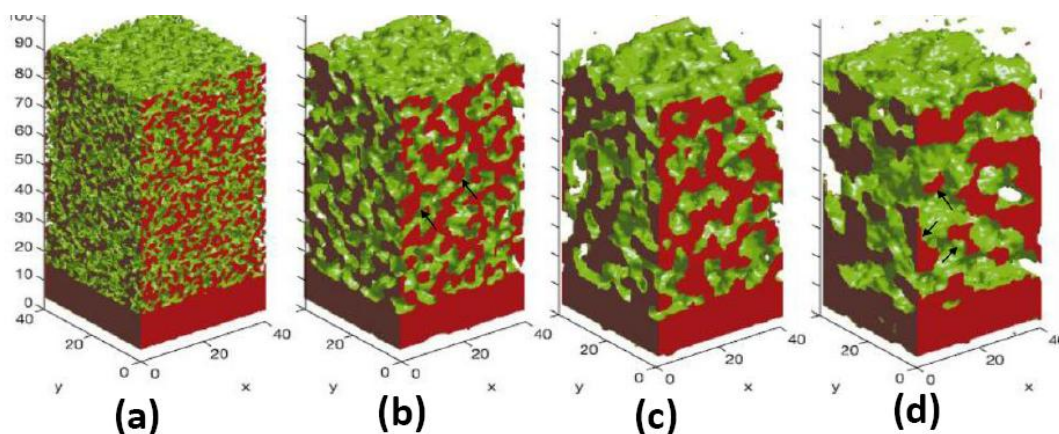
**Figure 7.4 – The simulated effects of annealing on the bulk morphology of a CuPc:PTCBI (4:1) thin film. CuPc is shown in red, PTCBI is left transparent and the interface between the two materials is shown in green. The simulated temperature was increased from (a) lowest to (d) highest[216].**

Peumans et al[216] simulated the effect of annealing at increasing temperatures on the morphology of a donor/acceptor thin film as shown in figure 7.4. It can be seen how the surface topography can give an insight into the bulk morphology. The surface roughness features correlate with the donor-acceptor domains. The following analysis assumes this relationship.

An atomic force microscope (AFM) was used to image each of the blended thin films, as described in chapter 3.6. We investigate areas of $5\times5\mu m^2$, $1\times1\mu m^2$ and $500\times500nm^2$, each area being composed of $1024\times1024$ data points. Figures 7.5 and 7.6 show 2D and 3D images respectively of all eight films, the main images are $5\times5\mu m^2$ with the $1\times1\mu m^2$ image inset for 2D. For each blend ratio it is shown that the roughness increases significantly when the sample was annealed at 200°C. Figure 7.5 shows that the samples annealed at high temperature have elongated grains, which appear crystalline, with well defined edges when the acceptor concentration is high. The films annealed at 120°C have more isotropic features.
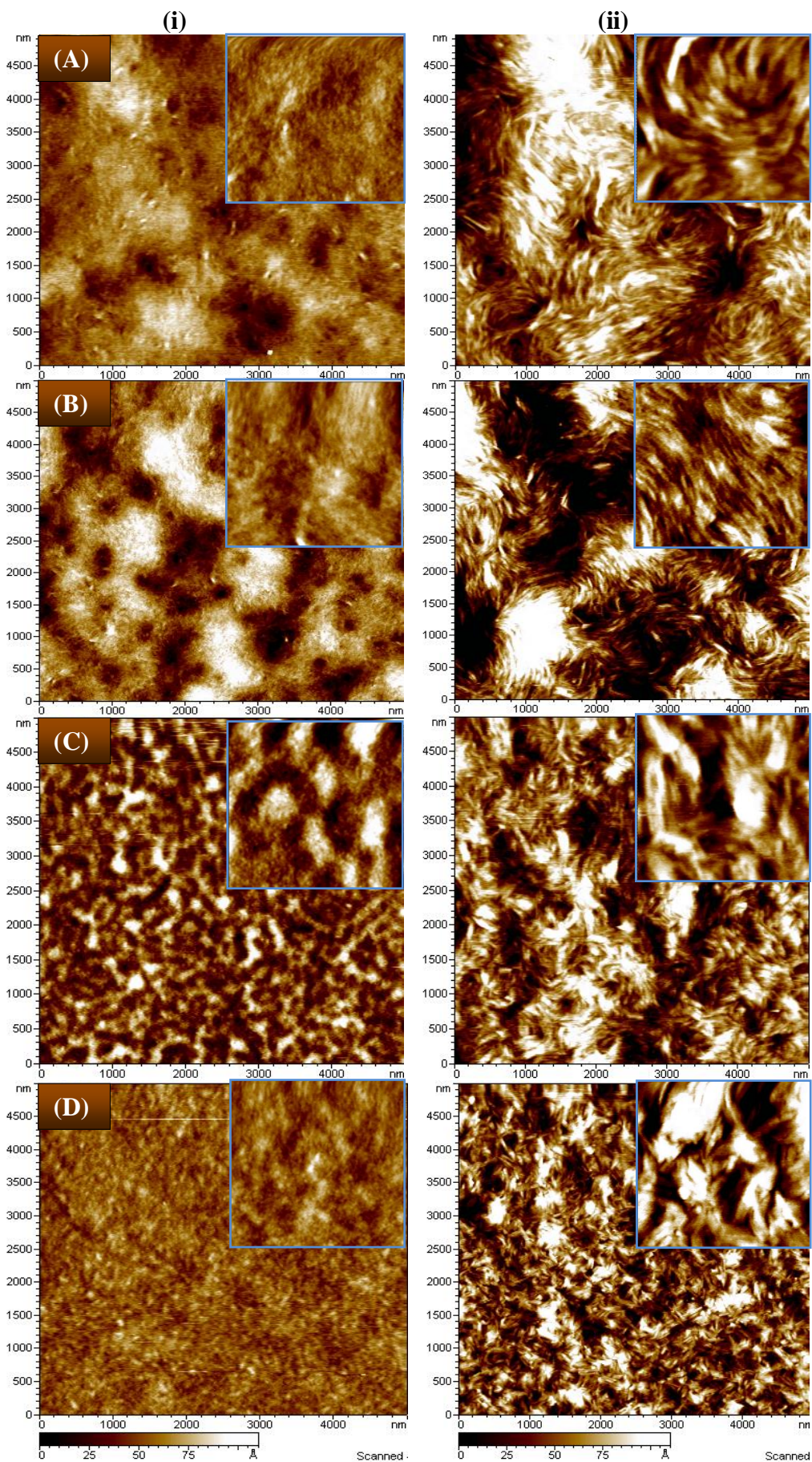
**Figure 7.5 – AFM topography image for all devices; (A) 4:3 mol, (B) 1:1 mol, (C) 1:2 mol, (D) 1:3 mol, left (i) annealed at 120°C and right (ii) annealed at 200°C. Main images are 5μm x 5μm with 1μm x 1μm inset.**
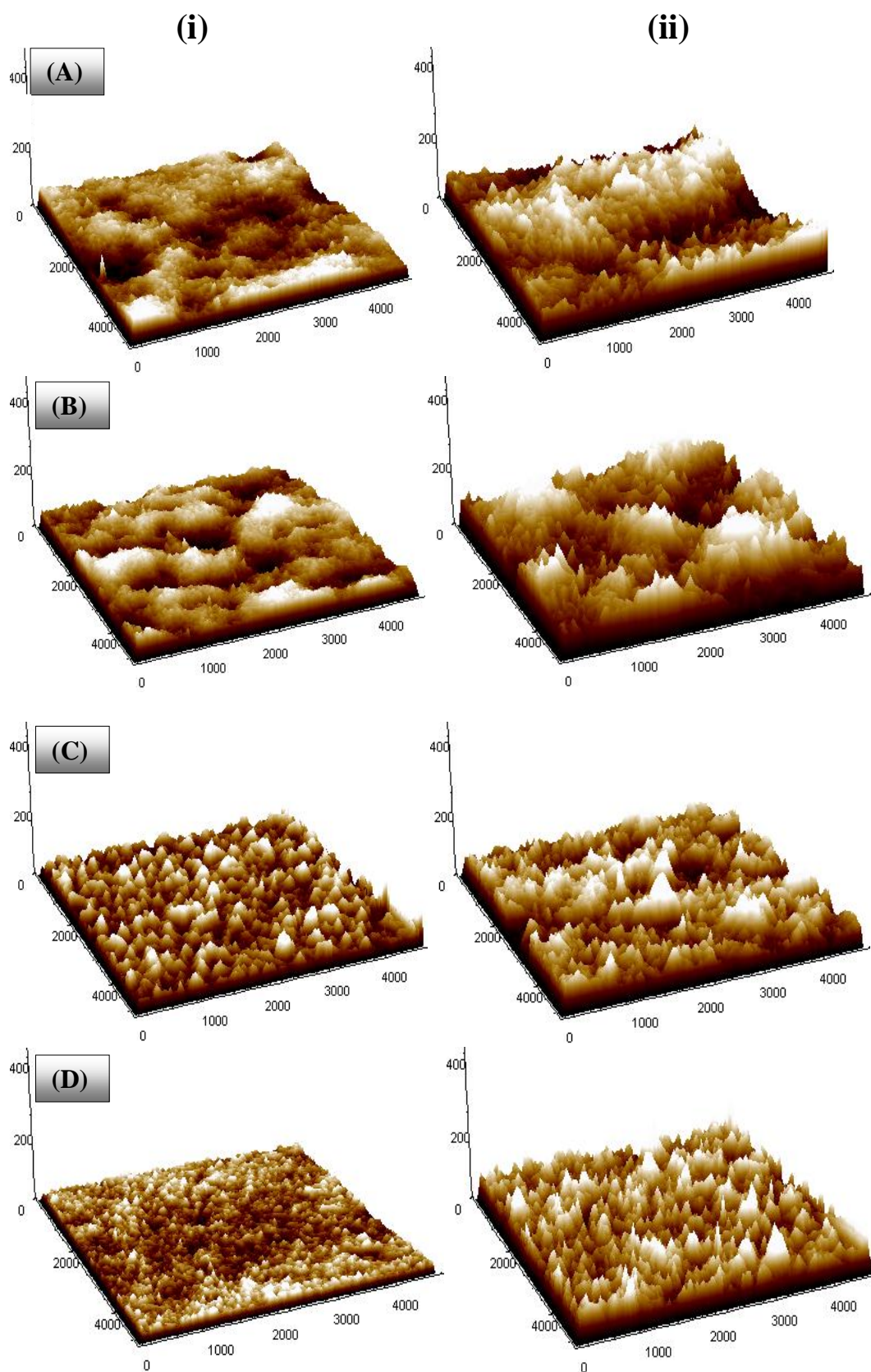
**Figure 7.6 – AFM 3D topography images for all devices; (A) 4:3 mol, (B) 1:1 mol, (C) 1:2 mol, (D) 1:3 mol, left (i) annealed at 120°C and right (ii) annealed at 200°C. Images are 5000nm x 5000nm; all units indicated in figure are nm.**

229
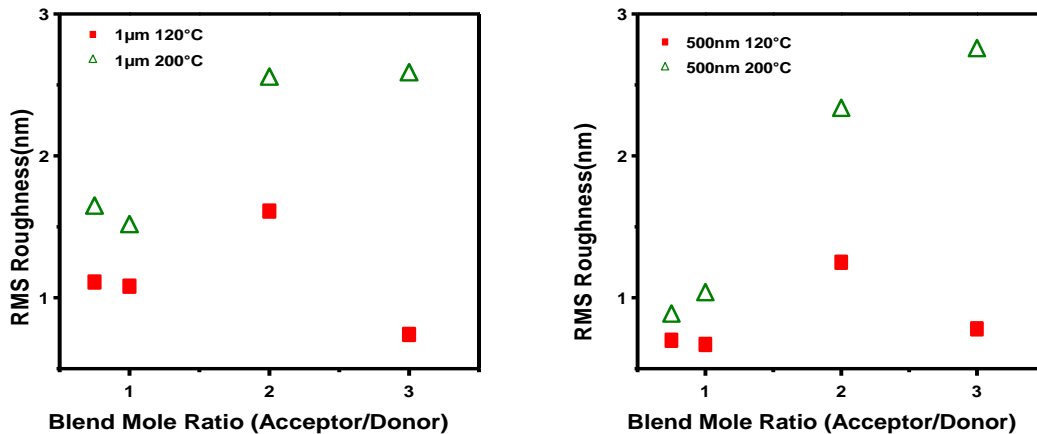
**Figure 7.7 – RMS roughness for each sample from 1µm image (left) and 500nm image (right).**

Figure 7.7 shows the RMS roughness as a function of the blend ratio for both annealing temperatures, using data extracted from the 1µm and 500nm images. This confirms what is shown visually in figures 7.5 and 7.6, i.e. that the roughness increases significantly after high temperature annealing.

Whilst the roughness drops from the 1:2 to 1:3 mol blends annealed at 120°C, the effect of annealing at 200°C on roughness is greatest for the 1:3 blend giving it the roughest active layer of all the devices. In contrast the 4:3 and 1:1 mol blends show a relatively small increase in roughness on annealing at 200°C. The 1:2 mol sample annealed at 120°C is anomalously rough.
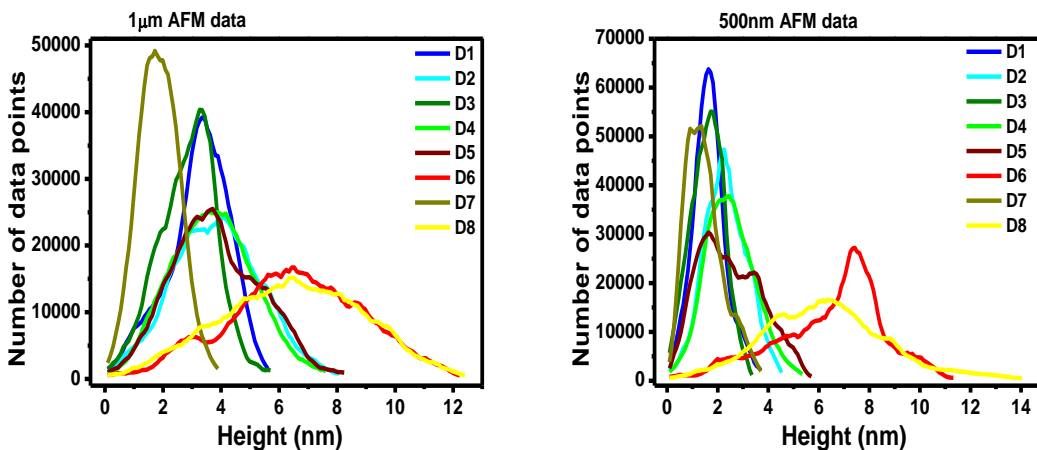


**Figure 7.8 – Height distribution for each sample from 1µm image (left) and 500nm image (right).**

Figure 7.8 shows the distribution of the surface height for all devices, using data from the 1μm and 500nm images. **D6** and **D8** are shown to have the widest range of height variation, This may lead to a poor contact between the active layer and the cathode, which in turn may lead to a poor fill factor as described in chapter 6.
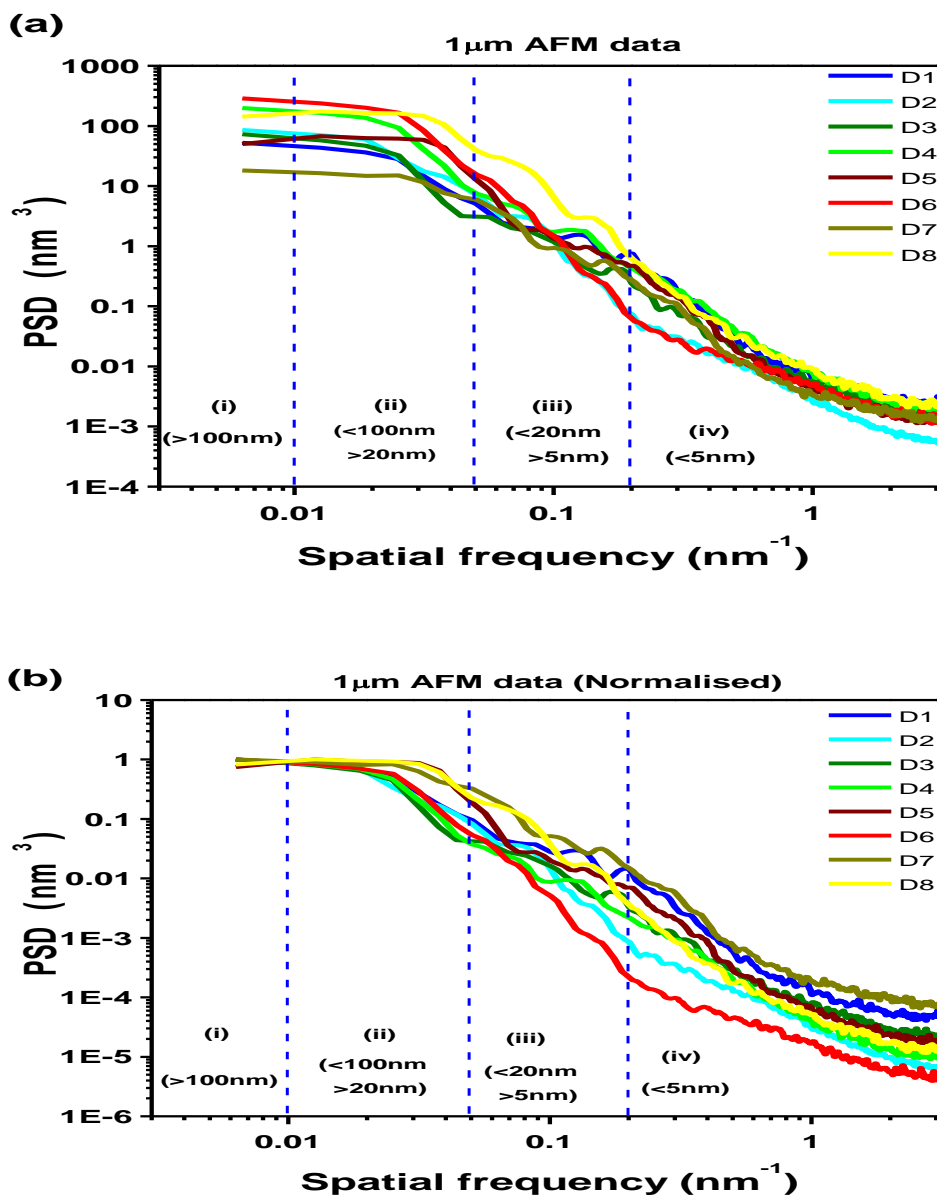


**Figure 7.9 – Power spectral density for each sample from 1μm image (a) raw data and (b) normalised.**

By performing a Fourier Transform on the AFM image data, as described in chapter 3.6, the power spectral density information was obtained and is shown in figure 7.9. The following analysis is based on the assumption that the morphological features reflect

phase separated domains. The plot is spilt into 4 regions to aid analysis of domain size. The lowest frequency (i) relates to domain sizes larger than 100nm, the second section (ii) relates to domains sizes from 20nm to 100nm, the third (iii) relates to domains from 5nm to 20nm and the highest frequency range (iv) indicates domains smaller than 5nm. Ideally we are looking for a morphology with domain sizes in region (iii) to allow the majority of excitons to reach a donor/acceptor interface within their 10nm diffusion length, as discussed in section 1. Domain sizes smaller than 5nm, whilst good for charge separation, may be too fine to allow for efficient charge transport. A recent study by Nam et al[217] found the optimum domain size to be around 6nm for P3HT:PCBM blends, in respect of the photocurrent and overall power conversion efficiency. Domains smaller than this were found to result in a poorly percolated domain structure and hence increased the probability of charge recombination.

Figure 7.9(a) shows that **D8** has by far the most domains overall, due the higher roughness of the thin film. Hence the PSD data was normalised in figure 7.9(b) to compare the proportion of different domain sizes for each device, rather than absolute number. Figure 7.9(b) shows that the highest proportion of domain sizes in region (iii) for efficient charge separation are produced by **D7** and **D8**, the 1:3 mol blend devices. When this blend is annealed at 200°C the proportion of smaller domains in the regions reduces slightly and the proportion of domains in region (iv) reduces significantly. This agrees with the images of figure 7.5 and 7.6 which show a fairly uniform domain size on high temperature annealing. Overall **D8** should produce a better device morphology than **D7**, as the significant reduction in domains <5nm will help produce better percolated charge pathways and reduce non-geminate recombination during charge transport. Similarly the fraction of small domains is significantly less for **D2** and **D6** in comparison to **D1** and **D5**. There appears to be no difference between the proportion of each domain size for **D3** and **D4** in figure 7.9(b).

Overall AFM shows that annealing at 200°C produces increased surface roughness and a greater proportion of domains in the range 10 – 20nm. This is consistent with the DSC results reported earlier. Annealing of the blended samples at 120°C, below the melting point, does not allow reorganisation of the non-equilibrium blend distribution obtained on evaporation. When the samples are annealed above the melting point of **3** the molecules can reorganise and form larger phase separated domains.

# 7.4 Photovoltaic Device Performance

Here we investigate the photovoltaic device performance of **D1** – **D8**, which were fabricated as described in the previous section.
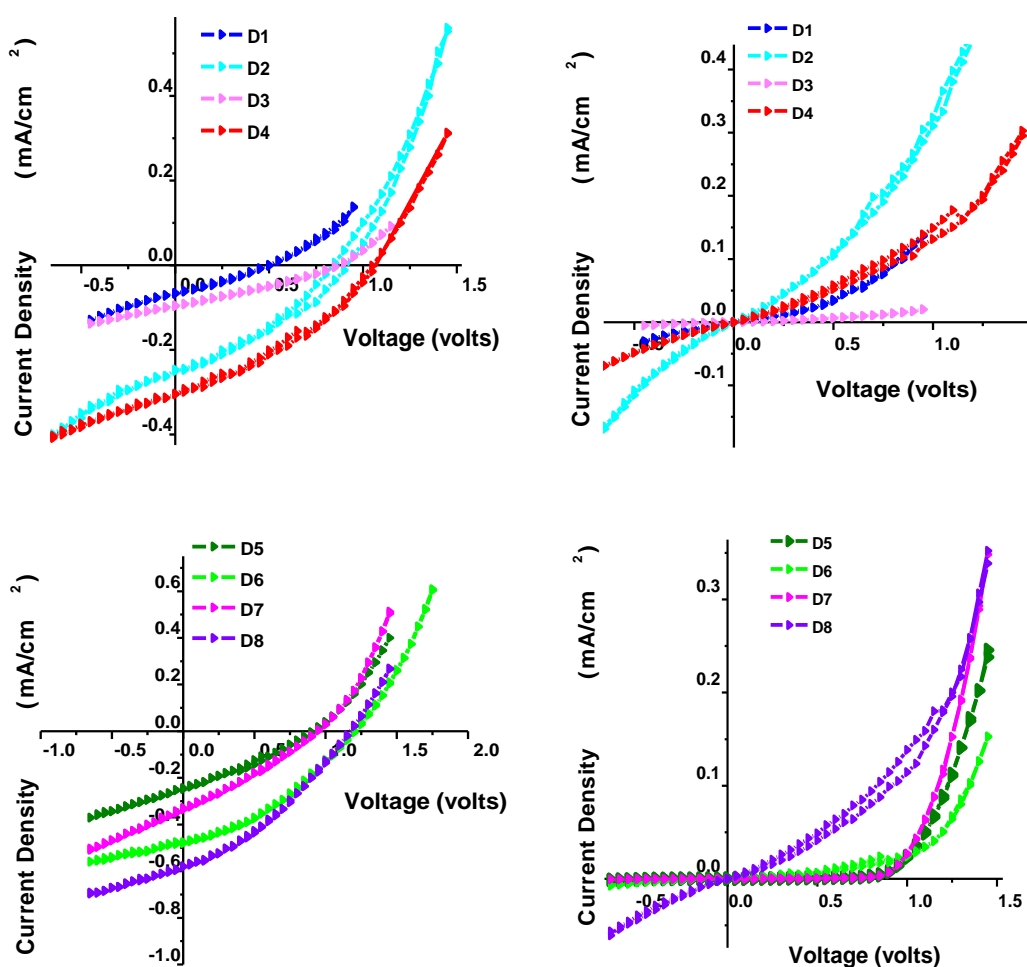


**Figure 7.10 – Light IV characteristics for all blends at an input irradiance of 24mWcm$^{-2}$ at a wavelength of 462nm (left) Dark IV characteristics (right).**

233

Figure 7.10 shows that the devices heated above the liquid crystal transition temperature produce a significantly higher photo current than those annealed at a maximum of 120°C. This indicates that high temperature annealing of the blend has improved the morphology for charge generation, for all blend ratios. The highest photocurrent was produced by **D8**, which had the highest ratio of acceptor material in the blend. Reducing the ratio of acceptor leads to a reduction in the photocurrent measured.

Figure 7.10 also shows the dark IV characteristics for each device. Here we see that the best rectification properties are the devices which were annealed at the standard temperature of 120°C. When heated above the liquid crystal transition temperature it can be seen that some current flow is evident in the reverse bias. This indicates that the improvement in photocurrent is accompanied with some current leakage. The blend ratio 1:2 mol (**D5** and **D6**) shows the best rectification behaviour overall, with just a small deviation from the ideal diode behaviour when annealed at 200°C.

**Table 7.5 – PV device performance parameters for all devices upon excitation with 24mWcm$^{-2}$ at 462nm**

| Device Number | $J_{SC}$ (Acm-2) | $V_{OC}$ (V) | FF | $\eta$ (%) | EQE (%) | $R_s$ (kΩcm$^{-2}$) | $R_{sh}$ (kΩcm$^{-2}$) | $R_s$ / $R_{sh}$ |
|---|---|---|---|---|---|---|---|---|
| D1 | $6.71 \times 10^{-5}$ | 0.50 | 0.31 | 0.04 | 0.75 | 5.10 | 9.76 | 0.52 |
| D2 | $2.49 \times 10^{-4}$ | 0.88 | 0.35 | 0.32 | 2.77 | 1.70 | 5.64 | 0.30 |
| D3 | $9.64 \times 10^{-5}$ | 0.87 | 0.30 | 0.11 | 1.07 | 4.17 | 11.5 | 0.36 |
| D4 | $3.05 \times 10^{-4}$ | 1.06 | 0.36 | 0.49 | 3.40 | 1.51 | 6.48 | 0.23 |
| D5 | $2.44 \times 10^{-4}$ | 0.91 | 0.32 | 0.30 | 2.72 | 2.38 | 5.35 | 0.44 |
| D6 | $4.80 \times 10^{-4}$ | 1.20 | 0.36 | 0.86 | 5.34 | 1.37 | 8.27 | 0.17 |
| D7 | $3.35 \times 10^{-4}$ | 0.94 | 0.30 | 0.39 | 3.73 | 1.80 | 3.65 | 0.49 |
| D8 | $5.80 \times 10^{-4}$ | 1.17 | 0.35 | 0.98 | 6.46 | 1.18 | 4.56 | 0.26 |

The PV device parameters are presented in table 7.5. In order to aid analysis we now examine plots of each characteristic in turn.



**Figure 7.11 – Variation of the $J_{SC(max)}$ and $V_{OC}$ with blend ratio and maximum annealing temperature.**

Figure 7.11 shows the variation of the $J_{SC(max)}$ and $V_{OC}$ with blend ratio and maximum annealing temperature. It is shown that the $J_{SC(max)}$ increases with the amount of acceptor used in the blend. It is also clearly shown that annealing above the liquid crystal transition temperature leads to a significant increases in the $J_{SC(max)}$. This agrees with the work by Sun et al[142] in 2007, who reported increases of 200%-400% in the $J_{SC(max)}$ using PCBM with liquid crystalline porphyrins. The improvement in efficiency was attributed to thermally induced alignment of the porphyrins in the columnar discotic phase. This alignment provided efficient charge transport along the columnar axis and optimised light harvesting[142]. Here, our devices show an increase in the $J_{SC(max)}$ in the range of 70% to almost 300% depending on the blend ratio, which is attributed to an improved donor/acceptor interface. The $V_{OC}$ is shown to increase with acceptor concentration, although a small reduction is shown as the ratio increases from 1:2 to 1:3 mol for the devices annealed at 200°C. However, for all blend ratios we see an increase in the $V_{OC}$, between 22- 76% depending on the blend ratio, when we anneal at 200°C.
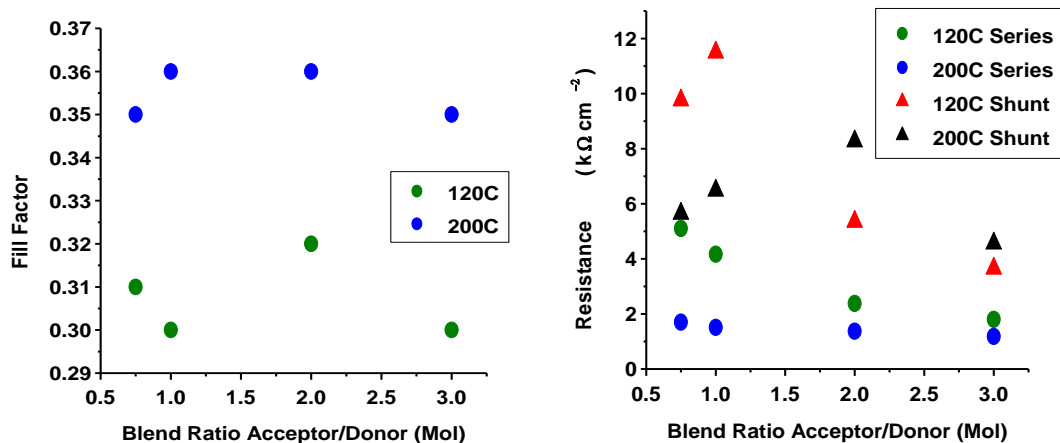
**Figure 7.12 – Variation of the *FF* and resistance ($R_s$, $R_{sh}$) with blend ratio and maximum annealing temperature.**

Figure 7.12 shows the variation of *FF* and resistance ($R_s$, $R_{sh}$), with the highest *FF* produced by the 1:2 mol blend. The *FF* increases for all blend ratios when annealed at 200°C. It is shown that $R_s$ reduces as the acceptor ratio is increased, and a further reduction is shown for devices heated at 200°C, which in turn contributes to a higher *FF*. The $R_{sh}$ is shown to initially increase with acceptor ratio, before falling at higher acceptor ratios. The 4:3 and 1:1 mol blends both show a reduced $R_{sh}$ when we anneal at 200°C which contributes to a lower *FF*, whilst the opposite is true for the 1:2 and 1:3 mol blends. Overall, lowest ratios of $R_s$ / $R_{sh}$ are 0.17 and 0.23 for **D6** and **D4** respectively, which both produced the best *FF* of all our devices here, at 0.36.
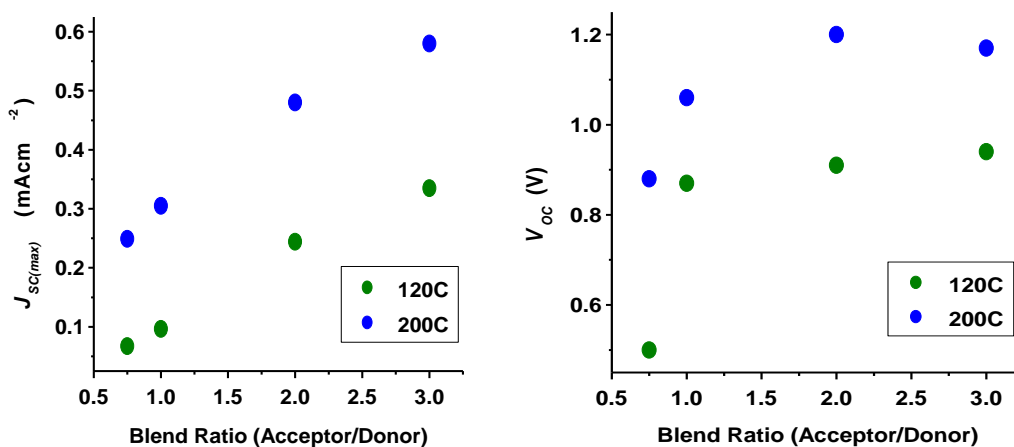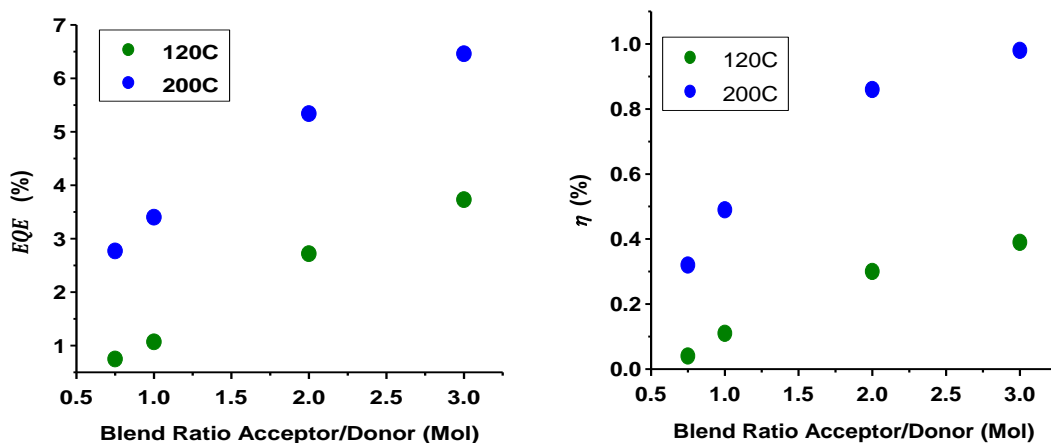
**Figure 7.13 – Variation of the *EQE* and $\eta$ with blend ratio and maximum annealing temperature.**

Figure 7.13 shows the variation of *EQE* and $\eta$ with the acceptor to donor mole ratio. It is shown that the *EQE* increases with acceptor concentration in the blend, indicating more efficient charge separation. A significant increase in *EQE* is also shown for all blend ratios when we anneal at 200°C. The overall device power conversion efficiency, $\eta$, is influenced by all of the characteristics described so far. It is shown that performance increases with acceptor concentration, the 1:3 mol blend producing the highest overall device efficiency. It is further shown that device performance increases significantly for all blend ratios when high temperature annealing is used. Wang et al[218] have just published similar results for a liquid crystalline P3HT/$C_{60}$-bp-CN blend, reporting an increase in efficiency from 0.22% to 0.65% when annealing above the LC transition temperature.

The best performing device here was **D8**, 1:3 mol blend heated to 200°C, which produced an efficiency of 0.98%. The improved device efficiency relative to **D7**, an increase of 150%, was mainly due to a 73% increase in the photocurrent and a 24% increase in the $V_{OC}$.
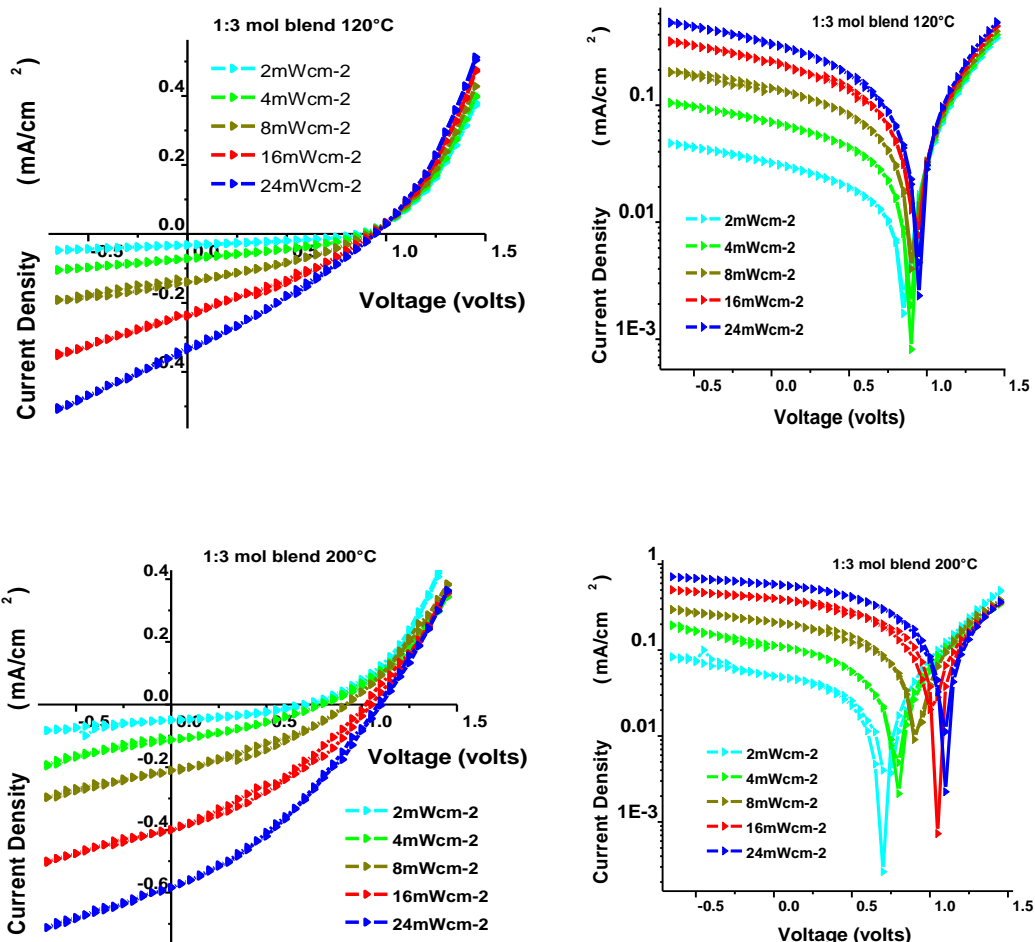
**Figure 7.14 – Light IV characteristics for 1:3 mol blend at 120°C and 200°C, linear plot (left) and semi log plot (right), at various incident intensities.**

Figure 7.14 shows the IV characteristics of the best performing blend, 1:3 mol, at 120°C and 200°C as the incident intensity is varied. It is shown that there is very little variation of the $V_{OC}$ for the blend annealed at 120°C. However, this changes on annealing at 200°C and figure 7.14 shows that the $V_{OC}$ now varies with intensity. As discussed in chapter 5, the dependence of $V_{OC}$ on input light intensity may be due to current leakage. Figure 7.10 shows that the increased photocurrent produced when we anneal at 200°C is accompanied by current leakage. At high intensity this leakage is small relative to the photo generated current, and hence a high $V_{OC}$ is seen. However, at lower intensities the leakage becomes more significant, leading to a reduced $V_{OC}$ as shown in figure 7.14 for the blend annealed at 200°C.
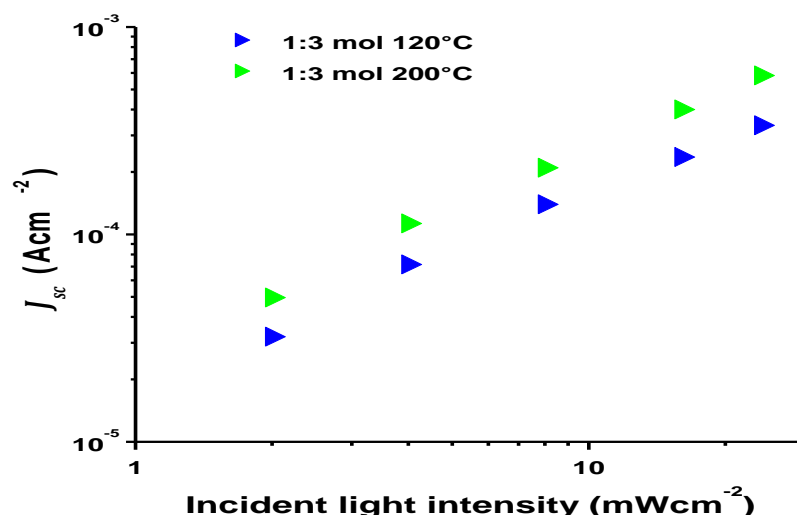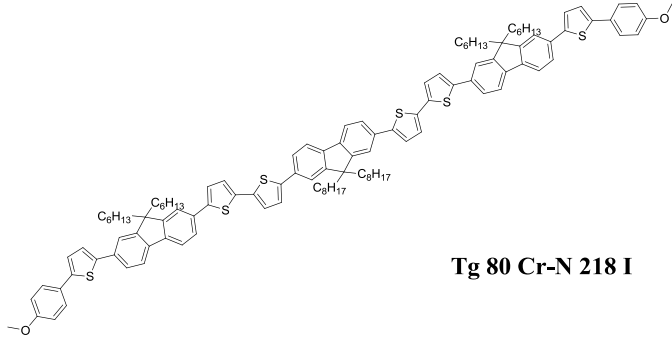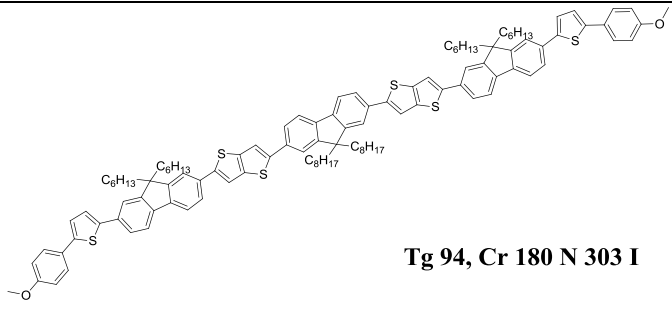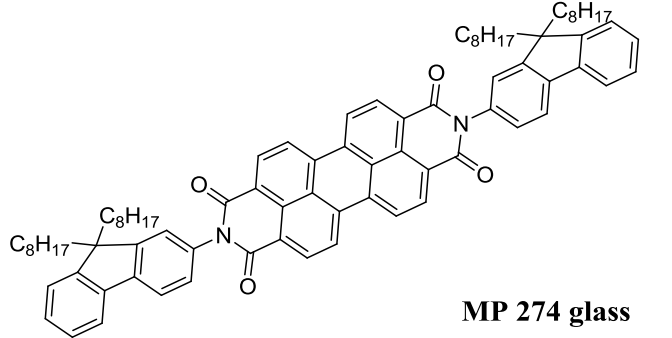
**Figure 7.15 – Log plot of *Jsc* as a function of incident light intensity.**

Figure 7.15 shows a double logarithmic plot of the $J_{SC}$ as a function of incident light intensity. As discussed in chapter 6.2.1 the slope from this plot, $\alpha$, indicates the dominant charge recombination type. The value found for $\alpha$ was 0.90 and 0.99 for the blends annealed at 120°C and 200°C respectively. This means that the small amount of bimolecular recombination which was evident when the device was annealed at 120°C has been virtually eliminated when the active layer is annealed at 200°C. The reduction in the number of small domains and improved phase separation may give better percolated charge pathways reducing the non geminate charge recombination. As bimolecular recombination may be due to low charge carrier mobility, it is possible that annealing in the liquid crystal phase has also improved the charge carrier mobility of the blend. Many studies have shown that mobility can be improved by utilising the liquid crystal phase[72,73,219,70], which supports our findings here. It has also been shown that mobility is improved for organic blends with liquid crystal additives[220,221].

# 7.5 Comparison of different donor blends

**Table 7.6 - Chemical Structure, phase transition temperatures and energy levels for compounds 1, 3 and 4.**

| Mate. | Structure | Energy Levels |
|---|---|---|
| 1 |  **Tg 80 Cr-N 218 I** | **IP  EA  E$_{g,op}$ (eV)** <br><br> $^O$ **5.52 , 3.15, 2.37 (R)** <br><br> **SPK516** |
| 3* |  **Tg 94, Cr 180 N 303 I** | **IP  EA  E$_{g,op}$ (eV)** <br><br> $^O$ **5.53 , 3.1 , 2.43 (R)** <br><br> **SPK523** |
| 4* |  **MP 274 glass** | **IP  EA  E$_{g,op}$ (eV)** <br><br> $^R$ **6.31, 4.19, 2.12 (QR)** <br><br> **MPA340** |

Here we consider the effects of annealing at different temperatures for two different donor blends, using donors **1** and **3** with acceptor **4**. The PV device data investigated in this section for the blend composed of donor **1** and acceptor **4** was produced by Alkhalifah[57], whilst the DSC data and polarisable microscope/AFM images were produced by me. Donor **1** has a glass transition at 80°C and a nematic to isotropic transition at 218°C. In this section we compare blends of 1:3 mol concentration for both donor systems.
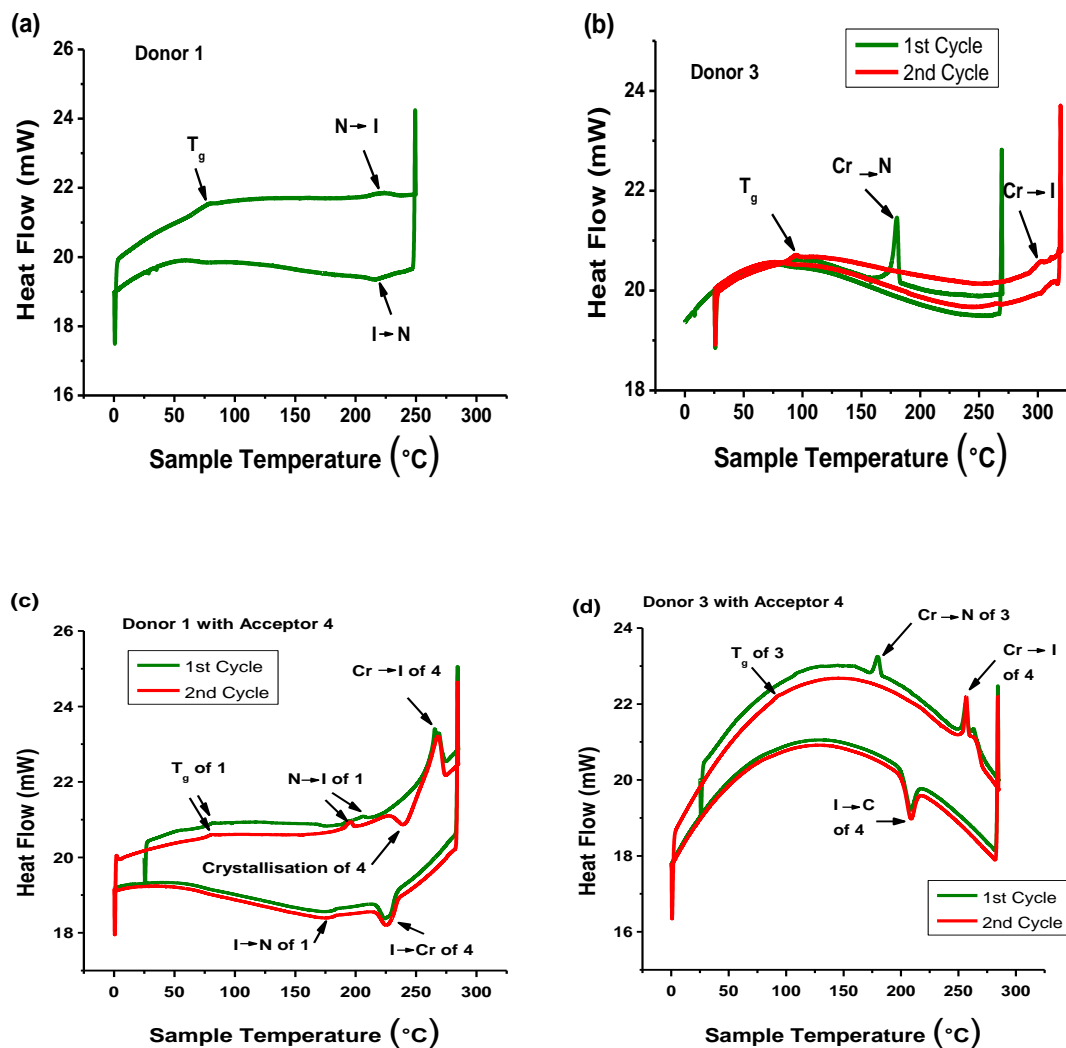
**Figure 7.16 - DSC trace for (a) Donor 1, (b) Donor 3, (c) 1 blended with 4 (d) 3 blended with 4, both blends are 1:3 mol ratio. DSC measurements of pure compounds (a) and (b) were made by Dr. Stuart Kitney, University of Hull.**

Despite the similarities in chemical structure for the two donors figure 7.16 illustrates that the phase transitions temperatures differ significantly for each compound, and also for each donor blend. A glass transition is shown for the blend using donor **1** at around 82°C, very close to that of the pure donor material. The clearing point of the donor component is 206°C during the 1st cycle and 196°C during the second cycle. Both heating cycles show a lower clearing point than that of the pure donor (218°C) due to the presence of the acceptor in the blend.

The Cr→I transition of the acceptor component is consistent over both heating cycles at around 267°C, only slightly lower than that of the pure acceptor (274°C). During cooling, re-crystallisation of the acceptor component is shown to occur at around 225°C for both cycles. There is also a small I→N transition at around 175°C for the donor component, significantly lower than that for the pure donor (215°C). There is also a feature only present during the second heating cycle at around 240°C, indicating an exothermic reaction. Here the acceptor partially re-crystallises out of the isotropic donor, quickly followed by the Cr→I transition at 267°C. This is due to only partial re-crystallisation of the acceptor occurring during the cooling cycle, meaning that some of the acceptor must be blended with the donor in the nematic phase.

Figure 7.17(a-d) shows the polarising microscope images for the donor **1** blend. The re-crystallisation of **4** during heating can be seen in figure 6.17 (a) against the dark background of **1** in the isotropic phase. Upon further heating above the Cr→I transition at around 270°C, the image becomes completely dark indicating a fully isotropic phase. Upon cooling the image in figure 7.17 (b) is visible between 225°C and 175°C. At this stage the nematic component is still in an isotropic phase whilst the acceptor has started to partially re-crystallise. However, a much finer crystalline structure is seen compared to that shown in figure 7.17 (a). Upon cooling below the I→N transition previously dark areas have become birefringent, as shown figure 7.17 (c), suggesting that the mainly donor component has entered the nematic phase. This image remains as the blend is cooled back to room temperature, shown in figure 7.17 (d), suggesting that a nematic glass has been formed by the blend. A comparison of figure 7.17 (d) with figure 7.17 (f) shows a similar end result for both blends, with birefringent and dark areas. This suggests that some phase separation has taken place, the birefringent areas representing the donor in nematic phase whilst the dark areas may indicate acceptor domains.
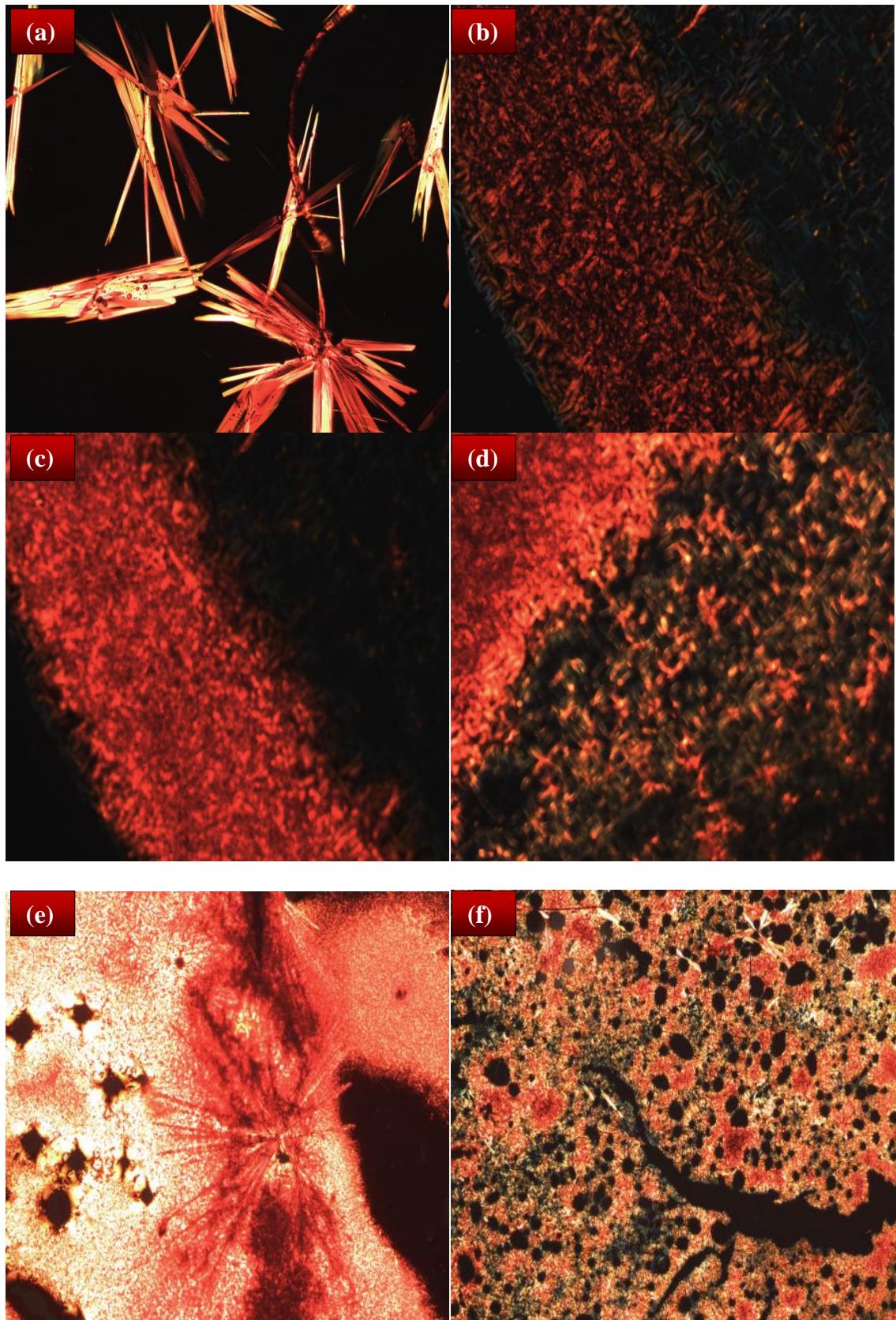
**Figure 7.17 – Polarised microscope images of the blend of 1 and 4 heated to (a) 255°C then cooled from 280°C to (b) 200°C, (c) 150°C and (d) 25°C. The blend of 3 and 4 is shown cooled from 300°C to (e) 210°C and (f) cooled back to room temperature. Images sizes are 1mm x 1mm.**

243

The morphology of the thin film is now investigated for each of the PV devices characterised in this section. Devices 7 and 8 are taken from section 7.4, whilst devices 9, 10 and 11 were prepared and measured by Alkhalifah[57]. All devices were made using the same standard technique as that used in this thesis, and annealing conditions are given in table 7.7.

**Table 7.7 – Blend materials and maximum annealing temperature for devices 7 – 11.**

| Device No. | D/A Materials | Max Annealing Temperature |
|---|---|---|
| 7 | 3 and 4 | 120°C |
| 8 | 3 and 4 | 200°C |
| 9 | 1 and 4 | 50°C |
| 10 | 1 and 4 | 120°C |
| 11 | 1 and 4 | 200°C |

Figures 7.18 and 7.19 show the 2D and 3D images taken for all five devices, the main images are 5x5µm$^2$ with a 1x1µm$^2$ image inset for 2D. It is shown for both blends that the roughness height increases for higher annealing temperatures. **D8** and **D11** were both annealed at the same temperature, 200°C, which means the donor component was in nematic LC and isotropic phase respectively. Both device morphologies show signs of some crystallisation, particularly **D11** which also demonstrated crystallisation in the polarisation microscopy images in figure 6.17(a).
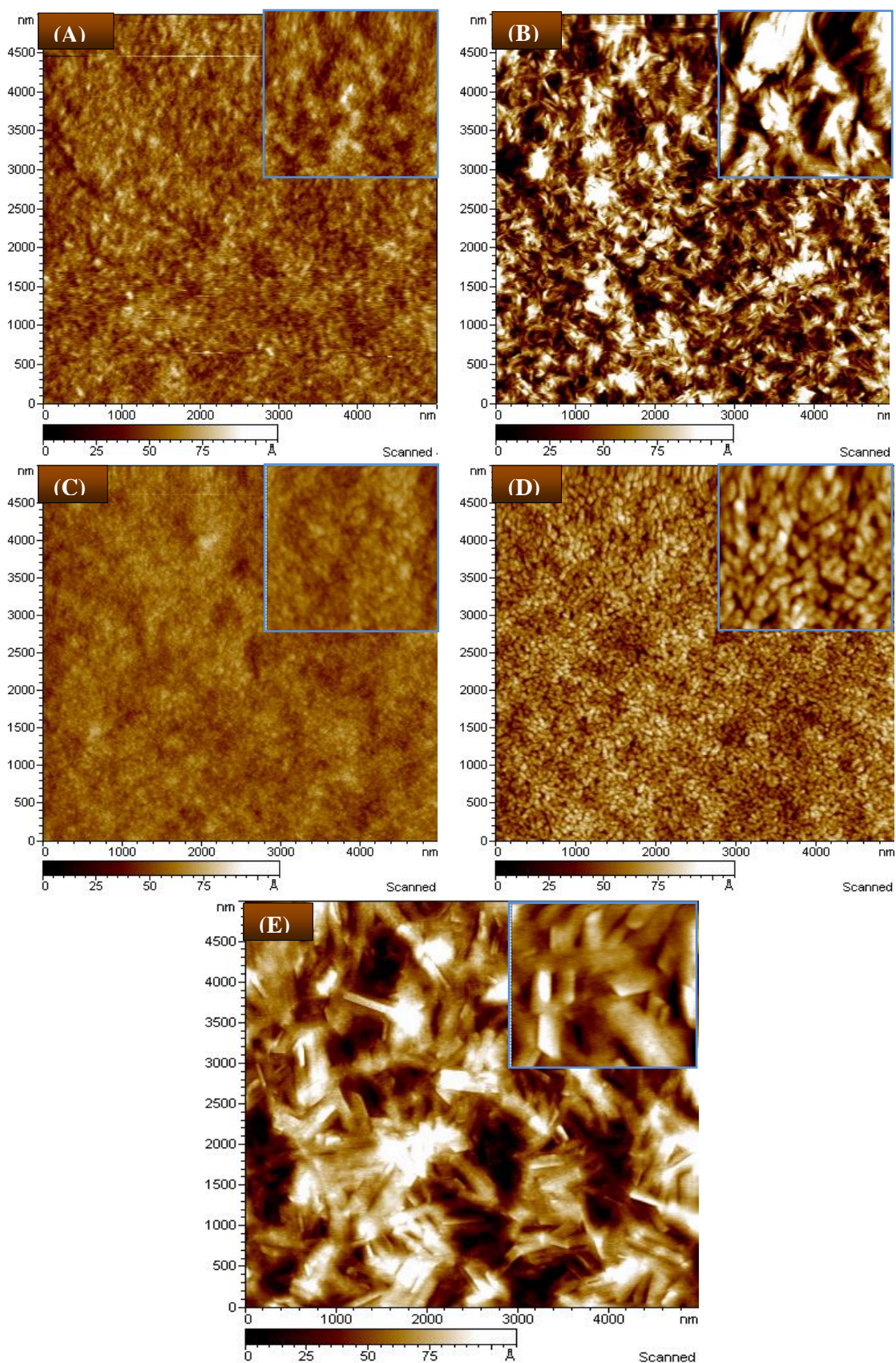
**Figure 7.18 – AFM Topography image for (a) D7, (b) D8, (c) D9, (d) D10 and (e) D11. Main images are 5µm x 5µm² with 1µm x 1µm² inset.**
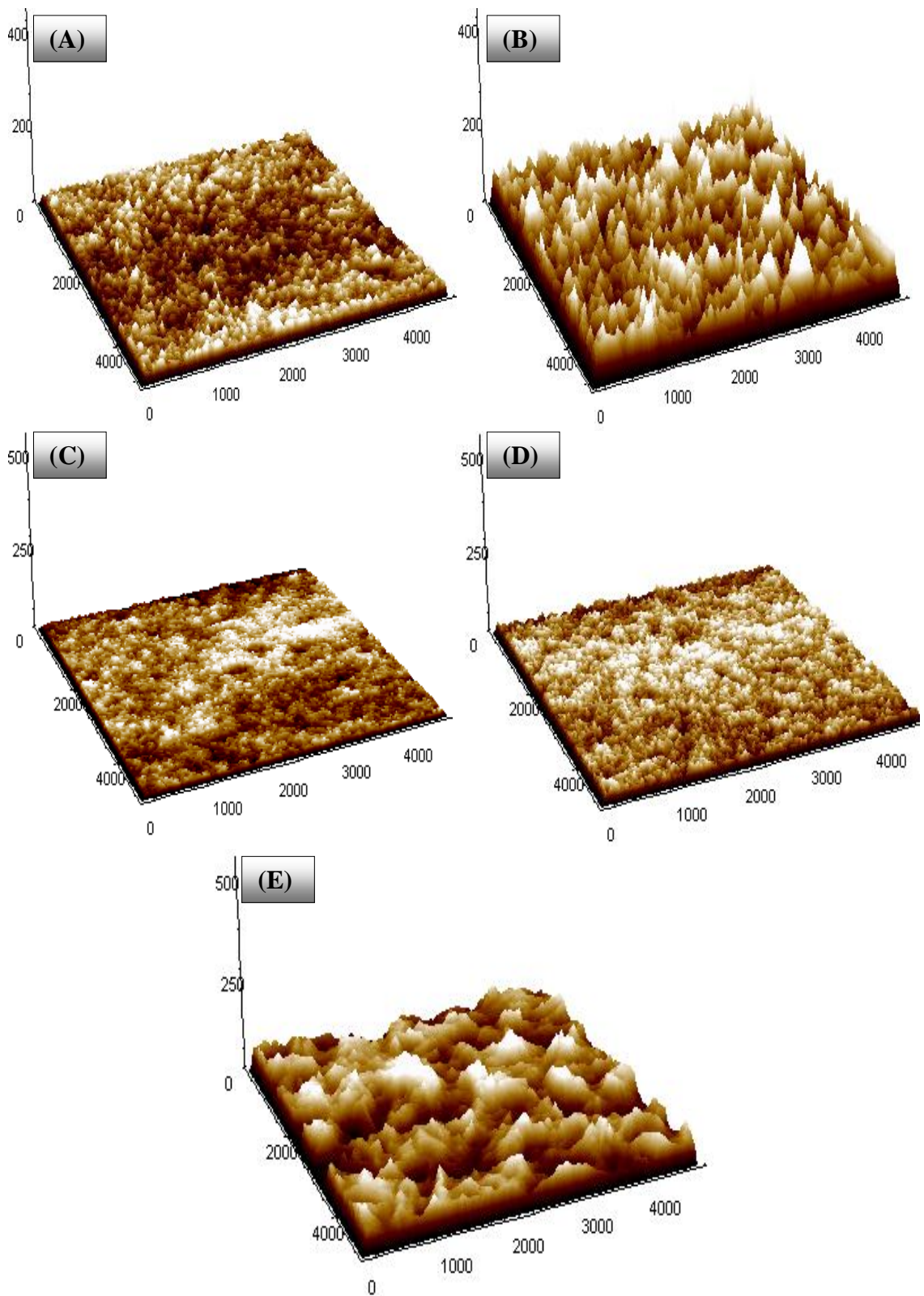
**Figure 7.19 – AFM 3D Topography image for (a) D7, (b) D8, (c) D9, (d) D10 and (e) D11. All units in nm.**

Figure 7.20 shows the RMS roughness (a) and height distribution (b) for each device. Figure 7.20 confirms that the roughness and height distribution increase with temperature for both blends. This increase is far more pronounced for the blend of **3** and **4**.
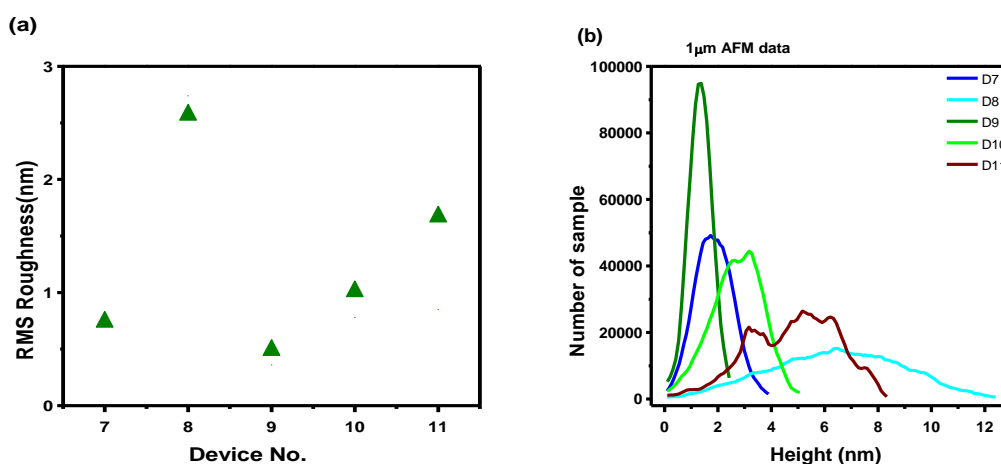


**Figure 7.20 – (a) RMS roughness and  (a) height distribution for all five devices.**

Figure 7.21 shows the PSD plot using (a) raw data and (b) normalised data for each device. Figure 7.21(b)(iii) shows that the highest proportion of ideal domain sizes for efficient charge separation are produced by **D10**. When this blend is annealed at 200°C , **D11**, the proportion of domains in (iii) and (iv) falls steeply accompanied by an increase in the proportion of large domains. This is consistent with the images in figures 7.18 and 7.19 which show large crystallites. When annealed at 50°C, **D9**, we see a smaller proportion of domains in (iii) and a higher proportion of finer domains in (iv). Based on this we would expect **D10** to produce the most efficient PV device using the blend of **1** and **4**. **D9** may have less well percolated charge pathways as a result of having a high proportion of domains that are too small. This would lead to increased non-geminate charge recombination. **D11** may have less efficient charge separation and increased geminate recombination as a result of having mostly large domains.

The domains for **D7** relative to **D8** were discussed in section 7.3. Comparing the two devices annealed at 200°C, **D8** and **D11**, we that the former has a larger proportion of domains within the ideal size range (iii). These results confirm a key difference between the two blends. The blend of **1** and **4** can reorganise in the nematic phase at 120°C whilst the blend of **3** and **4** requires a higher temperature to optimise morphology.
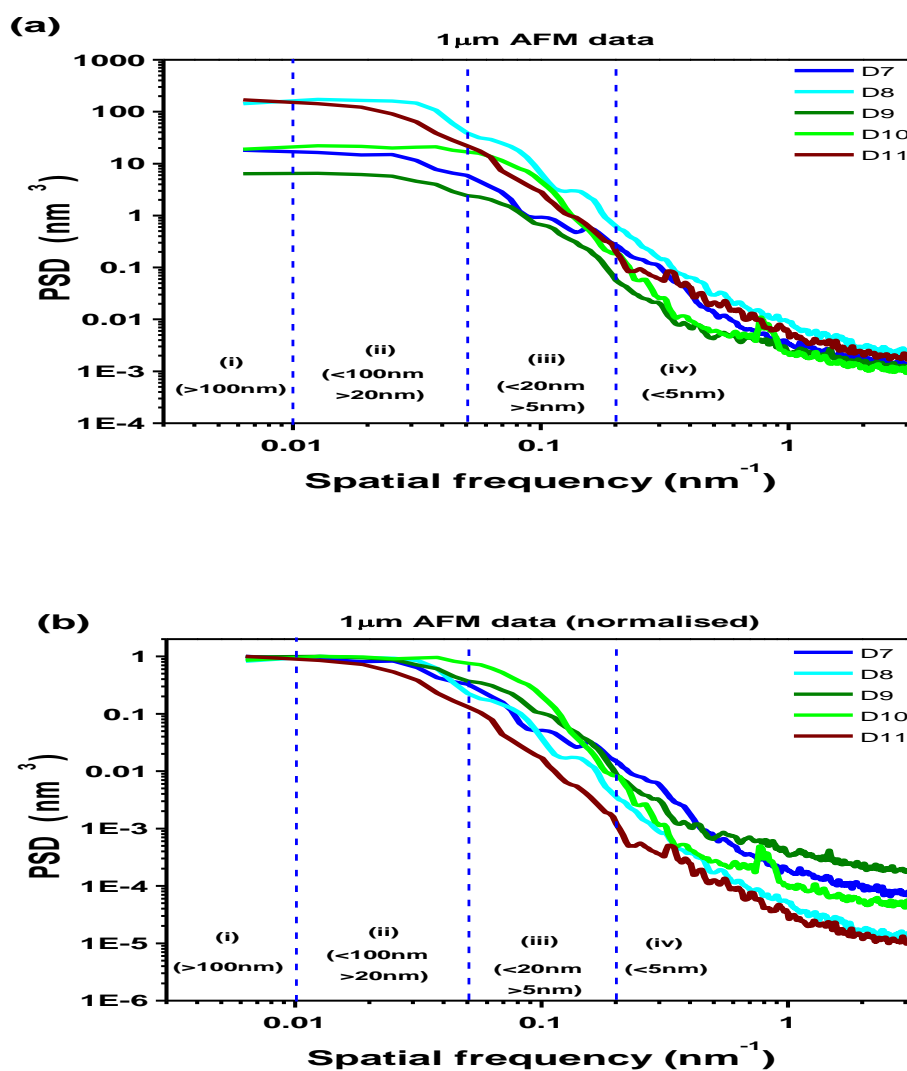


**Figure 7.21 – Power spectral density for each sample from 1μm image (a) raw data and (b) normalised.**

We now correlate the PV device performance to the morphology of the active layer, the device parameters are presented in table 7.8.

**Table 7.8 – PV device performance parameters for all D7 – D11 upon excitation with 24mWcm$^{-2}$ at 462nm. Measurements for D9, 10 and 11 made by Alkhalifah[57].**

| Device Number | $J_{SC}$ (Acm-2) | $V_{OC}$ (V) | FF | $\eta$ (%) | EQE (%) |
|---|---|---|---|---|---|
| D7 | 3.35 x 10$^{-4}$ | 0.94 | 0.30 | 0.39 | 3.73 |
| D8 | 5.8 x 10$^{-4}$ | 1.17 | 0.35 | 0.98 | 6.46 |
| D9 | 3.81 x 10$^{-4}$ | 0.85 | 0.22 | 0.32 | 4.61 |
| D10 | 7.08 x 10$^{-4}$ | 1 | 0.36 | 1.14 | 8.31 |
| D11 | 2.1 x 10$^{-4}$ | 0.85 | 0.24 | 0.19 | 2.6 |

The improvements in device efficiency between **D9** and **D10** are similar to the improvements shown between **D7** and **D8**. This may be due to the improved film morphology giving phase separation on the correct scale as a result of annealing in the nematic phase for both blends. However, upon annealing at 200°C for **D11** the device efficiency drops significantly. According to our phase transition measurements, the donor component of the blend of **1** and **4** may well be in the isotropic phase whilst the acceptor component may have started to crystallise out. This is in accord with the AFM data which shows large crystallites. This would explain the drop in performance, as the crystallisation creates domains which are too large for efficient charge separation. Overall the device efficiencies correlate with the domain sizes identified from figure 7.21.

The most efficient devices are produced by annealing at 120°C and 200°C for the blend of **1** and **4** and the blend of **3** and **4** respectively. The annealing temperatures required to optimise device performance corresponds to the nematic phase for each blend.

# 7.6 Conclusion

The phase transition temperatures have been investigated for four blend ratios of the liquid crystalline donor **3** and the acceptor **4**. Differential scanning calorimetry was used to identify the phase transition temperatures of each blend. Each phase transition was further investigated using a polarisation microscope. It was shown that the liquid crystalline texture varied depending on the acceptor concentration.

The morphology of each device was studied using an atomic force microscope. It was shown that annealing in the LC phase allowed molecular reorganisation resulting in a significantly lower proportion of small domains <5nm. This suggests that better percolated charge pathways may have formed, which would reduce bimolecular recombination as seen for **D8**. The surface roughness also increased substantially, but despite this the highest power conversion efficiencies were achieved. The PV device efficiency was highest for the blend with the highest acceptor concentration, indicating that continuous paths allowing transport of electrons limits performance at lower acceptor concentration.

Photovoltaic devices were fabricated for the four blend ratios, which were annealed below and above the liquid crystal transition temperature for comparison. It was shown that annealing in the LC phase of the active layer led to improved device efficiencies, $\eta$ increased by 150% to 700% depending on the blend ratio. This is attributed to improved thin film morphology of the active layer due to the self organisation of the liquid crystal phase. It was shown that higher $J_{SC}$ and $V_{OC}$ values contributed to the much higher device efficiencies. It was further shown that bimolecular charge recombination was virtually eliminated when the device was annealed in the LC phase.

The phase transition temperatures of two blends were compared, using two different donors (**1** and **3**) with one acceptor (**4**). It was shown that, despite having almost identical chemical structures, the phase transition temperatures varied significantly. The PV performance of devices annealed at various temperatures were correlated with the phase transitions for both blends. It was shown that the best device performance was achieved by annealing at 120°C and 200°C for the blends of **1** with **4** and **3** with **4** respectively. In both cases the best annealing temperature was in the respective nematic LC phase of each blend. It was shown that annealing the blend of **1** and **4** in the LC phase also produced an increase in the proportion of domains in the ideal range for efficient charge separation and a reduction in the proportion of small domains.

# 8. Conclusion and Future Work

## 8.1 Summary of Findings

We have studied the electrochemical and optical properties of 27 organic materials, synthesised in house at the University of Hull. Cyclic voltammetry was used to measure the oxidation and/or reduction reaction of each compound. The absorption spectrum was used to estimate the optical energy band gap for some materials. Molecular changes within the central 6 ring unit had the largest impact on the energy levels, whilst the end groups had no significant effect. The addition of electron rich thiophenes to a structure generally results in a raised HOMO energy level. Phenyl groups lower the HOMO and raise the LUMO energy levels, increasing the energy band gap. Carbazole groups were shown to raise the HOMO energy level as a result of the nitrogen atom lowering the oxidation potential. Benzothiadiazole-thiophene structured compounds were identified as low band gap semiconductors. The benzothiadiazole core raised the HOMO and lowered the LUMO energy levels. The energy offsets between the HOMO and LUMO energy levels of the donor and acceptor molecules used in photovoltaic devices was shown to be large, leading to around 50% of the optical energy being lost by relaxation for some blends.

Charge transport was investigated for pure donor compounds and D/A blends. The Time of Flight technique was used to measure the mobility values. Hole mobility showed a positive electric field dependence for pure compounds and blends, whilst electron mobility exhibited a negative field dependence. The mobility of the perylene acceptors was shown to increase by two orders of magnitude when blended with a donor. It was suggested that this was as a result of a reduction in trapping within the blend, due to improved molecular organisation. The blends investigated showed well balanced charge transport.

We fabricated and characterised photovoltaic devices using seven different donors with a perylene acceptor. The highest device efficiency was produced by the blend of **1** and **4** with a power conversion efficiency of 0.7% under monochromatic illumination. Overall the fluorene-thiophene structured donors produced the best devices. The benzothiadiazole-thiophene based donors produced relatively low efficiencies, but still significantly higher than the fluorene-carbazole structured donors. All devices showed poor fill factors and it was suggested that this was as result of space charge limited (SCL) effects. It was further suggested that the acceptor material was responsible for the SCL effects.

The phase transitions were investigated for four different blend ratios of donor **3** mixed with the perylene acceptor **4**. Each blend investigated showed a nematic liquid crystalline phase. It was shown that annealing above the melting transition temperature, in the donor nematic phase, resulted in significant improvements to PV device efficiency, by between 150% to 700%. The improvement in efficiency was primarily due to an increase in the $J_{sc}$ and $V_{oc}$. It was suggested that molecules were better able to reorganise into phase-separated domains of optimum size, when in the nematic phase. The best PV device efficiency was 1% for the blend with the highest acceptor concentration. This was attributed to better percolated charge pathways for electron transport when the acceptor concentration was high. Donor **1** blended with **4** also produced higher efficiency PV devices when annealed in the liquid crystal phase.

## 8.2 Future Work

It has been shown that the efficiency of our PV devices is poor overall. We highlight several areas of investigation to improve device efficiency.

The materials should be improved by designing the HOMO and LUMO energy levels of potential donors and acceptors to provide smaller energy offsets. This would reduce the loss of absorbed optical energy due to relaxation during charge separation. New acceptor materials should be designed, such as a perylene core without the outer phenyl or fluorene groups. This would promote better intermolecular charge transport between the perylene groups, which may be impeded by the large end groups in our acceptor. It will also be useful to mix our donors with a standard acceptor, such as PCBM, to identify if our acceptor materials are the cause of the poor fill factors shown for our devices.

The literature shows that annealing a thin film after deposition of the top electrode leads to an improved device efficiency. This was particularly so when Calcium is used as a buffer layer, rather than the LiF used here. Devices with a Ca buffer between the active layer and top Al electrode should be investigated for our devices, and electrode deposition carried out before and after annealing for comparison. This may also help to improve contact resistance, which may also be a source of the poor fill factors shown by our devices.

The narrow band donor materials show promise, and warrant further investigation. Various blend ratios of donor and acceptor should be considered to find the optimum blend for PV device efficiency. New blends can be considered using two or more donors mixed together with an acceptor material. The phase transitions of these new blends should be investigated, the aim being to lower the Cr→N melting temperature. Although annealing in the LC phase increased device efficiency for the blend of **3** and

**4**, the high temperature annealing required may also have had some adverse effect on morphology. A lower temperature LC phase transition would enable us to benefit from the improved LC ordering without the negative effects of annealing at too high a temperature. Crosslinking could be used to lock-in the preferred domain structure for long term stability.

# 9. References

[1] EIA, "International Energy Outlook 2011," U.S. Energy Information Administration (2011).

[2] P. Moriarty and D. Honnery, "What is the global potential for renewable energy?," Renewable and Sustainable Energy Reviews **16** (1), 244-252 (2011).

[3] Defra, edited by food and rural affairs Department for environment (Crown, 2008), p. 69.

[4] S. Teske, T. Pregger, S. Simon et al., "Energy [R]evolution 2010-a sustainable world energy outlook," Energy Efficiency **4** (3), 409-433 (2011).

[5] N. S. Lewis and D. G. Nocera, "Powering the planet: Chemical challenges in solar energy utilization," PNAS **103** (43), 15729 - 15735 (2006).

[6] G. Dennler, M. C. Sharber, and C. J. Brabec, "Polymer-Fullerene Bulk-Heterojunction Solar Cells," Advanced Materials **21**, 1323-1338 (2009).

[7] Y. Sun, G. C. Welch, W. L. Leong et al., "Solution-processed small-molecule solar cells with 6.7% efficiency," Nature Materials **11** (1), 44-48 (2012).

[8] Paul Buckley, "Heliatek claims world record for organic solar cells with certified 9.8 percent cell efficiency," EE Times Europe (2011).

[9] Y. Wang, W. Wei, X. Liu et al., "Research progress on polymer heterojunction solar cells," Solar Energy Materials and Solar Cells **98**, 129-145 (2012).

[10] Martin A. Green, Keith Emery, Yoshihiro Hishikawa et al., "Solar cell efficiency tables (version 39)," Progress in Photovoltaics: Research and Applications **20** (1), 12-20 (2012).

[11] A. Luque and S. Hegedus, *Handbook of Photovoltaic Science and Engineering*. (Wiley, 2003), p.1138.

[12] J. Nelson, *The physics of solar cells*. (Imperial College Press, London, 2003), p.363p.

[13] Hyper-Physics, (Department of Physics and Astronomy, Georgia State University, Atlanta, Georgia, 2010), Vol. 2012.

[14] SNL, (Sandia National Laboratories Albuquerque, 2011), Vol. 2012.

[15] V. Avrutin, N. Izyumskaya, and H. Morko, "Semiconductor solar cells: Recent progress in terrestrial applications," Superlattices and Microstructures **49** (4), 337-364 (2011).

[16] Z. Fang, X. C. Wang, H. C. Wu et al., "Achievements and challenges of CdS/CdTe solar cells," International Journal of Photoenergy **2011** (2011).

[17] K. Petritsch, Ph.D. thesis, University of Cambridge, United Kingdom and Technische Universitat Graz, Austria, 2000.

[18] H. Hoppe and N. S. Sariciftci, "Organic solar cells: An overview," Materials Research Society **19** (7), 1924 - 1945 (2004).

[19] J. M. Nunzi, "Organic photovoltaic materials and devices," Comptes Rendus Physique **3** (4), 523-542 (2002).

[20] R. Farchioni and G. Grosso, *Organic Electronic Materials: Conjugated Polymers and Low Molecular Weight Organic Solids*. (Springer, 2001), p.439.

[21] Manea S. Alkhalifah, Ph.D. thesis, University of Hull, 2009.

[22] David Muehlbacher, Comparative Study of the Electrochemical and the Optical Band Gap of Organic Semiconductors, Ph.D. thesis, Linz Institute for Organic Solar Cells (LIOS) , Johannes Kepler University 2002.

23   A. Gadisa, "Studies of Charge Transport and Energy Levels in Solar Cells Based on Polymer/Fullerene Bulk Heterojunction," Linkoping University (2006).

24   T. W. Graham Solomons, *Organic Chemistry*. (John Wiley & Sons Inc, 1996).

25   V. I. Arkhipov, P. Heremans, and H. Bãssler, "Why is exciton dissociation so efficient at the interface between a conjugated polymer and an electron acceptor?," Applied Physics Letters **82** (25), 4605-4607 (2003).

26   B. P. Rand, D. P. Burk, and S. R. Forrest, "Offset energies at organic semiconductor heterojunctions and their influence on the open-circuit voltage of thin-film solar cells," Physical Review B - Condensed Matter and Materials Physics **75** (11) (2007).

27   N. Blouin, A. Michaud, D. Gendron et al., "Toward a rational design of poly(2,7-carbazole) derivatives for solar cells," Journal of the American Chemical Society **130** (2), 732-742 (2008).

28   C. Brabec, V. Dyakonov, J. Parisi et al., *Organic Photovoltaics: Concepts and Realization*. (Springer, Berlin, 2003), p.297.

29   B. P. Rand, J. Genoe, P. Heremans et al., "Solar cells utilizing small molecular weight organic semiconductors," Progress in Photovoltaics: Research and Applications **15** (8), 659-676 (2007).

30   C. Deibel, "Notes on Disordered Matter," http://blog.disorderedmatter.eu/2008/03/02/how-do-organic-solar-cells-function-part-one/ (2008).

31   C. Winder and N. S. Sariciftci, "Low bandgap polymers for photon harvesting in bulk heterojunction solar cells," Journal of Materials Chemistry **14** (7), 1077-1086 (2004).

32   B. Kippelen and J. L. Bradas, "Organic photovoltaics," Energy and Environmental Science **2** (3), 251-261 (2009).

33   H. Spanggaard and F. C. Krebs, "A brief history of the development of organic and polymeric photovoltaics," Solar Energy Materials & Solar Cells **83**, 125 - 146 (2004).

34   C. W. Tang, "Two-layer organic photovoltaic cell," Applied Physics Letters **48** (2), 183-185 (1986).

35   G. Yu, J. Gao, J. C. Hummelen et al., "Polymer photovoltaic cells: Enhanced efficiencies via a network of internal donor-acceptor heterojunctions," Science **270** (5243), 1789-1791 (1995).

36   J. J. M. Halls, C. A. Walsh, N. C. Greenham et al., "Efficient photodiodes from interpenetrating polymer networks," Nature **376** (6540), 498-500 (1995).

37   J. Y. Kim, S. H. Kim, H. H. Le et al., "New Architecture for High Efficiency Polymer Photovoltaic Cells Using Solution Based Titanium Oxide as an Optical Spacer," Advanced Materials **18**, 572 - 576 (2006).

38   A. Hayakawa, O. Yoshikawa, T. Fujieda et al., "High performance polythiophene/fullerene bulk-heterojunction solar cell with a TiOx hole blocking layer," Applied Physics Letters **90**, 163517 (2007).

39   B. Ray, P. R. Nair, and M. A. Alam, "Annealing dependent performance of organic bulk-heterojunction solar cells: A theoretical perspective," Solar Energy Materials and Solar Cells **95** (12), 3287-3294 (2011).

40   D. Gupta, S. Mukhopadhyay, and K. S. Narayan, "Fill factor in organic solar cells," Solar Energy Materials and Solar Cells **94** (8), 1309-1313 (2010).

41   C.J. Brabec, D. Meissner, and N.S. Sariciftci, "The influence of materials work function on the open circuit voltage of plastic solar cells," Thin Solid Films **403-404**, 368-372 (2002).

42    M. Carrasco-Orgozco, W. C. Tsio, M. O'Neill et al., "New Photovoltaic Concept: Liquid-Crystal Solar Cells Using a Nematic Gel Template," Advanced Materials **18**, 1754 - 1758 (2006).

43    W. C. Tsoi, M. O'Neill, M. P. Aldred et al., "Distributed Bilayer Photovoltaics Based on Nematic Liquid Crystal Polymer Networks," American Chemical Society **19**, 5475 - 5484 (2007).

44    B. P. Rand, P. Peumans, and S. R. Forrest, "Long-range absorption enhancement in organic tandem thin-film solar cells containing silver nanoclusters," J. Appl. Phys. **96** (12), 7519-7526 (2004).

45    J. Xue, S. Uchida, B. P. Rand et al., "Asymmetric tandem organic photovoltaic cells with hybrid planar-mixed molecular heterojunctions," Applied Physics Letters **85** (23), 5757-5759 (2004).

46    Y. K. Jin, K. Lee, N. E. Coates et al., "Efficient tandem polymer solar cells fabricated by all-solution processing," Science **317** (5835), 222-225 (2007).

47    M. Drees, Ph.D. thesis, Virginia Polytechnic Institute and State University 2003

48    S. M. Sze and Kwok K Ng, *Physics of Semiconductor Devices*, 3rd ed. (John Wiley & Sons Inc, New Jersey, 2007), p.815.

49    H. Kawamoto, "The history of liquid-crystal displays," Proceedings of the IEEE **90** (4), 460-500 (2002).

50    G. W. Gray and P. A. Windsor, *Liquid Crystals & Plastic Crystals*. (Ellis Horwood Limited, Chichester, 1974), p.383.

51    R. J. Bushby and O. R. Lozman, "Photoconducting liquid crystals," Current Opinion in Solid State and Materials Science **6** (6), 569-578 (2002).

52    P. G. de Gennes, *The Physics of Liquid Crystals*. (Oxford University Press, Oxford, 1974), p.347.

53    V. G. Chigrinov, *Liquid Crystal Devices: Physics and Applications*. (Artech House, Boston, 1999), p.357.

54    A. Ciferri, *Liquid Crystallinity in Polymers: Principles and Fundamental Properties*. (VCH Publishers Inc., New York, 1991), p.438.

55    C. J. Barret, "Barrett Research Group Website," http://barrett-group.mcgill.ca/ (2009).

56    S. Elston and R. Sambles, *The Oprics of Thermotropic Liquid Crystals*. (Taylor & Francis Ltd, London, 1998), p.375.

57    M S. Alkhalifah, Ph.D. thesis, University of Hull, 2010.

58    M. O'Neill and S. M. Kelly, "Liquid Crystals for Charge Transport, Luminescence and Photonics," Advanced Materials **15** (14), 1135 - 1146 (2003).

59    N. A. Plate, *Liquid-Crystal Polymers*. (Plenum Press, New York, 1993).

60    L. M. Blinov and V. G. Chigrinov, *Electrooptic Effects in Liquid Crystal Materials*. (Springer, New York, 1994), p.463.

61    P. J. Collins and M. Hird, *Introduction to Liquid Crystals*. (Taylor & Francis, London, 1997), p.298.

62    E. T. Samulski, "Macromolecular structure and liquid crystallinity," Faraday Discussions of the Chemical Society **79**, 7-20 (1985).

63    A. M. Donald and A. H. Windle, *Liquid Crystalline Polymers*. (University Press, Cambridge, 1992), p.309.

64    Mary O'Neill and Stephen M. Kelly, ('Semiconducting Applications of Polymerizable Liquid Crystals', University of Hull, 2011), p. 42.

65    A. E. A. Contoret, S. R. Farrar, P. O. Jackson et al., "Polarized electroluminescence from an anisotropic nematic network on a non-contact photoalignment layer," Advanced Materials **12** (13), 971-974 (2000).

66    M. P. Aldred, A. E. A. Contoret, S. R. Farrar et al., "A full-color electroluminescent device and patterned photoalignment using light-emitting liquid crystals," Advanced Materials **17** (11), 1368-1372 (2005).

67    R. J. Baldwin, T. Kreouzis, M. Shkunov et al., "A comprehensive study of the effect of reactive end groups on the charge carrier transport within polymerized and nonpolymerized liquid crystals," J. Appl. Phys. **101** (2) (2007).

68    I. McCulloch, W. Zhang, M. Heeney et al., "Polymerisable liquid crystalline organic semiconductors and their fabrication in organic field effect transistors," Journal of Materials Chemistry **13** (10), 2436-2444 (2003).

69    Alicia Liedtke, PhD University of Hull, 2009.

70    S. Droge, M. S. A. Khalifah, M. O'Neill et al., "Grazing incidence X-ray diffraction of a photoaligned nematic semiconductor," Journal of Physical Chemistry B **113** (1), 49-53 (2009).

71    S. Droge, M. O'Neill, A. Lobbert et al., "A new approach to photoalignment: Photo-addition to a self-assembled monolayer," Journal of Materials Chemistry **19** (2), 274-279 (2009).

72    D. Adam, P. Schuhmacher, J. Simmerer et al., "Fast Photoconduction in the highly ordered phase of a discotic liquid crystal (hexhexylthio-triphenylene)," Nature **371**, 141-143 (1994).

73    K. L. Woon, M. P. Aldred, P. Vlachos et al., "Electronic Charge Transport in Extended Nematic Liquid Crystals," Chem. Mater. **18**, 2311 - 2317 (2006).

74    W. Pisula, M. Zorn, J. Y. Chang et al., "Liquid crystalline ordering and charge transport In semiconducting materials," Macromolecular Rapid Communications **30** (14), 1179-1202 (2009).

75    E. Bundgaard and F. C. Krebs, "Low band gap polymers for organic photovoltaics," Solar Energy Materials and Solar Cells **91** (11), 954-985 (2007).

76    R. Kroon, M. Lenes, J. C. Hummelen et al., "Small bandgap polymers for organic solar cells (polymer material development in the last 5 years)," Polymer Reviews **48** (3), 531-582 (2008).

77    F. B. Kooistra, J. Knol, F. Kastenberg et al., "Increasing the open circuit voltage of bulk-heterojunction solar cells by raising the LUMO level of the acceptor," Organic Letters **9** (4), 551-554 (2007).

78    M. C. Scharber, D. Mühlbacher, M. Koppe et al., "Design rules for donors in bulk-heterojunction solar cells - Towards 10 % energy-conversion efficiency," Advanced Materials **18** (6), 789-794 (2006).

79    S. S. Sun, "Optimum energy levels and offsets for organic donor/acceptor binary photovoltaic materials and solar cells," Materials Science and Engineering B: Solid-State Materials for Advanced Technology **116** (3 SPEC.ISS.), 251-256 (2005).

80    P. Peumans and S. R. Forrest, "Separation of geminate charge-pairs at donor-acceptor interfaces in disordered solids," Chemical Physics Letters **398** (1-3), 27-31 (2004).

81    J. S. Kim, J. H. Park, J. H. Lee et al., "Control of the electrode work function and active layer morphology via surface modification of indium tin oxide for high efficiency organic photovoltaics," Applied Physics Letters **91** (11) (2007).

82    H. Frohne, S. E. Shaheen, C. J. Brabec et al., "Influence of the anodic work function on the performance of organic solar cells," ChemPhysChem **3** (9), 795-799 (2002).

83    D. Cahen and A. Kahn, "Electron energetics at surfaces and interfaces: Concepts and experiments," Advanced Materials **15** (4), 271-277 (2003).

84 B. W. D'Andrade, S. Datta, S. R. Forrest et al., "Relationship between the ionization and oxidation potentials of molecular organic semiconductors," Organic Electronics: physics, materials, applications **6** (1), 11-20 (2005).

85 D. P. Piet, D. Danovich, H. Zuilhof et al., "Ionization potentials of porphyrins and phthalocyanines. a comparative benchmark study of fast improvements of Koopman's Theorem," Journal of the Chemical Society. Perkin Transactions 2 (8), 1653-1661 (1999).

86 A. J. Fry, *Synthetic organic electrochemistry*, 2nd ed. (Wiley, 1989), p.339.

87 P. A. Christensen and A. Hamnett, *Techniques and mechanisms in electrochemistry*. (Springer, 1994), p.379.

88 G. A. Mabbott, "An introduction to cyclic voltammetry," Journal of Chemical Education **60** (9), 697-702 (1983).

89 P. T. Kissinger and W. R. Heineman, "Cyclic voltammetry," Journal of Chemical Education **60** (9), 702-706 (1983).

90 Allen J. Bard and Larry R. Faulkner, *Electrochemical methods: Fundamentals and Applications*, 2nd ed. (John Wiley, New York, 2001), p.833.

91 S. Trasatti, "The absolute electrode potential: an explanatory note (Recommendations 1986)," Journal of Electroanalytical Chemistry **209** (2), 417-428 (1986).

92 Douglas A. Skoog, F. James Holler, and Timothy A. Nieman, *Principles of Instrumental Analysis*, 5th ed. (Sauders College Publishing, London, 1998), p.849.

93 A. M. Bond, E. A. McLennan, R. S. Stojanovic et al., "Assessment of conditions under which the oxidation of ferrocene can be used as a standard voltammetric reference process in aqueous media," Analytical Chemistry **50** (24), 2853-2860 (1987).

94 V. V. Pavlishchuk and A. W. Addison, "Conversion constants for redox potentials measured versus different reference electrodes in acetonitrile solutions at 25Â°C," Inorganica Chimica Acta **298** (1), 97-102 (2000).

95 R. R. GagnÃ©, C. A. Koval, and G. C. Lisensky, "Ferrocene as an internal standard for electrochemical measurements [1]," Inorganic Chemistry **19** (9), 2854-2855 (1980).

96 L. Micaroni, F. C. Nart, and I. A. HÃ¼mmelgen, "Considerations about the electrochemical estimation of the ionization potential of conducting polymers," Journal of Solid State Electrochemistry **7** (1), 55-59 (2003).

97 Jospeh Wang, *Analytical Electrochemistry*, 3rd ed. (John Wiley, Chichester, 2006), p.250.

98 David K. Gosser, *Cyclic Voltammetry: Simulation and Analysis of Reaction Mechanisms*. (VCH, Germany, 1993), p.154.

99 Cynthia G. Zoski, *Handbook of Electrochemistry*. (Elsevier, Oxford, 2007), p.892.

100 B. K. Tanner, *Introduction to the Physics of Electrons in Solids*. (Cambridge University Press, Cambridge, 1995), p.243.

101 S. Baranovski, *Charge Transport in Disordered Solids*. (John Wiley & Sons Ltd, 2006), p.460.

102 J. P. Colinge and C. A. Colinge, *Physics of semiconductor devices*. (Kluwer Academic, Boston, Mass, London, 2002), p.436.

103 M. Pope and C. E. Swenburg, *Electronic processes in organic crystals and polymers*. (Oxford University Press, Oxford, 1999).

104 O. D. Jurchescu, University of Groningen, 2006.

105 J. M. Marshall, "Carrier difusion in amorphous-seiconductors," Reports on Progress in Physics **46** (10), 1235-1282 (1983).

106 W Brütting, *Physics of organic semiconductors*. (Wiley-VCH, Weinheim, Chichester, 2005), p.536.

107 C .F Klingshirn, *Semiconductor Optics*. (Springer, New York, 1995), p.458.

108 F. Gutmann and L. E. Lyons, *Organic Semiconductors*. (John Wiley & Sons, Inc, New York, 1967), p.646.

109 James J. Brophy and John W. Buttrey, *Organic Semiconductors*, 1st ed. (The Macmillan Company, New York, 1962), p.243.

110 S. Tiwari and N. C. Greenham, "Charge mobility measurement techniques in organic semiconductors," Optical and Quantum Electronics **41** (2), 69-89 (2009).

111 J. Frenkel, "On pre-breakdown phenomena in insulators and electronic semi-conductors [3]," Physical Review **54** (8), 647-648 (1938).

112 S. D. Ganichev, E. Ziemann, W. Prettl et al., "Distinction between the Poole-Frenkel and tunneling models of electric-field-stimulated carrier emission from deep levels in semiconductors," Physical Review B - Condensed Matter and Materials Physics **61** (15), 10361-10365 (2000).

113 G. Pfister, "Hopping transport in a molecularly doped organic polymer," Physical Review B **16** (8), 3676-3687 (1977).

114 W. D. Gill, "Drift mobilities in amorphous charge-transfer complexes of trinitrofluorenone and poly-n-vinylcarbazole," J. Appl. Phys. **43** (12), 5033-5040 (1972).

115 H. Bassler, "Charge transport in random organic photoconductors," Advanced Materials **5** (9), 662-665 (1993).

116 A. Miller and E. Abrahams, "Impurity conduction at low concentrations," Physical Review **120** (3), 745-755 (1960).

117 H. Bassler, "Charge Transport in Disordered Organic Photoconductors a Monte Carlo Simulation Study," phys. stat. sol. (b) **175** (1), 15-56 (1993).

118 Paul M. Borsenberger and David S. Weiss, *Organic Photoreceptors for Xerography*, 1 ed. (CRC Press, New York, 1998), p.799.

119 T. Holstein, "Studies of polaron motion: Part I. The molecular-crystal model," Annals of Physics **281** (1-2), 706-724 (2000).

120 V. Coropceanu, J. Cornil, D. A. da Silva Filho et al., "Charge transport in organic semiconductors," Chemical Reviews **107** (4), 926-952 (2007).

121 R. A. Marcus, "Nonadiabatic processes involving quantum-like and classical-like coordinates with applications to nonadiabatic electron transfers," The Journal of Chemical Physics **81** (10), 4494-4500 (1984).

122 R. A. Marcus and N. Sutin, "Electron transfers in chemistry and biology," Biochimica et Biophysica Acta - Reviews on Bioenergetics **811** (3), 265-322 (1985).

123 N. Karl, K. H. Kraft, and J. Marktanner, "Charge carrier mobilities in dark-conductive organic thin films determined by the surface acoustoelectric travelling wave (SAW) technique," Synthetic Metals **109** (1), 181-188 (2000).

124 L. Dunn, B. Cobb, D. Reddy et al., "Dynamic characterization of charge transport in organic and polymer transistors," Applied Physics A: Materials Science and Processing **95** (1), 153-158 (2009).

125 Y. Ie, M. Nitani, T. Uemura et al., "Comprehensive evaluation of electron mobility for a Trifluoroacetyl- terminated electronegative conjugated oligomer," Journal of Physical Chemistry C **113** (39), 17189-17193 (2009).

126 M. Rao, R. P. Ortiz, A. Facchetti et al., "Studies of photogenerated charge carriers from donor-acceptor interfaces in organic field effect transistors. Implications for organic solar cells," Journal of Physical Chemistry C **114** (48), 20609-20613 (2010).

127 M. Schubert, C. Yin, M. Castellani et al., "Heterojunction topology versus fill factor correlations in novel hybrid small-molecular/polymeric solar cells," Journal of Chemical Physics **130** (9) (2009).

128 A. J. Mozer, N. S. Sariciftci, L. Lutsen et al., "Charge transport and recombination in bulk heterojunction solar cells studied by the photoinduced charge extraction in linearly increasing voltage technique," Applied Physics Letters **86** (11), 1-3 (2005).

129 M. J. Tan, W. P. Goh, J. Li et al., "Charge mobility and recombination in a new hole transporting polymer and its photovoltaic blend," ACS applied materials & interfaces **2** (5), 1414-1420 (2010).

130 G. Juska, N. Nekrasas, K. Genevicius et al., "Relaxation of photoexited charge carrier concentration and mobility in υc-Si:H," Thin Solid Films (451-452), 290-293 (2004).

131 R. G. Kepler, "Charge Carrier Mobility and Production in Anthracene," The Physical Review (119), 1226 (1960).

132 A. Pivrikas, N. S. Sariciftci, G. JuÅ¡ka et al., "A review of charge transport and recombination in polymer/fullerene organic solar cells," Progress in Photovoltaics: Research and Applications **15** (8), 677-696 (2007).

133 Kazuo Morigaki, *Physics of Amorphous Semiconductors*. (Imperial College Press, London, 1999), p.382.

134 T. Kreouzis, D. Poplavskyy, S. M. Tuladhar et al., "Temperature and field dependence of hole mobility in poly(9,9- dioctylfluorene)," Physical Review B - Condensed Matter and Materials Physics **73** (23) (2006).

135 H. Scher and E. W. Montroll, "Anomalous transit-time dispersion in amorphous solids," Physical Review B **12** (6), 2455-2477 (1975).

136 K. Kashima, H. Sato, K. Musha et al., "Carrier mobility for organic semiconductors: Reduction of noise of the short part drift time in the time of flight mobility method," Analytical Sciences **23** (10), 1249-1251 (2007).

137 Antonio M. Figueiredo Neto and Silvio R. A. Salinas, *The Physics of Lyotropic Liquid Crystals: Phase Transitions and Structural Properties*. (Oxford University Press, Oxford, 2005), p.400.

138 J. P. Schmidtke, R. H. Friend, M. Kastler et al., "Control of morphology in efficient photovoltaic diodes from discotic liquid crystals," The Journal of Chemical Physics **124**, 174704-174701 to 174704-174706 (2006).

139 L. S. Li and A. P. Alivisatos, "Semiconductor Nanorod Liquid Crystals and Their Assembly on a Substrate," Advanced Materials **15** (5), 408 - 411 (2003).

140 M.A. Carrasco-Orozco, T. Stirner, M. O'Neill et al., "Superlattices of organic/inorganic semiconductor nanostructures from liquid crystal templates," Physical Review **B75**, 035207 (2007).

141 G. Bergmann, P.O. Jackson, J.H.C. Hogg et al., "Photoinduced changes of surface order in coumarin side-chain polymer films used for liquid crystal photoalignment," Applied Physics Letters **87**, 061914-061911 to 061914-061913 (2005).

142 Q. Sun, L. Dai, X. Zhou et al., "Bilayer and bulk heterojunction solar cells using liquid crystalline porphyrins as donors by solution processing," Applied Physics Letters **91**, 253505 (2007).

143 S.R. Farrar, A.E.A Contoret, M. O'Neill et al., "Non-dispersive hole transport of liquid crystalline glasses and crosslinked networks for organic electroluminescence."

144 K. Binder, "Theory of first-order phase transitions," Reports on Progress in Physics **50** (7), 783 (1987).

145 Avraam I. Isayev, Thein Kyu, and Stephen Z. D. Cheng, *Liquid Crystalline Polymer Systems Technological Advances*. (American Chemical Society, Washington, DC, 1995), p.418.

146 G. W. Gray and P. A. Windsor, *Physico-Chemical Properties and Methods of Investigation*. (Ellis Horwood, Chichester, 1974), p.313.

147 Satyen Kumar, *Liquid Crystals in the Nineties and Beyond*. (World Scientific Publishing Co., London, 1995), p.457.

148 E. M. Barrall Ii, "Specific heats of nematic, smectic, and cholesteric liquid crystals by differential scanning calorimetry," Journal of Physical Chemistry **71** (4), 895-900 (1967).

149 G. M. Russell, B. J. A. Paterson, C. T. Imrie et al., "Thermal characterization of polymer-Dispersed liquid crystals by differential scanning calorimetry," Chemistry of Materials **7** (11), 2185-2189 (1995).

150 MaterialsSolutions, (National Physics Laboratory, 2004).

151 PolymerScienceLearningCentre, (Department of polymer science, The University of Southern Mississippi, 2005), Vol. 2011.

152 Henry Noton Southworth, *Introduction to Modern Microscopy*. (Wykeham Publications, London, 1975), p.213.

153 A. Nesrullajev and N. Avci, "Oriented and non-oriented textures of nematic liquid crystals: Comparative peculiarities of the thermotropic behavior," Materials Chemistry and Physics (2011).

154 J. Xue, B. P. Rand, S. Uchida et al., "A hybrid planar-mixed molecular heterojunction photovoltaic cell," Advanced Materials **17** (1), 66-71 (2005).

155 S. Walheim, M. Boltau, J. Mlynek et al., "Structure formation via polymer demixing in spin-cast films," Macromolecules **30** (17), 4995-5003 (1997).

156 E. Moons, "Conjugated polymer blends: Linking film morphology to performance of light emitting diodes and photodiodes," Journal of Physics Condensed Matter **14** (47), 12235-12260 (2002).

157 H. J. Snaith and R. H. Friend, "Morphological dependence of charge generation and transport in blended polyfluorene photovoltaic devices," Thin Solid Films **451-452**, 567-571 (2004).

158 H. Hoppe, T. Glatzel, M. Niggemann et al., "Efficiency limiting morphological factors of MDMO-PPV:PCBM plastic solar cells," Thin Solid Films **511-512**, 587-592 (2006).

159 J. Loos, "The art of SPM: Scanning probe microscopy in materials science," Advanced Materials **17** (15), 1821-1833 (2005).

160 Roland Wiesendanger, *Scanning Probe Microscopy and Spectroscopy Methods and Applications*. (Cambridge University Press, Cambridge, 1994), p.637.

161 S. Kossek and M. Flowers, (Nanoscience Instruments, 2002).

162 Peter J. Eaton and Paul West, *Atomic Force Microscopy*. (Oxford University Press, Oxford, 2010), p.248.

163 H. Hoppe, M. Niggemann, C. Winder et al., "Nanoscale morphology of conjugated polymer/fullerene-based bulk-heterojunction solar cells," Advanced Functional Materials **14** (10), 1005-1011 (2004).

164 T Vorburger and J Fu, "In The Rough," SPIE emagazine, 31-34 (2002).

165 D. J. Whitehouse, *Handbook of Surface and Nanometrology* (Institute of Physics Publishing, Bristol, 2003), p.1150.

166 Eugene Hecht, *Optics*, 4th (international) ed. (Pearson, London, 2002), p.680.

167 J. F. James, *A Student's Guide to Fourier Transforms: With Apllications in Physics and Engineering*, 3rd ed. (Cambridge University Press, Cambridge, 2011), p.160.

168 Steven W. Smith, *The scientist and engineer's guide to digital signal processing*. (California Technical Pub, San Diego, 1998), p.626.

169 M. Senthilkumar, N. K. Sahoo, S. Thakur et al., "Characterization of microroughness parameters in gadolinium oxide thin films: A study based on extended power spectral density analyses," Applied Surface Science **252** (5), 1608-1619 (2005).

170 R. Gavrila, A Dinescu, and D Mardare, "A power spectral density study of thin films morphology based on AFM profiling," Romanian Journal of Information Science and Technology **10** (3), 291-300 (2007).

171 Janelle Maureen Leger, University of California, 2005.

172 Laurell-Technologies, (Laurell Technologies Co., 2009).

173 Martin Tarr, (University of Bolton, Bolton, 2011), p. http://www.ami.ac.uk/courses/topics/0140_pl/index.html.

174 Philip C. Robinson and Michael W. Davidson, (MicroscopyU, The Florida State University, Florida, 2011), p. http://www.microscopyu.com/articles/polarized/polarizedintro.html.

175 A. Sharma, A. Haldi, W. J. Potscavage Jr et al., "Effects of surface modification of indium tin oxide electrodes on the performance of molecular multilayer organic photovoltaic devices," Journal of Materials Chemistry **19** (30), 5298-5302 (2009).

176 S. Besbes, H. B. Ouada, J. Davenas et al., "Effect of surface treatment and functionalization on the ITO properties for OLEDs," Materials Science and Engineering C **26** (2-3), 505-510 (2006).

177 A. Sharma, P. J. Hotchkiss, S. R. Marder et al., "Tailoring the work function of indium tin oxide electrodes in electrophosphorescent organic light-emitting diodes," J. Appl. Phys. **105** (8) (2009).

178 A. Sharma, A. Haldi, P. J. Hotchkiss et al., "Effect of phosphonic acid surface modifiers on the work function of indium tin oxide and on the charge injection barrier into organic single-layer diodes," J. Appl. Phys. **105** (7) (2009).

179 F. Steuber, J. Staudigel, M. Stössel et al., "Reduced operating voltage of organic electroluminescent devices by plasma treatment of the indium tin oxide anode," Applied Physics Letters **74** (23), 3558-3560 (1999).

180 I. M. Chan, W. C. Cheng, and F. C. Hong, "Enhanced performance of organic light-emitting devices by atmospheric plasma treatment of indium tin oxide surfaces," Applied Physics Letters **80** (1), 13-15 (2002).

181 I. Yoo, M. Lee, C. Lee et al., "The effect of a buffer layer on the photovoltaic properties of solar cells with P3OT:fullerene composites," Synthetic Metals **153** (1-3), 97-100 (2005).

182 Y. Kim, A. M. Ballantyne, J. Nelson et al., "Effects of thickness and thermal annealing of the PEDOT:PSS layer on the performance of polymer solar cells," Organic Electronics: physics, materials, applications **10** (1), 205-209 (2009).

183 L. S. C. Pingree, B. A. MacLeod, and D. S. Ginger, "The changing face of PEDOT:PSS films: Substrate, bias, and processing effects on vertical charge transport," Journal of Physical Chemistry C **112** (21), 7922-7927 (2008).

184 H. J. Snaith, H. Kenrick, M. Chiesa et al., "Morphological and electronic consequences of modifications to the polymer anode 'PEDOT:PSS'," Polymer **46** (8), 2573-2578 (2005).

185 S. Koyuncu, I. Kaya, F. B. Koyuncu et al., "Electrochemical, optical and electrochromic properties of imine polymers containing thiophene and carbazole units," Synthetic Metals **159** (11), 1034-1042 (2009).

186 K. Oyaizu, T. Iwasaki, Y. Tsukahara et al., "Linear Ladder-Type pi-Conjugated Polymers Composed of Fused Thiophene Ring Systems," Macromolecules **37** (4), 1257-1270 (2004).

187 P. Kumar, K. Ranjith, S. Gupta et al., "Electrochemical copolymerization of thiophene derivatives; A precursor to photovoltaic devices," Electrochimica Acta **56** (24), 8184-8191 (2011).

188 I. McCulloch, M. Heeney, M. L. Chabinyc et al., "Semiconducting thienothiophene copolymers: Design, synthesis, morphology, and performance in thin-film Organic transistors," Advanced Materials **21** (10-11), 1091-1109 (2009).

189 E. Lim, B. J. Jung, and H. K. Shim, "Synthesis and characterization of a new light-emitting fluorene-thieno[3,2-b]thiophene-based conjugated copolymer," Macromolecules **36** (12), 4288-4293 (2003).

190 A. Liedtke, M. O'Neill, S. M. Kelly et al., "Optical properties of light-emitting nematic liquid crystals: A joint experimental and theoretical study," Journal of Physical Chemistry B **114** (37), 11975-11982 (2010).

191 A. C. Grimsdale and K. Müllen, "Oligomers and polymers based on bridged phenylenes as electronic materials," Macromolecular Rapid Communications **28** (17), 1676-1702 (2007).

192 S. I. Kato, S. Shimizu, H. Taguchi et al., "Synthesis and electronic, photophysical, and electrochemical properties of a series of thienylcarbazoles," Journal of Organic Chemistry **77** (7), 3222-3232 (2012).

193 Y. Li, B. Xu, H. Li et al., "Molecular engineering of copolymers with donor-acceptor structure for bulk heterojunction photovoltaic cells toward high photovoltaic performance," Journal of Physical Chemistry C **115** (5), 2386-2397 (2011).

194 E. Bundgaard and F. C. Krebs, "Large-area photovoltaics based on low band gap copolymers of thiophene and benzothiadiazole or benzo-bis(thiadiazole)," Solar Energy Materials and Solar Cells **91** (11), 1019-1025 (2007).

195 A. V. Patil, W. H. Lee, K. Kim et al., "Synthesis and characterization of dithienothiophene/benzothiadiazole based low band gap donor-acceptor copolymers for bulk hetero junction photovoltaic cells," Synthetic Metals **161** (17-18), 1838-1844 (2011).

196 F. Shi, G. Fang, F. Liang et al., "Broad absorbing low-bandgap polythiophene derivatives incorporating separate and content-tunable benzothiadiazole and carbazole moieties for polymer solar cells," European Polymer Journal **46** (8), 1770-1777 (2010).

197 M. M. Ling, P. Erk, M. Gomez et al., "Air-stable n-channel organic semiconductors based on perylene diimide derivatives without strong electron withdrawing groups," Advanced Materials **19** (8), 1123-1127 (2007).

198 M. Funahashi and J. I. Hanna, "Impurity effect on charge carrier transport in smectic liquid crystals," Chemical Physics Letters **397** (4-6), 319-323 (2004).

199 M. O'Neill and S. M. Kelly, "Ordered materials for organic electronics and photonics," Advanced Materials **23** (5), 566-584 (2011).

200 J. D. Kotlarski, D. J. D. Moet, and P. W. M. Blom, "Role of balanced charge carrier transport in low band gap polymer: Fullerene bulk heterojunction solar cells," Journal of Polymer Science, Part B: Polymer Physics **49** (10), 708-711 (2011).

201 G. Li, V. Shrotriya, J. Huang et al., "High efficiency solution processable polymer photovoltaic cells by self-organization of polymer blends," Nature **4**, 864 - 868 (2005).

202  I. Riedel, J. Parisi, V. Dyakonov et al., "Effect of temperature and illumination on the electrical characteristics of polymer-fullerene bulk-heterojunction solar cells," Advanced Functional Materials **14** (1), 38-44 (2004).

203  P. E. Keivanidis, V. Kamm, W. Zhang et al., "Correlating emissive non-geminate charge recombination with photocurrent generation efficiency in polymer/perylene diimide organic photovoltaic blend films," Advanced Functional Materials **22** (11), 2318-2326 (2012).

204  S. Beaupre, P. L. T. Boudreault, and M. Leclrec, "Solar-energy production and energy-efficient lighting: Photovoltaic devices and white-light-emitting diodes using poly(2,7-fluorene), poly(2,7-carbazole), and poly(2,7-dibenzosilole) derivatives," Advanced Materials **22** (8), E6-E27 (2010).

205  A. Kumar, S. Sista, and Y. Yang, "Dipole induced anomalous S-shape I-V curves in polymer solar cells," J. Appl. Phys. **105** (9) (2009).

206  Z. E. Ooi, T. L. Tam, A. Sellinger et al., "Field-dependent carrier generation in bulk heterojunction solar cells," Energy & Environmental Science **1** (2), 300-309 (2008).

207  M. R. Lilliedal, A. J. Medford, M. V. Madsen et al., "The effect of post-processing treatments on inflection points in currentvoltage curves of roll-to-roll processed polymer photovoltaics," Solar Energy Materials and Solar Cells **94** (12), 2018-2031 (2010).

208  G. Garcia-Belmonte, "Temperature dependence of open-circuit voltage in organic solar cells from generationrecombination kinetic balance," Solar Energy Materials and Solar Cells **94** (12), 2166-2169 (2010).

209  Dan Credgington, Rick Hamilton, Pedro Atienzar et al., "Non-Geminate Recombination as the Primary Determinant of Open-Circuit Voltage in Polythiophene:Fullerene Blend Solar Cells: an Analysis of the Influence of Device Processing Conditions," Advanced Functional Materials **21** (14), 2744-2753 (2011).

210  W. M. Li, J. C. Guo, X. Q. Sun et al., "Effects of illumination intensity and temperature on double-layer heterojunction organic photovoltaic device performance," Faguang Xuebao/Chinese Journal of Luminescence **32** (7), 724-728 (2011).

211  L. Jan Anton Koster, Martijn Kemerink, Martijn M. Wienk et al., "Quantifying Bimolecular Recombination Losses in Organic Bulk Heterojunction Solar Cells," Advanced Materials **23** (14), 1670-1674 (2011).

212  H. Li, S. Sun, T. Salim et al., "Conjugated polymers based on dicarboxylic imide-substituted isothianaphthene and their applications in solar cells," Journal of Polymer Science, Part A: Polymer Chemistry **50** (2), 250-260 (2011).

213  Yasser A. M. Ismail, Tetsuo Soga, and Takashi Jimbo, "Investigation of Annealing and Blend Concentration Effects of Organic Solar Cells Composed of Small Organic Dye and Fullerene Derivative," Advances in OptoElectronics **2011**.

214  G. Li, V. Shrotriya, Y. Yao et al., "Investigation of annealing effects and film thickness dependence of polymer solar cells based on poly(3-hexylthiophene)," J. Appl. Phys. **98** (4), 1-5 (2005).

215  W. H. Tseng, M. H. Chen, J. Y. Wang et al., "Investigations of efficiency improvements in poly(3-hexylthiophene) based organic solar cells using calcium cathodes," Solar Energy Materials and Solar Cells **95** (12), 3424-3427 (2011).

216  P. Peumans, S. Uchida, and S. R. Forrest, "Efficient bulk heterojunction photovoltaic cells using small-molecular-weight organic thin films," Nature **425** (6954), 158-162 (2003).

[217]    Y. M. Nam, H. Huh, and W. H. Jo, "Optimization of thickness and morphology of active layer for high performance of bulk-heterojunction organic solar cells," Solar Energy Materials & Solar Cells **94**, 1118-1124 (2010).

[218]    P. Wang, K. Yao, L. Chen et al., "Self-assembled mesogens modified fullerene for efficiently stable bulk heterojunction solar cells," Solar Energy Materials and Solar Cells **97**, 34-42 (2012).

[219]    P. Vlachos, B. Mansoor, M. P. Aldred et al., "Charge-transport in crystalline organic semiconductors with liquid crystalline order," Chemical Communications (23), 2921-2923 (2005).

[220]    D. Kekuda, J. H. Huang, K. C. Ho et al., "Modulation of donor-acceptor interface through thermal treatment for efficient bilayer organic solar cells," Journal of Physical Chemistry C **114** (6), 2764-2768 (2010).

[221]    N. Yilmaz Canli, S. Gaines, A. Pivrikas et al., "Chiral (S)-5-octyloxy-2-[{4-(2-methylbuthoxy)-phenylimino}-methyl]-phenol liquid crystalline compound as additive into polymer solar cells," Solar Energy Materials and Solar Cells **94** (6), 1089-1099 (2010).